Die approbierte Originalversion dieser Dissertation ist in der Hauptbibliothek der Technischen Universität Wien aufgestellt und zugänglich.
http://www.ub.tuwien.ac.at

The approved original version of this thesis is available at the main library of the Vienna University of Technology.
http://www.ub.tuwien.ac.at/eng

Technische Universität Wien
Vienna University of Technology

Dissertation

The Silicon Vertex Detector for b-tagging at Belle II

ausgeführt zum Zwecke der Erlangung des akademischen Grades eines Doktors der technischen Wissenschaften unter der Leitung von

Univ.Doz. Dipl.-Ing. Dr. techn. Manfred Krammer

Institut für Hochenergiephysik
der Österreichischen Akademie der Wissenschaften
und
Atominstitut der Österreichischen Universitäten

eingereicht an der Technischen Universität Wien
Fakultät für Physik

von

Dipl.-Ing. Manfred Valentan

Matrikelnummer: 0230427
Rienößlgasse 15 / 16
1040 Wien

Wien, am 24. September 2013

Kurzfassung

Das Belle-Experiment am Forschungszentrum KEK[1] (Tsukuba, Japan) lief erfolgreich von 1999 bis 2010, und bestätigte die theoretischen Vorhersagen der CP[2]-Verletzung. Um die Strahlintensität zu erhöhen ist eine Verbesserung des KEKB[3]-Speicherrings vorgesehen, die 2015 in Betrieb geht. Die Luminosität soll auf $8 \times 10^{35}\mathrm{cm}^{-2}\,\mathrm{s}^{-1}$ gesteigert werden, was in etwa das 40-fache des bisherigen Spitzenwerts ist. Die Verbesserung des Beschleunigers bedingt auch Änderungen am Belle-Detektor[4] im Allgemeinen, und am innersten Spurdetektor, dem SVD[5], im Speziellen. Der SVD wird komplett ersetzt, da er schon bisher an den Grenzen seiner Leistungsfähigkeit gearbeitet hat. Auch alle anderen Subsysteme werden verbessert und angepasst, was zum neuen Belle II-Experiment führt.

Das Ziel von Belle II ist die Suche nach Abweichungen vom Standardmodell der Teilchenphysik durch extrem präzise Messungen von seltenen Teilchenzerfällen, was einen komplementären Ansatz zu den direkten Suchen der hochenergetischen Hadronen-Beschleuniger darstellt. Der verbesserte SuperKEKB[6]-Beschleuniger wird Elektronen und Positronen mit einer Energie kollidieren, die einem angeregten Zustand des Υ-Teilchens entspricht. Dieses Teilchen zerfällt ausschließlich in ein B-Meson und sein Antiteilchen. Der Zerfallspunkt dieser Mesonen muss präzise bestimmt werden, was die gemeinsame Aufgabe von Belle II SVD, PXD[7] und CDC[8] ist. Das erlaubt die Messung von zeitabhängiger, durch Quarkmischungen bedingter CP-Verletzung. Außerdem misst der SVD die Zerfallspunkte von anderen Zerfallskanälen, die D-Mesonen und τ-Leptonen enthalten.

Die Kollisionsenergie ist mit 10 GeV recht klein, weshalb die dabei entstehenden Teilchen niedrigen Impuls aufweisen und damit stark von Vielfachstreuung beeinflusst werden, wenn sie Sensormaterial durchdringen. Deswegen müssen die im Belle II SVD verwendeten Sensoren im Hinblick auf Materialdicke optimiert werden, während Signalausbeute und Positionsgenauigkeit erhalten bleiben müssen. Die Erfüllung dieser Vorgaben ist durch den Einsatz von dünnen, doppelseitigen Silizium-Streifensensoren möglich.

Diese Doktorarbeit beschreibt die physikalische Motivation eine hochintensive B-Mesonen-"Fabrik" und einen hochpräzisen Teilchendetektor zu bauen, und gibt eine Einführung in das Belle II-Experiment, wobei alle beteiligten Detektorsysteme kurz nach Zweck und Funktion beschrieben werden. Der Belle II SVD wird detaillierter erklärt, wobei auf die Themen der mechanischen Struktur, der Sensoren, der Ausleseelektronik und der Kühlung eingegangen wird. Weiters werden die Grundlagen der Halbleiterphysik und der Herstel-

[1] KEK (Kō Enerugī Kasokuki Kenkyū Kikō) ist eine japanische Organization, die das größte Teilchenforschungslabor Japans in Tsukuba (Präfektur Ibaraki) betreibt
[2] CP: Charge-Parity (Ladung-Parität), kurz für Ladungs-Paritäts-Konjugation
[3] KEKB: KEK B-Mesonen-"Fabrik"
[4] In der Teilchenphysik werden die Wörter "Experiment" und "Detektor" oft synonym verwendet
[5] SVD: Silicon Vertex Detector
[6] SuperKEKB: Super KEK B-Mesonen-"Fabrik", die Verbesserung von KEKB
[7] PXD: PiXel Detector
[8] CDC: Central Drift Chamber

lung von Mikroelektronik beleuchtet, und das Prinzip von einseitigen und doppelseitigen Silizium-Streifensensoren wird detailliert erklärt.

Die Hauptaufgabe des Autors war die Entwicklung eines trapezförmigen, doppelseitigen Silizium-Streifensensors für den Vorwärtsbereich des Belle II SVD, angefangen bei den CAD[9]-Zeichnungen bis zur Produktion. Der Autor hat ein Programm entwickelt, mit dem schnell und flexibel rechteckige und trapezförmige doppelseitige Silizium-Streifensensoren entworfen werden können. Mit dieser Software wurde ein ganzer Wafer mit einem Sensor im Originalmaßstab, mehreren Testsensoren zur Layoutoptimierung und Teststrukturen bestückt. Die englische Firma Micron Semiconductor Ltd. produzierte in enger Zusammenarbeit mit dem Autor mehrere Lose an Prototyp-Sensoren.

Der Wafer enthält kleine Testsensoren, die speziell für die Optimierung der n-seitigen Streifenisolierung entwickelt wurden. Diese Sensoren erlauben die Untersuchung der p-stop-Isolierungsmethode (in den drei Ausformungen atoll, common, und einer kombinierten Variante) und der p-spray-Isolierungsmethode. Eingehende Untersuchungen dieser Sensoren in Teilchenstrahlen und bei Gamma-Bestrahlungen zeigten, dass die atoll p-stop Methode am besten geeignet ist für die Anwendung in Belle II.

Die trapezoiden Sensoren wurden vom Autor eingehend getestet, sowohl im Halbleiterlabor als auch in Teilchenstrahlen, die Alterungsbeständigkeit der Sensoren wurde durch Bestrahlungen und Wärmelastspiel nachgewiesen. Die Erkenntnisse aus den Messungen der Testsensoren und der großen Sensoren wurden in eine Verbesserung des Sensordesigns gegossen, das nach Produktion eines weiteren Prototypen-Loses wieder eingehend evaluiert wurde. Es konnte gezeigt werden dass der Sensor die Ansprüche des Belle II SVD erfüllt, und das Sensordesign wurde für die Produktion freigegeben. Im Zuge der Sensortests reiste der Autor viermal zu Teilchenstrahl-Experimenten an den CERN[10], und war für die komplette Analyse der genommenen Daten zuständig.

[9] CAD: Computer Aided Design

[10] CERN: Organisation (Conseil) Européenne pour la Recherche Nucléaire, Europäische Organisation für Kernforschung

Abstract

The Belle experiment at KEK[11] (Tsukuba, Japan) was successfully operated from 1999 until 2010 and confirmed the theoretical predictions of CP[12] violation. In order to increase the beam intensity, a major upgrade of the KEKB[13] collider is foreseen until 2015. The final goal is to reach a luminosity of $8 \times 10^{35} \mathrm{cm}^{-2}\,\mathrm{s}^{-1}$, which is about 40 times higher than the previous peak value. This also implies changes to the Belle detector[14] and its innermost tracking subdetector, the SVD[15], in particular. The SVD will be completely replaced, as it had already operated close to its limits in the past. All other subsystems will also be upgraded. This leads to the new Belle II experiment.

The aim of Belle II is to search for deviations from the Standard Model of particle physics by providing extremely precise measurements of rare particle decays, thus representing a complementary approach to the direct searches performed at high energy hadron colliders. The upgraded SuperKEKB[16] machine will collide electrons and positrons at the center-of-mass energy of excited states of the Υ particle, which hereafter decays to a B meson and its anti-particle. The decay vertices of these mesons have to be precisely measured by the Belle II SVD, together with the PXD[17] and the CDC[18]. This allows the measurement of time-dependent, mixing-induced CP asymmetry. In addition, the SVD measures vertex information in other decay channels involving D meson and τ lepton decays.

Since the collision energy is quite low (around 10 GeV), the emerging particles have low momentum and are subject to strong multiple scattering when traversing material. Therefore, all sensors of the Belle II SVD have to be optimised in terms of material thickness, while preserving high signal yield and position measurement accuracy. This will be possible by the development of thin, double-sided silicon microstrip sensors.

This PhD thesis includes the physics motivation for building a high luminosity B factory and a high precision particle detector, and an introduction to the Belle II experiment, outlining purpose and working principle of the involved subdetectors. More details are given on the Belle II SVD, including mechanical structure, sensors, electrical readout and cooling. Furthermore, the basics of semiconductor physics and silicon processing are reviewed, and the principles of single-sided and double-sided silicon microstrip sensors are explained in detail.

[11] KEK (Kō Enerugī Kasokuki Kenkyū Kikō) is a japanese organization whose purpose is to operate the largest particle physics laboratory in Japan, which is located in Tsukuba of Ibaraki prefecture
[12] CP: Charge-Parity, short for charge-parity conjugation
[13] KEKB: KEK B factory
[14] In particle physics the words “experiment” and “detector” are often used synonymously.
[15] SVD: Silicon Vertex Detector
[16] SuperKEKB: Super KEK B factory, the upgrade of KEKB
[17] PXD: PiXel Detector
[18] CDC: Central Drift Chamber

The author's main task was to develop a trapezoidal double-sided silicon microstrip sensor for the forward region of the Belle II SVD, from the initial CAD[19] drawings to the production. He developed a software framework aiming at fast and flexible design of double-sided silicon microstrip sensors, both for rectangular and trapezoidal shapes. Using this framework, a whole wafer was equipped with a full-scale trapezoidal sensor, several test sensors for optimising the layout, and test structures. Several batches of prototype sensors were produced by Micron Semiconductor Ltd. in England, in close collaboration with the author.

The wafer contains small test sensors dedicated to investigating the strip insulation on the n-side, featuring the p-stop blocking method (in three geometry patterns: atoll, common and a combined variant) and of the p-spray blocking method. These sensors have been extensively tested by the author in particle beams and gamma irradiations, showing that the atoll p-stop pattern is best suited for application at Belle II.

The full-scale prototype sensors were thoroughly tested by the author in the semiconductor laboratory and in particle beams, long-term stability has been demonstrated by irradiation and thermal cycling campaigns. The knowledge gained by examining the test sensors and full-scale sensors led to an update of the design of the full-scale sensor. After production of another prototype batch the updated design was evaluated, compliance with the requirements of the Belle II SVD were shown, and the sensor layout was released for production. In the course of the sensor tests the author went to four beam tests at CERN[20], and performed the analysis of the data taken.

[19] CAD: Computer Aided Design

[20] CERN: Organisation (Conseil) Européenne pour la Recherche Nucléaire, European Organization for Nuclear Research

Contents

I. Physics and detector background information **1**

1. Introduction **3**
1.1. Physics motivation . . . 3
1.1.1. CP violation and quark mixing . . . 5
1.1.2. The potential of B physics . . . 7
1.1.3. Vertexing and b-tagging . . . 8
1.1.4. How physics requirements define the experimental setup . . . 9
1.2. The KEKB collider . . . 11
1.2.1. Upgrade to SuperKEKB . . . 13
1.3. The Belle detector . . . 14
1.3.1. Upgrade to Belle II . . . 15

2. Details of the Silicon Vertex Detector **23**
2.1. Requirements and solutions . . . 24
2.2. Mechanical structure . . . 25
2.2.1. Ladder design . . . 27
2.2.2. End-rings, windmill structure and overlap . . . 29
2.3. Sensors . . . 31
2.3.1. Barrel sensors . . . 32
2.3.2. Forward sensors . . . 33
2.4. Readout System . . . 35
2.4.1. The APV25 chip . . . 35
2.4.2. Front end electronics - the Origami chip-on-sensor concept . . . 37
2.4.3. Readout chain . . . 39
2.5. Cooling . . . 40

3. Basics on silicon technology **45**
3.1. Intrinsic properties of silicon . . . 45
3.2. Extrinsic properties of doped silicon . . . 49
3.3. Carrier Transport . . . 53
3.3.1. Drift . . . 53
3.3.2. Diffusion . . . 54
3.4. Carrier generation and recombination . . . 55
3.4.1. Thermal generation . . . 56
3.4.2. Generation by electromagnetic excitation . . . 57

3.4.3. Generation by charged particles . . . 57
3.4.4. Charge carrier lifetime . . . 59
3.5. Basic semiconductor structures . . . 61
3.5.1. The p-n-junction or diode . . . 61
3.5.2. The n+-n or p+-p junction . . . 68
3.5.3. The metal-semiconductor contact . . . 68
3.5.4. The metal-oxide-semiconductor structure . . . 70
3.5.5. The oxide-semiconductor contact . . . 77
3.5.6. The polysilicon resistor . . . 78
3.6. Radiation damage by gamma irradiation . . . 79
3.6.1. Bulk damage . . . 79
3.6.2. Surface damage . . . 80

4. Single- and double-sided silicon microstrip sensors 81
4.1. Working principle . . . 81
4.2. Signal generation . . . 85
4.3. Noise sources . . . 87
4.4. Measuring a particle's position . . . 89
4.4.1. Clusters with one strip . . . 90
4.4.2. Clusters with more than one strip - binary readout . . . 91
4.4.3. Clusters with more than one strip - pulse height readout . . . 92
4.5. Two-dimensional position measurement . . . 94
4.5.1. Dealing with ghost hits . . . 95
4.5.2. Lorentz angle and windmill structure . . . 96
4.6. Design basics of a silicon microstrip sensor . . . 99
4.6.1. Strip geometry . . . 101
4.6.2. Breakdown protection . . . 105
4.6.3. Contact pads . . . 105
4.7. Manufacturing of silicon sensors . . . 106
4.7.1. Production of pure silicon . . . 106
4.7.2. General processing steps in microelectronics industry . . . 108

II. Sensor development and production 115

5. CAD Framework and Design Rules 117
5.1. The CAD framework SiDDaTA . . . 117
5.1.1. Extension of SiDDaTA to trapezoidal DSSDs . . . 119
5.2. Design rules . . . 120
5.2.1. Wafer design rules . . . 120
5.2.2. Sensor design rules . . . 121
5.2.3. Strip design rules . . . 121
5.2.4. Contact pad design rules . . . 122
5.2.5. Wafer layout . . . 123

6. Production of the trapezoidal DSSD 125
6.1. The process sequence by Micron Semiconductor Ltd. . . . 125

6.2. The produced devices . . . 134
6.2.1. Main trapezoidal sensor . . . 135
6.2.2. Baby sensors . . . 136
6.2.3. Test structures . . . 140

III. Measurements and test results **145**

7. Optimisation of n-side strip insulation **147**
7.1. Electrical characterisation of the test sensors . . . 149
7.1.1. Measurement equipment and setup . . . 149
7.1.2. Global measurements . . . 152
7.1.3. Strip scans . . . 153
7.2. Beam test setup . . . 156
7.2.1. Gamma irradiation . . . 158
7.2.2. Readout system and triggering . . . 159
7.2.3. Definition of the measured observables . . . 160
7.3. Beam tests 2010 & 2011 . . . 164
7.3.1. Results of sensors with every strip connected to the readout . . . 167
7.3.2. Results of sensors with every second strip connected to the readout . 171
7.3.3. Enhanced conductivity in unimplanted areas . . . 175
7.3.4. Connection to the interstrip capacitance . . . 180
7.3.5. Conclusions of the beam tests 2010 and 2011 . . . 182
7.4. Beam test 2012 . . . 183
7.4.1. Results of sensors with every strip connected to the readout . . . 185
7.4.2. Results of sensors with every second strip connected to the readout . 189
7.4.3. Irradiation effects on the SNR . . . 192
7.4.4. Irradiation effects on the relative signal . . . 193
7.4.5. Tracking and resolution estimation . . . 193
7.4.6. Conclusions of the beam test 2012 . . . 194
7.5. Beam test experience - lessons learned . . . 195

8. Quality assurance of the trapezoidal DSSD **197**
8.1. Electrical characterisation . . . 198
8.1.1. Global measurements . . . 198
8.1.2. Strip scans p-side . . . 199
8.1.3. Strip scans n-side . . . 202
8.1.4. Conclusions . . . 204
8.2. Long term measurement and thermal cycling . . . 205
8.2.1. Dark current . . . 206
8.2.2. Aluminium resistance . . . 210
8.2.3. Conclusions . . . 212
8.3. Beam test results . . . 213
8.3.1. Performance of the p-side . . . 217
8.3.2. Performance of the n-side . . . 221
8.4. Conclusions . . . 224
8.4.1. Sensor design experience - lessons learned . . . 225

9. Conclusion and outlook **227**

IV. Addendum **231**

10. Further details **233**
10.1. Geometrical definitions 233
10.1.1. The coordinate system 233
10.1.2. Acceptance region, barrel region, forward and backward region . . . 234
10.1.3. Parametrization of the trajectory of charged particles 236
10.2. AMPLE code example - the fundamental shape: a polygon with rounded corners 238

11. Geometry of the Belle II DSSDs - data sheets **247**
11.1. Large rectangular sensor 248
11.2. Small rectangular sensor 252
11.3. Trapezoidal sensor 256

Glossary **261**

Acronyms **287**

Bibliography **293**

Part I.

Physics and detector background information

New directions in science are launched by new tools more often than by new concepts. The effect of a concept-driven revolution is to explain old things in new ways. The effect of a tool-driven revolution is to discover new things that have to be explained.

Freeman Dyson

1 Introduction

1.1. Physics motivation

At the begin of the universe, matter and anti-matter were created from pure energy. In a perfect world, matter and anti-matter would have been created in equal amounts, so for every particle there is a matching anti-particle. However, when they meet, they annihilate back into energy.

In today's universe, all celestial bodies we see are made of matter, and throughout the whole visible universe there is no sign for the huge amounts of anti-matter that must have been created during the big bang. That consequently means that there must have been *more* matter than anti-matter, reflecting a so-called "baryon asymmetry" between particles and anti-particles. In 1967, the russian physicist Andrei Dmitrievich Sakharov found the criteria necessary for this form of asymmetry [1], being

- Violation of baryon number conservation
- Violation of charge conjugation symmetry and of charge-parity conjugation symmetry
- Thermal non-equilibrium

In nowadays particle physics a huge effort is taken to investigate charge-parity conjugation symmetry violation ("CP violation"). The current theory describing the interactions between elementary particles – the so-called Standard Model (SM[1]) – is one of the best verified physics theories ever. It explains three of the four known fundamental forces of nature[2],

[1] SM: Standard Model of particle physics
[2] The fourth fundamental force is gravitation

namely the electromagnetic force, the strong force and the weak interaction[3], and predicts their behaviour. These predictions have been verified experimentally with great accuracy, which led the scientific community to thoroughly accept the SM to be the state-of-the-art theory of fundamental interactions.

However, many basic questions remain unanswered in the SM. It is unknown why there are exactly three generations of elementary fermions[4]. The masses of the SM fermions and boson are external parameters of the theory, which have to be determined experimentally. The origin of mass itself is explained by spontaneous breaking of the electro-weak symmetry. This predicts the Higgs boson, which probably has been observed at CERN by the experiments ATLAS[5] and CMS[6] at the LHC[7], with a mass of about $126\,\mathrm{GeV/c^2}$ [2]. But to achieve such a low Higgs mass in theory, an unnatural cancellation (fine tuning) of SM parameters is needed. Furthermore, there is a roughly diagonal hierarchy of the CKM matrix[8], which describes quark mixing. This matrix also introduces a source of CP violation, which is needed to explain why there is no anti-matter in the universe. However, the CP violation of the CKM matrix is by far too little to be the only source of CP violation.

Summing up, the SM is a very successful and precise phenomenological concept, but there must be an underlying fundamental theory that explains all the mentioned discrepancies and phenomena.

There are several alternative theories and concepts that account for these problems, the best known are the concept of supersymmetry (SUSY[9]) and the so-called string theories, which require additional spatial dimensions. These and other scenarios beyond the SM predict new fundamental particles and processes, which – if they really exist – can either be generated directly by providing enough energy, or they can make themselves noticeable by tiny deviations from the predictions of the SM. Hence, research tries to find physics beyond the SM on two frontiers: the energy frontier and the rare/precision frontier. The former is pursued by high energetic particle colliders like the LHC with the multi-purpose experiments CMS and ATLAS.

The Belle II experiment and the KEKB collider operate at the rare/precision frontier. The collider is tuned to deliver a huge number of B mesons by colliding electrons and positrons. With this approach even very rare processes can be observed. Apart from that, colliding fundamental particles has the undisputed advantage of creating a very well known initial state, from which said B mesons emerge. Furthermore, the Belle II experiment is able to precisely measure the decay products of these B mesons. This leads to very accurate measurements of well known processes, which hereafter can be compared to the predictions

[3] The weak interaction acts on such short distances that it doesn't make sense to call it a "force". It neither accelerates particles nor holds them in bound states, as is the case for the other forces. Apart from that distinction, the terms "force" and "interaction" are interchangeable in particle physics
[4] Please refer to the glossary for explanations of technical terms
[5] ATLAS: A Toroidal LHC AparatuS
[6] CMS: Compact Muon Solenoid
[7] LHC: Large Hadron Collider
[8] CKM matrix: Cabbibo-Kobayashi-Maskawa matrix
[9] SUSY: SUperSYmmetry

of the SM. An observed discrepancy can be interpreted in terms of models beyond the SM.

1.1.1. CP violation and quark mixing

In modern day particle physics, nature's laws are expressed in terms of only a few fundamental concepts. One of these concepts is symmetry: Whenever a physical system is unchanged under a certain transformation, there must be a associated quantity, that is conserved in this transformation [3].

For a long time it was assumed that the so-called CP transformation leaves a system unchanged. The CP transformation is the combination of the charge conjugation ("C" charge reversal, i.e. reversion of all quantum numbers, converting a particle into it's anti-particle) and the parity conjugation ("P" transformation, mirroring a vector at its foot point). So, a system involving particles and a system involving anti-particles in an inverted coordinate system should behave exactly the same. But it turned out that the CP symmetry is violated [4].

CP violation was formally introduced in the standard model by Makoto Kobayashi and Toshihide Maskawa in 1973 [5]. Generalising the mechanism of quark mixing [6], Kobayashi and Maskawa used the complex unitary 3 x 3 CKM matrix, which postulates a third generation of quarks and reads

$$\begin{pmatrix} V_{\mathrm{ud}} & V_{\mathrm{us}} & V_{\mathrm{ub}} \\ V_{\mathrm{cd}} & V_{\mathrm{cs}} & V_{\mathrm{cb}} \\ V_{\mathrm{td}} & V_{\mathrm{ts}} & V_{\mathrm{tb}} \end{pmatrix} \begin{pmatrix} \mathrm{d} \\ \mathrm{s} \\ \mathrm{b} \end{pmatrix} = \begin{pmatrix} \mathrm{d}' \\ \mathrm{s}' \\ \mathrm{b}' \end{pmatrix}. \tag{1.1}$$

The CKM matrix formally takes into account that the mass eigenstates and the weak eigenstates[10] of the quarks are slightly different. So, the weak eigenstates are a linear combination of the mass eigenstates, and vice versa. On the left side of equation 1.1 the CKM matrix is multiplied by the down-type quarks' weak eigenstates to obtain the corresponding mass eigenstates.

Kobayashi and Maskawa realised that CP violation is only possible when the elements V_{ub} and V_{td} have a complex phase. Using the most common Wolfenstein parameterization [7], the CKM matrix from equation 1.1 can be written as

$$V_{\mathrm{CKM}} = \begin{pmatrix} 1 - \frac{\lambda^2}{2} & \lambda & A\lambda^3(\rho - j\eta) \\ -\lambda & 1 - \frac{\lambda^2}{2} & A\lambda^2 \\ A\lambda^3(1 - \rho - j\eta) & -A\lambda^2 & 1 \end{pmatrix}. \tag{1.2}$$

[10] Also called flavour eigenstates

The imaginary term η is the so-called Kobayashi-Maskawa phase, and A, λ and ρ are real numbers. Since the CKM matrix is unitary, we can use the relations

$$\Sigma_i V_{ij} V_{ik}^* = \delta_{jk} \qquad \text{and} \qquad \Sigma_i V_{ij} V_{kj}^* = \delta_{jk}. \tag{1.3}$$

This leaves us with six resulting combinations, which can be represented as triangles in the complex plane. Each of these equivalent combinations is called an "unitarity triangle". These triangles differs in shape, but enclose the same area, which is related to the CP violating Kobayashi-Maskawa phase η. The equation

$$(V_{\mathrm{ud}} V_{\mathrm{ub}}^* + V_{\mathrm{cb}} V_{\mathrm{cd}}^* + V_{\mathrm{td}} V_{\mathrm{tb}}^*)/(V_{\mathrm{cb}} V_{\mathrm{cb}}^*) = 0 \tag{1.4}$$

defines the most commonly used unitarity triangle, which is displayed in figure 1.1.

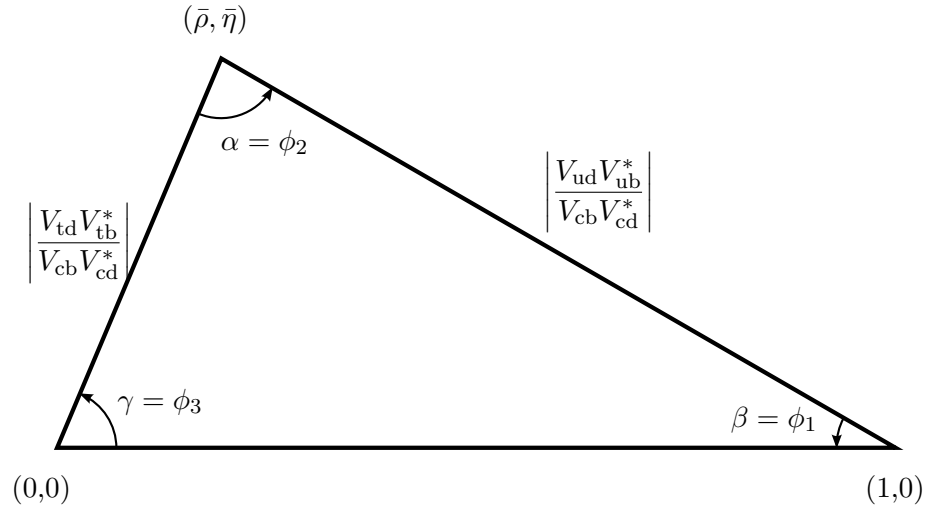

Figure 1.1.: The most common unitarity triangle. The sides and angles are subject to precision measurements, as the area is related to the CP violating Kobayashi-Maskawa phase η.

The aim is to determine the sides and angles of this triangle by precision measurements. This has been done – among others – by the experiments BaBar at Stanford, USA and Belle at Tsukuba, Japan. Up to now the results of these measurements show that equation 1.4 is valid and the triangle indeed is closed. With their theory confirmed, Kobayashi and Maskawa were awarded the nobel prize in physics of the year 2008, together with Yoichiro Nambu [8].

1.1.2. The potential of B physics

When trying to find new signs of CP violation and new physics phenomena, looking at B mesons has a number of advantages. These advantages make it feasible to build particle colliders and detectors specifically for studying B mesons:

1. B mesons contain a very heavy b quark, which is accompanied by a very light quark. This system is considerably easier to describe theoretically than a meson containing quarks of similar masses. So, the theoretical predictions can be calculated with high accuracy. This leads to highly significant results when comparing these predictions to the measurements.

2. When the b quark decays to a different quark flavour, this decay is mediated by the weak interaction. On the tree level, the down-type b quark has to decay to an up-type quark, and these decay modes are known to violate the CP symmetry (see figure 1.2). Including higher order effects, the b quark can decay to down-type quarks as well. These decay modes are sensitive to signs of physics beyond the SM[11].

3. B mesons can oscillate into their corresponding $\overline{\mathrm{B}}$ anti-mesons, and vice versa. This opens the possibility to study the time-dependent effects of CP violation.

4. B mesons are heavy enough to have τ leptons as possible decay products. These (semi-) leptonic decays are sensitive to the extended Higgs sector, which predicts charged Higgs particles. The interaction with the Higgs particle is proportional to the interacting particle's mass, so it is beneficial to be able to access the heaviest lepton.

5. B mesons can easily be generated in lepton colliders, which provide very clean collisions with tuneable energy. The beam energies are chosen to generate an excited state of the Υ particle, which has a mass slightly above the production threshold of a B meson and its corresponding anti-particle. So, the Υ particles decay almost exclusively to B mesons. Hence, a lepton collider provides a highly efficient tool to provide huge amounts of B mesons.

6. B mesons have a convenient life time in the order of 10^{-12} s [9], which can be measured by the (relativistically boosted) flight distance between the production point and the decay point. So, the life time measurement is translated to a position measurement, which can be carried out very precisely using state-of-the-art vertex detectors.

[11] In principle, the same reasoning can be applied to the kaon system. But because the B mesons contain a quark of the third generation, the number of decay possibilities is doubled, enhancing the potential to see signs of physics beyond the SM

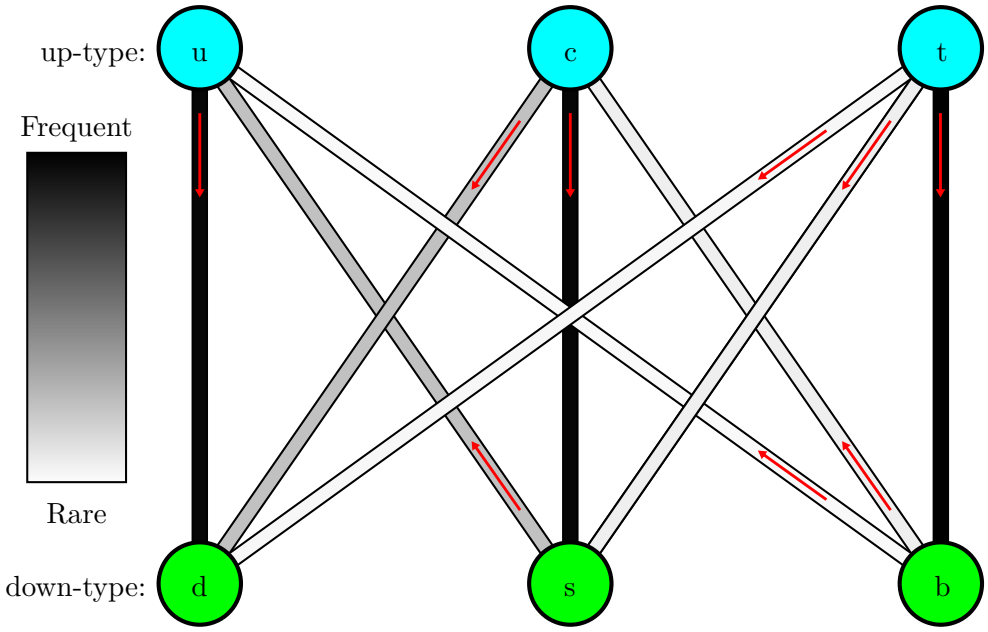

Figure 1.2.: The six quarks (up, down, charm, strange, top, bottom) and their weak decay possibilities. At tree level, an up-type quark has to decay to a down-type quark, and vice-versa. Black lines indicate frequent decays, other decay channels are suppressed and therefore happen less often.

1.1.3. Vertexing and b-tagging

Due to quark oscillations, B mesons and $\bar{\mathrm{B}}$ anti-mesons show a time-dependent asymmetry, which can be defined as follows:

$$a(\Delta t) = \frac{\Gamma\left(\mathrm{B}^0_{\mathrm{phys}}(t) \to f\right) - \Gamma\left(\bar{\mathrm{B}}^0_{\mathrm{phys}}(t) \to f\right)}{\Gamma\left(\mathrm{B}^0_{\mathrm{phys}}(t) \to f\right) + \Gamma\left(\bar{\mathrm{B}}^0_{\mathrm{phys}}(t) \to f\right)} = \sin(2\phi_1)\sin(\Delta m \Delta t), \tag{1.5}$$

where Γ denotes the branching fraction, $\mathrm{B}^0_{\mathrm{phys}}$ and $\bar{\mathrm{B}}^0_{\mathrm{phys}}$ are pure B^0 and $\bar{\mathrm{B}^0}$ mesons at the time of creation $t = 0$, f denotes a final state of the decay, Δm is the mass difference of the B mesons' mass eigenstates $\mathrm{B}_{\mathrm{heavy}}$ and $\mathrm{B}_{\mathrm{light}}$, Δt is the decay time difference, and ϕ_1 is one of the angles in the unitarity triangle. When using asymmetric beam energies, the Υ particle and thus the $\mathrm{B}^0\bar{\mathrm{B}^0}$ pair is not created at rest, but in motion. Thus, any decay time difference translates into a difference in decay position according to

$$\Delta z = \beta\gamma c \Delta t, \tag{1.6}$$

with $\beta = \frac{v}{c}$, v is the center-of-mass velocity, c is the speed of light, and $\gamma = \frac{1}{\sqrt{1-\beta^2}}$. The factor $\beta\gamma$ is the relativistic boost, which stretches the flight distance to a measurable magnitude.

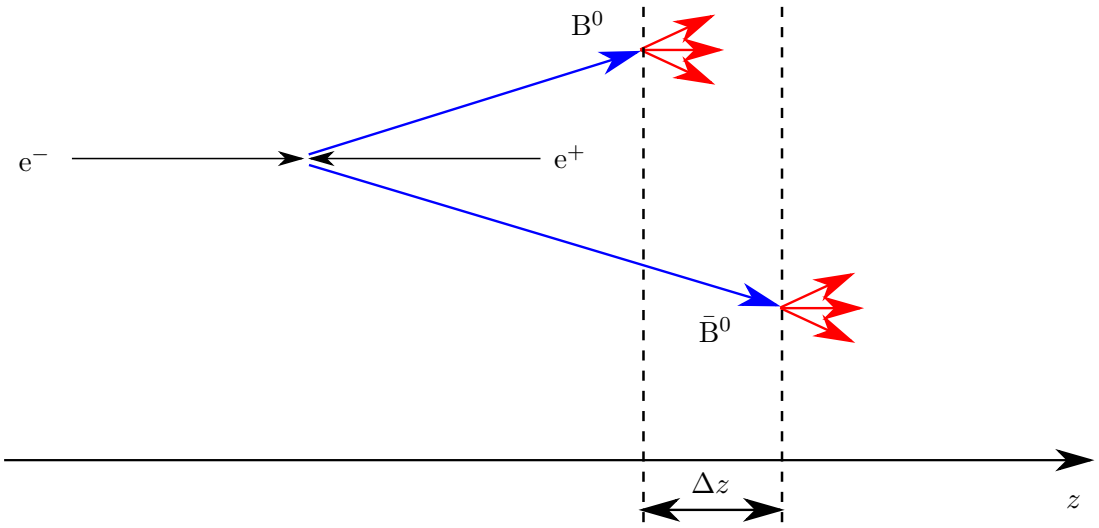

Figure 1.3.: Schematic sketch of a B event. The decay vertices of the B^0 meson and its anti-particle $\bar{B}^0$ are a distance Δz apart.

A B event can be identified by its quite distinctive decay pattern. Due to its quite long life time, a B meson can travel a considerable distance in the order of 150 µm before decaying, creating a secondary vertex. Since B mesons are created in a particle – anti-particle pair, one has to be able to distinguish the two secondary vertices from each other[12]. This is displayed in figure 1.3. Furthermore, one has to make sure that the decayed particle indeed was a B meson. This is done by analysing the decay products in terms of particle type and four-momentum. This procedure is called "b-tagging".

1.1.4. How physics requirements define the experimental setup

In usual particle physics experiments, the experimental setup is often defined by the available technology and financial feasibility rather than by the physics requirements. After determining what can be built, one can calculate which measurements can be done, and how much data has to be collected to yield meaningful results.

In contrast, for Belle II and already the predecessor experiment Belle there is the measurement of the decay time difference of the B meson and its anti-particle, which poses strict requirements on the detector setup. The mean flight distance between their decay points is in the order of $\Delta z \approx 150\,\mu\text{m}$. So, the decay vertices have to be measured with adequate accuracy to ensure clear distinction between a B meson and its anti-particle.

The inner tracking detector of a particle physics experiment has to be able to measure the traversing particles' tracks with enough accuracy to ensure sufficient vertex resolution. The

[12]Note that the primary decay vertex of the Υ particle is invisible

tracking accuracy of single tracks is usually expressed in terms of "impact parameter resolution". The impact parameter is the three-dimensional point of closest approach (PCA[13]) of the reconstructed track with respect to the real starting point. The width of the distribution of these PCAs is called impact parameter resolution.

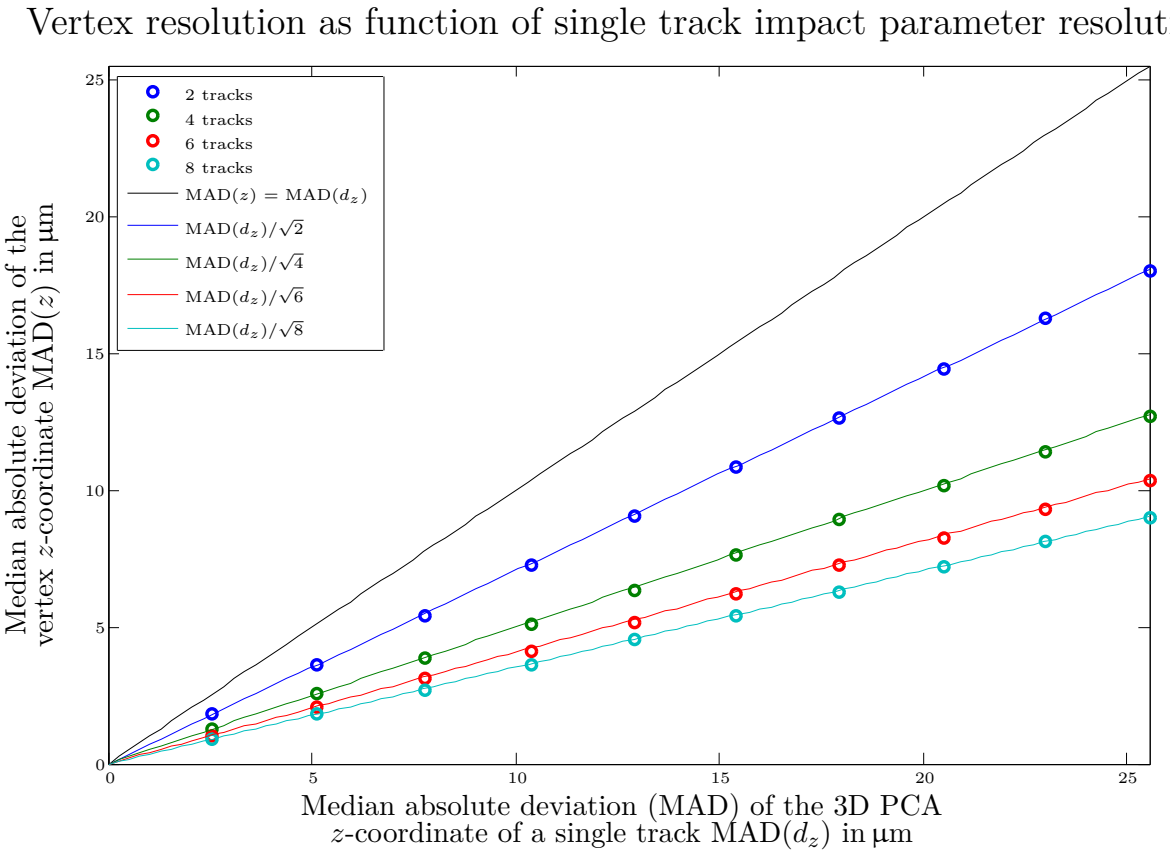

Figure 1.4.: Median absolute deviation vertex resolution in z as function of the impact parameter resolution in z. For parallel tracks the vertex resolution is always a factor $1/\sqrt{n}$ better than the single track impact parameter resolution, where n is the number of tracks used to reconstruct the vertex.

Figure 1.4 shows the vertex resolution as function of the impact parameter resolution – both expressed as MAD[14] – in direction of the beam axis[15], for simulated tracks perpendicular to the beam axis[16]. Simulation and reconstruction used the fast simulation tool LDT[17] [10], vertexing was performed with the RAVE[18] toolkit [11]. The simulation shows that in case of parallel[19] tracks the vertex resolution is always a factor $1/\sqrt{n}$ better than the single

[13] PCA: Point of Closest Approach
[14] MAD: Median Absolute Deviation
[15] The usual choice of the coordinate system puts the z-axis in direction of the beam, the x-axis is horizontal, and the y-axis is vertical. See section 10.1.1 for details.
[16] The details of the detector setup are irrelevant for vertexing, it only depends an the final impact parameter resolution of the single tracks, and their geometrical and kinematical relationship. The impact parameter resolution was varied by changing the position measurement accuracy of a sample detector setup.
[17] LDT: LiC Detector Toy, where LiC stands for "Linear Collider"
[18] RAVE: Reconstruction Algorithms in Versatile Environments
[19] All tracks perpendicular to the beam axis (z-axis) can be considered parallel, when determining the vertex resolution in z direction.

track impact parameter resolution, where n is the number of tracks used to reconstruct the vertex. For non-parallel tracks the impact parameter resolution poses an upper bound for the vertex resolution.

To securely be able to distinguish the two different vertices, the vertex resolution must be one order of magnitude better than the distance between the vertices. Therefore, the required impact parameter resolution becomes $\sigma(d_z) \leq 20\,\mu\text{m}$.

1.2. The KEKB collider

KEKB is an asymmetric electron-positron collider located at the High Energy Accelerator Research Organization (KEK) in Tsukuba, Japan [12]. Asymmetric means that the two particle beams operate at different (kinetic) energies. The collider is a so-called B factory aiming to produce B and $\bar{\text{B}}$ meson pairs exclusively. To this end, the center-of-mass energy is tuned to match the $\Upsilon(4\text{S})$ resonance at an energy of 10.58 GeV, or the $\Upsilon(5\text{S})$ resonance at an energy of 10.65 GeV [9]. The production energy threshold for a B-$\bar{\text{B}}$ pair is only slightly lower, and consequently the $\Upsilon(4\text{S})$ particle decays almost exclusively to B mesons, while the $\Upsilon(5\text{S})$ particle has more decay possibilities.

The reaction rate R in a collider is defined by

$$R = \sigma\mathcal{L}, \tag{1.7}$$

where σ is the energy dependent production cross section of the particle to be produced (the $\Upsilon(4\text{S})$ particle in case of KEKB), and $\mathcal{L}$ is called the luminosity, usually expressed in $\text{cm}^{-2}\text{s}^{-1}$.

The production cross section σ is a physical quantity which cannot be influenced. One can only tune the beam energy to match a peak (resonance) in the energy spectrum of the cross section. On the other hand, the luminosity is a parameter which is defined by the collider setup. In order to maximise the number of produced $\Upsilon(4\text{S})$ particles, one can aim to optimise the particle accelerator. For head-on colliding particle bunches, the luminosity can be expressed as

$$\mathcal{L} = fn\frac{N_1 N_2}{\sigma_x \sigma_y}. \tag{1.8}$$

Here, f is the revolution frequency, n is the number of bunches in the beams, N_1 and N_2 are the number of particles in the two colliding bunches, and the product $\sigma_x\sigma_y$ is the geometrical cross section of the beams.

Electrons and positrons are fed into two storage rings, the HER[20] for electrons and the LER[21] for positrons. Those rings are installed in the former TRISTAN tunnel which has a

[20] HER: High Energy Ring
[21] LER: Low Energy Ring

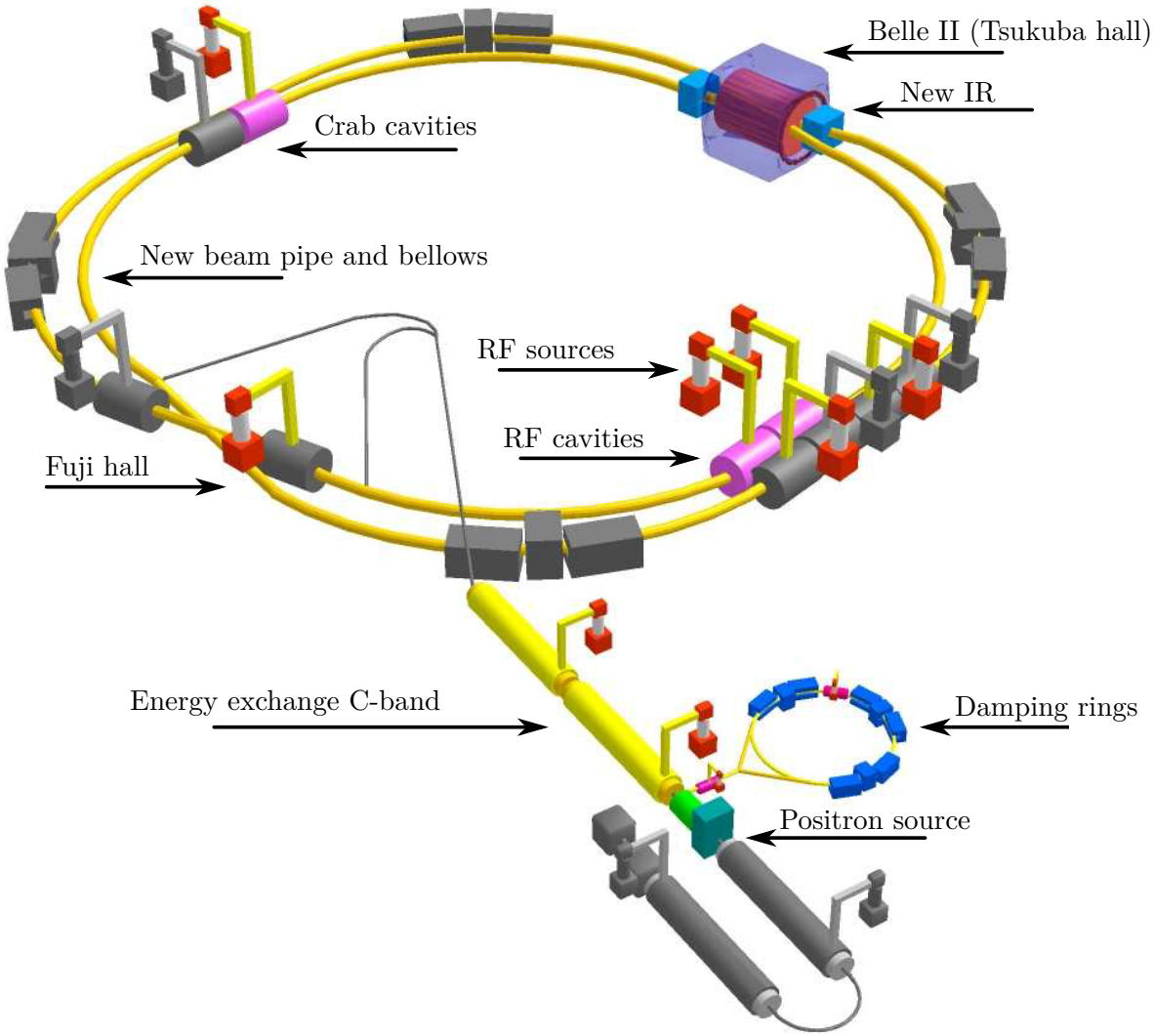

Figure 1.5.: Overview of the main differences between the KEKB and SuperKEKB colliders, and location of the Belle II detector [13]

3 km circumference and features four experimental halls. The Tsukuba hall hosts the Belle experiment and is the only interaction point (IP[22]) at KEKB. The Fuji hall is used for the beam injection from the adjacent LINAC[23] and allows to extract a particle beam for beam tests. A schematic layout of KEKB (and the future SuperKEKB) is shown in figure 1.5. The design luminosity of KEKB was $10^{34}\,\mathrm{cm}^{-2}\mathrm{s}^{-1}$, but with the introduction of several upgrades the peak luminosity reached a value of $2.108 \times 10^{34}\,\mathrm{cm}^{-2}\mathrm{s}^{-1}$ in June 2009 [14], breaking the luminosity world record.

[22]IP: Interaction Point
[23]LINAC: LINear ACcelerator

1.2.1. Upgrade to SuperKEKB

SuperKEKB is designed to have a 40 times higher luminosity than KEKB, with $\mathcal{L} = 8 \times 10^{35}\,\mathrm{cm}^{-2}\mathrm{s}^{-1}$. This will be achieved by adopting the so-called Nano-Beam scheme (see figure 1.6).

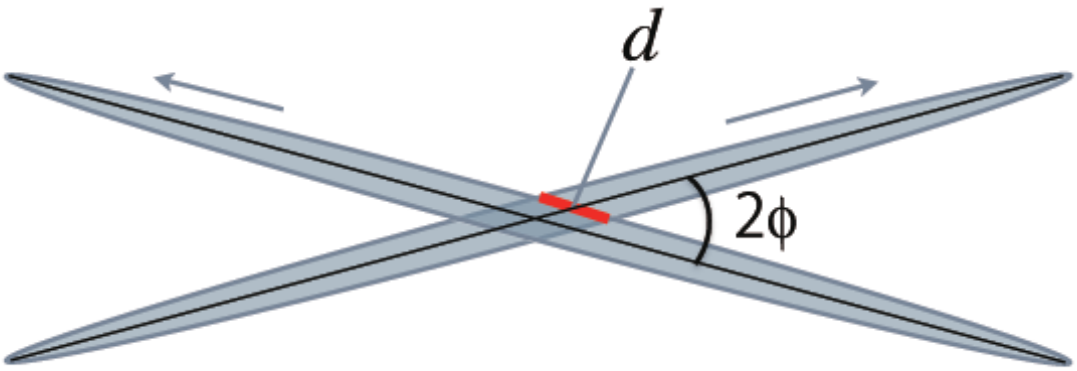

Figure 1.6.: Schematic view of beam collision in the Nano-Beam scheme [15].

Among others, the luminosity is inversely proportional to the vertical beta function β_y^* [15]:

$$\mathcal{L} \propto \frac{1}{\beta_y^*}. \tag{1.9}$$

The Nano-Beam scheme squeezes the vertical beta function β_y^* by minimizing the longitudinal size of the overlap region d of the two beams at the IP [15], which is a lower bound for the vertical beta function:

$$\beta_y^* > d, \qquad \text{with} \qquad d \cong \frac{\sigma_x^*}{\phi}. \tag{1.10}$$

The overlap d is minimized by increasing the overlap angle to $\phi = 41.5\,\mathrm{mrad}$ and squeezing the horizontal beam size to $\sigma_x^* = 10.2\,\mu\mathrm{m}$. A summary of important collider parameters is collected in table 1.1.

Due to the asymmetric beam energies, the center of mass system of the emerging particles is not at rest, but is in motion. So, a particle decaying after a life time t can travel a distance

$$z = \beta\gamma ct, \tag{1.11}$$

Table 1.1.: Machine Parameters of SuperKEKB.

Parameter	Symbol	LER (e^+)	HER (e^-)	unit
Beam energy	E	4	7	GeV
Half crossing angle	ϕ	41.5		mrad
Horizontal beam size	σ_x^*	10.2	7.75	µm
Vertical beam size	σ_y^*	59	59	µm
Bunch length	σ_z	6.0	5.0	mm
Beam current	I	3.6	2.62	A
Number of bunches/ring	N_b	2503		
Luminosity	$\mathcal{L}$	8×10^{25}		$cm^{-2}s^{-1}$
Radio frequency	f_R	≈ 508		MHz
Bunch collision rate	f_B	$f_R/(2 \ldots 3)$		MHz

along the z-axis, with $\beta = \frac{v}{c}$, v is the center-of-mass velocity, c is the speed of light, and $\gamma = \frac{1}{\sqrt{1-\beta^2}}$. For the beam energies to be used in Belle II the Lorentz boost factor becomes $\beta\gamma = 0.28$ [15].

1.3. The Belle detector

The former Belle experiment was a particle detector specifically designed to precisely measure the decay products of B mesons. The decay cascade ends up in particles long-lived enough to enter the detector to be measured. Consequently, the detector has to be able to measure each of these "final state" particles with high precision, in order to have a chance of reconstructing what happened in the primary interaction. Generally speaking, the long-lived particles to be measured in the detector are:

- Hadrons:
  - The proton p and the neutron n, and their anti-particles $\overline{p}$ and $\overline{n}$ (baryons)
  - The charged pions π^+ and π^- (mesons)
  - The charged kaons K^+ and K^-, the long-lived neutral kaon K_L^0 (mesons)
- Leptons:
  - The electron e^- and its anti-particle, the positron e^+
  - The muon μ^- and its anti-particle μ^+
- The photon γ

The neutrinos ν and their anti-particles are long-lived as well, but they interact only weakly with matter and can not be measured. They appear indirectly in form of "missing energy".

The instable particles K_S^0 (short-lived neutral kaon) and the mesons Δ^0, Σ^+, Ξ^0, Ξ^+, Ω^+ and their anti-particles can live long enough to leave signals in the tracking subdetectors before decaying into other particles. So, they can be detected directly by pattern recognition and track reconstruction and/or by their decay products.

The main components of the Belle detector are:

- Silicon Vertex Detector (SVD): Four layers of double-sided silicon microstrip sensors, aiming at precisely reconstructing the decay vertices of the B mesons.
- Central Drift Chamber (CDC): A large gaseous detector acting as main tracking device, measuring the tracks and momenta of the decay products.
- Silica-Aerogel Cherenkow Counter (ACC[24]): Used for particle identification, mainly to distinguish between pions and kaons.
- Time-of-Flight Counters (TOF[25]): Uses plastic scintillators to perform particle identification by measuring the particles' velocities, and provides precise timing signals for triggering and gating.
- Electromagnetical Calorimeter (ECL[26]): Detects photons and measures their energy and position with thallium-doped caesium iodide crystals.
- Kaon and Muon Detection System (KLM[27]): As outermost system the KLM detects muons and long-lived neutral kaons, and distinguishes between them, using alternating layers of glass-electrode resistive plate counters and iron plates.
- Superconducting Solenoid: Provides a homogeneous magnetic field of 1.5 T along the beam axis, which spans over all detector systems but the KLM. The coil wire is made of a superconducting Niobium-Titanium alloy, cooled down to 5 K using liquid helium. The iron layers of the KLM act as return yoke.

1.3.1. Upgrade to Belle II

With the advent of the new SuperKEKB collider, also the Belle detector needs a thorough overhaul. The 40-fold increase in luminosity poses considerable challenges especially to the innermost detector systems. The goal is to maintain the detector performance achieved by the former Belle experiment under tightened conditions in terms of background radiation and occupancy of the innermost layers.

The overall dimensions and the outer shape stay the same as in Belle. Some subdetector systems can even be reused. Figure 1.8 illustrates the upgrades in a cut view of the detector.

[24] ACC: silica-Aerogel Cherenkov Counter
[25] TOF: Time Of Flight
[26] ECL: Electromagnetic CaLorimeter
[27] KLM: K_L and Muon detection system

Figure 1.7.: The logo of the Belle II collaboration. It shows an "e" (which stands for an electron) and a mirrored "e" (which stands for a positron), that form a "B" meson. Without a B, Belle is reduced to the time-reversal-invariant palindronomic French pronoun "elle".

The following changes to the former Belle experiment will establish a comparable or better performance in the upgraded Belle II experiment:

- The innermost detector PXD will be made of two-layers of silicon pixel sensors based on the DEPFET[28] technology, which gives unambiguous 2D position measurements.
- The Silicon Vertex Detector (SVD) extends from just outside the PXD to a larger radius than before.
- The readout of the SVD is based on the APV25 chip with a much shorter shaping time than the previous readout based on the VA1TA chip, thus minimising the occupancy.
- The CDC has a finer granularity than in Belle and extends to a larger radius.
- The particle identification devices are renewed and yield higher performance while being more compact, with very fast readout electronics.
- The electronics of the ECL is upgraded, and a faster and radiation tolerant replacement of the endcap scintillator crystal is considered.
- The KLM endcap part is replaced by scintillators instrumented with silicon photomultipliers.
- The new data acquisition system (DAQ[29]) meets the requirements of considerably higher event rates.

With these changes, Belle II will offer improved performance than Belle on the following fields:

- The vertex resolution is improved by the excellent spatial resolution of the two innermost pixel detector layers.

[28] DEPFET: DEpleted P-channel Field Effect Transistor
[29] DAQ: Data AcQuisition

- The efficiency for reconstructing K_S decays to two charged pions with hits in the SVD is improved due to its larger volume.
- The new particle identification devices in the barrel and endcap regions extend the very good pion/kaon separation to the kinematic limits of the experiment.
- The new electronics of the ECL considerably reduce the occupancy, which is of particular importance for missing-energy studies.

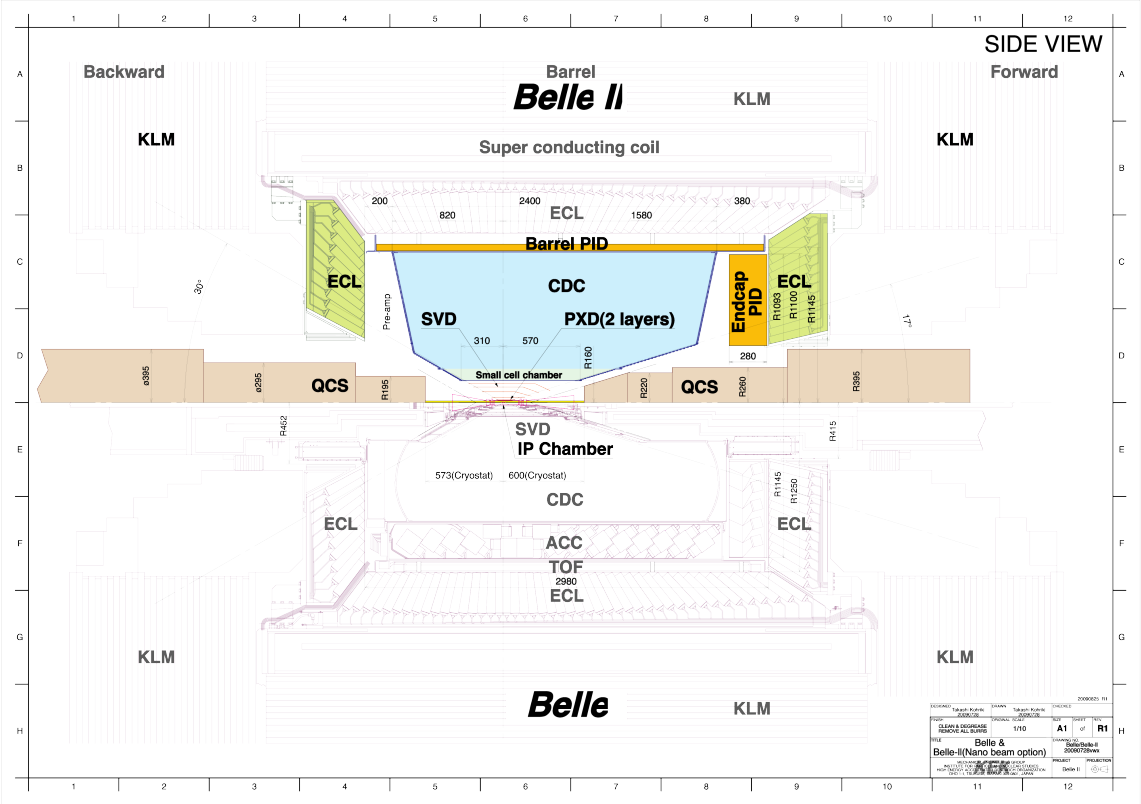

Figure 1.8.: Upgraded Belle II detector (top half) as compared to the former Belle detector (bottom half) [15].

The following sections describe the various subsystems in more detail. The information presented here is taken from the Belle II Technical Design Report [15]. Figure 1.8 shows a cross section of the detector and its subsystems.

Pixel Detector (PXD)

The high radiation environment at the heart of Belle II makes particle track measurements using silicon microstrip sensors impossible, because it drastically increases the occupancy. The increase in radiation is not only due to the enhanced luminosity, but also because of the reduced beam pipe radius. Therefore, the innermost detector layers are closer to the interaction point (IP). This leads to a higher vertex resolution, but also to increased radiation levels. Silicon microstrip sensors can't resolve these huge particle

densities, so the two innermost layers of track sensitive sensors will use silicon pixel sensors.

The PXD features DEPFET pixel sensors with a thickness of 75 µm, arranged in two cylindrical layers at the nominal radii of 14 mm and 22 mm. Being a low power device, which is "on" only during readout, cooling by cold air flow is sufficient. The pixel size is $50 \times 50\,\mu m^2$ for the inner layer and $50 \times 75\,\mu m^2$ for the outer layer.

Due to the large number of readout channels, it's not feasible to read out all pixels for each event. Therefore, the SVD will perform quick particle tracking to formulate so-called "regions of interest" in the PXD. Only the channels defined by these regions are read out.

Silicon Vertex Detector (SVD)

The Belle II SVD[30] consists of four layers equipped with double-sided silicon microstrip sensors (DSSD[31]s) at the nominal radii of 38 mm, 80 mm, 104 mm and 135 mm. Its task is to reconstruct the decay vertices of the B meson pairs, together with the CDC and the PXD. Furthermore it helps in measuring the deflection of charged particles in the solenoidal magnetic field, thus determining their momenta.

Due to the asymmetrical beam energies, also the SVD will be asymmetrical. The forward[32] part of the detector will have a conical shape instead of a cylindrical one, to save sensors, readout channels, material and money while still covering the acceptance region. The SVD is built to provide precise 2D measurement points of the particles' trajectories while maintaining a very lightweight structure to minimise scattering of traversing particles.

The PXD and the SVD team up symbiotically. Using a simple and fast tracking algorithm, the SVD will provide the "regions of interest" in the PXD, which makes readout of the PXD possible in the first place. In return, the PXD provides very precise and unambiguous 2D position measurements with low occupancy, which would not be possible with silicon microstrip sensors. The combined system of PXD and SVD will provide an impact parameter resolution of $\sigma(d_z) \approx 20\,\mu m$ in the z direction.

The readout system is built completely new, because it has to deal with the increased luminosity. The most prominent change is the new readout chip APV25 (developed the CMS experiment at the LHC), which replaces the considerably slower TA1VA chip. Section 2 gives some more detailed insights in the SVD.

[30] Not to be confused with the updated Silicon Vertex Detector of the former Belle experiment, which was called "SVD 2".
[31] DSSD: Double-Sided Silicon Detector
[32] See section 10.1.2 for a definition of the "forward" and "backward" parts and acceptance region

Central Drift Chamber (CDC)

The CDC is a large gaseous detector, which fulfils three major tasks: First, it reconstructs charged tracks and measures their momenta precisely from their deflection in the magnetic field. Second, it provides particle identification information using measurements of energy loss within its gas volume. Third, it provides efficient and reliable trigger signals for charged particles. The CDC of Belle worked very reliably, so the Belle II CDC will see only minor modifications.

The Belle II CDC consists of 56 cylindrical layers and a total number of 14336 sense wires. The length of the CDC is 1960 mm and its inner and outer radii are 160 and 1130 mm, respectively. In contrast to Belle, the inner part of the Belle II CDC will feature a reduced spacing between the wires to increase the granularity.

A mixture of 50% helium and 50% ethane is used, with a radiation length of about 640 m and a drift velocity that saturates at 4 cm/µs. The sense wires are made of gold-plated tungsten with 30 µm diameter, and are embedded in a grid of 126 µm thick aluminium field wires which produce a proper electrical field. The performance is assumed to be similar or better to what was achieved in Belle: The CDC provides a position resolution of 2 mm in z and about 100 µm in $R\Phi$ direction, and its relative momentum resolution is $\sigma(p_\mathrm{t})/p_\mathrm{t} = 0.2\,p_\mathrm{t} \oplus 0.30\%/\beta$, where p_t denotes the transverse momentum[33].

Particle identification devices

In the barrel region, the TOF and ACC of Belle are replaced by a so-called Time-of-Propagation (TOP[34]) ring imaging Cherenkov counter (RICH[35]). This counter measures the propagation time of Cherenkov photons which are internally reflected inside a quarz radiator. The Cherenkov image of traversing particles is reconstructed in 3D using the lateral 2D position information and the precise timing information as a third coordinate. This Cherenkov image is different for different particles, and allows distinction especially of kaons and pions.

The TOP instruments the barrel region around the CDC with synthetic fused silica quarz bars with size of $440 \times 1200 \times 20\,\mathrm{mm}^3$, which are arranged in 16 segments. The K/π separation efficiency is expected to be $> 99\%$, with a pion fake probability of $< 0.5\%$.

In forward and backward regions will feature a RICH with a 4 cm thick focusing aerogel radiator (ARICH[36]). The Cherenkov photons are produced in the radiator, which is follwed by an expansion volume of 20 cm thickness, allowing the photons to form rings on the adjacent position sensitive photon detectors. This detector system meets two strict

[33] $A \oplus B$ means $\sqrt{A^2 + B^2}$.
[34] TOP: Time Of Propagation
[35] RICH: Ring Imaging Cherenkov Counter
[36] ARICH: Aerogel Ring Imaging Cherenkov Counter

requirements: a high number of Cherenkov photons, and single-photon detectors that work in the high magnetic field of Belle II.

The K/π separation efficiency is expected to be 96%, with a pion fake probability of 1%, both measured at 4 GeV/c.

Electromagnetical Calorimeter (ECL)

In Belle II, the ECL of Belle will be reused. The accumulated radiation dose from ten years of operation in Belle has caused a light yield loss between 7% and 13%, in good agreement with the expectation. The light loss after operation at Belle II radiation levels will be in the order of 30%, which is perfectly tolerable.

The main tasks of the ECL are detection of photons from B meson decays with high efficiency and good resolution in energy and position, electron identification (together with the inner tracking devices), generation of trigger signals, luminosity measurements, and kaon detection (together with the KLM). The ECL consists of a highly granular array of thallium-doped caesium iodide crystals (CsI(Tl)). When a charged particle enters the calorimeter, its whole energy is deposited in the crystals whereby light is emitted. The intensity of this emitted light is proportional to the deposited energy, and is measured with photodiodes. Most of the particles that should be detected are products of cascade decays and thus have relatively low energy, hence the ECL is designed to have a good performance below 0.5 GeV.

The 3 m long ECL extends from a radius of 125 cm to 162 cm with 6624 crystals, complemented by endcaps at $z = -102$ cm and $z = 196$ cm for hermeticity, consisting of 2112 crystals in total. The expected relative energy resolution is $\sigma(E)/E = 0.02\%/E \oplus 1.6\%/\sqrt[4]{E} \oplus 1.2\%$ (E in GeV).

Superconducting Magnet

The superconducting solenoid provides a homogeneous magnetic field of 1.5 T in the central volume (length: 4 m, diameter 3.4 m) of the Belle II detector. All subdetectors except the KLM are located inside this magnetic field. It consists of a fixed barrel part, which includes the iron plates of the KLM and two movable endcaps to allow access to the inner components of the detector for maintenance. The coil wire is made of a superconducting Niobium-Titanium alloy, cooled down to 5 K using liquid helium. The magnetic field is used to determine the momentum of charged particles from the curvature of their trajectories, as well as to minimise the background of uninteresting low energetic particles.

Kaon and Muon Detection System (KLM)

The K_L^0 and muon detector (KLM) is the outermost, characteristically octagonal shaped subsystem of Belle II and consists of an alternating sandwich of 14 iron plates (5 cm thick) and 15 active detector elements in a 4 cm gap, located outside the superconducting solenoid. The iron plates serve as the magnetic flux return for the solenoid and as overall mechanical support for the detector as a whole. It is designated to detect muons and K_L^0 mesons, which penetrate through most materials and thus are hardly seen by the other detector subsystems. These particles interact with the iron plates and initiate a local shower of ionising particles, which are detected by the sensitive planes. The multiple layers of charged particle detectors and iron allow the discrimination between muons and kaons, since muons are more penetrating and leave the detector, while the kaons can be completely stopped.

The barrel part reuses the glass-electrode resistive plate counters from Belle, which can be operated at SuperKEKB conditions, too. The endcaps, however, are located in a much harsher radiation environment, so the resistive plate counters are replaced by scintillators instrumented with silicon photomultipliers.

The KLM will provide an angular measurement of K_L^0 mesons with an accuracy of 20 mrad in the barrel region and 10 mrad in the endcaps, and a hadron fake rate of about 1% for muons.

2

Details of the Silicon Vertex Detector

The main purpose of the Belle II SVD – together with the PXD and CDC – is to determine the decay vertices of the two B mesons for the measurement of CP violation, as well as to precisely measure the momentum of charged particles.

Only a subset of the particles traversing the detector leave a signal in the tracking subdetectors. The particles have to interact electromagnetically, so only the charged particles out of the ones mentioned in section 1.3 can be tracked[1].

The Belle II SVD pursues the good characteristics of predecessor: high precision, low mass, immunity to background hits, long-term stability and radiation tolerance. It is based on silicon microstrip sensors to avoid the large number of readout channels which are characteristic for silicon pixel sensors without compromising the vertexing capability of Belle II.

SuperKEKB collides electron and positron beams at $7\,\mathrm{GeV/c}$ and $4\,\mathrm{GeV/c}$, respectively. This results in a Lorentz boost factor of the center-of-mass system of $\beta\gamma = 0.28$, about two-thirds of what was used in Belle. Consequently, there will be less geometrical separation between the B meson vertices. However, the beam pipe radius at the interaction region is reduced proportionally, so the vertexing performance of the combined system of SVD and PXD is expected to be as good as or better than in Belle. The higher beam current and luminosity require the detectors to run at up to 30 kHz trigger rate and at a beam background up to 30 times larger.

[1] In principle, the photon interacts electromagnetically, too. However, when it interacts, it usually dissolves into a shower, which is only properly measurable in the ECL. The only way to leave a signal in a tracking sensor plane is via the Compton effect, in which a photon scatters at an electron in the material, giving it part of its energy. This electron can subsequently create a normal signal in the sensor.

2.1. Requirements and solutions

The main challenges of the Belle II SVD and their solutions in a nutshell:

- The SVD has to cover the full acceptance of $17° < \theta < 150°$.
- It has to be mechanically stable during installation, operation, maintenance and earthquakes.
- It has to be lightweight with a low material budget to reduce multiple scattering.
- Proper alignment has to be ensured by including enough sensor overlap.

These requirements are fulfilled by a careful mechanical structure based on lightweight ladder ribs made of a carbon fiber compound. The use of a slanted detector part in the forward region reduces the number of sensors and readout channels needed for covering the whole acceptance region. See section 2.2 for details.

- The SVD has to provide two-dimensional space points with excellent point resolution, while keeping the material budget to a minimum.
- It has to be radiation tolerant throughout the lifetime of Belle II, while maintaining reliable performance.

This is done using thin double-sided silicon microstrip sensors, and by applying the so-called "Origami" chip-on-sensor readout concept. Please find details in sections 2.3 and 2.4.

- Experience with Belle shows that the occupancy should be below 10% to allow the correct association of hits in the SVD with tracks reconstructed in the CDC.
- The SVD should operate with very low dead-time in the high trigger rate and beam-background environment of SuperKEKB.

This is achieved by using completely new readout electronics, based on a new readout chip with shorter shaping time and pipelined readout. See section 2.4 for details.

- The heat load has to be removed efficiently by its cooling system.

This is achieved by the closed two-phase CO_2 cooling system, which works highly efficient while requiring only very small cooling pipes. See section 2.5 for details.

The SVD therefore promises the following performance, compared to the former Belle SVD2:

- It improves the quality of charged track reconstruction.
- It provides data to extrapolate the tracks reconstructed in the CDC to the PXD with high efficiency.

- In combination with the PXD, it is able to reconstruct low-p_t tracks, down to a few tens of $^{\mathrm{MeV}}/_{\mathrm{c}}$, that do not leave enough (or any) hits in the CDC.
- It is able to reconstruct K_S mesons that decay outside of the PXD volume.

2.2. Mechanical structure

The mechanical structure is dictated by the requirements of a low-energy B physics experiment. The created particles have low momenta, thus being very sensitive to multiple scattering. Reducing the amount of material inside the acceptance region is therefore the top priority for designing the mechanical layout of the SVD.

Compared to the previous SVD, the new Belle II SVD has to operate under more challenging conditions. The radiation level is increased due to the changes to the collider, which not only poses strict requirements to the speed of the readout electronics. The mechanical setup of the SVD is influenced as well. To cope with the increased occupancy levels especially at small radius, the innermost detector layers can not be equipped with silicon microstrip sensors anymore, so silicon pixel sensors are used instead (forming the PXD). The innermost layer of the SVD is located at larger radius than in the previous Belle SVD2.

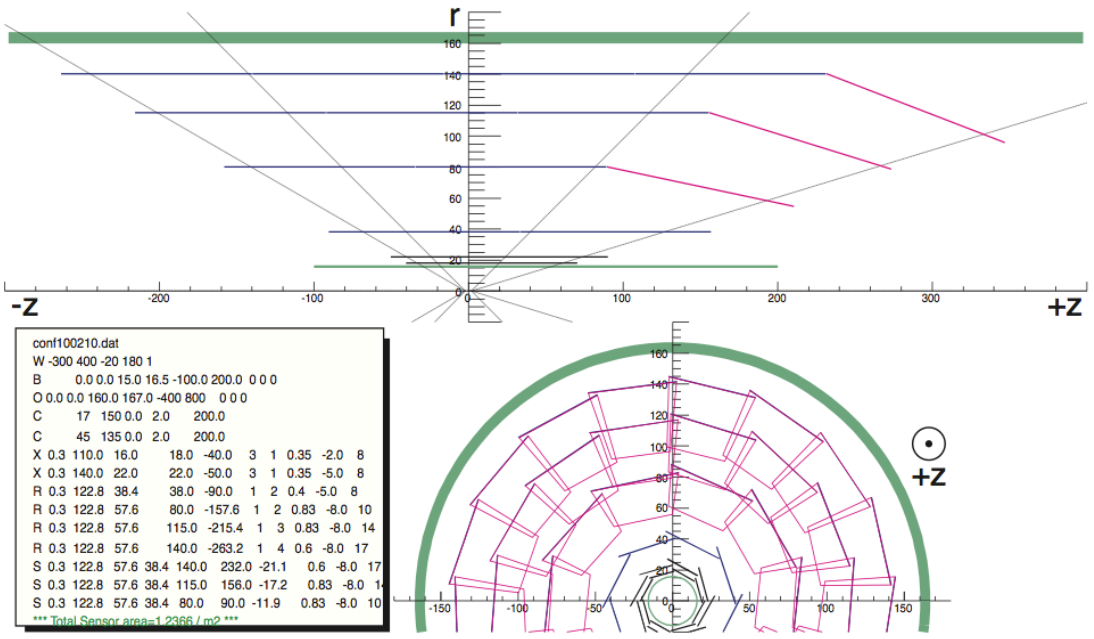

Figure 2.1.: Sketch of the four SVD layers, with slanted sensors in the forward region, and the two PXD layers. [15]

Despite the large area that has to be covered with sensors, the structure has to be as lightweight and transparent for particles as possible, while maintaining enough rigidity and stability for installation, operation and maintenance. The sensors are made as large as

possible, to save the relative amount of structural material. Moreover, the forward part is equipped with trapezoidal sensors, which introduce a conical shape of the detector layers. This saves material budget, sensors, readout channels and money while still covering the acceptance region. However, it also implies a more complex mechanical structure, and an additional challenge for particle tracking. A principal sketch of the SVD is shown in figure 2.1

Table 2.1.: Main parameters of the SVD layers and ladders [16]. Dimensions are given in mm.

Layer	Radius	Ladders	Length	Height	Sensors	Overlap	Angle (°)
6	135	16	644.0	46	80	10.8%	21.1
5	104	12	521.5	34	48	5.1%	16.0
4	80	10	398.5	26	30	17.6%	11.9
3	38	7	285.0		14	5.9%	

Table 2.1 gives an overview of the main parameters of the SVD. It consists of four layers[2] at increasing nominal radii[3]. Each layer consists of a number of identical basic building blocks, called "ladders". The ladders are composed of the sensors equipped with readout electronics and the support structure. Layers 4 to 6 feature trapezoidal (or wedge) sensors in the forward region, which are slanted w.r.t. the beam axis (see figure 2.2). The ladders of these layers are similar, thus allowing to apply the same construction and assembly methods. The ladders of layer 3, however, will reside in immediate vicinity of the PXD, making a different support structure mandatory.

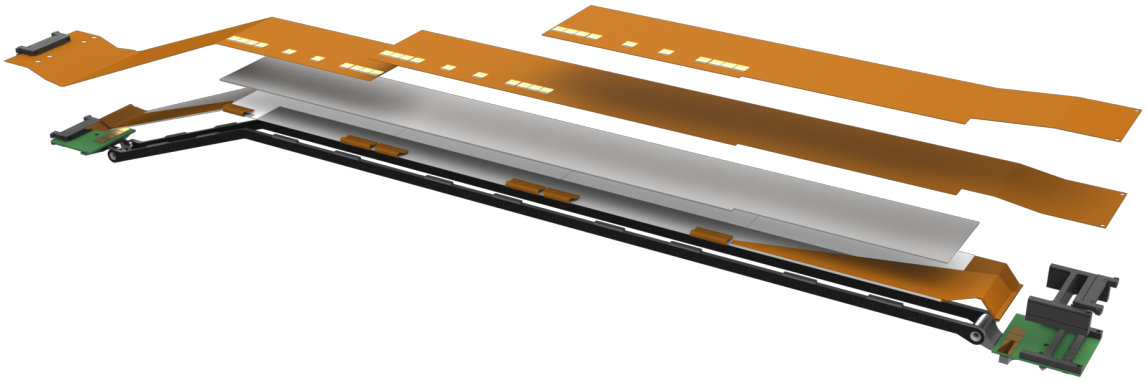

Figure 2.2.: The basic building block of the SVD is a "ladder". The ladder of layer 6 consists of four rectangular sensors, one trapezoidal sensor, readout electronics atop, support ribs at the bottom and mounting blocks at the ends. The dimensions of the hybrid board (green) and the connector stack above it are most critical when combining several ladders to a complete layer [16].

[2]The layers are counted from inside outwards, starting with number 3. The layers with numbers 1 and 2 are those of the PXD.

[3]For a definition of the nominal radius and the overlap see figure 2.7.

2.2.1. Ladder design

The ladder is the most important structural building block of the SVD. The sensors are mounted on ribs made of a carbon fiber sandwich structure. These ribs will support the sensors from "below", i.e. facing the beam axis[4] (see figure 2.2). From a physics point of view this solution is not ideal, because particles can be scattered or absorbed by the structural material before they even reach the sensors. However, the "top" side of the sensors (facing outwards) can only provide a warped surface for mounting the ribs due to the high density of electronics and cooling components found there (see sections 2.4 and 2.5).

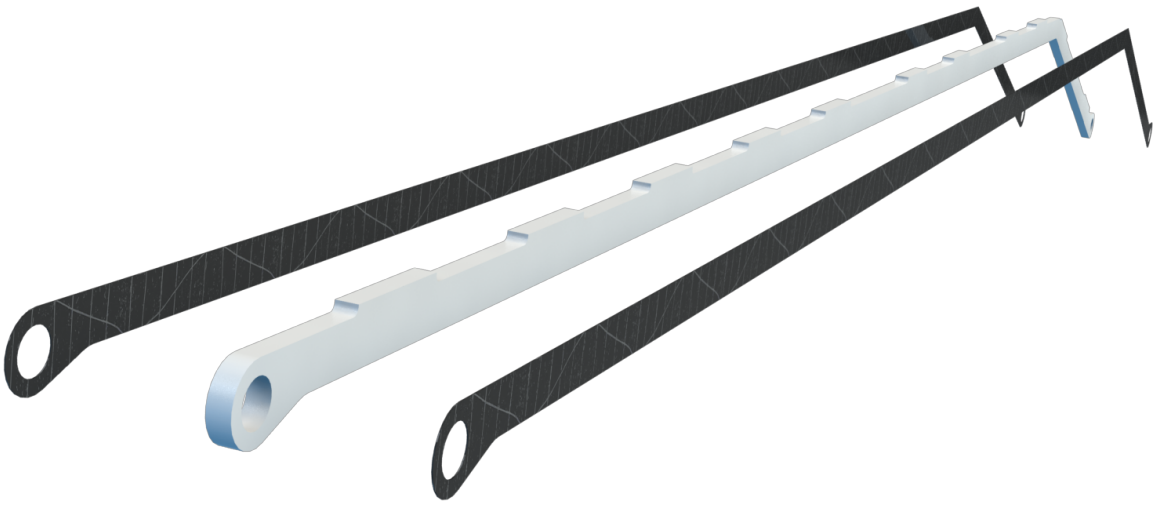

Figure 2.3.: Explosion drawing of the carbon fiber sandwich rib of layer 6. The core is made of Airex® R82.80.

The ribs are a sandwich structure with an Airex® R82.80 foam core [17] enclosed by two carbon fiber plies, as is displayed in figure 2.3. With this structure we can achieve enough mechanical stability with very lightweight materials. The stiff carbon fiber plies carry the load where the mechanical strain is high, while the lighter Airex® R82 foam core separates the plies, increasing the area moment of inertia.

The ribs are slim and roughly facing the interaction point, which makes it geometrically unlikely that a particle hits the structural material. Moreover the used materials have a very large radiation length, which leads to a small probability for interaction with the material, even if a particle does hit the rib. The averaged material budget of a ladder is close to 0.57% of a radiation length including ribs, sensors, electronics and cooling. Most of this material budget has its origin in the sensor material itself, the support structure accounts only for 0.08% [15].

The foam core features extensions along the top to which the sensors are glued. The electrically conductive carbon fiber plies do not cover these extensions to ensure proper

[4] except for layer 3, where the ribs are "above" the sensors due to space constraints

insulation. Furthermore these offsets prevent interference of mechanical structures with wire bonds on the sensors.

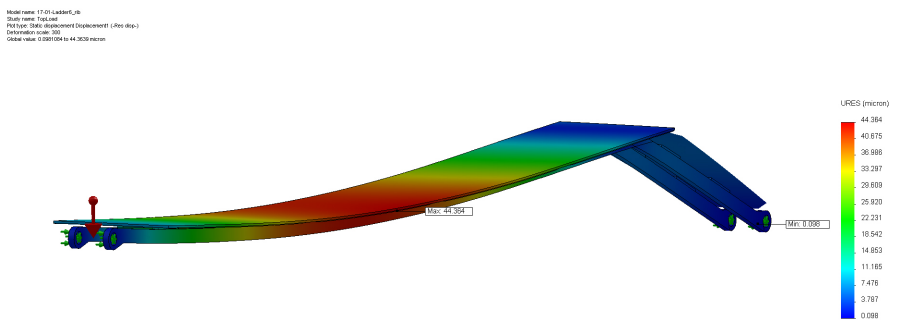

(a) 12 o'clock position: Maximum deformation ≈ 44 µm

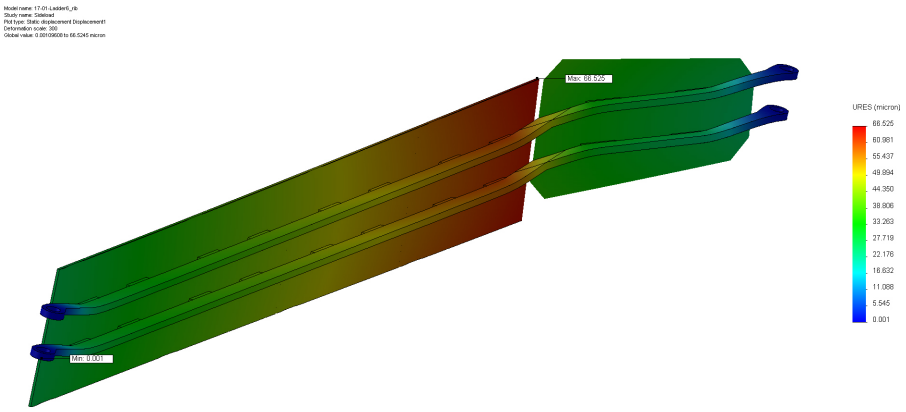

(b) 9 o'clock position: Maximum deformation ≈ 66 µm

Figure 2.4.: Simulated sag of a layer 6 ladder under its own weight (a) for the position on top of the SVD and (b) for the position at the center [16].

Static FEA[5] simulations were made to ensure mechanical stability of the ladders [16], an example is given in figure 2.4. This simulation determined the sag of a layer 6 ladder under its own weight with a realistic albeit simplified model. The deformation stays well below the required maximum of 100 µm. However, the real deformation can only be determined through measurements of a prototype ladder under realistic thermal condition, since the simulation can't take into account production inefficiencies, resin saturations, material imperfections, etc. Nevertheless, the real deformation is expected to fit the requirements.

[5]FEA: Finite Elements Analysis

2.2.2. End-rings, windmill structure and overlap

The ladders are arranged around the beam pipe roughly following a cylindrical surface. To do so, they are mounted on so-called "end-rings" (see figure 2.5), which provide the interface between the ladders and the overall support structure of the SVD (see figure 2.6).

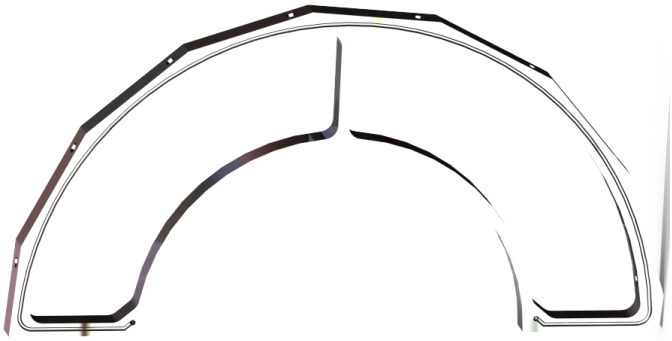

Figure 2.5.: Half of layer 6 backward end-ring, exposing the cooling channel. The end-rings arrange the ladders cylindrically around the beam pipe.

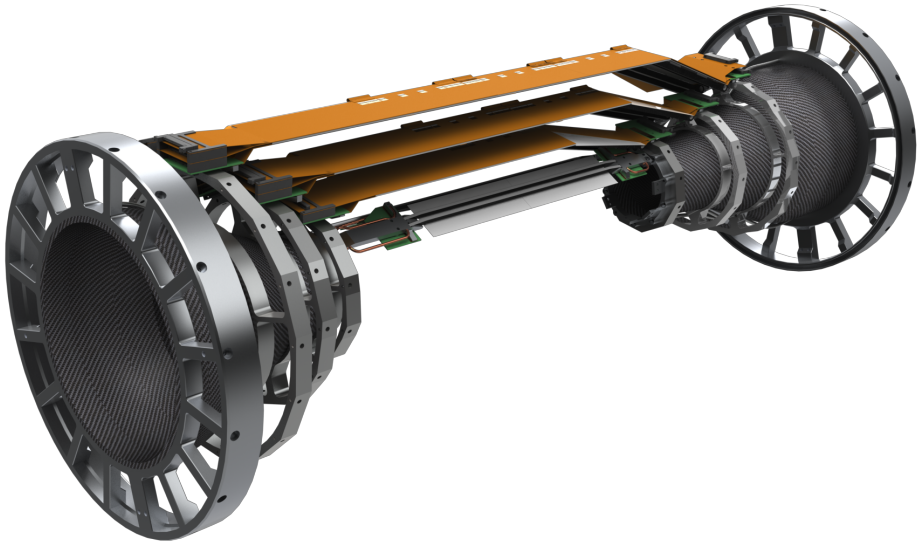

Figure 2.6.: Rendering of the support structure including the end flanges.

The SVD is assembled in two half-shells, which contain half the ladders of each layer[6]. These half-shells are hereafter combined to form the SVD. The end-rings are crucial for the correct positioning of the ladders, thus demanding highly precise machining.

To avoid blind spots in the SVD, the ladders have to implement a certain overlap[7]. This is also required for the alignment of the sensors w.r.t. each other. The direction of the

[6] Layer 3 has an odd number of layers, so one half of layer 3 contains more ladders than the other one

[7] There is only overlap of one ladder to the next one, but none inside the ladder itself. So, the sensors of one ladder are parallel and mounted head-to-head, hence leaving a small gap of inactive area between the sensors.

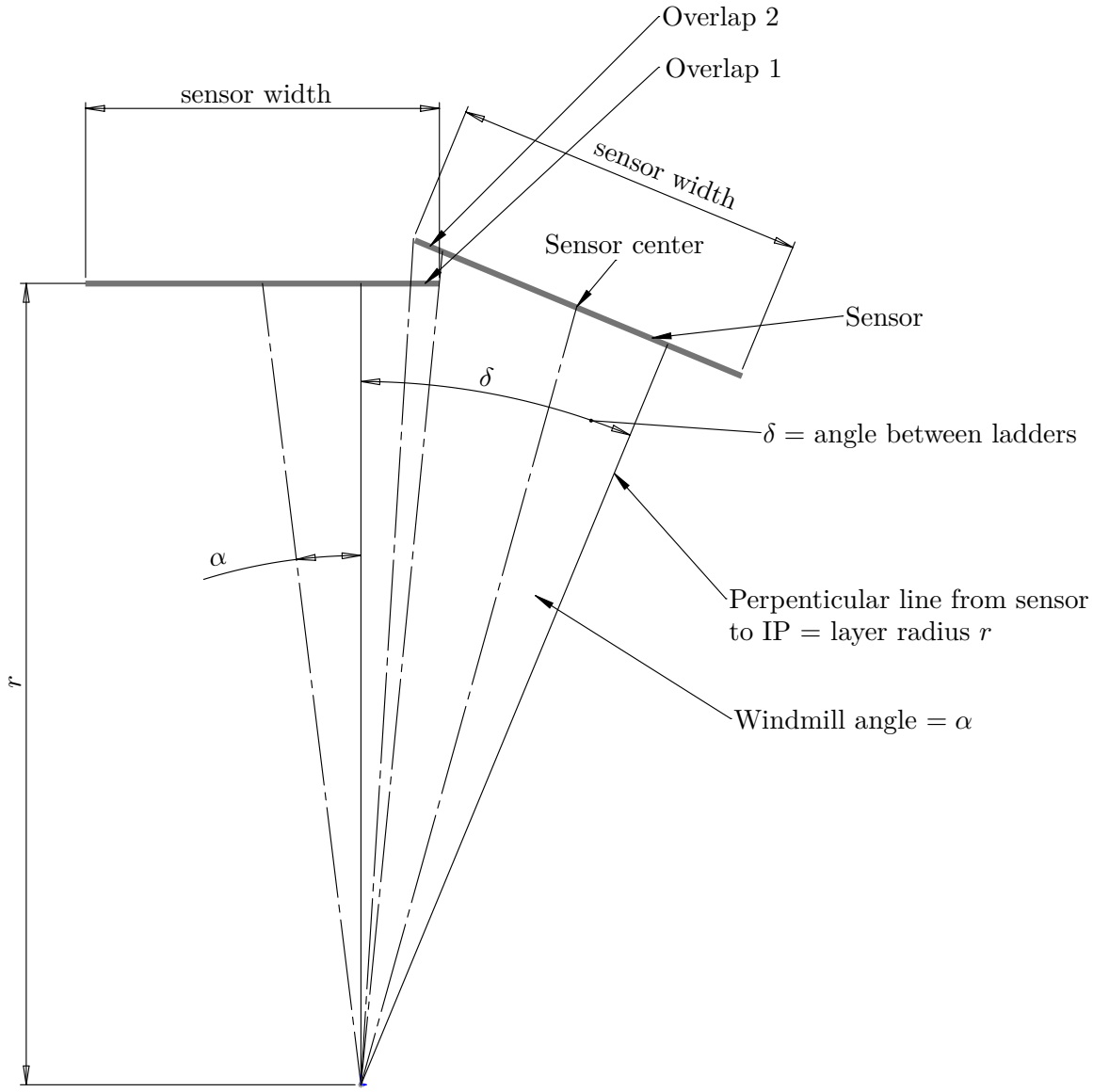

Figure 2.7.: The windmill structure of the SVD, as seen when looking along the z-axis, i.e. from the backward region to the forward region. The nominal radius is the perpendicular displacement of the sensor w.r.t. the beam axis. The windmill angle is measured between the radius vector and the vector to the sensor center. The overlap is the sum of the geometrical overlaps on both sensors (minus the inactive margin of the sensor), relative to the total active sensor width [16].

overlap – the so-called "windmill structure" – is determined by the physics of the charge carrier drift inside the silicon sensors and depends on the direction of the magnetic field (see section 4.5.2 for details). Figure 2.7 shows a sketch of the windmill structure, together with definitions of some of the fundamental properties of the layers found in table 2.1, like the nominal radius and the overlap.

2.3. Sensors

The design of the silicon microstrip sensors for the SVD is determined mainly by the requirement of a minimal material budget. So, we use the largest sensors commercially available to reduce the relative amount of support structure material. Moreover, double-sided sensors (DSSDs) are a natural choice, because these sensors measure a particle's position in two dimensions with the same sensor thickness like a single-sided sensor. However, this also means increased complexity and cost per sensor.

Nowadays, typical semiconductor processing facilities are able to manufacture sensors on 150 mm wafers[8], making a sensor with outer dimensions of about $12 \times 6\,\mathrm{cm}^2$ possible. The Belle II sensors will be made on a standard material widely used in industry, with a high resistivity n-type bulk and a thickness of 300 – 320 µm. The SVD will apply sensors of three different shapes: two rectangular ones for the barrel part, and one trapezoidal (or wedge shaped) for the forward part.

The sensing strips are implanted in the n-type bulk either with acceptors or donors, depending on the sensor side. The acceptor-implanted side is called "p-side" or "junction side", while the other side is called "n-side" or "ohmic side"[9].

The p-sides of the sensors feature long strips with small strip distance, which measure the $R\Phi$-coordinate. For layers 4 – 6 these strips face the beam axis. The opposite n-sides offers shorter strips with larger strip distance, perpendicular to the strips of the p-side. These strips measure the z-coordinate. See section 10.1.1 for details about the coordinate system.

All sensors will be AC-coupled with integrated bias resistors, and feature non-floating intermediate strips between the readout strips on *both* sides. For details about the working principle of a silicon microstrip sensor refer to section 4.

Two vendors were assigned:

- Hamamatsu Photonics K.K. (HPK) [18]: located in Hamamatsu City, Prefecture Shinuoka, Japan, manufacturing the rectangular sensors for the barrel part of the SVD
- Micron Semiconductor Ltd. [19]: located in Lancing, Sussex, England, manufacturing the trapezoidal sensors for the forward part of the SVD.

[8] sometimes referred to as "6 inch", although the diameter is actually 5.9 inch. Sensors made with this technology are often called "6 inch sensors".

[9] While the nomenclature "p-side" and "n-side" can be used for sensors on all types of base materials, the nomenclature "junction side" and "ohmic side" means different things for p-type and n-type base materials. The junction side is where the p-n-junction is located. This is the p-side for n-type material, and the n-side for p-type material.

The total number of strips per side is always a multiple of 128, which is the number of input channels of the readout chip. The geometry of the sensors – including the pitch – is mainly driven by this requirement and the size of the wafers, on which the sensors are manufactured.

2.3.1. Barrel sensors

HPK manufactures two different rectangular sensors for SVD's barrel part on 150 mm diameter wafers with a thickness of 320 µm. The sensors for layer 3 differ from the ones in layers 4 – 6 in channel count, pitch and geometric dimensions.

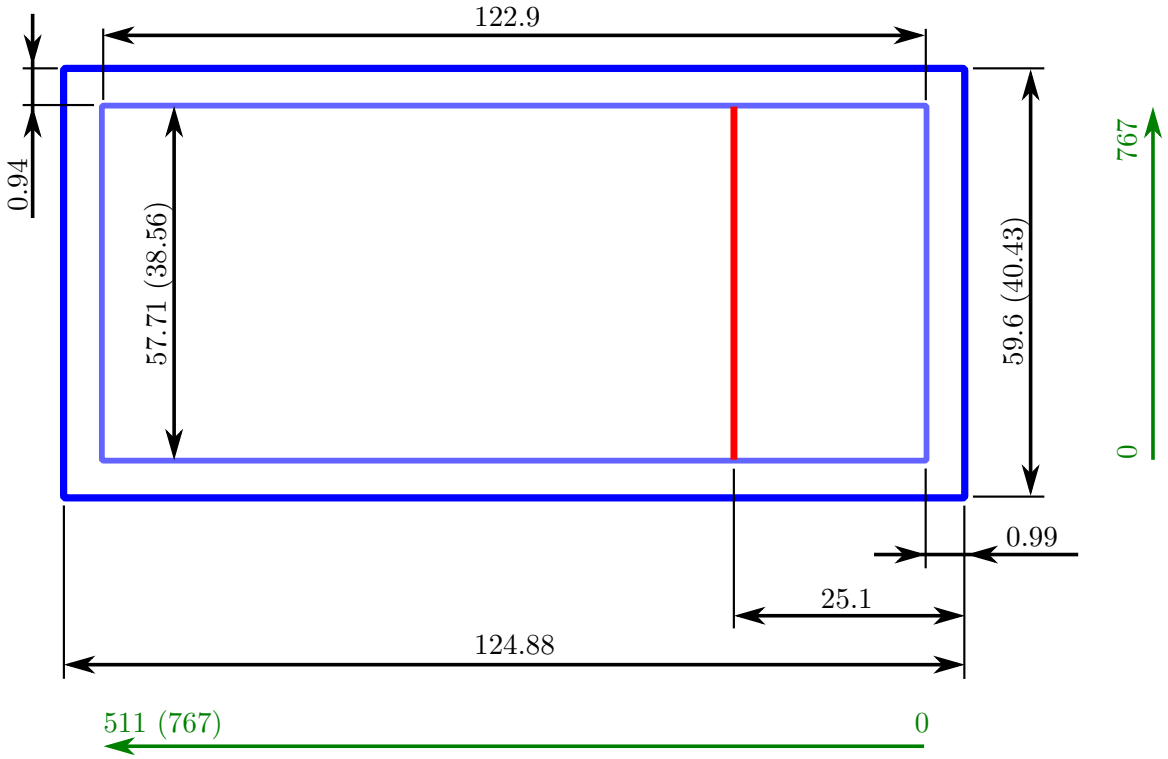

Figure 2.8.: Geometric dimensions (not to scale) of the rectangular sensors in mm, as seen when looking at the p-side. Values in parentheses apply to the small sensor. Dark blue: outer dimensions. Light blue: active area. Red: additional pad row. Green: strip numbering. See sections 11.1 and 11.2 for data sheets with geometry details [18].

Figure 2.8 shows the outer dimensions of the rectangular sensors in dark blue, and the active area in light blue. Values in parentheses are valid for the small sensor. The large sensor will be used with conventional readout as well as with special hybrids implementing a chip-on-sensor concept (see section 2.4). Therefore, it features an additional pad row (displayed in red) on the p-side. The small sensor has this pad row as well, but it won't be used in the experiment. Tables 2.2 and 2.3 give an overview of the basic geometrical and electrical parameters.

Table 2.2.: Geometric parameters of the rectangular sensors [15]. See sections 11.1 and 11.2 for data sheets with geometry details.

Quantity	Large sensor	Small sensor
# strips p-side	768	768
# strips n-side	512	768
Pitch p-side	75 µm	50 µm
Pitch n-side	240 µm	160 µm
Area (total)	7442.85 mm^2	5048.90 mm^2
Area (active)	7029.88 mm^2 (94.5%)	5048.90 mm^2 (93.8%)

Table 2.3.: Electrical parameters of the rectangular sensors [15]

Quantity	Value
Base material	n-type Si, 8 kΩcm
Full depletion voltage V_{FD}	< 120 V
Breakdown voltage	$\geq V_{FD} + 50$ V
Polysilicon resistor	4 MΩ (min.), 10 MΩ (typ.)
Coupling capacitance	> 100 pF
Breakdown voltage of AC coupling	> 20 V
Bias dark current at V_{FD}	1 µA (typ.), 10 µA (max.)

2.3.2. Forward sensors

The SVD features slanted sensors in the forward part to cover the full acceptance region while minimising the material budget. Consequently, these sensors have to be trapezoidal. Figure 2.9 shows the outer dimensions of the trapezoidal sensor in dark blue, and the active area in light blue. This sensor features a special guard ring design implemented by Micron Semiconductor Ltd., which makes the inactive margin a little bit larger. Therefore the outer dimensions of this sensor are larger than for the large rectangular sensor. Tables 2.4 and 2.5 give an overview of the basic geometrical and electrical parameters.

The strips of the p-side feature a variable pitch, resulting in a fan shape. The large pitch was chosen to match the p-side pitch of the large rectangular sensor, while the small pitch matches the small rectangular sensor. The slant angles are calculated by requiring that the edges of overlapping trapezoidal sensors should be parallel, thus providing a roughly rectangular overlapping area. Equivalently one can require that the (virtual) extensions of the p-side strips coincide at the z-axis, while disregarding windmill angles and shifts.

The strips of the n-side are parallel and perpendicular to the central strip of the p-side, but with varying length. The electrical strip separation is achieved by the p-stop

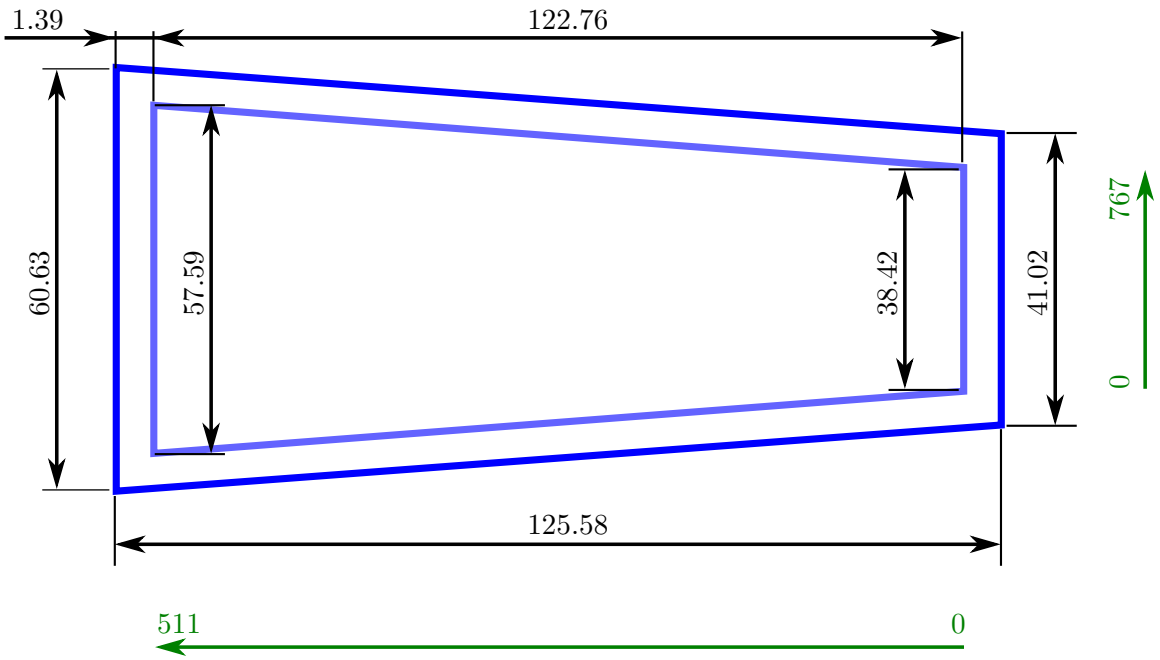

Figure 2.9.: Geometric dimensions (not to scale) of the trapezoidal sensor in mm, view at the p-side. Dark blue: outer dimensions. Light blue: active area. Green: strip numbering. See section 11.3 for a data sheet with details about the geometry [19].

Table 2.4.: Geometric parameters of the trapezoidal sensor [15]. See section 11.3 for a data sheet with details about the geometry.

Quantity	Value
# strips p-side	768
# strips n-side	512
Pitch p-side	75 . . . 50 µm
Pitch n-side	240 µm
Area (total)	6382.6 mm^2
Area (active)	5890.0 mm^2 (94.5%)
Slant angles	layer 6: 21.1°
	layer 5: 16.0°
	layer 4: 11.9°

blocking method, where we found the atoll pattern to match our needs best (see section 7).

The development, production and characterisation of the trapezoidal sensor is the main topic of this thesis.

Table 2.5.: Electrical parameters of the trapezoidal sensor [15]

Quantity	Value
Base material	n-type Si, 8 kΩcm
Full depletion voltage V_{FD}	40 V (typ.), 70 V (max)
Operation voltage	$V_D \dots 2 \times V_D$
Breakdown voltage	$\geq 2.5 \times V_{FD}$
Polysilicon resistor	10 MΩ (min.), 15 ± 5 MΩ (max.)
Interstrip resistance, p-side	100 MΩ (min.), 1 GΩ (typ.)
Interstrip resistance, n-side	10 MΩ (min.), 100 MΩ (typ.)

2.4. Readout System

The readout system has to comply with the increased spontaneous luminosity of SuperKEKB, which requires a much faster readout than before. A shaping time in the order of $\mathcal{O}(50\,\text{ns})$ is necessary to suppress background hits. The previously used VA1TA chip cannot be used anymore, so the SVD will adopt the APV25 chip, which was developed for and used in the CMS experiment at the LHC. Consequently, the whole readout chain is built completely new.

2.4.1. The APV25 chip

The APV25 chip [20] is a low noise front-end amplifier chip with a noise figure of $250\,\text{e} + 36\,\text{e/pF}$ [21]. It is produced in 0.25 µm CMOS[10] technology, radiation hard up to more than 1 MGy and was found to be fully compatible with the Belle II trigger and readout strategy. The chip is produced on 200 mm wafers, and can be thinned down from its nominal thickness of 700 µm to a thickness of 325 µm. It can be operated at a wide range of frequencies. In the SVD, it will operate at a fraction of the collider's radio frequency, either at $f_R/16 \approx 31.8\,\text{MHz}$ (default) or at $f_R/12 \approx 42.2\,\text{MHz}$ (optional). Figure 2.10 shows a block diagram of one of the 128 identical input channels of the APV25 chip.

An input channel of the APV25 consists of

- a low noise preamplifier: This amplifier picks up the raw current signal of the strip an amplifies it to a usable level for the subsequent stages.
- an inverter: This switch optimises the dynamic range depending on the polarity of the signal, i.e. reading out positive detector currents on the p-side (inverter on) or negative detector currents on the n-side (inverter off).
- a shaper stage: The nominal shaping time of 50 ns can be adjusted to match the needs.

[10] CMOS: Complementary Metal-Oxide-Semiconductor, a technology for constructing integrated circuits

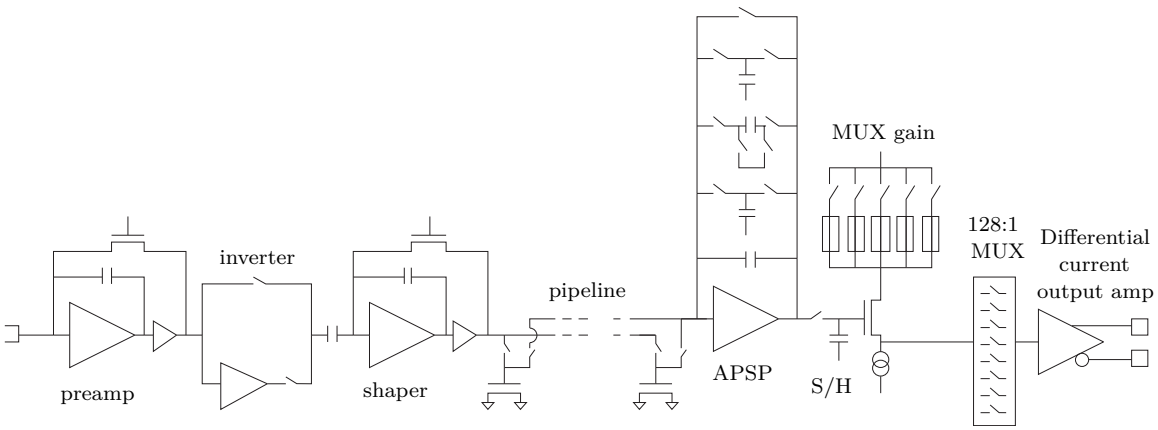

Figure 2.10.: Building blocks of one channel of the APV25 readout chip [15].

- a 192 cell pipeline: The shaper output is written to a ring-buffer at the clock frequency. An index FIFO[11] can label up to 32 cells pending for readout. These cells are not overwritten when taking data, therefore the available pipeline depth is between 160 and 192 cells. Multiplying the pipeline depth with the clock period yields the maximum allowed trigger latency time, which is either 5.04 µs at 31.8 MHz or 3.78 µs at 42.4 MHz, respectively.
- an analog pulse shape processor (APSP[12]): This is a switched capacitor filter, which uses three consecutive samples to reverse the shaping function, thus being able to unambiguously identify bunch crossings. This can be used when the clock rate of the APV25 chip is synchronised to the bunch crossing rate. However, the bunch crossings of the SuperKEKB collider occur almost continuously, so the APSP is not used in Belle II.
- an analog multiplexer: The strip data are multiplexed through three hierarchical stages and sent to the output.
- a differential current output amplifier: This amplifier drives the output signal, which is picked up by the periphery.

The APV25 chip allows to record multiples of three consecutive samples. By taking six samples in the so-called "multi-peak mode", one can correct for the non-constant phase shift between the bunch crossings and the APV25 clock, by reconstructing the peak time of the signal ("hit time finding"). Moreover, this allows to process the data outside of the chip to identify hits that belonged to the triggered event, and to reject off-time background hits. Figure 2.11 illustrates how this process of hit time finding leads to an occupancy reduction of a factor of about 100 relative to the previously used VA1TA chip, yielding a timing precision of 3 ns. This precise timing information is a vital input for the PXD, whose integration time is three orders of magnitude larger.

[11] FIFO: First In First Out, a kind of low-level memory array
[12] APSP: Analog Pulse Shape Processor

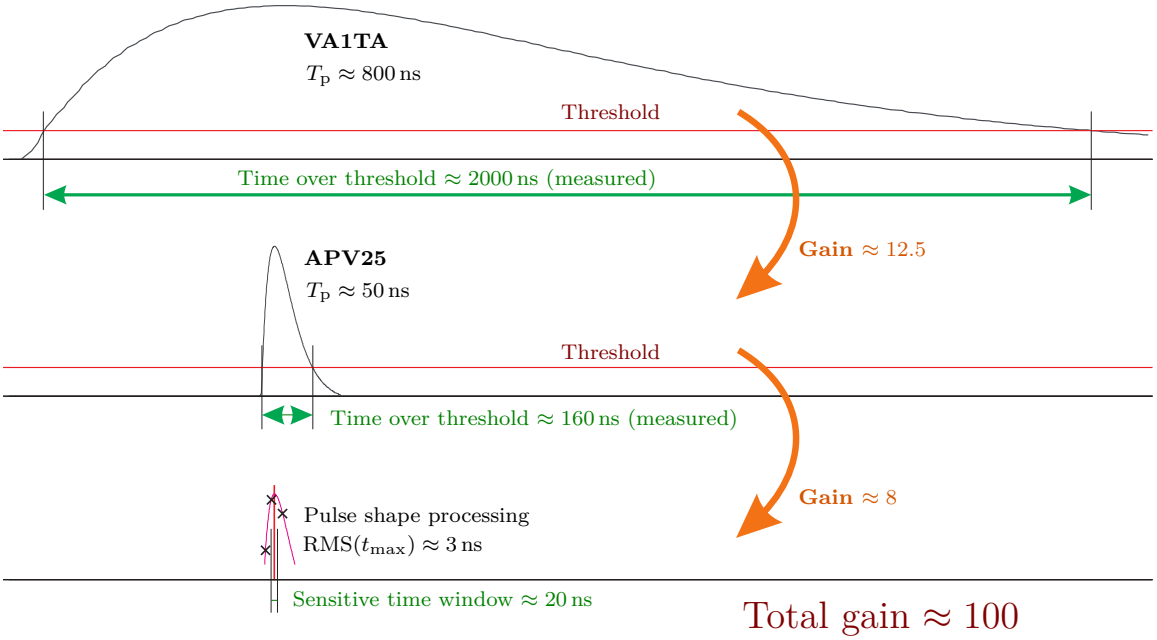

Figure 2.11.: The APV25 chip offers an occupancy reduction of $\mathcal{O}(100)$ w.r.t. the previous readout chip by a short integration time and hit time finding using a fit to the shaped signal [22].

2.4.2. Front end electronics - the Origami chip-on-sensor concept

A readout chip with fast shaping (i.e. a short integration time) is naturally more prone to noise. This noise is mainly influenced by the load capacitance seen by the input channel of the APV25 chip, which therefore has to be minimised. To achieve this, the APV25 chips have to be mounted as close as possible to the sensor strips, together with the corresponding periphery, while still maintaining a low material budget.

For sensors at the edge of the acceptance region one can use conventional hybrid boards for housing the APV25 chips, which are mounted outside of the sensitive volume. For the inner sensors, however, a different readout scheme has to be applied. The Origami chip-on-sensor concept was developed to fulfil the requirements of proximity to the sensor and low material budget at the same time.

In the Origami scheme, the APV25 chips for readout of both sensor sides are placed on a single flexible circuit, mounted on the n-side (outer side) of the sensor. This flexible hybrid is made of several Kapton and copper layers. The short n-side strips (measuring the z-coordinate, facing away from the beam axis) are connected by a pitch adapter, which is integrated into the hybrid itself. The long p-side strips (measuring the $R\Phi$-coordinate, facing the beam axis) are connected by small flexible pitch adapter fanouts wrapped around the edge of the sensor (see figures 2.12a and 2.12b). That's why this scheme is called Origami. All connections between pitch adapters, sensor and APV25 chips are made by wire bonds.

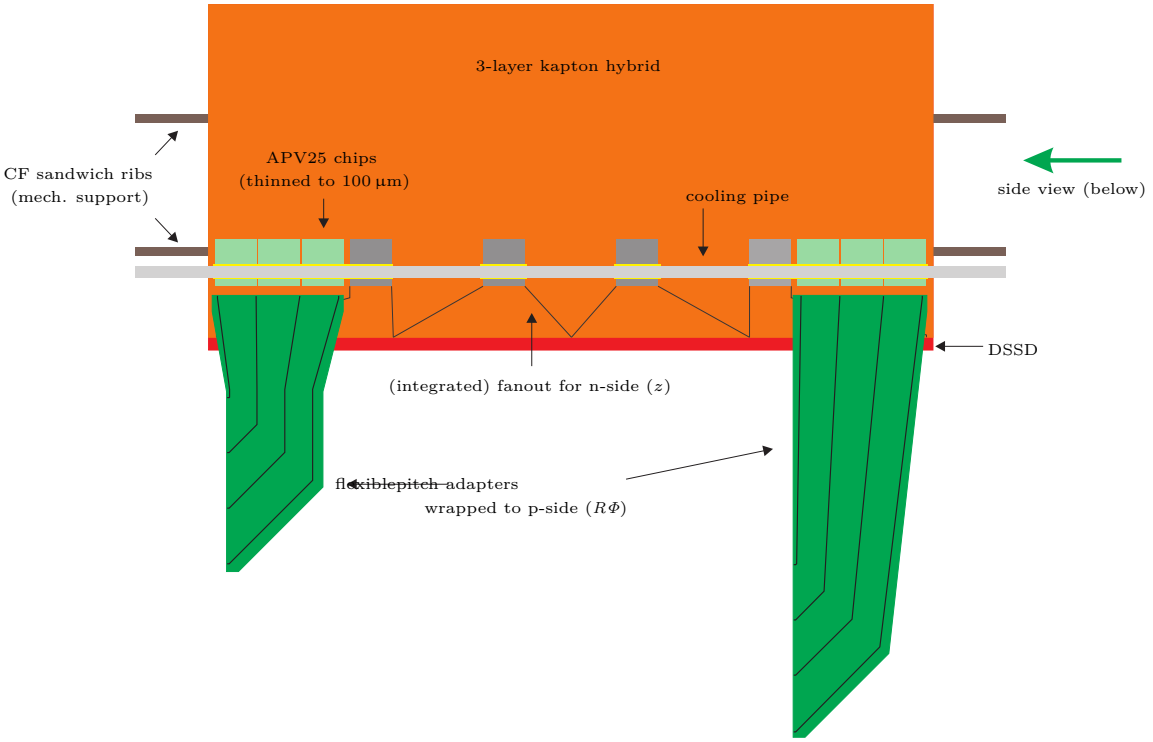

(a) Top view

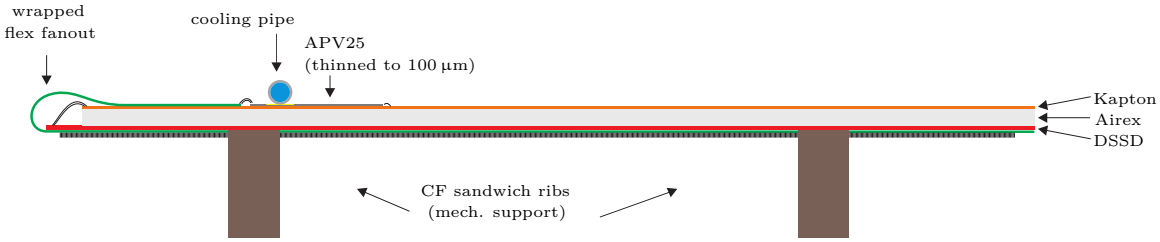

(b) Side view

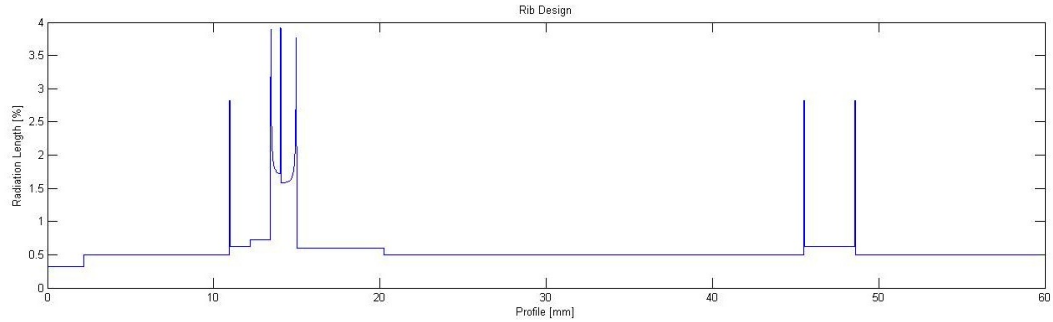

(c) Calculated material budget

Figure 2.12.: The Origami chip-on-sensor concept for a 6 inch DSSD. (a) Top view: The six APV25 chips reading out the strips on the opposite side are displayed in green, the flexible double-layer pitch adapters to be wrapped around the sensor are unfolded. The four APV25 chips reading out the top side are shown in grey, with the integrated pitch adapter next to them. (b) Side view: The flexible pitch adapter connecting to the bottom side strips is located at the left side [15]. (c) Calculated material budget across the width of the ladder [16].

All APV25 chips reading out both sides are located on one side only, arranged in a row. Hence, all chips can be cooled at once using one single cooling pipe. Insulation – both thermal and electrical – between sensor and hybrid is achieved by a 1 mm sheet of Airex®R82.

Naturally, such a hybrid inside the acceptance region increases the material budget w.r.t. the bare sensor. However, there is no other readout solution that would maintain low noise and acceptable signal-to-noise ratio with the short integration time of the APV25 chip. However, the APV25 chips are thinned down to approximately 325 µm, to keep the material budget as low as possible. Consequently, the resulting average material budget of a ladder with Origami sensors becomes 0.57% of a radiation length (see figure 2.12c).

2.4.3. Readout chain

Our readout system builds on the SVD3 prototype readout system, which was intended for a partial upgrade of the former Belle SVD2. However, this partial upgrade was never implemented, instead the whole experiment is renewed. Figure 2.13 shows a schematic view of the readout chain.

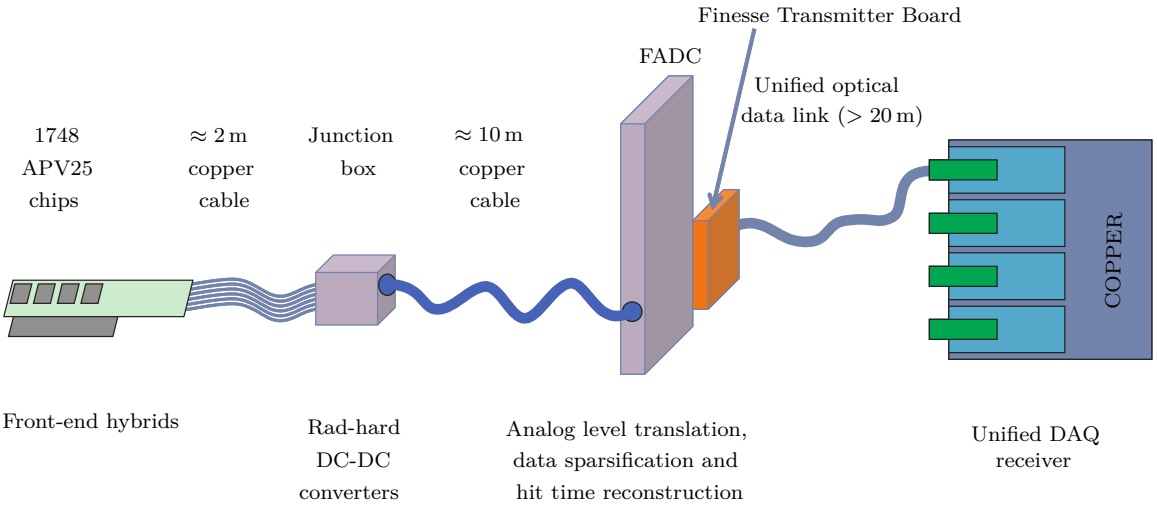

Figure 2.13.: Schematic view of the SVD readout chain [15].

The main components are:

- APV25 chips: These chips read out the sensor signals and provide shaped and amplified analog output.
- Front-end hybrid boards: These boards house the APV25 chips, supply them with power and command signals, and interface them to the cables. Conventional PCBs[13] read out the sensors at the edge of the acceptance region, while the central sensors apply flexible Origami hybrids.

[13] PCB: Printed Circuit Boards

- Junction box: The analog output of the APV25 chips is sent to the junction box via 2 m long copper cables. The main purpose of these boxes is to avoid having even longer cables attached directly to the front-end electronics, which would make assembly difficult. Moreover, the junction boxes contain radiation-hard DC[14]-DC converters to protect the front-end hybrids from transient overvoltages when powering the hybrids. Using these DC-DC converters also allows to reuse the existing power supplies.
- FADC[15]: The Flash Analog-to-Digital Converter boards are 9 units high VME[16] boards that implement the analog level translation[17], analog-digital-converters (flash ADCs[18]) and FPGAs[19] which perform low-level data processing. This includes reordering, pedestal subtraction, a two-pass common mode correction, zero suppression (sparsification) and hit time finding.
- FTB[20] and COPPER[21]: The preprocessed data are propagated to the Finesse Transmitter Board (FTB), which is the main device for data streaming. It converts the electrical signals to optical ones and subsequently sends the information over unified optical data links to the COPPER system, which is the interface to the central data acquisition system (DAQ) of Belle II. COPPER also performs some data formatting and module-level event building using an on-board CPU[22].

Parallel to the FTB and COPPER system, a replica optical output named DATCON[23] is foreseen to make SVD data available for the Pixel Detector (PXD). The PXD will use low-level track information to predict the "regions of interest" in the PXD which should show a real particle hit, and veto readout in uninteresting regions. This online data reduction is vital for the PXD, which otherwise would be crucially prone to occupancy due to the long readout time (20 µs integration time) of the DEPFET sensors.

2.5. Cooling

A Belle II ladder can in principle be operated without cooling whatsoever. The sensor itself doesn't dissipate much heat, and the APV25 chips – which are the main heat source – are known to work even at elevated temperatures. The heat dissipation of a single APV25 chips is about 0.4 W, which leads to a total heat load in the order of 700 W [16]. However, the noise of the readout chips increases with increased temperature. So, in order to achieve

[14] DC: Direct Current
[15] FADC: Flash Analog-to-Digital-Converter
[16] VME bus: Versa Module Eurocard-bus
[17] The APV25 chips operate at the same potential as the sensor sides the are reading out, which have a potential difference of $\mathcal{O}(100\,\mathrm{V})$. The analog level translation converts the baselines of the signals to the common ground level.
[18] ADC: Analog-to-Digital-Converters
[19] FPGA: Field Programmable Gate Arrays
[20] FTB: Finesse Transmitter Board
[21] COPPER: COmmon Pipeline Platform for Electronics Readout
[22] CPU: Central Processing Unit
[23] DATCON: DATa CONcentrator

a decent signal-to-noise ratio sufficient cooling is crucial. Beam test results show that a temperature below 0 °C is required [23], ruling out simple water as cooling fluid.

The cooling system of the SVD has to comply with a number of requirements:

- Coolant temperature: −20 °C.
- The heat load has to be efficiently extracted from the sensitive volume, i.e. with low coolant mass flow.
- The cooling pipes have to be radiation hard and insensitive to corrosion, while securely withstanding the coolant pressure.
- The coolant has to be radiation tolerant, cheap, easily available, and uncritical during operation and in case of leakage.
- The material budget has to be minimised both to reduce multiple scattering and because of tight space constraints.

To fulfil these requirements, we chose to implement a two-phase CO_2[24] cooling system. CO_2 cooling is a two-phase evaporation process, which relies on the large latent heat of the coolant of about $\Delta h \approx 250\,\mathrm{kJ/kg}$ [16]. The cooling system provides liquid CO_2 at the inlet of the cooling pipe leading to the APV25 chips. The evaporation temperature of a saturated fluid is determined by its pressure only. In case of CO_2, a pressure of 2 MPa (20 bar) translates to an evaporation temperature[25] of −20 °C. The heat from the readout chips causes the CO_2 to evaporate, while the coolant temperature stays constant per definition. The coolant mass flow has to be chosen carefully to maintain a mixture of at least 40% liquid CO_2, in order to ensure proper wetting of the cooling pipe and to avoid drying-out.

The advantages of a two-phase CO_2 cooling are:

- The large latent heat allows to apply a low coolant mass flow in thin cooling pipes while still maintaining sufficient cooling performance.
- The low mass flow and the low viscosity of CO_2 also lead to a small pressure drop along the cooling pipe, which ensures a similar coolant temperature at the locations of all heat sources.
- The supply lines can be operated with high pressure (up to 6 MPa), so the pressure drop along the supply lines leaves the actual cooling circuit untouched.
- The coolant is nontoxic, cheap, uncritical in case of leakage and non-corrosive.

To successfully operate a CO_2 system, one has to provide the following boundary conditions:

[24] CO_2: Carbon Dioxide

[25] This coolant temperature was chosen because the corresponding pressure can be securely handled in the CO_2 system, and the temperature stays well away from the dew point of the surrounding air volume to allow for accidental pressure drops

- A low temperature sensitive volume to reduce the thermal gradient to the cooling tubes.
- A dry air sensitive volume with less than 4% relH to eliminate condensation [16].
- A constant gas volume exchange, to securely keep humidity out of the sensitive volume.
- A slight overpressure inside the SVD volume to create a gas flow towards the outside of the detector.

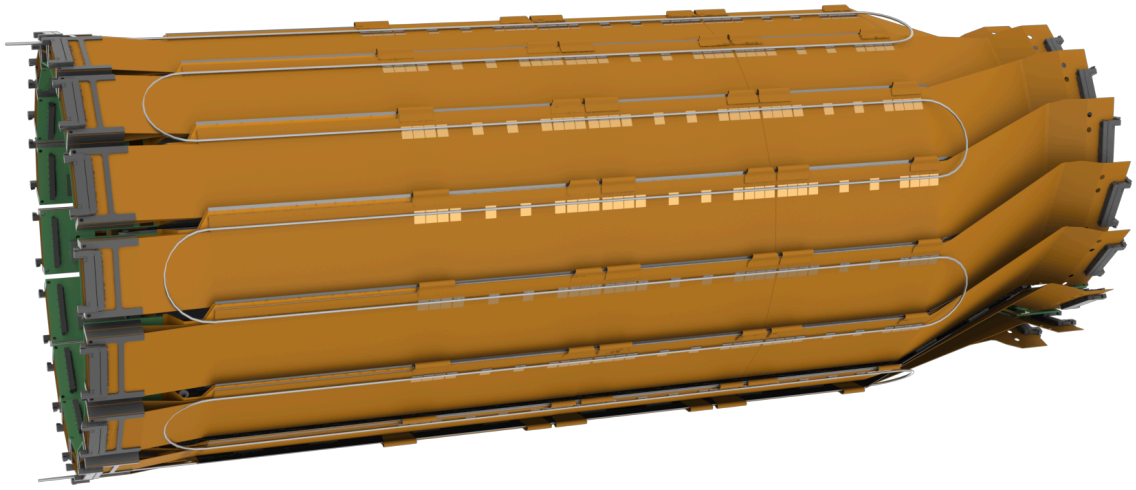

Figure 2.14.: Cooling tube layout of layer 6. The cooling pipe runs in serpentines along the aligned readout chips of all Origami sensors of a whole half-shell [16].

The cooling tube layout foresees to implement nine different cooling circuits per SVD half shell. Six of them are directly integrated in the end-rings (see figure 2.5) to cool the conventional hybrid boards which read out the sensors at the edge of the acceptance region. The two hybrid boards for reading out the two sensor sides are mounted back-to-back on the so-called mount-blocks, separated by a thin layer of electrically insulating and thermally conductive material. The readout chips of both boards are cooled from one side through a cooling channel inside the end-ring. The end-rings of layers 3 and 4 will be connected and share a cooling circuit, while the end-rings of layers 5 and 6 will have separate circuits.

The other three circuits apply cooling tubes that run in serpentines along the aligned readout chips of the Origami hybrids, which read out the inner sensors (see figure 2.14). Layer 3 has no Origami sensors, layers 4, 5 and 6 will have their own cooling circuit, each. Please refer to [24] for details about how to mount the cooling pipes onto the Origami hybrids.

The use of CO_2 enables us to use smaller and thinner cooling pipes compared to systems applying different coolants. The stainless steel cooling tubes used in the final design have an inner diameter of 1.4 mm and a wall thickness of 0.1 mm [16].

Cooling efficiency and practical operation of CO_2 cooling was shown with an open (blow) test system (see figure 2.15), which was used in beam tests for cooling test modules with Origami readout and conventional readout of trapezoidal sensors [24]. The real cooling system will implement a closed cooling circuit, where the evaporated CO_2 will be liquified, accumulated and reused.

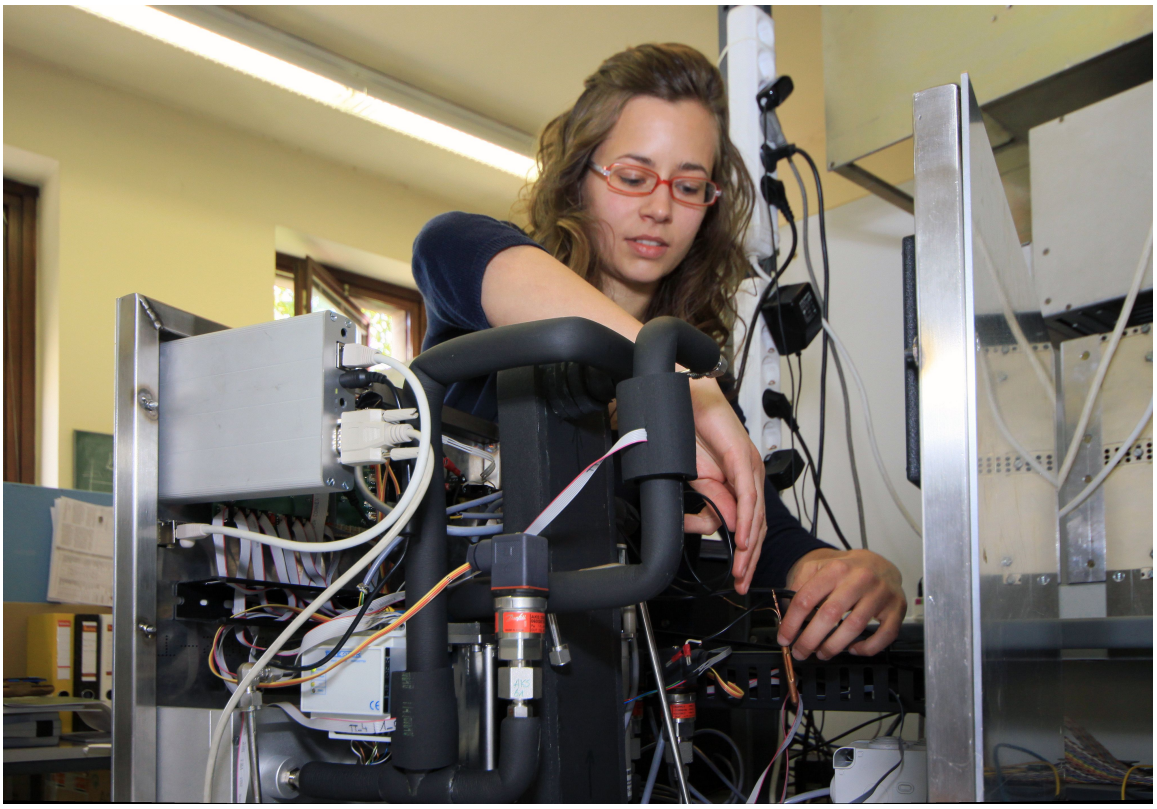

Figure 2.15.: The open test cooling plant used in our beam tests.

People always fear change. People feared electricity when it was invented, didn't they? People feared coal, they feared gas-powered engines... There will always be ignorance, and ignorance leads to fear. But with time, people will come to accept their silicon masters.

Bill Gates

3

Basics on silicon technology

Silicon microstrip sensors offer a number of advantages when used in high energy physics experiments:

- moderate material budget
- precise spatial resolution
- sufficient radiation hardness
- reasonable cost

The production of silicon microstrip sensors makes use of the infrastructure and processes developed in the IC[1] industry. Therefore, these sensors can be manufactured with high quality with quite low costs.

The following sections explain the basic properties of silicon which are necessary to understand the working principle of silicon microstrip sensors and their production.

3.1. Intrinsic properties of silicon

Silicon has the atomic number 14 and belongs to group IV in the periodic table of elements, giving it four electrons in the valence shell available for covalent bonds. Its crystallographic structure is a combination of two face-centered cubic lattices[2], each with a spacing of

[1] IC: Integrated Circuit

[2] Alternatively, one can describe the lattice as a single face-centered cubic lattice with a two-atomic base at each lattice point

$a = 5.430710\,\text{Å}$ (0.5430710 nm). The two lattices are shifted by ($a/4$, $a/4$, $a/4$) along the space diagonal, as shown in figure 3.1, forming the so-called "diamond structure"[3]. Table 3.1 summarises the most important properties of silicon.

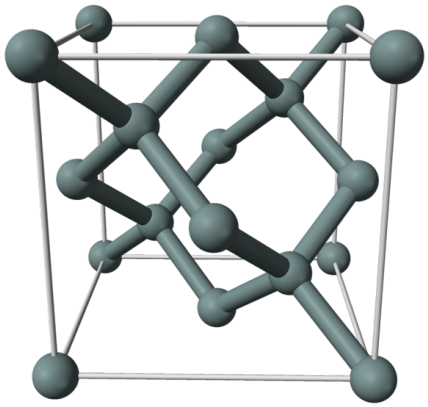

Figure 3.1.: The unit cell of silicon, the small lines denote the lattice spacing a. Its crystallographic structure is a combination of two face-centered cubic lattices shifted along the space diagonal (diamond structure).

Substance	Si	Ge	GeAs	Diamond
Lattice	diamond	diamond	zinc blende	diamond
Atomic number	5.4307	5.657	5.653	3.5668
Average atomic mass	14	32	31+33	6
Density in g/cm^3	2.329	5.323	5.317	3.515
Melting point in ℃	1415	937	1238	3907
Thermal expansion coefficient in 10^{-6} $1/K$	2.56	5.90	6.86	1.0
Thermal conductivity in W/cmK	1.56	0.60	-0.45	10
Intrinsic resistivity	230 kΩcm	47 Ωcm		
Radiation length in cm	9.36	2.30		12.15
Refractive index	3.42	3.99	3.25	2.42
Dielectric constant	11.9	16.2	12.9	5.7
Breakdown field in V/cm	$\approx 3 \times 10^5$			
Band gap in eV	1.12	0.67	1.42	5.48
Intrinsic carrier concentration in $1/cm_3$	1.45×10^{10}	2.33×10^{13}	2.1×10^6	
Mean energy for e-h-pair creation in eV	3.63	2.96	4.35	13.1
Drift mobility (electrons) in cm^2/Vs	1450	3900	8800	1800
Drift mobility (holes) in cm^2/Vs	505	1800	320	1600

Table 3.1.: Important properties of silicon and other common semiconductors [25].

The electrical and chemical properties of silicon are based on its energy band structure. Figure 3.2 shows the principal energy band structures that can be found in solid materials.

[3] In a semiconductor, some lattice atoms have a shorter spacing than others. It is the presence of these two different characteristic distances inside the unit cell of the crystal which introduces the band gap in the first place

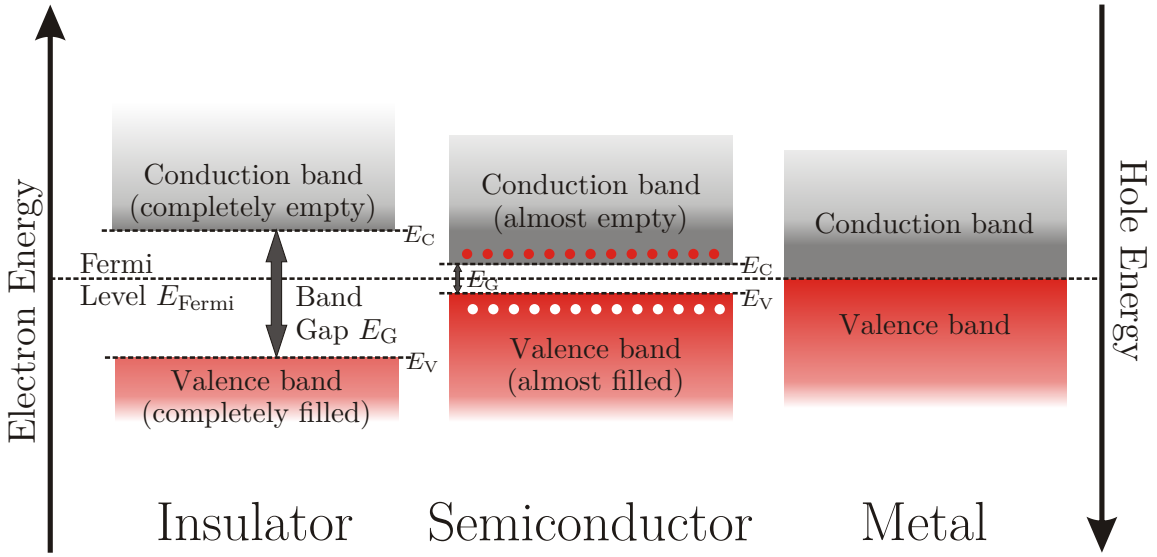

Figure 3.2.: The energy band structure in solids in a simplified view. The valence band is red, the conduction band is grey [26].

The characteristic areas in the energy band structure in figure 3.2 are:

- Valence band (red): At absolute zero temperature all available energy states of the valence band are filled with electrons. The energy of the highest filled energy state is E_V. The electrons are bound to their atoms and unable to move through the crystal, therefore no charge carriers are available for building an electric current.
- Conduction band (grey): At absolute zero temperature all available energy states of the conduction band are empty. The energy of the lowest available energy state is E_C. An electron occupying an energy state in the conduction band can move freely through the crystal, thus being able to establish an electrical current.
- Band gap: This is the "forbidden" area between the energy bands, where no energy states are available. The band gap has a width of $E_G = E_C - E_V$.

One distinguishes three types of solids depending on the size of E_G:

$E_G \gg 0$ **(Insulator):** A very large band gap prevents electrons to be excited from the valence band to the conduction band by thermal excitation. The conduction band is empty even at room temperature and above, and no free charge carriers are available that could form an electric current.

$E_G > 0$ **(Semiconductor):** For a small band gap electrons can be thermally excited to the

conduction band even at room temperature, therefore it is sparely populated with electrons. There is a smooth transition between an insulator and a semiconductor, so the limits are arbitrarily chosen. A band gap between $0.5\,\mathrm{eV} < E_\mathrm{G} < 6\,\mathrm{eV}$ classifies the material as semiconductor. The band gap of intrinsic silicon is $E_\mathrm{G}^\mathrm{Si} = 1.12\,\mathrm{eV}$, which therefore is regarded as a semiconductor.

$E_\mathrm{G} < 0$ **(Metal):** A material with overlapping valence and conduction bands is called metal. there are always enough electrons available to form an electric current.

The occupation probability $F(E)$ for an energy state with energy E is calculated with the Fermi-Dirac probability density function:

$$F(E) = \frac{1}{1 + \exp\left(\frac{E - E_\mathrm{Fermi}}{k_\mathrm{B} T}\right)} \tag{3.1}$$

where E_Fermi is the Fermi energy level, T is the temperature and k_B is the Boltzmann constant. For electron energies far away from the Fermi energy ($|E - E_\mathrm{Fermi}| > 3\,k_\mathrm{B}$) the Fermi-Dirac probability density function can be approximated by:

$$F_\mathrm{e}(E) \approx \exp\left(-\frac{E - E_\mathrm{Fermi}}{k_\mathrm{B} T}\right) \tag{3.2}$$

The non-occupied states in the valence band are treated as quasi-particles called “holes”. A similar approximation yields (with $F_\mathrm{e} + F_\mathrm{h} = 1$):

$$F_\mathrm{h}(E) = 1 - F_\mathrm{e}(E) \approx \exp\left(-\frac{E_\mathrm{Fermi} - E}{k_\mathrm{B} T}\right) \tag{3.3}$$

While the Fermi-Dirac probability density function determines the probability if an existing energy state is occupied by a charge carrier, the state density determines if there is an energy state at the given energy in the first place. The state density near the bottom of the conduction band reads:

$$N(E) = \frac{\left(2 m_\mathrm{e}^\mathrm{eff}\right)^{\frac{3}{2}}}{2\pi^2 \hbar^3 \sqrt{E - E_\mathrm{C}}}. \tag{3.4}$$

The effective electron mass $m_\mathrm{e}^\mathrm{eff} = 0.32\,m_\mathrm{e}$ and depends on the curvature of the conduction band in the dispersion relation (see figure 3.7)[4] and therefore on the orientation of the silicon lattice [27]. The density of electrons in the conduction band n is ob-

[4] The effective hole mass $m_\mathrm{h}^\mathrm{eff}$ similarly depends on the curvature of the valence band in the dispersion relation

tained by convoluting the state density $N(E)$ and the corresponding occupation probability $F_\mathrm{e}(E)$:

$$n = \int_{E_\mathrm{C}}^{\infty} N(E)F(E)\mathrm{d}E = \frac{2}{\hbar^3}\left(2\pi m_\mathrm{e}^\mathrm{eff} k_\mathrm{B}T\right)^{\frac{3}{2}} \exp\left(-\frac{E_\mathrm{C}-E_\mathrm{Fermi}}{k_\mathrm{B}T}\right) \tag{3.5}$$

$$= N_\mathrm{C} \exp\left(-\frac{E_\mathrm{C}-E_\mathrm{Fermi}}{k_\mathrm{B}T}\right) \tag{3.6}$$

Derived in an analog way, the free hole density reads:

$$p = N_\mathrm{V} \exp\left(-\frac{E_\mathrm{Fermi}-E_\mathrm{V}}{k_\mathrm{B}T}\right) \tag{3.7}$$

The constants N_V and N_C are called the band weights of the valence band and conduction band, respectively. At thermal equilibrium, the free electron density and the free hole density of an intrinsic semiconductor are equal and given by:

$$n_\mathrm{i} = n = p = \sqrt{N_\mathrm{C}N_\mathrm{V}} \exp\left(-\frac{E_\mathrm{G}}{2k_\mathrm{B}T}\right) \tag{3.8}$$

In case of intrinsic silicon this charge carrier density is given by $n_\mathrm{i} = n = p \approx 1.45 \times 10^{10}\ \mathrm{cm}^{-3}$ at $T = 300\,\mathrm{K}$, and the intrinsic Fermi energy level $E_\mathrm{Fermi,i}$ inside the band gap results in:

$$E_\mathrm{fermi,i} = \frac{E_\mathrm{C}+E_\mathrm{V}}{2} + \frac{3k_\mathrm{B}T}{4} \ln\left(\frac{m_\mathrm{h}^\mathrm{eff}}{m_\mathrm{e}^\mathrm{eff}}\right) \tag{3.9}$$

For small temperatures the second term vanishes and the Fermi energy is located in the middle of the band gap.

3.2. Extrinsic properties of doped silicon

The main advantage of semiconductors is the ability to adjust their conductivity over a range of several orders of magnitude by doping. When doping a semiconductor, one replaces atoms of the crystal lattice with foreign atoms (“dopants”). To increase the electron density, one uses donors (elements from group V of the periodic table). To increase the hole density, one uses acceptors (elements from group III of the periodic table). This is illustrated in figure 3.3.

The usual donors phosphorus (P) and arsenic (As) have one electron more than silicon in the valence shell. This additional electron is only weakly bound to its atom because it has no bonding partner in the surrounding lattice. It can therefore easily be transferred to the conduction band and corresponds to an energy state inside the band gap, slightly below the edge E_C of the conduction band (see figure 3.4). The energy difference ($E_\mathrm{C} - E_\mathrm{donor} = 0.045\,\mathrm{eV}$ for phosphorus in silicon and $E_\mathrm{C} - E_\mathrm{donor} = 0.054\,\mathrm{eV}$ for arsenic in silicon) is very small and can easily be overcome by thermal excitation. Therefore, these states are almost fully ionised at room temperature, and the electrons are added to the conduction band. This excess of negative charge carriers makes the silicon “n-type”.

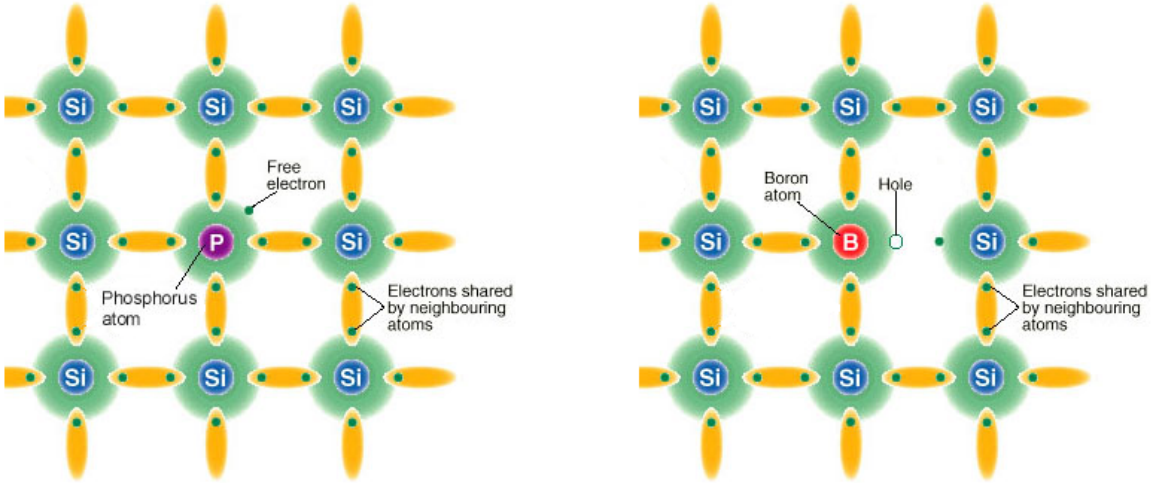

Figure 3.3.: Silicon doped with a donor becomes an n-type material (left), while silicon doped with an acceptor becomes a p-type material (right).

The usual acceptor boron (B) has one electron less than silicon in the valence shell. This vacant state is very eager to be filled with an electron, and corresponds to an energy state inside the band gap, slightly above the edge E_V of the valence band. Due to the small energy barrier ($E_\mathrm{acceptor} - E_\mathrm{V} = 0.045\,\mathrm{eV}$ for boron in silicon) this state can easily be filled by an electron from the valence band by thermal excitation at room temperature, leaving a hole in the band (see figure 3.4). This excess of positive charge carriers makes the silicon "p-type".

Doping shifts the Fermi energy E_Fermi for an n-type material towards the conduction band and for a p-type material towards the valence band. Assuming that the electron density $n \approx N_\mathrm{donor}$ approximately equals the donor density N_donor in an n-type material (and equivalently $p \approx N_\mathrm{acceptor}$ for a p-type material), the shifted Fermi energy E_Fermi can be obtained from equations 3.6 and 3.7, respectively:

$$E_\mathrm{Fermi,n} = E_\mathrm{C} - k_\mathrm{B}T \ln\left(\frac{N_\mathrm{C}}{N_\mathrm{donor}}\right), \text{ for n-type} \tag{3.10}$$

$$E_\mathrm{Fermi,p} = E_\mathrm{V} + k_\mathrm{B}T \ln\left(\frac{N_\mathrm{V}}{N_\mathrm{acceptor}}\right), \text{ for p-type.} \tag{3.11}$$

Consequently, the charge carrier concentration becomes:

$$n_\mathrm{n} = n_\mathrm{i} \exp\left(\frac{E_\mathrm{Fermi,n} - E_\mathrm{Fermi,i}}{k_\mathrm{B}T}\right) \tag{3.12}$$

$$p_\mathrm{p} = n_\mathrm{i} \exp\left(\frac{E_\mathrm{Fermi,i} - E_\mathrm{Fermi,p}}{k_\mathrm{B}T}\right). \tag{3.13}$$

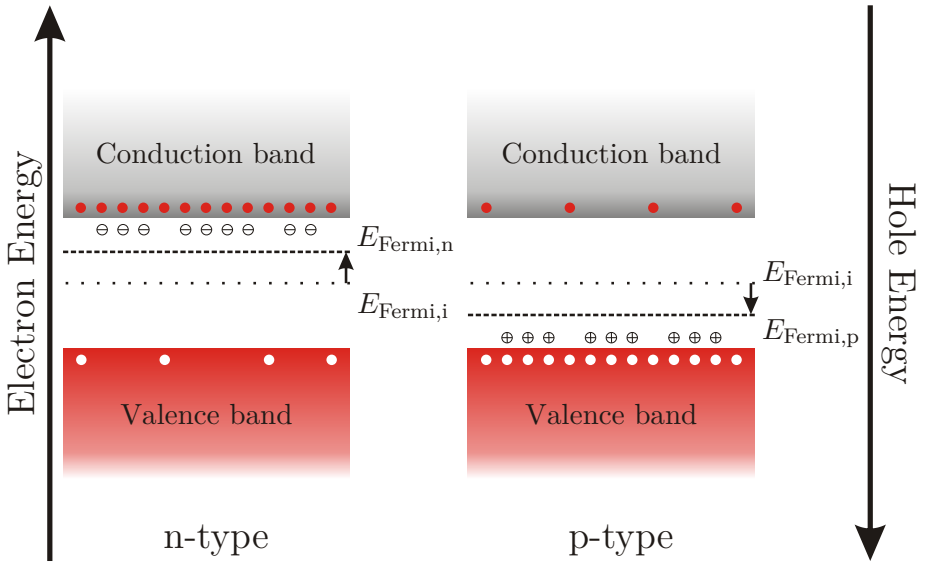

Figure 3.4.: Band structure of a doped semiconductor. The n-type material has donor states slightly below the conduction band (left), while for p-type materials the acceptor states are slightly above the valence band [26].

The mass action law states that an increase in majority charge carriers must be counteracted by a decrease of minority carriers, yielding (with $n_{\mathrm{n,p}} \cdot p_{\mathrm{n,p}} = n_{\mathrm{i}}^2$):

$$p_{\mathrm{n}} = \frac{n_{\mathrm{i}}}{n_{\mathrm{n}}} \qquad \text{and} \qquad n_{\mathrm{p}} = \frac{n_{\mathrm{i}}}{p_{\mathrm{p}}}. \tag{3.14}$$

Consequently, the majority carriers of an n-type material are electrons, and those of a p-type material are holes.

Figure 3.5 compares the state density, the Fermi-Dirac probability density function and the final density of free charge carriers for intrinsic, n-type and p-type silicon. While the state density is the same in all cases, the Fermi-Dirac probability density function follows the shift of the Fermi energy. Being the convolution of the two latter densities, the free charge carrier density becomes asymmetrical for extrinsic (doped) silicon.

Figure 3.6 shows the majority charge carrier concentration in n-type silicon $n_{\mathrm{n}}(T)$ as a function of the temperature T. The additional charge carriers introduced by doping are only effective at intermediate temperatures. At low temperatures, the thermal excitation is too weak to ionise even the weakly bound electrons of the donors, the charge carriers "freeze out". At high temperatures the thermal excitation can overcome the whole band gap and the conduction band is flooded with intrinsic charge carriers, the additional charge carriers introduced by doping lose significance. So, the charge carrier concentration converges to the intrinsic concentration at high temperatures.

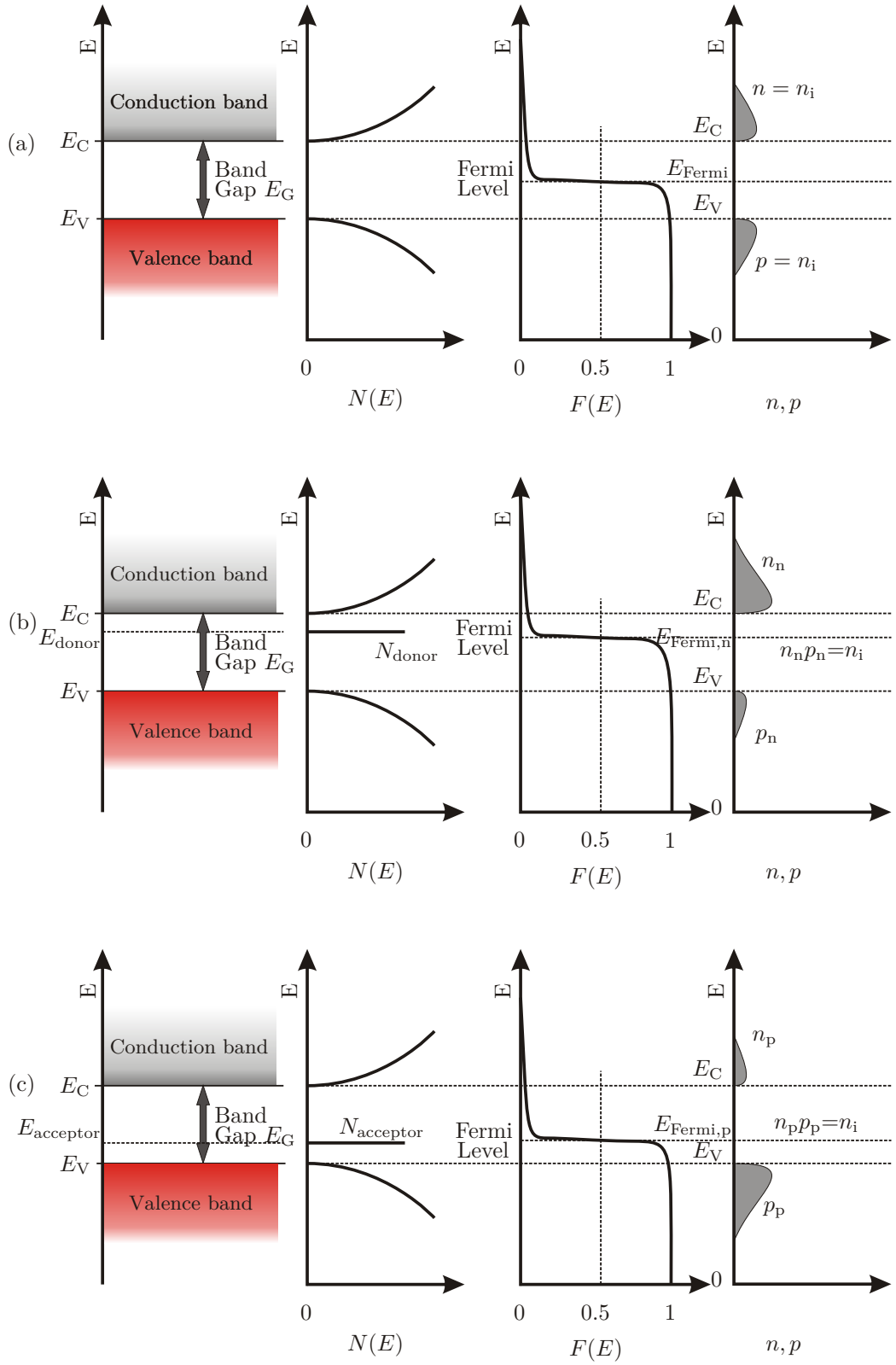

Figure 3.5.: State density $N(E)$, Fermi energies E_{Fermi}, $E_{\text{Fermi,n}}$, $E_{\text{Fermi,p}}$ and free charge densities in silicon. The state density$N(E)$ is the identical for intrinsic (a) and extrinsic silicon (b and c). The Fermi-Dirac probability density function follows the change of the Fermi energy for n-type (b) and p-type (c) silicon, causing the final free charge densities to change [26].

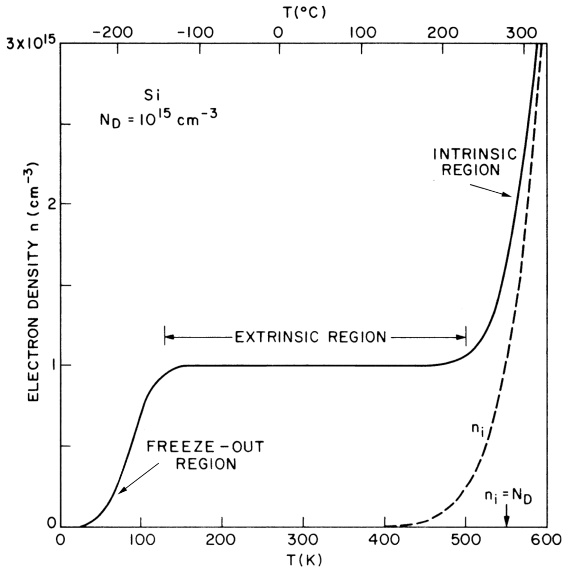

Figure 3.6.: Majority charge carrier density $n_\mathrm{n}(T)$ in n-type silicon as function of the temperature T [27]. At low T thermal excitation can't overcome the energy barrier between the donors and the conduction band. For intermediate T the electron concentration in the conduction band approximately equals the number of donors ("extrinsic region"). At high T ($k_\mathrm{B}T \approx E_\mathrm{G}$) the electron concentration converges to the intrinsic behaviour.

3.3. Carrier Transport

Up to now we looked at semiconductors in equilibrium, that is without applying any external fields, and with a geometrically homogeneous charge carrier distribution. However, a silicon microstrip sensor only works with an external voltage applied, therefore in the following sections we discuss the phenomena occurring in semiconductors in a non-equilibrium state.

3.3.1. Drift

Without external electric field $\vec{E} = 0$ the average displacement of charge carriers is zero. With $\vec{E} \neq 0$ the charge carriers will move along the electric field lines, where the direction of this movement is determined by the charge of the carrier. This movement is called "drift". Assuming that the time between two random collisions at lattice imperfections is small enough, the charge carriers will only accelerate little and their velocity will be small compared to the "intrinsic" thermal motion[5]. In this case, the average drift velocity is determined by:

[5]The mean kinetic energy due to temperature is $E_\mathrm{kin}^\mathrm{therm} = {}^3\!/_2 k_\mathrm{B}T$, yielding a velocity of about $v^\mathrm{therm} \approx 10^7\,{}^\mathrm{cm}\!/_\mathrm{s}$ at room temperature. Thermal vibrations (phonons) introduce imperfections in the lattice which scatter and decelerate the charge carriers, giving them a mean free path of about 10^5 cm and a mean free time of $\tau_C \approx 10^{-12}$ s

$$\vec{v}_\mathrm{n} = -\frac{q\tau_C}{m_\mathrm{e}^\mathrm{eff}}\vec{E} = -\mu_\mathrm{n}\vec{E} \tag{3.15}$$

$$\vec{v}_\mathrm{p} = \frac{q\tau_C}{m_\mathrm{h}^\mathrm{eff}}\vec{E} = \mu_\mathrm{p}\vec{E} \tag{3.16}$$

where q is the charge, τ_C is the mean free path between two random collisions and $\mu_\mathrm{n,p}$ are the mobilities of electrons and holes, respectively. The drift current density consequently becomes:

$$\vec{J}_\mathrm{n}^\mathrm{drift} = -qn\vec{v}_\mathrm{n} = qn\mu_\mathrm{n}\vec{E} \tag{3.17}$$

$$\vec{J}_\mathrm{p}^\mathrm{drift} = qp\vec{v}_\mathrm{p} = qp\mu_\mathrm{p}\vec{E} \tag{3.18}$$

For very high fields $\vec{E}$ this linearity is lost, the drift velocities are rendered independent of $\vec{E}$ and saturate at absolute values of $v_\mathrm{n,s}$ and $v_\mathrm{p,s}$. An empirical relation for the saturating drift velocities reads [27]:

$$\vec{v}_\mathrm{n} = \frac{\mu_\mathrm{n}\vec{E}}{\sqrt{1 + (\mu_\mathrm{n}\vec{E}/v_\mathrm{n,s})}} \tag{3.19}$$

$$\vec{v}_\mathrm{p} = \frac{\mu_\mathrm{p}\vec{E}}{\sqrt{1 + (\mu_\mathrm{p}\vec{E}/v_\mathrm{p,s})}} \tag{3.20}$$

The concentration of majority charge carriers defines the resistivity of an extrinsic semiconductor. In the extrinsic temperature region (see figure 3.6) this charge carrier concentration equals the doping concentration, yielding

$$\rho = \frac{1}{q\mu_\mathrm{n}N_\mathrm{donor}} \qquad \text{for} \quad N_\mathrm{donor} \gg N_\mathrm{acceptor} \quad \text{(n-type)} \tag{3.21}$$

$$\rho = \frac{1}{q\mu_\mathrm{p}N_\mathrm{acceptor}} \qquad \text{for} \quad N_\mathrm{acceptor} \gg N_\mathrm{donor} \quad \text{(p-type)} \tag{3.22}$$

The lattice imperfections causing the scattering of the charge carriers depend on temperature and doping concentration. Consequently, the carrier mobilities μ_n and μ_p are functions of temperature and doping concentration, too. See [27] for further details.

3.3.2. Diffusion

The charge carriers in the conduction band of a semiconductor tend to level out geometrical distribution inhomogeneities by random particle movement. This process is called "diffusion". For a mathematical description we consider an inhomogeneous charge carrier distribution and neglect the electric fields that are created by the doping atoms and the

inhomogeneous carrier distribution. Assuming all this, we describe the diffusion by the diffusion equations:

$$\vec{F}_\mathrm{n} = -D_\mathrm{n}\nabla n \tag{3.23}$$

$$\vec{F}_\mathrm{p} = -D_\mathrm{p}\nabla p \tag{3.24}$$

where $\vec{F}_\mathrm{n}$ and $\vec{F}_\mathrm{p}$ are the charge carrier flux densities and D_n and D_p are the diffusion constants of electrons and holes in silicon. The diffusion current densities $\vec{J}^\mathrm{diff}_\mathrm{n,p}$ are obtained by multiplying the flux densities with the charge $\pm q$.

We now can combine equations 3.17, 3.18 with 3.23, 3.24 to calculate the total current densities for the combination of drift and diffusion:

$$\vec{J}^\mathrm{total}_\mathrm{n} = \vec{J}^\mathrm{drift}_\mathrm{n} + \vec{J}^\mathrm{diff}_\mathrm{n} = qn\mu_\mathrm{n}\vec{E} + qD_\mathrm{n}\nabla n \tag{3.25}$$

$$\vec{J}^\mathrm{total}_\mathrm{p} = \vec{J}^\mathrm{drift}_\mathrm{p} + \vec{J}^\mathrm{diff}_\mathrm{p} = qp\mu_p\vec{E} - qD_\mathrm{p}\nabla p \tag{3.26}$$

Assuming a system at equilibrium ($\vec{J}^\mathrm{total}_\mathrm{n,p} = 0$) we can determine the diffusion constants. This yields the so-called "Einstein relations", which relate the diffusion constants to the charge carrier mobilities:

$$D_\mathrm{n} = \frac{k_\mathrm{B}T}{q}\mu_\mathrm{n} \tag{3.27}$$

$$D_\mathrm{p} = \frac{k_\mathrm{B}T}{q}\mu_\mathrm{p} \tag{3.28}$$

3.4. Carrier generation and recombination

To establish an electrical current, on has to provide free charge carriers, i.e. electrons in the conduction band and/or holes in the valence band. These free charge carriers can be generated by a number of mechanisms:

- Thermal excitation
- Optical excitation
- Ionisation by charged particles

These mechanisms lift an electron to the conduction band while leaving a hole in the valence band. So, positive and negative charge carriers are created in *pairs*, the so-called e-h-pairs. These mechanisms will be discussed in more detail in this section.

Other mechanisms alter the free charge carrier concentrations more directly:

- Doping: The number of charge carriers is directly influenced by donors and acceptors. This has been discussed in section 3.2.

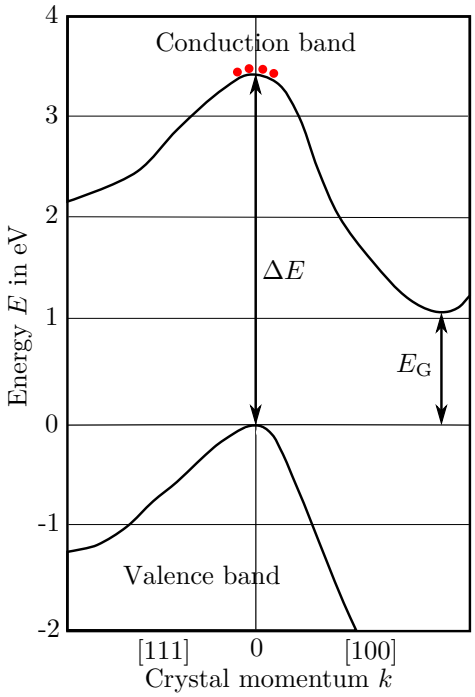

Figure 3.7.: The dispersion relation $E(k)$ of silicon as function of the crystal momentum k for two different crystal orientations. Silicon is an indirect semiconductor, the minimum of the conduction band and the maximum of the valence band are located at different crystal momenta. The creation of an e-h-pair – if not accompanied by a momentum change by a phonon – has to overcome an energy barrier $\Delta E > E_G$ larger than the band gap.

- External fields: Charge carriers can be injected in a p-n-junction by a forward bias voltage or removed by a reverse bias voltage. This will be discussed in section 3.5.

Silicon is an indirect semiconductor, meaning that the minimum of the conduction band and the maximum of the valence band are located at different crystal momenta (see figure 3.7). Excitation of a valence electron usually occurs vertically in this diagram, because the crystal momentum can only be changed by a phonon. Therefore, the energy barrier for excitation $\Delta E = 3.6\,\mathrm{eV} > E_G$ is larger than the band gap.

3.4.1. Thermal generation

The environment of a semiconductor at a temperature T can transfer heat energy of $E_{\mathrm{therm}} = k_B T$ to an electron. At room temperature $T \approx 300\,\mathrm{K}$ the available energy becomes $E_{\mathrm{therm}} = 0.0259\,\mathrm{eV}$. This energy is too small to overcome the energy barrier ΔE directly, but it can create e-h-pairs via energy states inside the forbidden gap which are created by impurities and imperfections of the crystal lattice. These thermally created e-h-pairs cause a random fluctuation of the charge carrier concentration, which overlays the charge created by the actual signal of the sensor. Thermal generation is therefore considered as a noise source.

3.4.2. Generation by electromagnetic excitation

The energy barrier ΔE can be overcome if a valence electron absorbs a photon with enough energy. This changes the charge carrier concentration depending on the intensity and wavelength of the incident light, and is applied to photodetectors and solar cells. A silicon microstrip sensor would therefore in principle be able to detect photons. However, the detection of a photon usually involves its absorption, which should only happen in detector systems that can determine the photon's energy, i.e. in the ECL.

3.4.3. Generation by charged particles

When traversing the semiconductor, charged particles lose a part of their energy and ionise the silicon atoms, thus generating e-h-pairs. Here, electrons and positrons have to be treated separately from heavier particles.

Electrons and positrons

Figure 3.8 shows the processes by which electrons and positrons lose their energy as function of the particle energy. For high particle energy the relative energy loss is dominated by bremsstrahlung, while low energy particles share their energy loss among ionisation as main contribution, Møller scattering and Bhabha scattering.

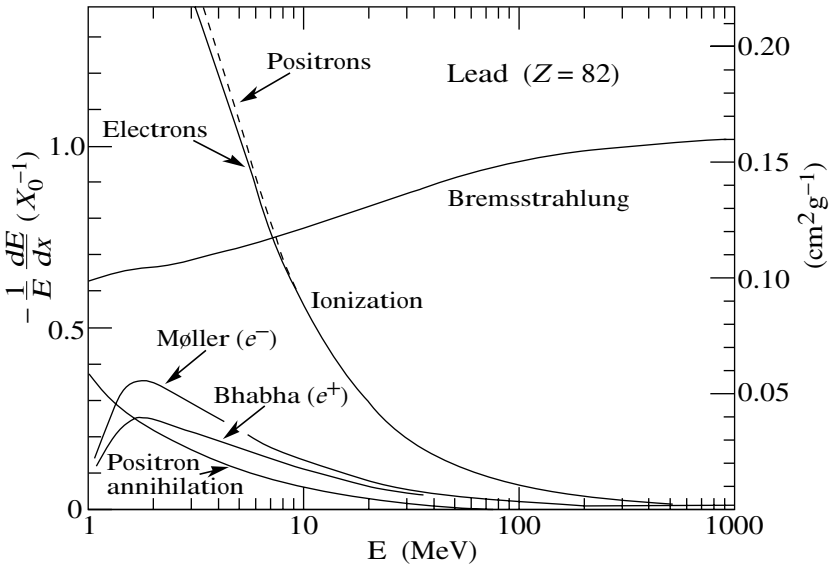

Figure 3.8.: Relative energy loss per radiation length as a function of the particle energy in lead [28]. Electron and positron scattering is called ionisation for an energy loss per collision below 0.255 MeV, and Møller scattering and Bhabha scattering for higher energy loss.

The characteristic material property for the overall energy loss is the radiation length X_0. High energy electrons and positrons lose all but $1/e$ of their energy after traversing a material thickness of one X_0. A phenomenological fit formula calculates X_0 as follows [28]:

$$X_0 = \frac{716.4 \cdot A}{Z(Z+1)\ln\left(\frac{287}{\sqrt{Z}}\right)} \, g/cm^2 \times \frac{1}{\rho} \qquad \text{with} \qquad Z > 4 \tag{3.29}$$

where A is the mass number, Z is the atomic number and ρ is the density of the material in g/cm^3. Silicon has a density of $\rho = 2.33\ g/cm^3$, so its radiation length becomes $X_0^{\mathrm{Si}} = 9.36\,\mathrm{cm}$.

Other charged particles

The Bethe-Bloch equation 3.30 allows the calculation of the mean energy loss (or "stopping power") per traversed material thickness as function of the particle's energy [28]:

$$\left\langle -\frac{\mathrm{d}E}{\mathrm{d}x} \right\rangle = K z^2 \frac{Z}{A} \frac{1}{\beta^2} \left[\frac{1}{2} \ln \frac{2 m_e c^2 \beta^2 \gamma^2 T_{\max}}{I^2} - \beta^2 - \frac{\delta(\beta\gamma)}{2} \right] \tag{3.30}$$

where the quantities in the equation are defined as follows:

Symbol	Definition	Units or Value
Z	atomic number of absorber	
A	atomic mass of absorber	
K	$4\pi N_{\mathrm{A}} r_{\mathrm{e}}^2 m_{\mathrm{e}} c^2 / A$	$0.307075\,\mathrm{MeV\,cm^{-1}}$
N_{A}	Avogadro's number	$6.022 \times 10^{23}\ \mathrm{mol^{-1}}$
r_{e}	classical electron radius	$\frac{e^2}{4\pi\epsilon_0 m_{\mathrm{e}} c^2}$
ze	charge of incident particle	
$m_{\mathrm{e}}c^2$	electron mass $\times c^2$	0.511 keV
β	$\frac{v}{c}$	
γ	$(1-\beta^2)^{-1/2}$	
I	mean excitation energy	eV
$\delta(\beta\gamma)$	density effect correction	
$T_{\max}$	$E_{\mathrm{kin}}^{\max}$ per collision	MeV

The graph of the Bethe-Bloch equation 3.30 is shown in figure 3.9. The minimal energy loss is located at $\beta\gamma \approx 3$ regardless of the particle type. For muons this corresponds to an energy of about 350 MeV, for pions to about 470 MeV, and for protons to about 3.2 GeV. A particle which loses a minimum of energy – and thus creates the smallest possible signal in the sensor – is called "minimum ionising particle" (MIP[6]), and is an important

[6] MIP: Minimum Ionising Particle

benchmark when testing a sensor with real particles. In a real particle physics experiment, one can assume that most particles to be detected are minimum ionising particles or at least close.

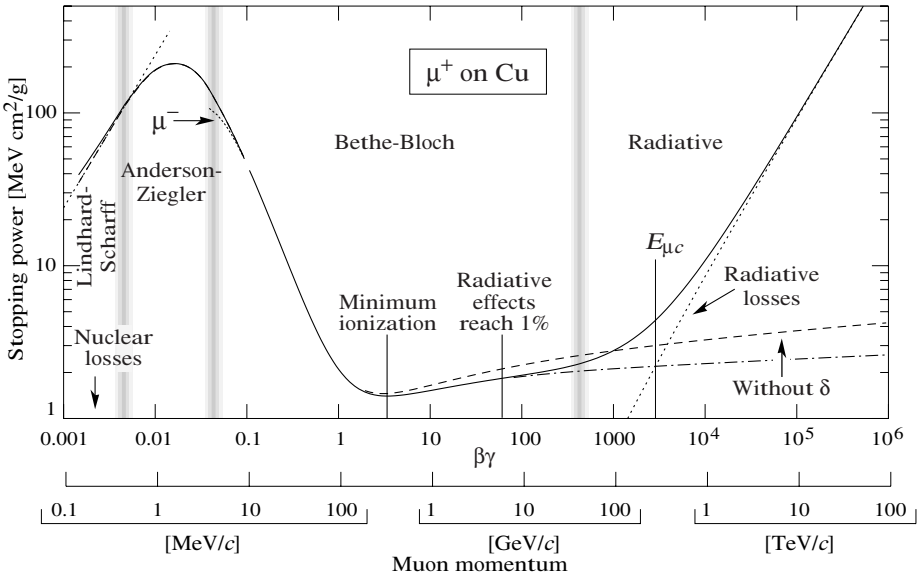

Figure 3.9.: Mean energy loss per material thickness ($\langle -\mathrm{d}E/\mathrm{d}x \rangle$) for positive muons in copper as function of $\beta\gamma = p/mc$ over nine orders of magnitude in momentum (12 orders of magnitude in kinetic energy) [28]. The solid line describes the sum of all mechanisms. Different approximation regions are indicated by vertical bands.

The Bethe-Bloch equation 3.30 calculates the *mean* energy loss of particles in matter, and not the energy loss of a single particle for a single traversal of material. The actual energy loss is a random quantum process and fluctuates according to a Landau probability density function (see section 4).

3.4.4. Charge carrier lifetime

The lifetime of majority and minority charge carriers in a semiconductor is usually expressed in terms of the generation rate and the recombination rate. Those rates describe the relaxation of the system from a state of non-equlilibrium back to equilibrium. The non-equilibrium can be created either by removing charge carriers or injecting additional charge carriers. The former animates the system to charge carrier generation, while the latter leads to charge carrier recombination.

Additional minority charge carriers can be created by a light pulse or by exposing the semiconductor to ionising radiation. The system is disturbed and relaxes back into equilibrium after a certain time by charge carrier recombination. The equilibruim recombination rate

R is determined by thermally generated charge carriers only, and can be assumed to be proportional to both the electron and the hole concentration:

$$R_{\mathrm{therm}} = \beta n_0 p_0 = \beta n_{\mathrm{i}}^2 \qquad \beta = \mathrm{const.} \tag{3.31}$$

A disruption of the system by external radiation leads to an additional generation rate G_{rad} by creating additional e-h-pairs. This increases the equilibrium charge carrier concentrations n_0 and p_0 by the same amount $\Delta n = \Delta p = \Delta$, each. Hence, the non-equilibrium recombination rate reads:

$$R_{\mathrm{non-eq}} = \beta(n_0 + \Delta)(p_0 + \Delta). \tag{3.32}$$

The situation in a direct semiconductor can easily be calculated. The average hole and electron concentrations at thermal equilibrium are constant over time, so the thermal generation rate G_{therm} and the thermal recombination rate R_{therm} must be equal:

$$G_{\mathrm{therm}} = R_{\mathrm{therm}} = \beta n_0 p_0. \tag{3.33}$$

We can now express the non-equilibrium state in terms of an excess recombination rate U which vanishes at the thermal equilibrium:

$$U = R_{\mathrm{non-eq}} - R_{\mathrm{therm}} = \beta\left((n_0 + \Delta)(p_0 + \Delta) - n_0 p_0\right). \tag{3.34}$$

The additional radiation-induced generation rate G_{rad} must be counteracted by the excess recombination rate U:

$$\begin{aligned} G_{\mathrm{rad}} = U &= \beta(n_0 + \Delta)(p_0 + \Delta) - \beta n_0 p_0 && (3.35)\\ &= \beta(n_0 p_0 + n_0\Delta + p_0\Delta + \Delta^2 - n_0 p_0) && (3.36)\\ &= \beta\Delta(n_0 + p_0 + \Delta) && (3.37) \end{aligned}$$

As long as the number of externally generated e-h-pairs is small against the number of majority charge carriers ($\Delta \ll n_0$ for n-type and $\Delta \ll p_0$ for p-type material) we can simplify equation 3.37 to:

$$G_{\mathrm{rad}} = \beta n_0 \Delta = \frac{\Delta}{\tau_{\mathrm{r}}} \qquad \text{for n-type material with} \qquad \tau_{\mathrm{r}} = \frac{1}{\beta n_0} \tag{3.38}$$

$$G_{\mathrm{rad}} = \beta p_0 \Delta = \frac{\Delta}{\tau_{\mathrm{r}}} \qquad \text{for p-type material with} \qquad \tau_{\mathrm{r}} = \frac{1}{\beta p_0}, \tag{3.39}$$

where the recombination lifetime τ_{r} is the characteristic time constant describing relaxation of the minority carrier density back to the thermal equilibrium.

The opposite situation (all charge carriers removed by e.g an external voltage) can be described with similar considerations as before. Now, the initial recombination rate vanishes, so that the generation rate equals the thermal generation rate. Consequently, the generation lifetime τ_{g} for the relaxation to the equilibrium reads:

$$\tau_{\mathrm{g}} = \frac{n_{\mathrm{i}}}{G_{\mathrm{therm}}} = \frac{1}{\beta n_{\mathrm{i}}}, \tag{3.40}$$

The situation in direct semiconductors like silicon is more complicated. Here, the maximum of the valence band and the minimum of the conduction band are located at different crystal momenta (see figure 3.7). Recombination can only happen with a simultaneous change of the crystal momentum, and is therefore carried out in a two-step process, which involves energy states inside the forbidden band gap. These additional states are introduced by lattice defects and impurities (the so-called "trapping centers") and can capture charge carriers and subsequently release them. This process is called "trapping", and stops the motion of a drifting charge carrier, which therefore cannot contribute to the sensor signal anymore (for details see section 4). The number of trapping centers can be increased by radiation damage.

3.5. Basic semiconductor structures

Semiconductor structures unleash their full power when p-type and n-type materials are combined. When adding insulators and metals, one can create the basic building blocks needed for ICs and silicon microstrip sensors. In the following sections we review the most important combined structures needed for understanding the sensor principle.

3.5.1. The p-n-junction or diode

The diode is the simplest semiconductor device. It can be compared to a check valve, as it permits a current in one direction only, thus showing a rectifying behaviour. A diode has a very low resistance for the conducting direction and a very high one for the reverse direction.

Joining n-type silicon and p-type silicon creates a so-called p-n-junction. As soon as these material have contact, the diffusion will try to even out the sudden imbalance in charge carrier concentration. The n-type region has an excess of electrons, which diffuse into the p-type region and recombine with the holes, and vice versa. This leads to an excess of donor and acceptor atoms, whose overall electrical charge is not compensated anymore by the free charge carriers. A so-called "space charge region[7]" is created in the area of the recombining charge carriers. The space charge region develops an electric field which limits the diffusion of charge carriers into the "foreign" area. So the dimension of the space charge region is limited, and the p-n-junction shows a region free of charge carriers between n-type and p-type material, which is also called depletion region. Figure 3.10 shows various electrical quantities as functions of the coordinate normal to the p-n-junction.

The Fermi energies of n-type and p-type materials are shifted in different directions inside the band gap (see equations 3.10 and 3.11). Once in contact, the materials try to establish equilibrium, and the Fermi energies have to be the same $E_{\text{Fermi,n}} = E_{\text{Fermi,p}} = E_{\text{Fermi}}$. This leads to a bending of the overall conduction band and valence band, see figure 3.10 b).

[7] Also called "depletion zone" or "depletion region"

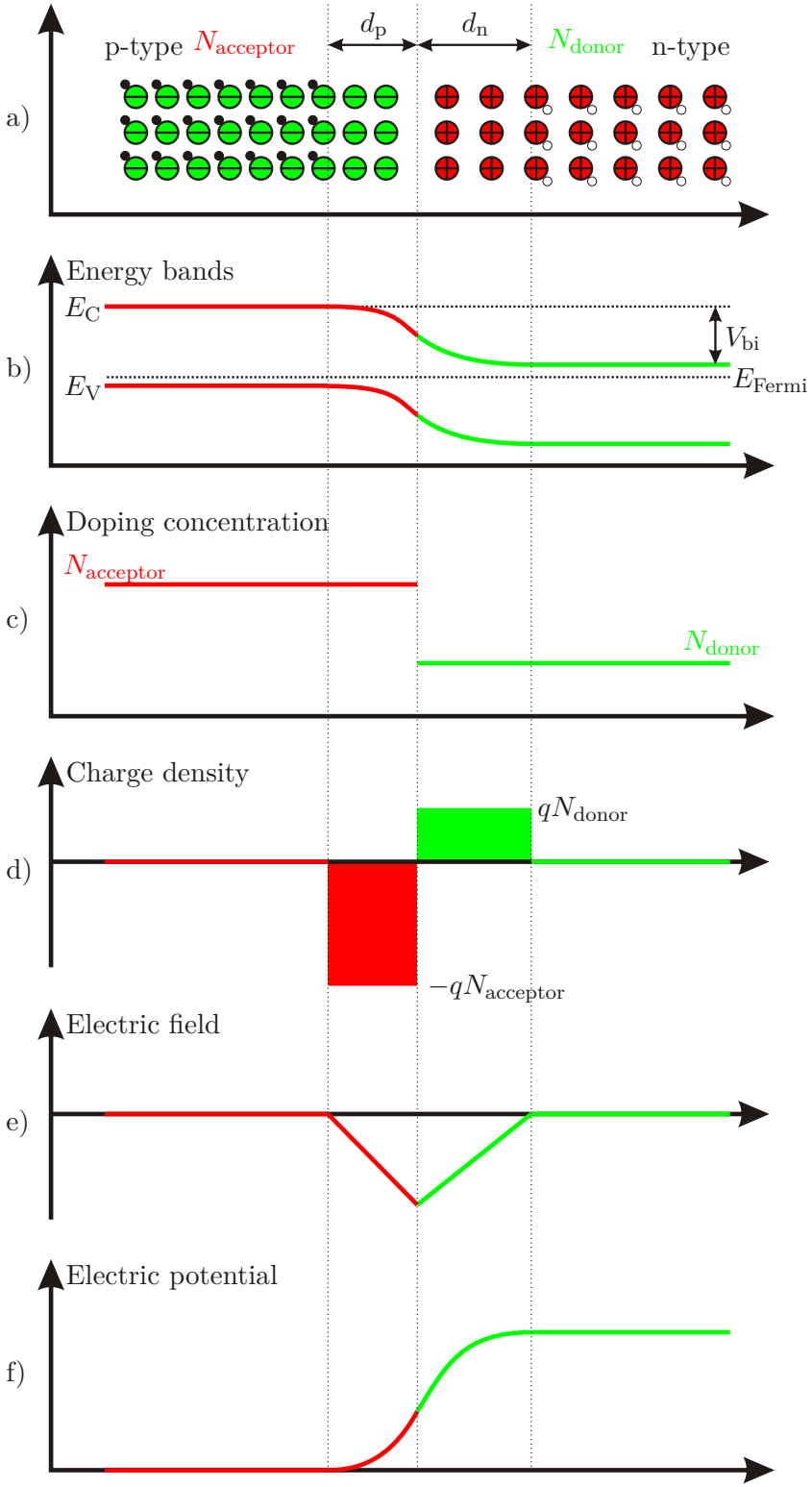

Figure 3.10.: Various electrical quantities around a p-n-junction. a) Schematic distribution of donors, acceptors and the depletion region; b) Bent energy bands; c) Dopant concentration; d) Charge density; e) Electric field; f) Electric potential [26].

Consequently, a p-n-junction develops a potential difference, the so-called "built-in voltage" of diffusion voltage V_{bi}. Using equations 3.12 and 3.13 and assuming that all dopant atoms are fully ionised we find:

$$n_{\mathrm{n}} = N_{\mathrm{donor}}, \qquad p_{\mathrm{p}} = N_{\mathrm{acceptor}} \tag{3.41}$$

$$N_{\mathrm{donor}} \cdot N_{\mathrm{acceptor}} = n_{\mathrm{i}}^2 \exp \frac{E_{\mathrm{Fermi,p}} - E_{\mathrm{Fermi,n}}}{k_{\mathrm{B}} T} \tag{3.42}$$

$$V_{\mathrm{bi}} = \frac{1}{q}(E_{\mathrm{Fermi,p}} - E_{\mathrm{Fermi,n}}) = \frac{k_{\mathrm{B}} T}{q} \ln \frac{N_{\mathrm{acceptor}} N_{\mathrm{donor}}}{n_{\mathrm{i}}^2}. \tag{3.43}$$

The dimension of the depletion regions in the p-type material d_{p} and in the n-type material d_{n} are calculated as [25]:

$$d_{\mathrm{n}} = \sqrt{\frac{2\epsilon\epsilon_0}{q_{\mathrm{e}}} \frac{N_{\mathrm{acceptor}}}{N_{\mathrm{donor}}(N_{\mathrm{acceptor}} + N_{\mathrm{donor}})} V_{\mathrm{bi}}} \tag{3.44}$$

$$d_{\mathrm{p}} = \sqrt{\frac{2\epsilon\epsilon_0}{q_{\mathrm{e}}} \frac{N_{\mathrm{donor}}}{N_{\mathrm{acceptor}}(N_{\mathrm{acceptor}} + N_{\mathrm{donor}})} V_{\mathrm{bi}}} \tag{3.45}$$

$$d = d_{\mathrm{n}} + d_{\mathrm{p}} = \sqrt{\frac{2\epsilon\epsilon_0 (N_{\mathrm{acceptor}} + N_{\mathrm{donor}})}{q_{\mathrm{e}} N_{\mathrm{acceptor}} N_{\mathrm{donor}}} V_{\mathrm{bi}}} \tag{3.46}$$

In realistic applications one forms p-n-junctions with a highly doped region inside a lowly doped bulk substrate. Lets assume the case of a highly doped p-type region in an n-type bulk $N_{\mathrm{acceptor}} \gg N_{\mathrm{donor}}$, then equation 3.46 simplifies to:

$$d = \sqrt{\frac{2\epsilon\epsilon_0}{q_{\mathrm{e}} N_{\mathrm{donor}}} V_{\mathrm{bi}}}. \tag{3.47}$$

The depletion region spreads predominantly into the lower doped area, and the thickness of this region is determined by the lower doping concentration. Applying an external voltage[8] V to the p-n-junction, the following happens: The voltage drop can only occur inside the space charge region, because only there the p-n-junction has a high resistivity (i.e. it is free of charge carriers). Consequently, the built-in voltage V_{bi} has to be replaced by $V_{\mathrm{bi}} + V$:

$$d = \sqrt{\frac{2\epsilon\epsilon_0 (N_{\mathrm{acceptor}} + N_{\mathrm{donor}})}{q_{\mathrm{e}} N_{\mathrm{acceptor}} N_{\mathrm{donor}}} (V_{\mathrm{bi}} + V)}. \tag{3.48}$$

In the forward bias case $V < 0$ the electric field limiting the diffusion is reduced, the space charge region shrinks until the p-n-junction becomes conductive at $V \approx -V_{\mathrm{bi}}$. In the

[8] Note that sign of the external voltage V can be chosen arbitrarily. In our convention – in accordance with the setup of our measurement devices in the laboratory – V is counted as positive from the p-type region to the n-type region, so that a positive external voltage corresponds to reverse biasing

reverse bias case $V > 0$ the electric field is enhanced, the space charge region grows, and the p-n-junction stays insulating.

With the same realistic simplification $N_{\text{acceptor}} \gg N_{\text{donor}}$, equation 3.48 becomes:

$$d = \sqrt{\frac{2\epsilon\epsilon_0}{q_e N_{\text{donor}}}(V_{\text{bi}} + V)}. \tag{3.49}$$

Current–Voltage characteristics (IV-curve)

As already mentioned in the previous section, the diode shows a very different behaviour depending on the polarity of the external voltage V:

Equilibrium ($V = 0$): The unequal charge distributions of the p-n-junction manifest a diffusion current from the majority region to the minority region, which leaves immobile dopant atoms unbalanced and causes a charge-up of the depletion region (space charge region). The emerging electrical field causes a drift current in the opposite direction to the diffusion. At equilibrium, these currents are equal.

Forward bias ($V < 0$): An external voltage $V < 0$ drops at the high-resistivity space charge region and causes the electrical field to decrease and eventually vanish, eliminating the drift current. The space charge region is flooded with diffusing charge carriers, making the diode conductive.

Reverse bias ($V > 0$): An external voltage $V > 0$ drops at the high-resistivity space charge region and causes the electrical field to increase. The region reachable by the diffusion current is pushed back, thus increasing the space charge region. The diode stays insulating with a very small leakage current (or dark current).

In case on an ideal diode the total current density through the p-n-junction is described by the Shockley equation:

$$J = J_0 \left(\mathrm{e}^{-\frac{q_e V}{k_B T}} - 1 \right). \tag{3.50}$$

The reverse bias current density saturates at the saturation current density J_0, while for forward biasing it grows exponentially. Figure 3.11 shows the current density as function of the bias voltage in the so-called "IV-curve". The measurement of this IV-curve is an important benchmark in the quality assurance of silicon microstrip sensors.

The saturation current density J_0 is calculated by [27]:

$$J_0 = \frac{q_e D_p p_{n0}}{L_p} + \frac{q_e D_n n_{p0}}{L_n} \tag{3.51}$$

$D_{n,p}$ are the diffusion constants for electrons and holes (see equations 3.28 and 3.27), p_{n0} and n_{p0} are the minority charge carrier densities at the respective "foreign" sides of the

p-n-junction at thermal equilibrium, and $L_\mathrm{n} = \sqrt{D_\mathrm{n}\tau_\mathrm{n}}$ and $L_\mathrm{p} = \sqrt{D_\mathrm{p}\tau_\mathrm{p}}$ denote the so-called diffusion lengths of electrons and holes, with $\tau_\mathrm{n,p}$ being the respective minority charge carrier lifetimes.

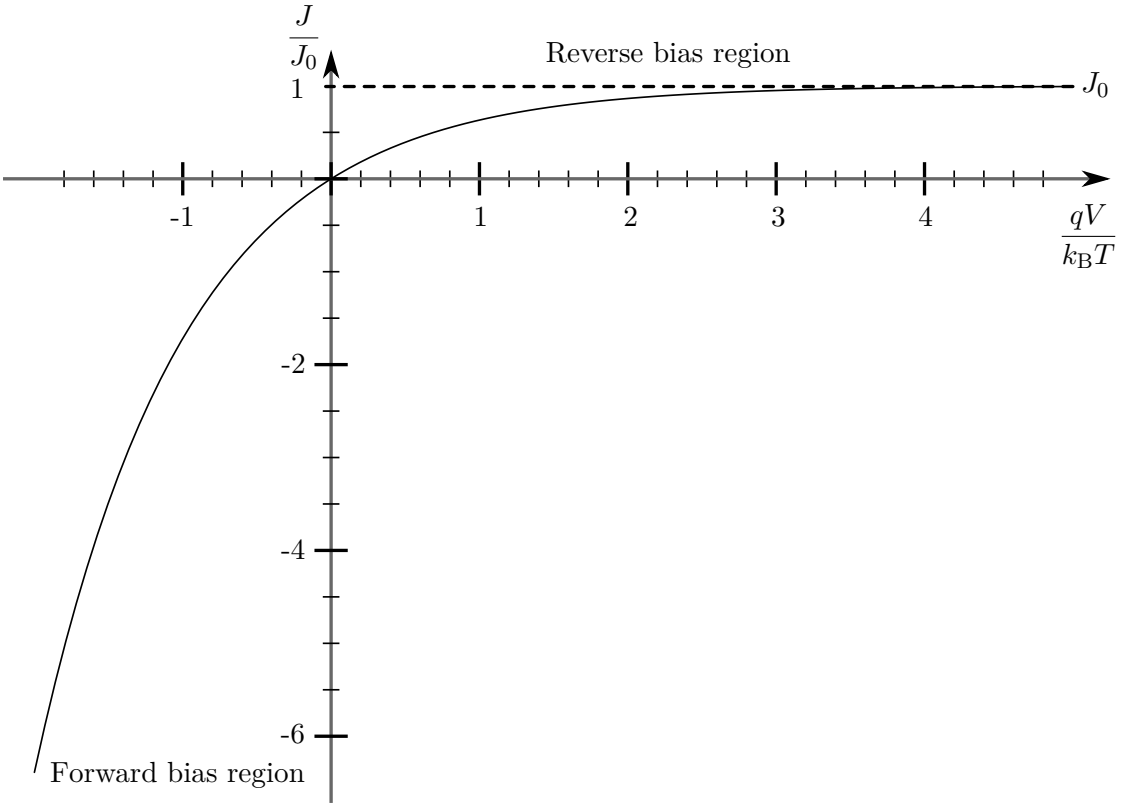

Figure 3.11.: Ideal IV-curve of a p-n-junction.

Capacitance–Voltage characteristics (CV-curve)

The conductive regions sandwiching the space charge region act like the electrodes of a capacitor, the capacitance of which strongly depends on the width of the depletion region. As is derived in [25], the inverse capacitance of the p-n-junction with a small strongly doped p-type region in an n-type bulk reads:

$$\frac{1}{C} = \frac{W}{\epsilon_0\epsilon} - \frac{k_\mathrm{B}T}{q_\mathrm{e}}\frac{1}{q_\mathrm{e}N_\mathrm{donor}^2}\frac{\mathrm{d}N_\mathrm{donor}}{\mathrm{d}W} \approx \frac{d}{\epsilon_0\epsilon}, \tag{3.52}$$

where W is the width of the space charge region[9]. The variation of the doping concentration N_donor in an n-type substrate can be assumed to be very constant, thus allowing us to neglect the corresponding term in equation 3.52. This allows to determine the width of the space charge region from the capacitance:

$$d = W = \frac{\epsilon_0\epsilon}{C}, \tag{3.53}$$

[9]The width of the space charge region is called W here in contrast to the previous nomenclature d. This is to avoid confusion with the differential operator d

where we re-introduced the previous nomenclature of the width d of the space charge region. The derivation of equation 3.53 was performed for a one-dimensional p-n-junction (i.e. a capacitor with unit area electrodes), while in reality the area A of the diode and thus the area of the capacitor is limited. Thus, equation 3.53 is expanded to:

$$d = W = A\frac{\epsilon_0\epsilon}{C}, \tag{3.54}$$

which is exactly the capacitance formula of a parallel plate capacitor with electrodes of area A separated by a dielectric with dielectric constant ϵ and a thickness of d.

One can determine the dopant concentration N_{donor} from equation 3.52 as function of d and consequently as function of the external bias voltage V. So, one can unfold the doping profile $N_{\mathrm{donor}}(V)$ from the so-called CV-curve $C(V)$ [25]:

$$\frac{\mathrm{d}(1/C^2)}{\mathrm{d}V} = \frac{\mathrm{d}(1/C^2)/\mathrm{d}W}{\mathrm{d}V/\mathrm{d}W} = \frac{2W/(\epsilon_0\epsilon)^2}{q_\mathrm{e}N_{\mathrm{donor}}W/(\epsilon_0\epsilon)} = \frac{2}{q_\mathrm{e}N_{\mathrm{donor}}\epsilon_0\epsilon} \tag{3.55}$$

$$N_{\mathrm{donor}}(V) = \frac{2}{q_\mathrm{e}\epsilon_0\epsilon\frac{\mathrm{d}1/C^2}{\mathrm{d}V}}. \tag{3.56}$$

Equation 3.55 shows that for a constant doping concentration N_{donor} the inverse square of the capacitance grows linearly with the reverse bias voltage V. Equation 3.56 calculates the doping concentration N_{donor} from the CV-curve as function of the reverse bias voltage V. The width of the space charge region d and thus the depth inside the doping profile depends on the bias voltage V according to equation 3.49.

Full depletion voltage

According to equation 3.52 the capacitance of the p-n-junction changes when the width of the depletion region changes. When ramping up the reverse bias voltage V, the space charge region will eventually cover the full thickness of the device at a certain voltage $V = V_{\mathrm{FD}}$, the so-called "full depletion voltage". Equation 3.55 states that the inverse square of the capacitance grows linearly for $V < V_{\mathrm{FD}}$, while for $V \geq V_{\mathrm{FD}}$ the capacitance stays constant at a value of $C = C_{\mathrm{FD}}$, as is sketched in figure 3.12.

According to equation 3.49 the width of the depletion region can be calculated from the reverse bias voltage. Choosing $V = V_{\mathrm{FD}}$ and neglecting the small built-in voltage V_{bi} allows to calculate the thickness d of a device:

$$d = \sqrt{\frac{2\epsilon_0\epsilon}{q_\mathrm{e}N_{\mathrm{donor}}}V_{\mathrm{FD}}}. \tag{3.57}$$

The doping concentration of the base material (the wafer) is usually expressed in terms of the bulk resistivity. Therefore, we rewrite the above equation using the definition of the resistivity from equation 3.22:

$$d = \sqrt{2\epsilon_0\epsilon\mu_\mathrm{n}\rho V_{\mathrm{FD}}}. \tag{3.58}$$

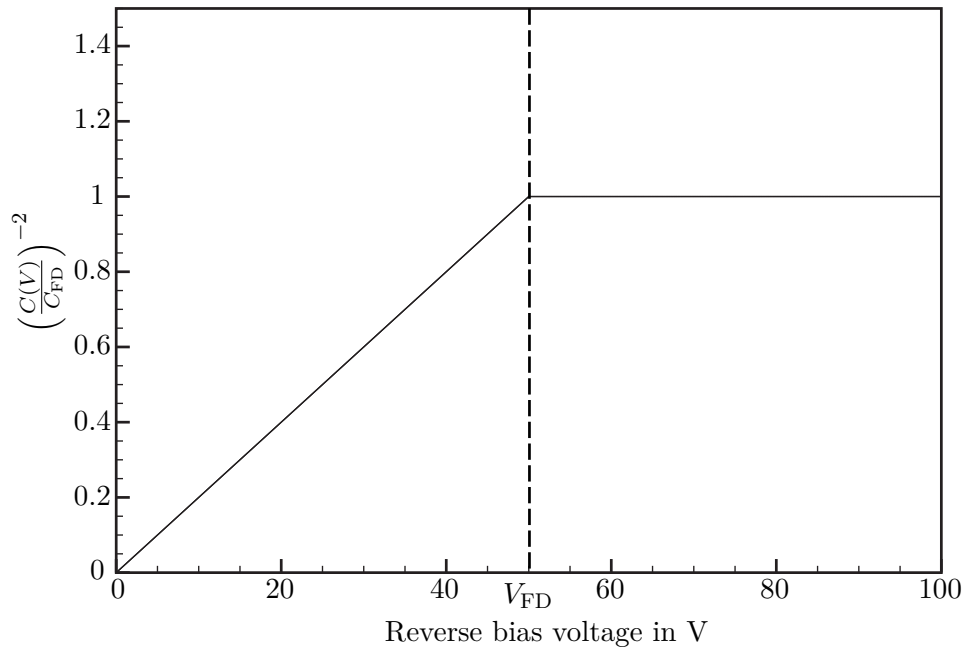

Figure 3.12.: CV-curve of an ideal bulk diode. For reverse bias voltages $V < V_{\mathrm{FD}}$ the inverse square capacitance grows linearly. At $V = V_{\mathrm{FD}}$ the depletion region can't grow any further because the device is fully depleted. Hence, the capacitance remains constant at its full-depletion value $C = C_{\mathrm{FD}}$ [26].

In real silicon microstrip sensors the "electrodes" of the p-n-junction are segmented and therefore don't qualify for an ideal diode. The calculation of the voltage drop in the space charge region is more complicated, a correction to the formula of the full depletion voltage V_{FD} is given in [29]:

$$V_{\mathrm{FD,sensor}} = V_{\mathrm{FD,diode}} \left[1 + 2\frac{p}{d} f\left(\frac{w}{p}\right)\right], \tag{3.59}$$

where p denotes the pitch between neighbouring strips[10] and w is the width of the strip implant. The numerical approximation function $f(w/p)$ depends on the width-to-pitch ratio and reads [29]:

$$f(x) = -0.00111x^{-2} + 0.0586x^{-1} + 0.240 - 0.651x + 0.355x^2. \tag{3.60}$$

[10]This is the pitch of *all* implanted strips, not the distance between readout strips only

The width-to-pitch ratio usually is in the order of 0.25, yielding the following relations between resistivity, thickness and full depletion:

$$d = \sqrt{\frac{2\epsilon_0\epsilon\mu_\mathrm{n}\rho V_\mathrm{FD,sensor}}{1 + 2\frac{p}{d}0.3161}} \tag{3.61}$$

$$\rho V_\mathrm{FD,diode} = \frac{\rho V_\mathrm{FD,sensor}}{1 + 2\frac{p}{d}0.3161} = \frac{d^2}{2\epsilon_0\epsilon\mu_\mathrm{n}} \tag{3.62}$$

$$\rho V_\mathrm{FD,sensor} = \frac{d^2(1 + 0.6322\frac{p}{d})}{2\epsilon_0\epsilon\mu_\mathrm{n}} = \frac{d^2 + 0.6322pd}{2\epsilon_0\epsilon\mu_\mathrm{n}}. \tag{3.63}$$

3.5.2. The n+-n or p+-p junction

When combining an n-type material with a p-type material, the space charge region is developed due to the high difference in charge carrier concentrations. The majority charge carriers of one material are the minority in the other one, and vice versa. A similar situation occurs even in single-type semiconductors when the doping concentration and thus the majority charge carrier concentration changes rapidly in a small region[11]. Just like for p-n-junctions, the Fermi energies are shifted differently due to the different doping concentrations. Here, the shifts have the same direction inside the band gap, but a different magnitude. Aligning the Fermi energies again causes the energy bands to bend, and a space charge region develops.

3.5.3. The metal-semiconductor contact

Similar to the p-n-junction, also the metal-semiconductor contact shows rectifying behaviour. This so-called "Schottky contact" forms at the interface between a metal and a lowly doped semiconductor. This combination manifests a similar situation as for a p-n-junction: The Fermi energies of metal and semiconductor are different, and upon contact have to align, bending the energy bands in the semiconductor.

In a metal, the Fermi energy is defined via the work function $q_\mathrm{e}\Phi_\mathrm{m}$, which is the minimal energy needed to remove an electron from the metal. The potential difference $\Phi_\mathrm{m} = (E_\mathrm{Vacuum} - E_\mathrm{Fermi})/q_\mathrm{e}$ between the Fermi energy and the vacuum depends on the metal, and differs from the corresponding potential difference $\Phi_\mathrm{s} < \Phi_\mathrm{m}$ found in the semiconductor. While Φ_s heavily depends on the Fermi energy and thus on the doping of the semiconductor, the so-called "electron affinity" $q_\mathrm{e}\chi = q_\mathrm{e}(E_\mathrm{Vacuum} - E_\mathrm{V})$ does not, as it is defined as the potential difference between the vacuum energy and the lower edge of the conduction band.

[11] Regions with high dopant concentrations are called n+ and p+, depending on the polarity of the dopants. Hence, single-type junctions are called n+-n and p+-p junctions

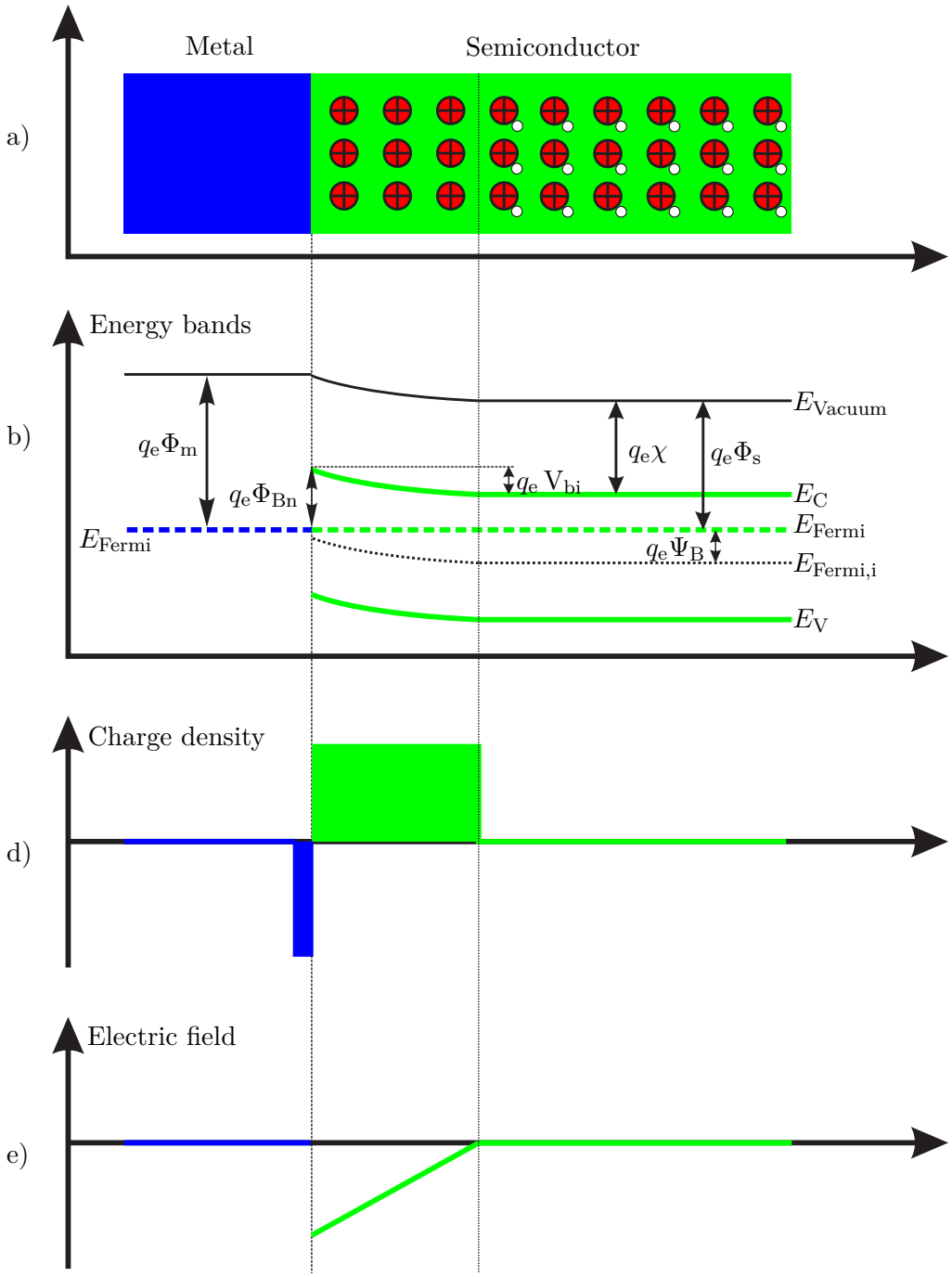

Figure 3.13.: An n-type semiconductor in contact with a metal layer develops a rectifying Schottky contact. While the barrier $q_{\mathrm{e}}\Phi_{\mathrm{Bn}}$ for electrons going from metal to semiconductor stays the same, the barrier for electrons going in the other direction depends on the voltage between metal and semiconductor.

Upon contact of metal and n-type semiconductor[12], the Fermi energies line up bending the energy bands in the semiconductor near the metal, which creates a built-in voltage $V_{\mathrm{bi}} = \Phi_{\mathrm{m}} - \Phi_{\mathrm{s}}$. This animates the charge carriers in the semiconductor to move according to the changed situation of the energy bands. The conduction band is bent upwards, thus removing conduction electrons from the surface, leading to a positive charge-up. In contrast, the number of free electrons in the metal is so huge that the Schottky contact does not change the overall energetic situation. Only at the interface metal electrons are accumulated to counteract the positive surface charge inside the semiconductor. The bent conduction band introduces an energy barrier for electrons diffusing from the metal to the semiconductor, they height of which is calculated as follows:

$$q_{\mathrm{e}}\Phi_{\mathrm{Bn}} = q_{\mathrm{e}}(\Phi_{\mathrm{m}} - \chi) \tag{3.64}$$

Since the lower edge of the conduction band is *above* the common Fermi energy, the barrier for electrons going from the semiconductor to the metal is smaller. The metal-to-semiconductor barrier is fixed, as it only depends on the initial difference of the Fermi energies, and cannot be influenced by an external voltage. On the other hand, the semiconductor-to-metal barrier indeed can be changed, allowing it to vanish for a certain external voltage. This introduces a rectifying behaviour similar to what is found in diodes.

Schottky contacts occur in silicon microstrip sensors whenever the metallisation layer touches the substrate without an oxide layer in between, which usually applies to contact pads for electrical measurements or connections on the sensor itself. The rectifying behaviour is disadvantageous and should be avoided by highly doping the semiconductor side of the Schottky contact. This pushes the Fermi energy into the conduction band[13], almost nullifying the energy barrier. Via electron tunneling [27] the semiconductor is conductive like a metal, and the Schottky contact becomes a normal ohmic contact.

3.5.4. The metal-oxide-semiconductor structure

The MOS[14] structure is a very important structure found on a wide range of semiconductor devices. In case of AC-coupled silicon microstrip sensors every strip is a MOS structure, additionally one often implements dedicated MOS test structures for monitoring the quality of the production process.

A MOS structure is a layer of insulating material sandwiched by a semiconductor and a metal layer. The insulator is often made of SiO_2[15]. Similar to the situation in a Schottky contact, the behaviour of a MOS structure can be understood when looking at the

[12] The same arguments hold for the contact of a metal and a p-type semiconductor when looking at holes as majority charge carriers and taking into account the different position of the Fermi energy inside the band gap. This usually leads to energy bands bent in the other direction

[13] A semiconductor so highly doped that the Fermi energy moves into the conduction band (n-type) or into the valence band (p-type) is called "degenerate"

[14] MOS: Metal-Oxide-Semiconductor

[15] SiO_2: Silicon Dioxide

bending of the energy bands and the resulting changes in charge carrier concentrations in the vicinity of the interface. To simplify the discussion of the properties, we first look at an n-type semiconductor in thermal equilibrium and assume the oxide layer to be free of charges. When an external voltage V is applied between the semiconductor and the metal layers, one can distinguish four different scenarios: flat-band, accumulation, depletion and inversion.

Flat-band situation ($V = V_{\mathrm{FB}}$)

As already discussed before, the Fermi energies of different materials in contact and thermal equilibrium have to line up, leading to a bending of the energy bands. If we assume equal work functions of metal and semiconductor for simplicity, then no adjustments of the Fermi energies is needed, the energy bands are *not* bent, the MOS structure is in flat-band situation. The absence of oxide charges ensures that the vacuum energy levels of the metal and the semiconductor are equal.
When the work functions of metal $q_{\mathrm{e}}\Phi_{\mathrm{m}}$ and semiconductor $q_{\mathrm{e}}\Phi_{\mathrm{s}}$ are different, the Fermi energies need to adjust themselves, and we have to apply an external voltage $V = V_{\mathrm{FB}}$ between the semiconductor and the metal to compensate this difference:

$$V_{\mathrm{FB}} = \Phi_{\mathrm{m}} - \Phi_s \tag{3.65}$$

Figure 3.14 shows a sketch of the flat-band situation.

Accumulation situation

For an external voltage $V > V_{\mathrm{FB}}$ the energy bands at the semiconductor-side bend downwards. This creates energetically advantageous states near the interface which are filled with electrons accumulating in a thin layer. The migration of electrons towards the interface stops as soon as the equilibrium condition is fulfiled:

$$\frac{n}{n_{\mathrm{i}}} = \exp \frac{E_{\mathrm{Fermi}} - E_{\mathrm{Fermi,i}}}{k_{\mathrm{B}}T} \tag{3.66}$$

where n_{i} is the intrinsic and n is the actual charge carrier concentration. This yields a surface charge density of:

$$Q_{\mathrm{acc}} = -\epsilon_0\epsilon_{\mathrm{ox}} \frac{V - V_{\mathrm{FB}}}{d_{\mathrm{ox}}} = -C_{\mathrm{ox}}(V - V_{\mathrm{FB}}) \tag{3.67}$$

where ϵ_{ox}, d_{ox} and C_{ox} are the dielectric constant, the thickness and the capacitance per unit area of the oxide.

Figure 3.15 shows a sketch of the accumulation situation. When always positively charged oxide charges are included, this electron layer occurs at any interface between semiconductor and oxide. In case of an n-type bulk material the accumulation situation develops the so-called accumulation layer made from majority charge carriers, while for a p-type bulk

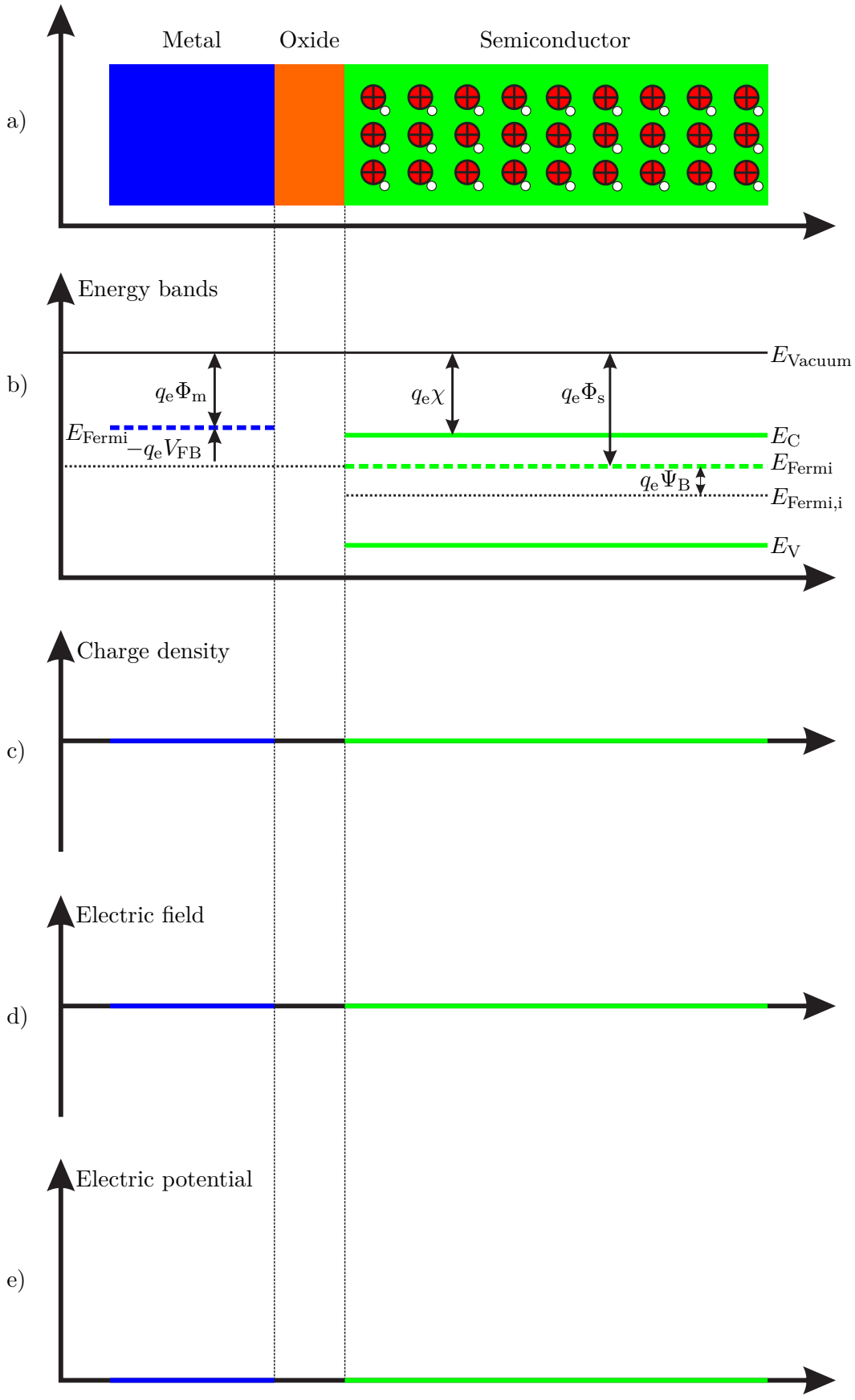

Figure 3.14.: An n-type MOS structure in the flat-band situation $V = V_{\mathrm{FB}}$ [26]. The oxide is assumed to be free of charges.

material the inversion situation creates the so-called inversion layer consisting of minority charge carriers (see section 3.5.4). If any structure at this surface uses electrons as majority charge carriers, the accumulation layer (or inversion layer) needs to be interrupted to ensure electrical insulation. More details on how to interrupt this layer are given in section 7.

Depletion situation

For an external voltage $V < V_{\mathrm{FB}}$ the energy bands at the semiconductor-side bend upwards. This reduces the electron concentration at the interface – a depletion region is formed.

The depth of this depletion region is calculated by [25]:

$$d_{\mathrm{s}} = \sqrt{\frac{\epsilon_0 \epsilon_{\mathrm{s}}}{q_{\mathrm{e}} N_{\mathrm{donor}}}(V_{\mathrm{FB}} - V) + \left(\frac{\epsilon_{\mathrm{s}}}{\epsilon_{\mathrm{ox}}} d_{\mathrm{ox}}\right)^2} - \frac{\epsilon_{\mathrm{s}}}{\epsilon_{\mathrm{ox}}} d_{\mathrm{ox}} \tag{3.68}$$

where ϵ_{s} is the dielectric constant of the semiconductor material.

Figure 3.16 shows a sketch of the depletion situation.

Inversion situation

For an external voltage $V \ll V_{\mathrm{FB}}$ considerably smaller than the flat-band voltage the energy bands at the semiconductor-side bend upwards, increasing the intrinsic Fermi energy $E_{\mathrm{Fermi,i}}$ in the bent area by an amount of $q_{\mathrm{e}}\Phi_{\mathrm{s}}$. For $V \ll V_{\mathrm{FB}}$ $E_{\mathrm{Fermi,i}}$ can exceed the extrinsic Fermi energy E_{Fermi} in the unbent area. In this case, a "majority" of holes "accumulates" at the interface, and the situation is called "inversion". The hole density reaches the same magnitude as the bulk electron density for $\Phi_{\mathrm{s}} = -2\Phi_{\mathrm{B}}$. This situation is called "strong inversion". In that case, the depletion depth of electrons reaches its maximum and saturates, i.e. a further increase of V doesn't change the depletion depth anymore [25]:

$$d_{\mathrm{max}} = \sqrt{\frac{4\epsilon_0 \epsilon_{\mathrm{s}} \Phi_{\mathrm{B}}}{q_{\mathrm{e}} N_{\mathrm{donor}}}}. \tag{3.69}$$

Figure 3.17 shows a sketch of the weak inversion situation.

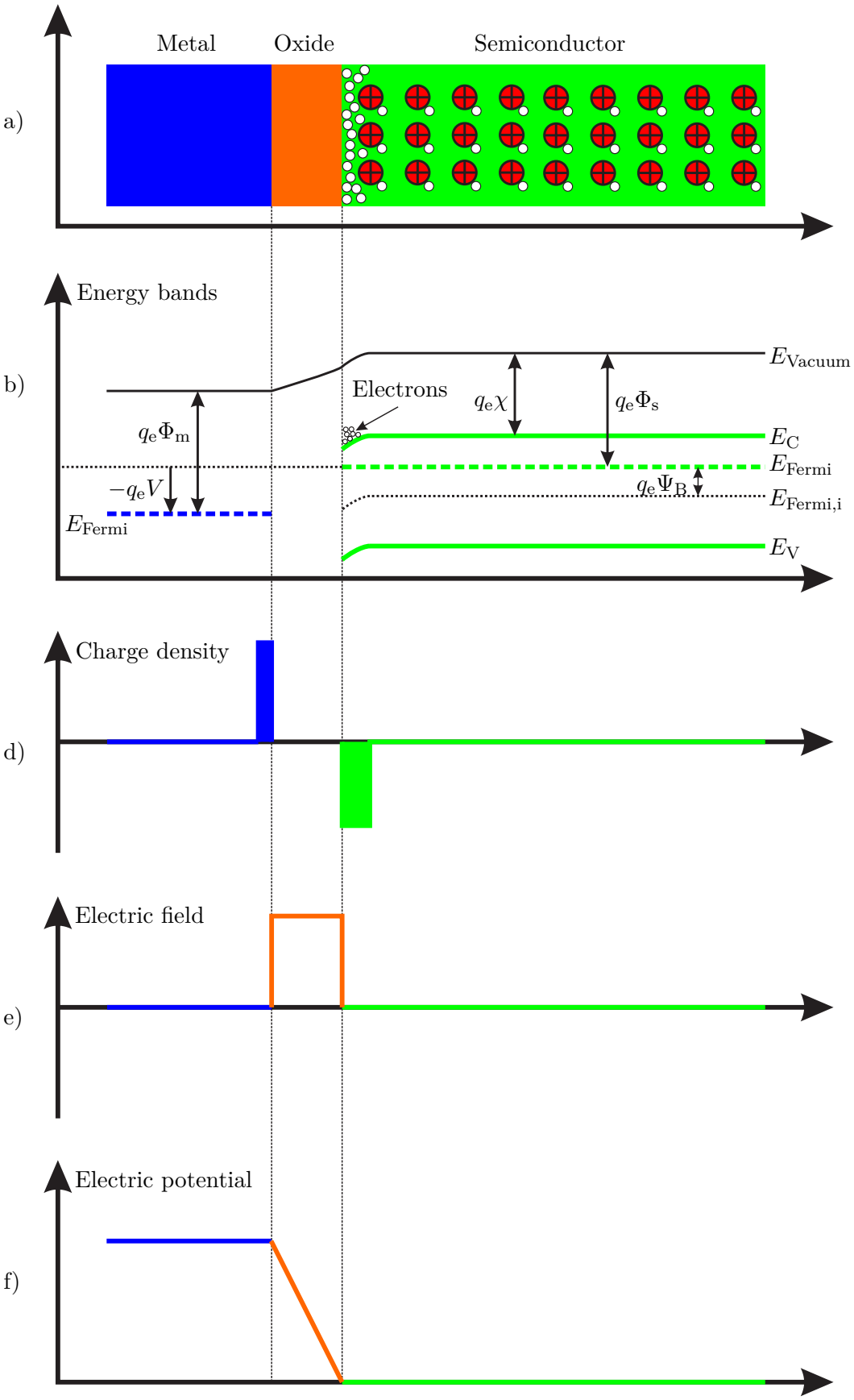

Figure 3.15.: An n-type MOS structure in the accumulation situation $V > V_{\mathrm{FB}}$ [26]. The oxide is considered to be free of charges.

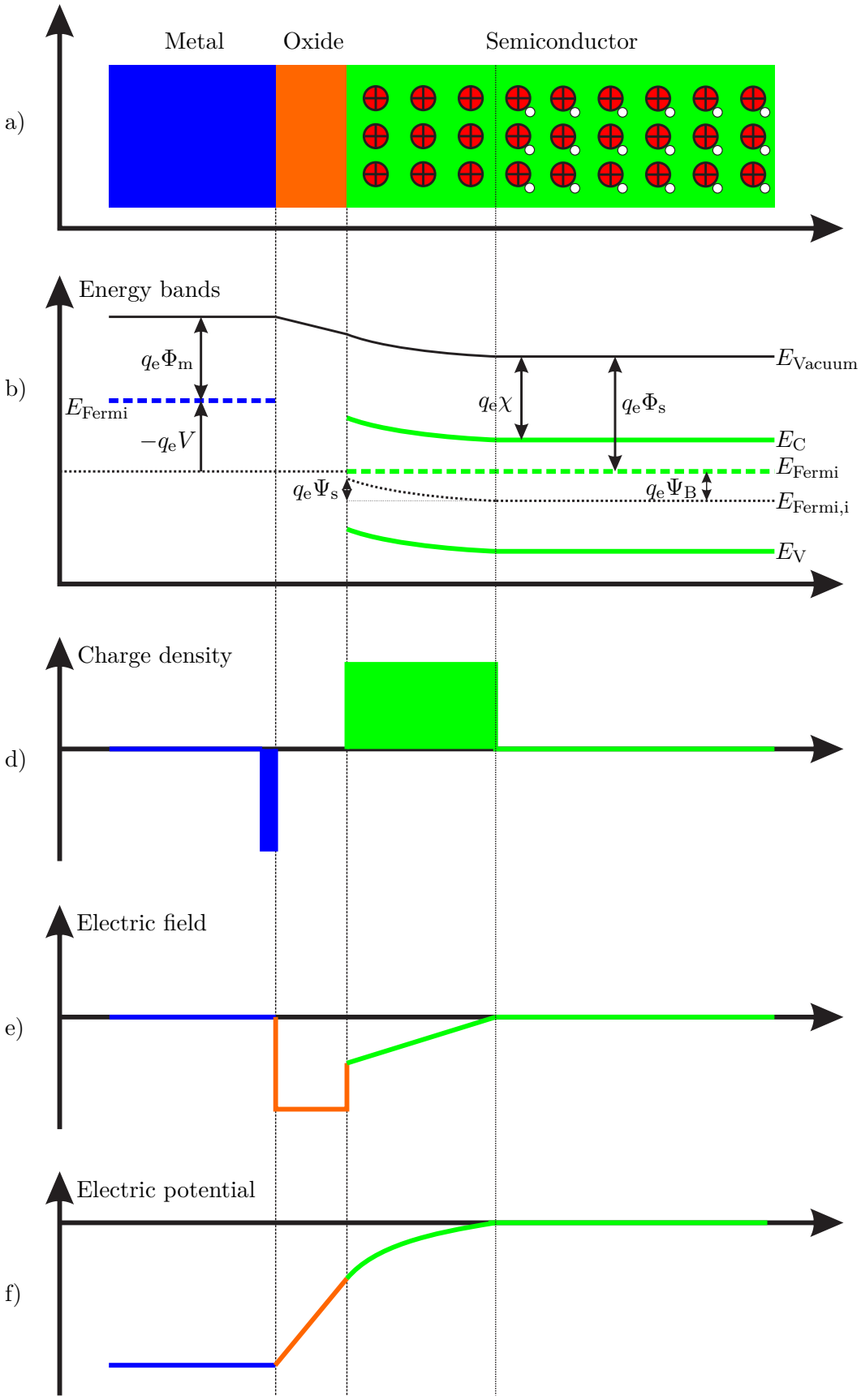

Figure 3.16.: An n-type MOS structure in the depletion situation $V < V_{FB}$ [26]. The oxide is considered to be free of charges.

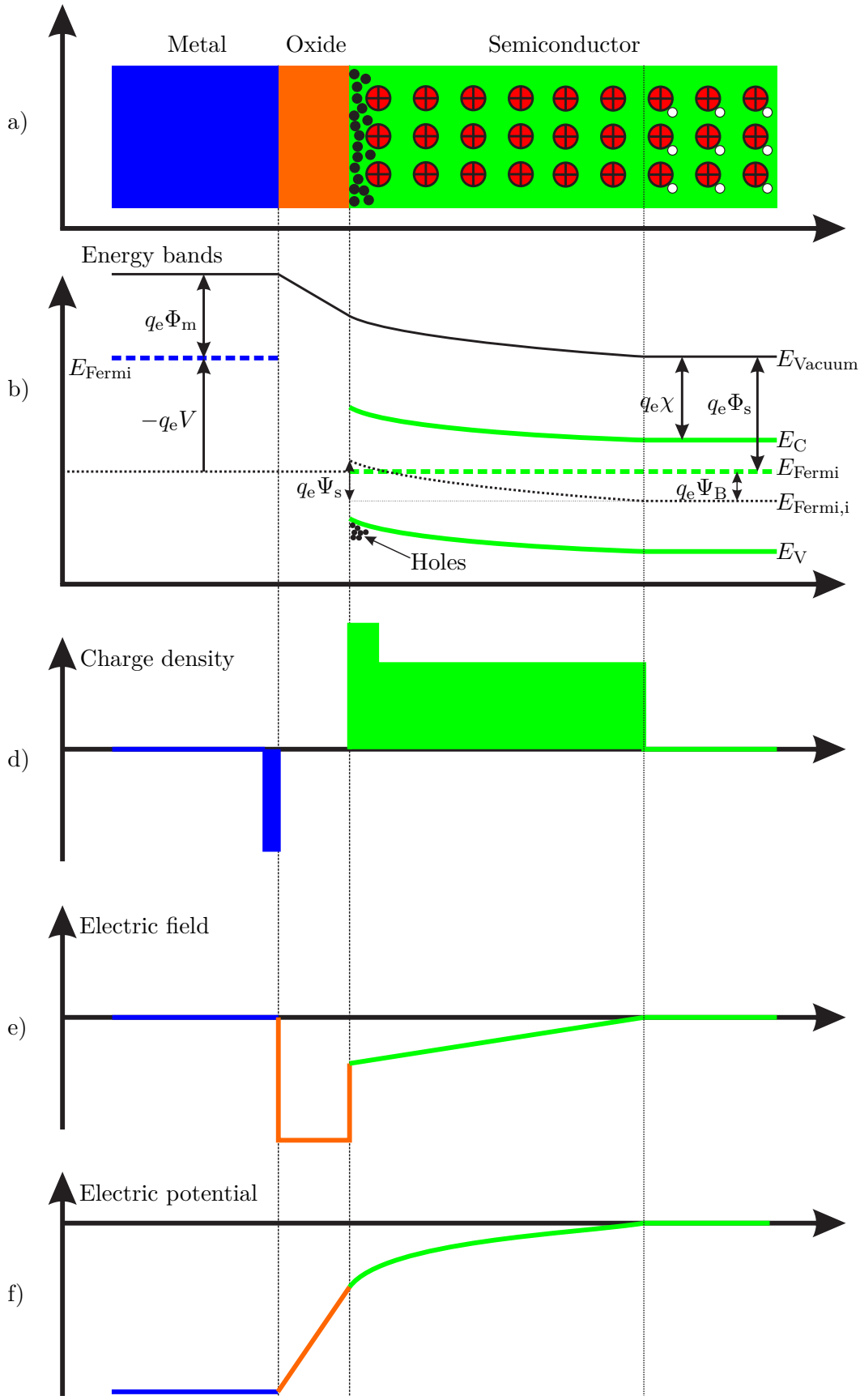

Figure 3.17.: An n-type MOS structure in the (weak) inversion situation $V \ll V_{FB}$ [26]. The oxide is considered to be free of charges.

Capacitance–Voltage characteristics

On can measure the capacitance of a MOS structure by applying a DC voltage modulated with a small AC[16] voltage. The system response is determined by the relation between the relaxation time constant of the structure and the frequency of the AC voltage, and is thus strongly frequency dependent.

For a low frequency of the AC voltage we can assume ($C_{\mathrm{ox}} = \frac{\epsilon_0 \epsilon_{\mathrm{ox}}}{d_{\mathrm{ox}}}$, $C_{\mathrm{s}} = \frac{\epsilon_0 \epsilon_{\mathrm{s}}}{d_{\mathrm{s}}}$):

- Accumulation region: $C = C_{\mathrm{ox}}$
- Depletion region: $C = \frac{C_{\mathrm{ox}} C_{\mathrm{s}}}{C_{\mathrm{ox}} + C_{\mathrm{s}}}$, because the capacitance of the depletion layer and of the oxide and are in series.
- Inversion region: $C = C_{\mathrm{ox}}$ because the width of the depletion layer stays constant, while the charge density at the interface changes with the applied voltage V.

For high frequencies of the AC voltage the measured capacitance again is $C = \frac{C_{\mathrm{ox}} C_{\mathrm{s}}}{C_{\mathrm{ox}} + C_{\mathrm{s}}}$, because the surface charge density stays constant while the width of the depletion layer varies with the AC voltage.

3.5.5. The oxide-semiconductor contact

The oxide of a real MOS structure will in general contain fixed positive oxide charges. These charges cause the vacuum energies E_{Vacuum} of metal and semiconductor to be different, which results in a changed flat-band voltage V_{FB}. This change is influenced by the amount and distribution of the fixed oxide charges $\rho(x)$, and can be calculated as:

$$\Delta V_{\mathrm{FB,oxB}} = \frac{1}{\epsilon_0 \epsilon_{\mathrm{ox}}} \int_0^{d_{\mathrm{ox}}} \rho(x) x \, \mathrm{d}x. \tag{3.70}$$

The effect to the interface region can be expressed in terms of a thin charged layer with a charge density σ separated by a distance d_{ox} from the metal:

$$\Delta V_{\mathrm{FB,oxI}} = -\frac{\sigma d_{\mathrm{ox}}}{\epsilon_0 \epsilon_{\mathrm{ox}}}. \tag{3.71}$$

Consequently, equation 3.65 is expanded by a correction term:

$$V_{\mathrm{FB}} = \Phi_{\mathrm{m}} - \Phi_{\mathrm{s}} - \frac{1}{\epsilon_0 \epsilon_{\mathrm{ox}}} \left[\sigma d_{\mathrm{ox}} + \int_0^{d_{\mathrm{ox}}} \rho(x) x \, \mathrm{d}x \right]. \tag{3.72}$$

Even without metal layer the difference in Fermi energies of oxide and semiconductor causes a bending of the energy bands and attracts negative charge carriers to the interface between silicon bulk and the oxide layer, as is sketched in figure 3.18.

[16] AC: Alternating Current

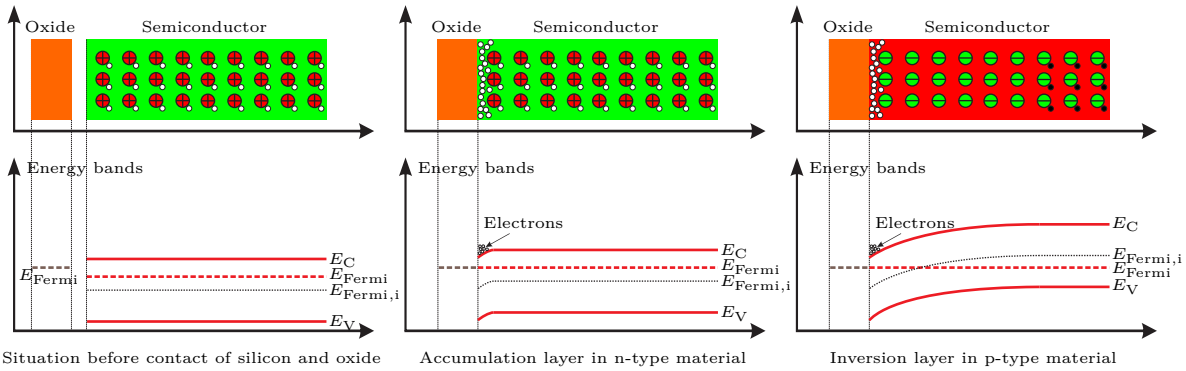

Figure 3.18.: The Fermi energies of oxide and doped silicon are different (left). Upon contact, the Fermi energies line up, leading to an accumulation situation in case of an n-type bulk (middle), and to an inversion situation in case of a p-type bulk.

In case of n-type bulk, the bent energy bands accumulate majority charge carriers, and this conductive electron layer is called "accumulation layer" (see also section 3.5.4). It connects to the negative majority charge carriers in n-type implanted areas, shorting them together.

The right plot in figure 3.18 shows the situation in a p-type bulk material, which has holes as majority charge carriers. The positive oxide charges repel the holes from the surface, forming a depleted region. However, the energy bands are strongly bent, and the bent intrinsic Fermi energy falls below the Fermi energy of the whole system. In this inversion situation, minority charge carriers (again electrons) are attracted to the surface. A negative conductive "inversion layer" is formed, which shorts n-type doped regions.

The amount of oxide charges is determined by the quality of the oxide, and therefore depends on the manufacturing process. A measure for the oxide quality is the flat-band voltage V_{FB}, which has to be applied to a MOS structure to make the energy bands flat (see section 3.5.4). The higher this voltage, the stronger is the bending of the energy bands, and the denser is the accumulation layer or inversion layer. One has to foresee a way to interrupt or compensate the conductive layer, see section 4.6.1 for details.

3.5.6. The polysilicon resistor

The deposition of polycrystalline silicon[17] allows the creation of resistors on semiconductor devices. While the resistivity of pure polysilicon is 230 kΩcm, it can be adjusted over orders of magnitude by doping. Usually polysilicon resistors are connected to the metallisation layers at some point, so one has to make sure to avoid a rectifying Schottky contact. This is done by heavily implanting the contact area between polysilicon and metal, which creates an ohmic contact (see section 3.5.3).

[17] Often abbreviated to "polysilicon"

3.6. Radiation damage by gamma irradiation

The Belle II SVD is exposed to irradiation by a range of particle types, the dominant ones of which are photons, followed by neutrons [30]. This section will focus on main radiation damage by photons; the performance of the SVD's silicon microstrip sensors has been monitored under gamma irradiation.

Particle radiation can interact with the electron cloud of the detector material, or with the nuclei of the crystal lattice. While the former is the desired detection effect (see section 4.1), the latter can lead to permanent changes of the material, which often degrades the detector performance. Depending on the damage mechanism, the bulk and/or the surface of the sensor material is affected.

3.6.1. Bulk damage

The bulk of the sensor material is characterised as a regular crystal lattice, which can be disturbed by the following processes:

- Displacement of lattice atoms: This leads to unbound atoms ("interstitials") and empty lattice sites ("vacancies").
- Nuclear interactions: e.g. nucleus transmutation and neutron capture.
- Secondary processes: e.g. defect clusters from cascade scattering processes.

The average recoil energy to displace a silicon atom is $E_\mathrm{d} = 25\,\mathrm{eV}$ [25]. Depending on the recoil energy and energy transfer direction the scattering particle will create lattice vibrations, isolated point defects, cluster defects, or combinations of all of them.

Defects in the silicon bulk affect the sensor performance in the following ways:

- They act as generation-recombination centers: Defects can capture and emit electrons and holes. In the space charge region of a silicon microstrip sensor this leads to an increased reverse bias dark current and consequently increases the noise (see section 4.3).
- They act as trapping centers: Signal charge carriers can be caught and released too late for detection, which causes a signal reduction (see section 4.2).
- They can change the charge density in the space charge region: Heavy irradiation can convert an n-type material to a p-type one ("type inversion"). This consequently changes the voltage needed to fully deplete the sensor, too.

Bulk damage is mainly caused by heavy, strongly interacting particles like protons, neutrons and pions. Gamma radiation from a ^{60}Co source (as used for irradiation of the SVD sensors, see section 7.2.1) can only create relatively harmless point defects by Coulomb scattering [31]: The photon kicks an electron out of the atom, and this electron can afterwards

displace a silicon atom. On the other hand, gamma radiation can influence the surface of silicon microstrip sensors severely.

3.6.2. Surface damage

The surface is a very critical region of a silicon microstrip sensor where all structures are located. In addition, most of a sensor's surface is covered with a layer of SiO_2 (see section 4.6). The regions connecting highly doped silicon and isolating oxide develop high electrical field strengths, caused by the positive charges located at the semiconductor-oxide interface. In this region, the crystal lattice naturally is irregular over many lattice spacings, so that additional displaced lattice atoms don't pose a threat for the detector's performance. Instead, the properties of the interface are altered by additional charge carriers created by ionising radiation such as photons and charged particles.

The mobility of electrons in the oxide is several orders of magnitude larger than the mobility of holes [25]. Therefore, the electrons from e-h-pairs generated by ionising radiation diffuse out of the oxide quickly, while the holes stay in place semi-permanently, leading to a positive charge-up of the oxide. The electrical field strength near the interface rises, and the high voltage stability of the sensor is reduced. Therefore, the breakdown protection structures (see section 4.6.2) have to be designed to withstand the increased field strengths after irradiation. Furthermore, the increased oxide charge density attracts a denser accumulation layer (or inversion layer, depending on the polarity of the bulk material, see section 3.5.5), which has to be interrupted by accordingly designed insulation structures (see section 4.6.1).

Summing up, gamma irradiation with ^{60}Co photons affects the sensor in terms of

- an increase of the dark current
- a reduction of the signal
- an increase of the noise
- a reduction of high-voltage stability

^{60}Co photons don't change the effective charge density in the space charge region as much as irradiation with strongly interacting particles does. Therefore, type inversion will not occur for the expected radiation dose accumulated over the lifetime of Belle II.

A semiconductor detector is a device that uses a semiconductor (usually silicon or germanium) to detect traversing charged particles or the absorption of photons. In the field of particle physics, these detectors are usually known as silicon detectors.

Wikipedia on **Semiconductor detector**

4

Single- and double-sided silicon microstrip sensors

Every high energy physics experiment needs to be able to track the trajectories of the particles emerging from the interaction point. Among the many possibilities to perform this task, silicon microstrip sensors have proven to be very suitable, thus making them the favoured tracking sensors used in the track sensitive part of particle detectors. The design basics were first developed for the NA11 experiment at CERN [32], and – although not changed much – have seen some improvements in design and production technology.

First, silicon microstrip sensors were applied as vertex detectors in direct vicinity of the IP, and particle tracking was performed by large-scale gaseous detectors. Later, silicon microstrip sensors were also used in the tracking parts of the experiments. The following sections will review the working principle of single-sided silicon microstrip sensors in general and expand it to double-sided silicon microstrip sensors (DSSDs) and their production.

4.1. Working principle

The primary task of a silicon microstrip sensor is to determine the position of a traversing ionising particle with high accuracy. The particle interacts electromagnetically with the sensor material, which hereafter manifests itself as a measurable electric current. Sections 3.4.3 and 3.4.2 describe the details of the interaction of charged particles and photons with the silicon bulk.

A traversing particle creates an almost negligible number of e-h-pairs compared to the intrinsic charge carrier density. This number depends on the mean energy loss $(\mathrm{d}E/\mathrm{d}x)_{\mathrm{mean}}$ of a MIP in silicon, on the minimum energy E_{pair} needed to create an e-h-pair, and on the thickness d_{sensor} of the sensor. With $(\mathrm{d}E/\mathrm{d}x)_{\mathrm{mean}} = 388\,^{eV}/_{\mu\mathrm{m}}$ [28], $E_{\mathrm{pair}} = 3.63\,\mathrm{eV}$ (see table 3.1), and a typical thickness of $d_{\mathrm{sensor}} = 300\,\mu\mathrm{m}$, the number of e-h-pairs becomes:

$$\frac{(\mathrm{d}E/\mathrm{d}x)_{\mathrm{mean}} \times d_{\mathrm{sensor}}}{E_{\mathrm{pair}}} = \frac{388 \times 300}{3.63} \approx 32 \times 10^3 \text{ e-h-pairs.} \tag{4.1}$$

For comparison, the intrinsic charge carrier density n_{i} for silicon at $T = 300\,\mathrm{K}$ is $n_{\mathrm{i}} = 1.45 \times 10^{10}\,\mathrm{cm}^{-3}$. Silicon with an area of $A_{\mathrm{sensor}} = 1\,\mathrm{cm}^2$ and a thickness of $300\,\mu\mathrm{m}$ has an intrinsic number of e-h-pairs of:

$$n_{\mathrm{i}} \cdot d_{\mathrm{sensor}} \cdot A_{\mathrm{sensor}} = 1.45 \times 10^{10}\,\mathrm{cm}^{-3} \cdot 0.03\,\mathrm{cm} \cdot 1\,\mathrm{cm}^2 \approx 4.4 \times 10^8 \text{ e-h-pairs.} \tag{4.2}$$

This number of intrinsic e-h-pairs is four orders of magnitude larger than what can be created by an MIP. Therefore one has to reduce the number of intrinsic e-h-pairs drastically. The best way to do so is to use a p-n-junction in reverse bias mode.

The main sensor element is the depletion zone (or space charge region) of a silicon microstrip sensor's p-n-junction. This very asymmetrical p-n-junction is created by heavily doping a small layer at the surface (e.g. p-type) inside a pre-doped bulk material (e.g. n-type). The space charge region is hereafter augmented by applying a reverse bias voltage, where all intrinsic charge carriers are removed from the bulk of the sensor.

The task of this reverse bias voltage is twofold:

1. Only the depleted part of the sensor thickness is sensitive to the e-h-pairs created by ionising particles. So one has to apply a reverse bias voltage $V \geq V_{\mathrm{FD}}$ of more than the full depletion voltage to make the whole sensor thickness d_{sensor} sensitive.

2. The reverse bias voltage creates an electric field inside the detector, which animates the particle-induced e-h-pairs to drift towards the electrodes (see section 3.3.1). While travelling, they induce an electric current on the electrodes [33], which serves as the measurable sensor response.

Figure 4.1 illustrates the basic principle of e-h-pair generation and drift.

Energy deposition and therefore the number of created e-h-pairs is a stochastic process which follows the asymmetric Landau probability density function [34] (see figure 4.2). A more realistic correction is given in [35].

The Landau probability density function is highly asymmetric, which causes the the mean value of the probability density to be higher than the most probable value (MPV[1]), i.e.

[1] MPV: Most Probable Value

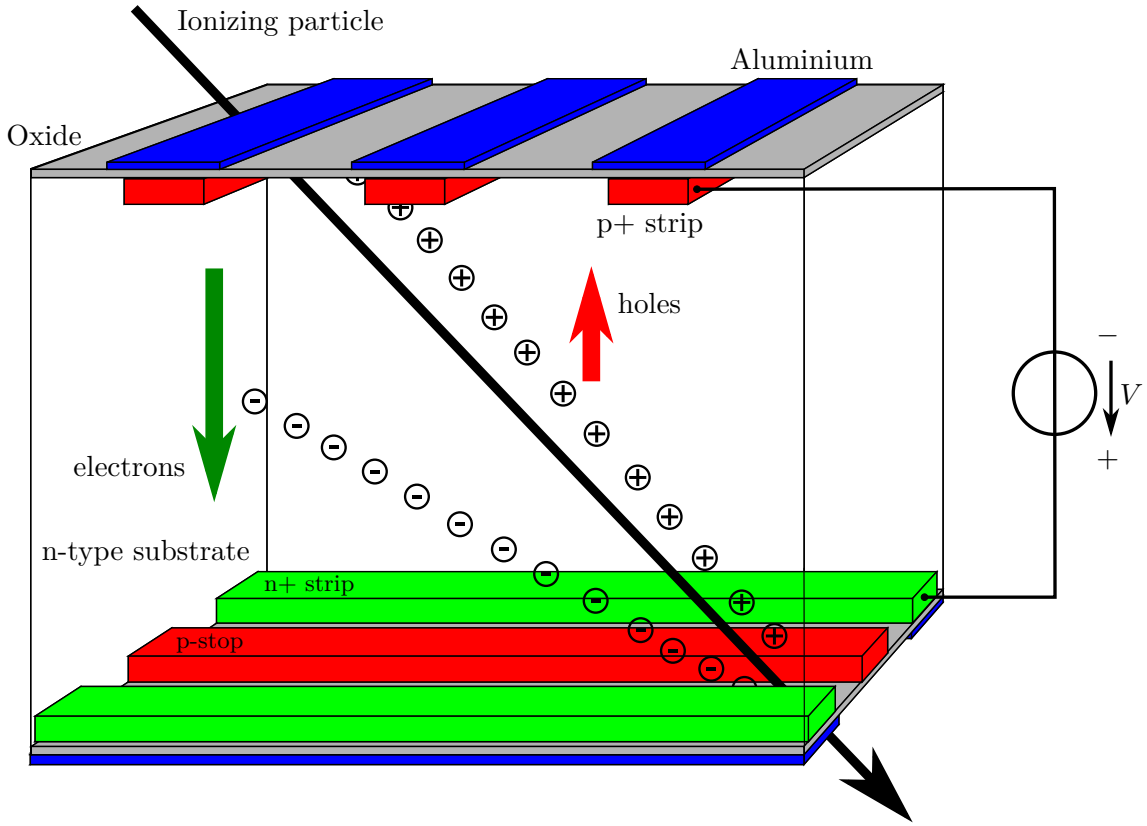

Figure 4.1.: Working principle of a DSSD. The reverse bias voltage is applied between the p+ strips and the n+ strips. In our convention, the reverse bias voltage is counted as positive from p-side to n-side. The color code matches the one used for the photo mask layout in section 5.1.

its peak. For a thickness of $d_{\text{sensor}} = 300\,\mu\text{m}$ the most probable value of the energy loss is $(\mathrm{d}E/\mathrm{d}x)_{\text{MPV}} = 276\,{}^{eV}/\mu\text{m}$, leading to a most probable number of e-h-pairs of:

$$\frac{(\mathrm{d}E/\mathrm{d}x)_{\text{MPV}} \times d_{\text{sensor}}}{E_{\text{pair}}} = \frac{276 \times 300}{3.63} \approx 23 \times 10^3 \text{ e-h-pairs.} \tag{4.3}$$

This is the number of e-h-pairs which is often used in literature.

The drifting charge carriers inside the bulk induce a current signal at the electrodes (see section 4.2 for details), which allows a position measurement when the electrodes are segmented. The segment closest to the e-h-pairs will "collect" most of the electric field lines and will thus see most of the signal, while the segments in the vicinity will see a part of the signal, if any (see section 4.4 for details). The sensing segments have to be electrically isolated but located on the same sensor substrate. The segmentation can be done arbitrarily, but for practical reasons one can distinguish two different main segmentation patterns:

Pixel sensors segment one electrode in a two-dimensional array[2] of rectangular or quadratic

[2]This two-dimensional array is often called "matrix"

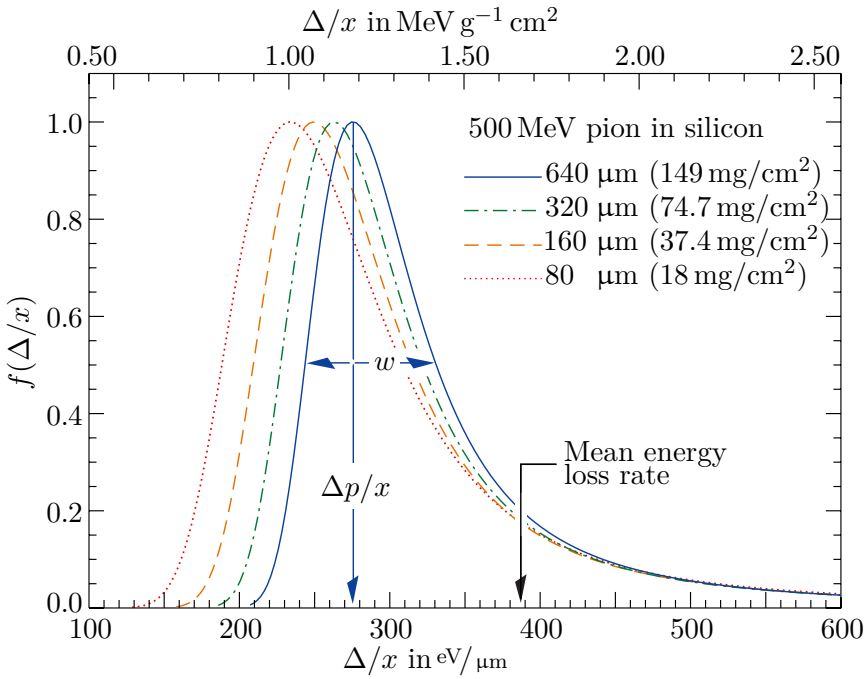

Figure 4.2.: Straggling functions in silicon for 500 MeV pions, normalised to unity at the most probable value $\Delta_{p/x}$. The width w is the full width at half maximum [28].

sensor elements, which are called "pixels". The two-dimensional arrangement of segments allows to determine the position of a traversing ionising particle in two dimensions. Each pixel is a readout channel of its own, and its readout amplifier sometimes serves as power supply, too. A typical pixel size is $50 \times 50\,\mu\text{m}^2$, which allows to place a huge number of pixels on one sensor. This high number of readout channels makes the cost of pixel sensors very high.

Silicon microstrip sensors segment one electrode in a one-dimensional array of long and slim sensor elements, which are called "strips". Usually these strips extend over the full length or width of the sensor, and allow a one-dimensional position measurement of a traversing ionising particle. The reverse bias voltage is supplied to all strips at once through a shared connection line. The strip width is usually in the order of a few tens of micrometers, while the strip distance (the pitch) can vary from 25 µm up to several 100 µm. Silicon microstrip sensors have a much smaller number of readout channels and are therefore cheaper, which allows to use them to instrument large areas of a tracking subdetector. Segmenting also the electrode on the other side of the sensor in perpendicular direction yields a double-sided silicon detector (DSSD), which allows two-dimensional position measurement.

4.2. Signal generation

As already mentioned, the electric field created by the reverse bias voltage animates the electrons and holes to drift in two different directions towards the electrodes. According to Ramo's theorem [33] this drift induces an time-dependent electric current signal i between the electrodes[3]:

$$i(t) = \frac{q_\mathrm{e}}{d_\mathrm{sensor}} \left(\sum_{j=1}^{n(t)} v_{\mathrm{n},j}(t) + \sum_{k=1}^{p(t)} v_{\mathrm{p},k}(t) \right), \tag{4.4}$$

where $v_{\mathrm{n},j}(t)$ and $v_{\mathrm{p},k}(t)$ are the time-dependent drift velocities of electrons and holes. The charge carriers generally drift along the electric field lines and induce their signal in the electrode segment at which the electric field lines end. Therefore, the electrode segments nearest the ionising particle will receive most of the signal.

The electric field is not constant over the thickness of the sensor, it rather varies linearly due to the space charge region, and thus the drift velocities depend on the position of the individual charge carrier. For a given starting point of the charge carrier, the drift velocity is a function of the drift time, and so the drift velocities have to be determined for each charge carrier individually. Note that the mobilities of electrons and holes are different, with $\mu_\mathrm{e} \approx 3\,\mu_\mathrm{h}$ (see table 3.1). A charge carrier can only contribute to the signal as long as it is in motion, and stops to contribute as soon as it arrives at the electrode. This is reflected in the time-dependent upper limits of the summation $n(t)$ and $p(t)$, which denote the actual number of drifting electrons and holes, respectively. Figure 4.3 shows the signal currents as function of the time for electrons and holes separately, for different numbers of e-h-pairs.

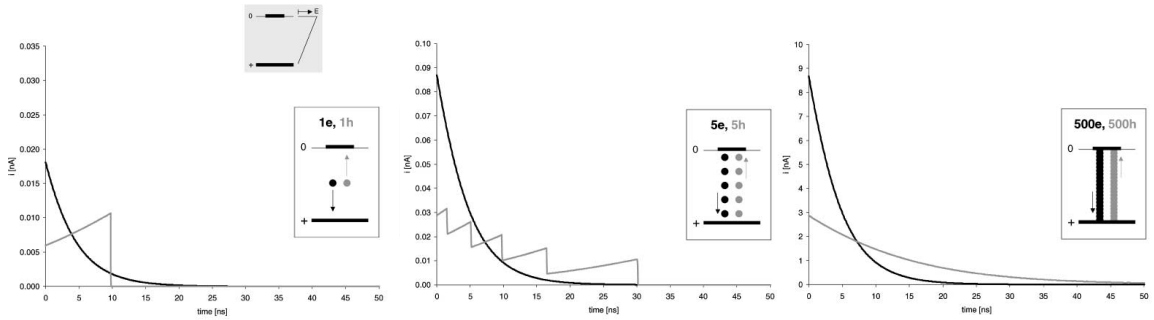

Figure 4.3.: The signal current $i(t)$ as function of the time t in an n-type material [36]. Left: a single e-h-pair is created in the middle of the sensor. The electron (black) drifts in direction of the decreasing field and is decelerated, approaching the electrode asymptotically. The hole (grey) drifts in direction of the increasing field and is accelerated until is reaches the electrode. Middle: Five evenly distributed e-h-pairs. Right: 500 evenly distributed e-h-pairs, both curves are smoothed.

[3] Another way of explaining this behaviour uses the concept of "mirror charges": The charges in the electrodes move along the electrode surface to ensure normal incidence of the electric field lines at the electrodes. The moving charge alters the electric field line configuration, and the mirror charges react, thus inducing a current

For an n-type bulk material the electric field E increases starting from the n-side and reaches its maximum value at the p-side[4]. If the external voltage $V = V_{\mathrm{FD}}$ equals the full depletion voltage, the electric field E is zero at the n-side. An electron drifting to the n-side will therefore approach the electrode asymptotically, thus (theoretically) stretching the signal time to infinity. When the sensor is "overdepleted" ($V > V_{\mathrm{FD}}$) the field at the n-side is greater than zero, the drift velocity of electrons stays finite and the signal time is limited. Moreover, a high reverse bias voltage $V \gg V_{\mathrm{FD}}$ will make the drift velocities nearly constant, either by saturation or because the electric field $E \approx$ const. becomes nearly flat[5]. The resulting signal curves are sketched in figure 4.4.

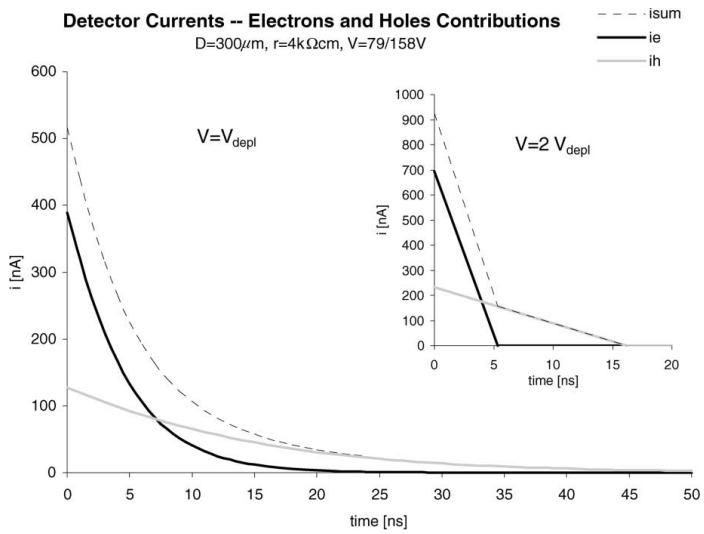

Figure 4.4.: The total signal (dashed line) is the sum of the electron (black) and hole (grey) signals. For small electric fields ($V = V_{\mathrm{FD}}$) the drift velocities depend on the position, and the signal curves are roughly exponential. For high electric fields ($V = 2\,V_{\mathrm{FD}}$) the drift velocities are constant, and the signal curves are roughly linear. Since electrons and holes are always created in pairs, the area under the electron signal curve must equal the area under the hole curve [36].

The integral over the current yields the charge, which is proportional to the energy deposited in the material. Hence, the integration time t_{int} of the readout chip determines the maximum charge which can be collected:

$$Q_0 = \int_0^{t_{\mathrm{int}}} i(t)\,\mathrm{d}t = Q_{\mathrm{n}} + Q_{\mathrm{p}} \qquad \text{with} \qquad Q_{\mathrm{n}} = Q_{\mathrm{p}}. \tag{4.5}$$

The APV25 is an integrating amplifier, i.e. it measures the total charge rather than the current as function of the time. Therefore, the exact time dependence of the current signal is irrelevant for the chip's output signal. The integrated signal curve is hereafter shaped internally, so that the amplitude of the shaped signal pulse is proportional to the collected charge, regardless of the amplitude and shape of the actual current signal. This is sketched in figure 4.5.

[4] Due to the other polarity of the space charge region in a p-type material, the maximal E field is found at the opposite side of the sensor

[5] For high full depletion voltages V_{FD} the effect of velocity saturation occurs first, while for small V_{FD} the field becomes flat more quickly

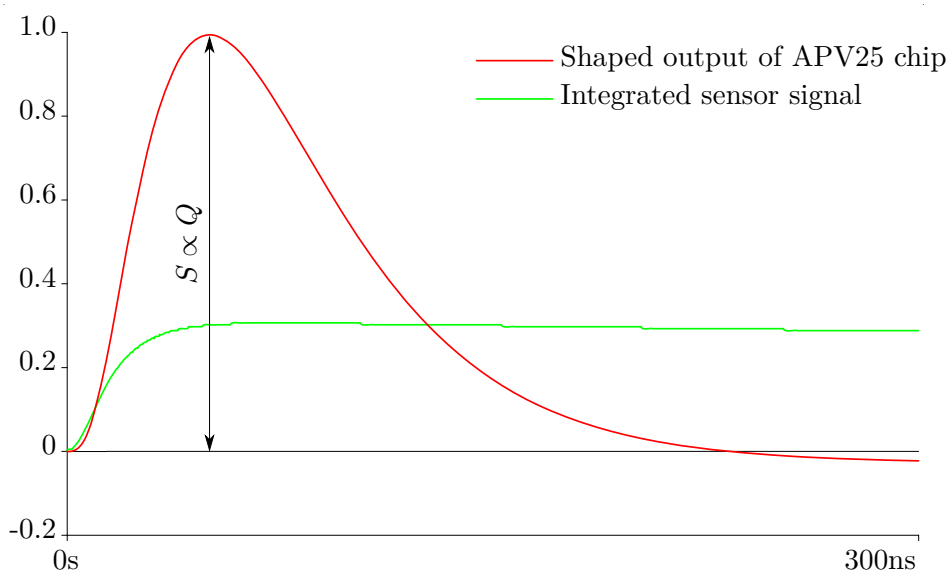

Figure 4.5.: The APV25 chip integrates (green) the current signal of the sensor (see figure 4.4) and generates a shaped output pulse (red), the signal amplitude S of which is proportional to the collected charge Q.

The total energy deposited in the sensor scales linearly with the sensor thickness $Q_0 \propto d_{\text{sensor}}$. A thick sensor will thus give a high signal $S \propto d_{\text{sensor}}$ and consequently also a high signal-to-noise ratio, but will also cause more multiple scattering. The thickness of a sensor must therefore be chosen carefully and has to be appropriate for the application.

When the movement of a charge carrier is stopped during the integration time t_{int} – e.g. by being caught in a trapping center induced by irradiation, or by recombination with an energy state created by lattice imperfections – it ceases to contribute to the current signal, and thus decreases the measured total charge to $Q_c < Q_0$. This effect is measured by the so-called charge collection efficiency (CCE[6]):

$$CCE = \frac{Q_c}{Q_0}. \tag{4.6}$$

4.3. Noise sources

The signal of a strip is determined by the number of e-h-pairs induced by ionising particles. However, the readout electronics has to be able to distinguish this small number of charges from the stochastic fluctuations seen by the input channels. These fluctuations are called "noise", and are expressed in terms of the "equivalent noise charge" (ENC[7]), using electrons as unit:

$$ENC^2 = ENC_C^2 + ENC_J^2 + ENC_{R_P}^2 + ENC_{R_S}^2. \tag{4.7}$$

[6]CCE: Charge Collection Efficiency
[7]ENC: Equivalent Noise Charge

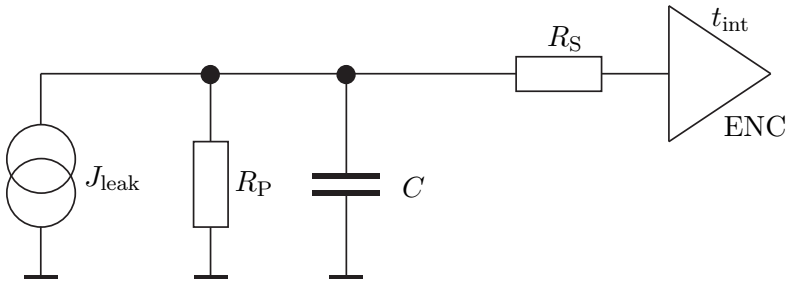

Figure 4.6.: The noise sources of a readout strip and its readout channel [37].

The individual contributions are sketched in figure 4.6, and describe the following noise sources:

Capacitive load noise ENC_{C}: The capacitive load C of a single readout channel can be approximated by:

$$ENC_{\text{C}} = a + b \cdot C \qquad \text{with} \qquad C \approx C_{\text{int}} + C_{\text{back}}, \tag{4.8}$$

with a and b being constants depending on the readout chip. The capacitive load C is the sum of the interstrip capacitance C_{int} and the backplane capacitance $C_{\text{back}} = C_{\text{total}}/n$, where n is the number of strips [29]. Therefore one aims to minimise the capacitive load on the readout channels, which leads to the Origami chip-on-sensor concept, which is applied in the Belle II SVD (see section 2.4).

Dark current noise ENC_{J}: The dark current consists of thermally generated charge carriers, and shows inherent fluctuations which manifest themselves as noise. The noise contribution of the dark current reads:

$$ENC_{\text{J}} = \frac{\text{e}}{2}\sqrt{\frac{J_{\text{leak}} t_{\text{int}}}{q_{\text{e}}}} \approx 107\sqrt{J_{\text{leak}} t_{\text{int}}}, \tag{4.9}$$

where $\text{e} \approx 2.71828$ is Euler's number, J_{leak} denotes the dark current in nA, and t_{int} is the integration time of the readout chip in µs. Note that a short integration time t_{int} reduces the noise.

Parallel resistor noise $ENC_{R_{\text{P}}}$: A parallel connected resistor R_{P} introduces a thermal noise of:

$$ENC_{R_{\text{P}}} = \frac{\text{e}}{q_{\text{e}}}\sqrt{\frac{k_{\text{B}} T t_{\text{int}}}{2R_{\text{P}}}} \approx 772\sqrt{\frac{t_{\text{int}}}{R_{\text{P}}}}, \tag{4.10}$$

where R_{P} is measured in MΩ. Note that a large parallel resistor R_{P} minimises this noise contribution. Therefore, one tries to maximise the bias resistor, which passes the reverse bias voltage to the strips, as far as the voltage drop caused by the dark current through the strips allows. See section 4.6.1 for more information about biasing of the strips. Again, a short integration time t_{int} reduces the noise.

Serial resistor noise $ENC_{R_{\text{S}}}$: A serial line resistor R_{S} introduces a noise contribution of:

$$ENC_{R_{\text{S}}} = \frac{\text{e}C}{q_{\text{e}}}\sqrt{\frac{k_{\text{B}} T R_{\text{S}}}{6t_{\text{int}}}} \approx 0.395C\sqrt{\frac{R_{\text{S}}}{t_{\text{int}}}}, \tag{4.11}$$

where R_S is measured in Ω and the detector capacitance is measured in pF. The main source of serial resistors is the resistance of the aluminium line above the implanted strip (see section 4.6.1), to which the input of the readout chip is connected. Note that a short integration time t_{int} *increases* this noise contribution.

The integration time $t_{int} = 50\,ns$ of the APV25 chip is chosen to minimise the total ENC, so that the achievable signal-to-noise ratio (SNR[8]) becomes a maximum:

$$SNR = \frac{S}{ENC} \rightarrow \max. \tag{4.12}$$

The SNR is an important quantity to measure the sensor performance in beam tests, as is described in sections 7.2 and 8.3.

4.4. Measuring a particle's position

The achievable position resolution of a silicon microstrip sensor depends heavily on how the signal of the sensor is read out. There are two readout options:

- Binary readout: As soon as the signal of a strip is above a certain threshold, the strip is flagged as hit. The traversing particle's position is determined by the positions of the flagged strips. This digital readout option is very fast and can therefore be used at very high bunch crossing rates, but the achievable position resolution is limited.
- Pulse height readout: As soon as the signal of a strip is above a certain threshold, the strip is flagged as hit, and the amplitude of the signal is recorded. The traversing particle's position is determined by the positions of the hit strips and refined by their signal amplitudes. This analog readout option takes more computation time, but yields a position resolution at least as good as for binary readout, in most cases it is superior.

The threshold is usually defined using the signal-to-noise ratio (SNR). The signal seen by a strip must be a certain factor higher than the noise of this strip. Therefore, the absolute value of the threshold varies depending on the noise of the strips. For the Belle II SVD, the threshold of the seed strip (i.e. the highest signal in a cluster of strips above threshold) is five times the noise of this strip, while the neighbour strips need to achieve a signal three times as high as the noise.

[8] SNR: Signal-to-Noise Ratio

4.4.1. Clusters with one strip

If the signal of only one strip is above threshold, then the position of the traversing particle is defined to be the position of this strip, regardless of the signal height:

$$\tilde{x} = x_i = i \cdot p, \tag{4.13}$$

where x_i is the position of the strip number i, and p is the pitch[9]. The position and its resolution do *not* depend on the readout option in this case. Due to lack of more information the real position could have been up to half a pitch away from the strip, as is sketched in figure 4.7. So, the underlying distribution of real positions x creating 1-strip-clusters is a uniform distribution extending to a half pitch around the hit strip:

$$f_1(x) = \begin{cases} 1/p & \text{for } \tilde{x} - p/2 \le x \le \tilde{x} + p/2 \\ 0 & \text{otherwise} \end{cases} \tag{4.14}$$

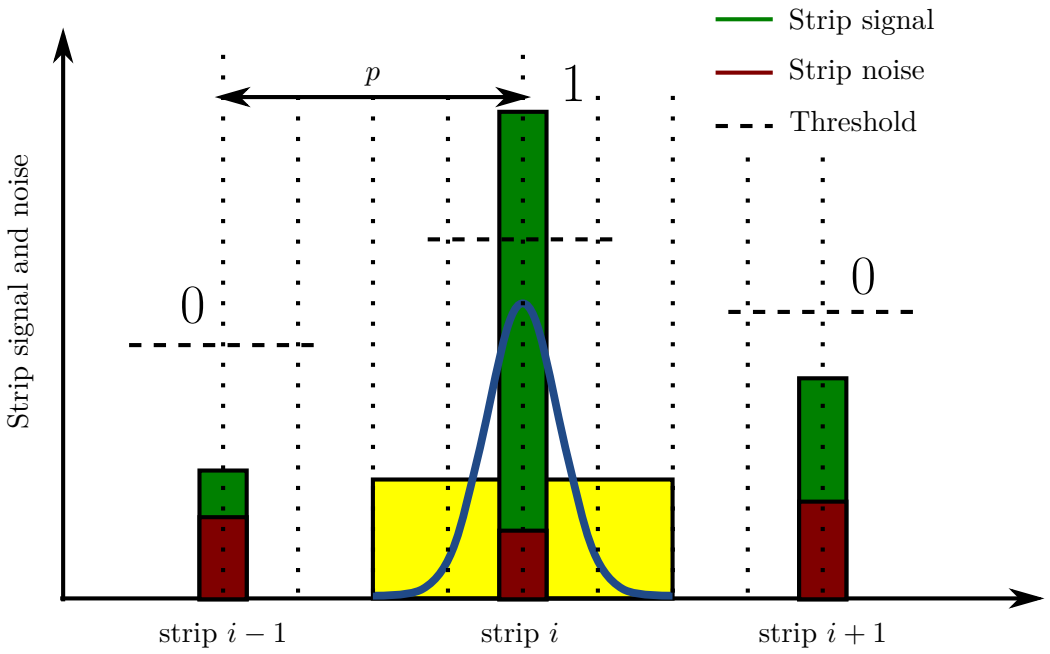

Figure 4.7.: A cluster with one strip above threshold. The real positions of the traversing particles creating this signal configuration are uniformly distributed (yellow).

Reconstruction algorithms usually assume normally distributed measurement errors, so one has to express the uniform distribution in terms of the standard deviation of the uniform distribution. This yields a position resolution σ_1 for a 1-strip-cluster of:

$$\sigma_1(\tilde{x}) = \sqrt{\mathrm{var}(x)} = \sqrt{\int x^2 f_1(x)\,\mathrm{d}x} = \sqrt{\frac{1}{p}\int_{\tilde{x}-p/2}^{\tilde{x}+p/2} x^2\,\mathrm{d}x} = \frac{p}{\sqrt{12}}. \tag{4.15}$$

[9] Assuming that strip numbering starts at zero

4.4.2. Clusters with more than one strip - binary readout

When more than one strips are above threshold, the position is determined by the average of the strip positions:

$$\tilde{x} = \frac{1}{n} \sum_{i=i_{\min}}^{i_{\max}} x_i = \frac{p}{n} \sum_{i=i_{\min}}^{i_{\max}} i, \tag{4.16}$$

where $n = i_{\max} - i_{\min} + 1$ is the number of consecutive strips above threshold, the so-called "cluster width". This measured position is either centred on a strip or lies in the middle between two strips. The distribution of the true positions is a uniform distribution reading:

$$f_{n,\mathrm{bin}}(x) = \begin{cases} {}^{n}/_{p} & \text{for } \tilde{x} - {}^{p}/_{(2\cdot n)} \leq x \leq \tilde{x} + {}^{p}/_{(2\cdot n)}, \\ 0 & \text{otherwise} \end{cases} \tag{4.17}$$

which is displayed in figure 4.8 for the case of two strips above threshold.

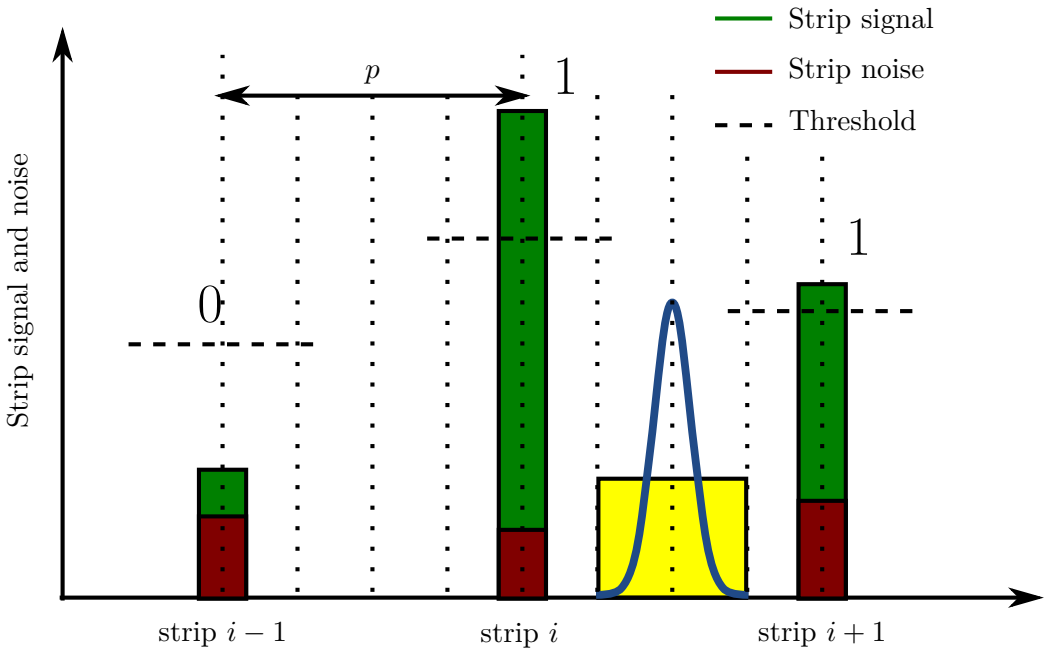

Figure 4.8.: A cluster with two strips above threshold. The real positions of the traversing particles creating this signal configuration are uniformly distributed (yellow).

Using the same calculation rule as before, the position resolution becomes:

$$\sigma_{n,\mathrm{bin}}(\tilde{x}) = \frac{p}{\sqrt{12} \cdot n} \tag{4.18}$$

4.4.3. Clusters with more than one strip - pulse height readout

When the pulse height of the strips above threshold is read out, the position can be refined furthermore by calculating the traversing particle's position with the center-of-gravity (COG[10]) method:

$$x_{\mathrm{COG}} = \frac{\sum_{i=i_{\min}}^{i_{\max}} x_i \cdot S_i}{\sum_{i=i_{\min}}^{i_{\max}} S_i} = x_{i_{\min}} + p \cdot \frac{\sum_{j=1}^{n-1} j S_{j+i_{\min}}}{\sum_{j=0}^{n-1} S_{j+i_{\min}}} = x_{i_{\min}} + p \cdot \eta, \tag{4.19}$$

where S_i is the signal height measured for strip number i, and η is the distance from the first strip $i_{\min}$ of the cluster to the center-of-gravity position in units of the strip pitch. The measured position x_{COG} can be anywhere between two strips, as is sketched in figure 4.9.

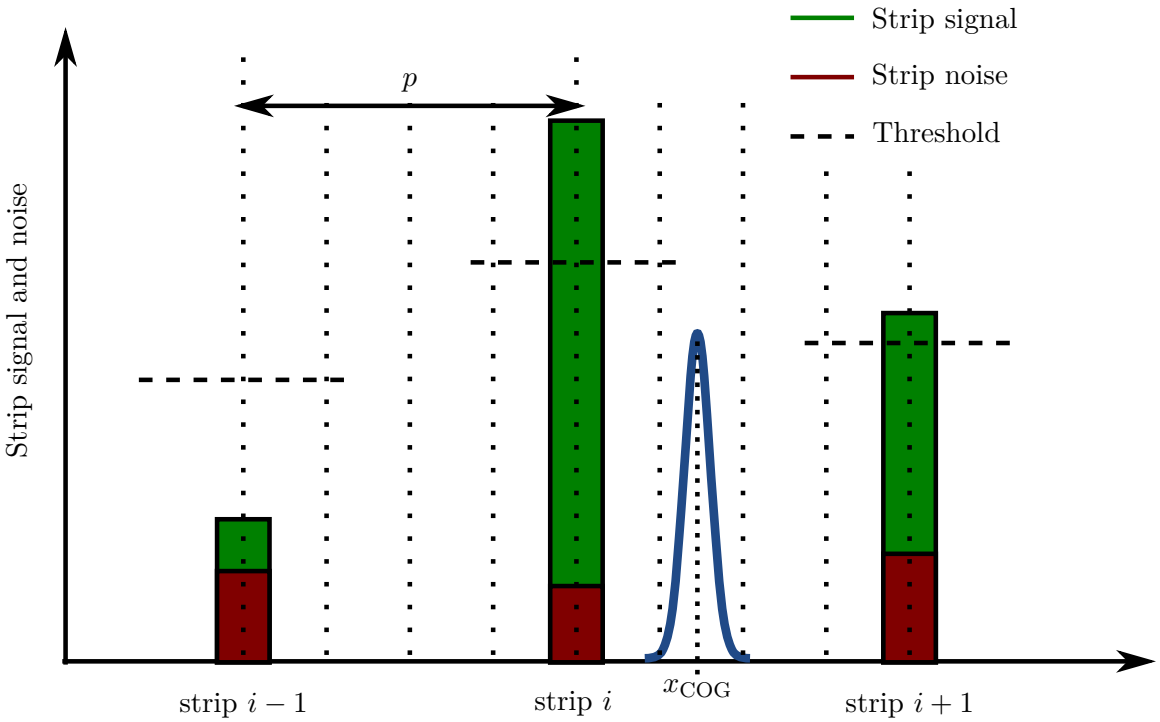

Figure 4.9.: A cluster with two strips above threshold. The signal height gives additional information, which can be used to refine the measured position between the readout strips.

The special case of perpendicular tracks

The width of the charge cloud created by a perpendicularly traversing particle is quite small, in the order of 10 µm. Therefore, these tracks usually create only 1-strip-clusters and 2-strip-clusters. The created e-h-pairs are only shared among two strips, when the charge cloud crosses the middle between the strips, which only occurs for a certain fraction of all tracks, depending on the pitch of the sensor. The relation between particle position and

[10]COG: Center-Of-Gravity

charge sharing is nonlinear, i.e. the interpolated particle position x_{COG} does *not* resemble the actual particle position x. This nonlinearity is reflected in the distribution of the quantity η, as is seen in the left plot of figure 4.10. The real particle positions are uniformly

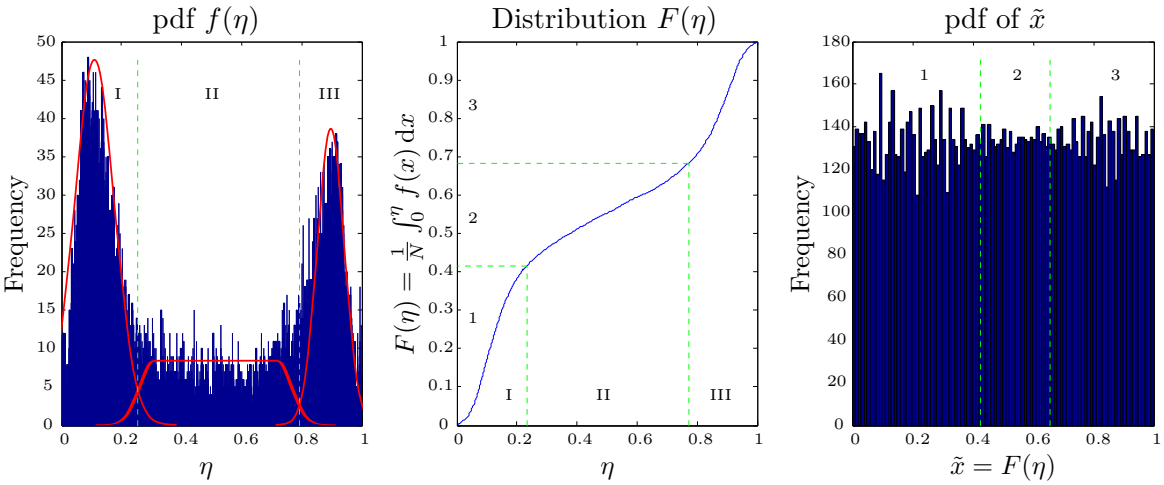

Figure 4.10.: The interpolated positions η are not uniformly distributed (left), although the real particles' positions are. The eta correction (middle) accounts for this non-linearity and makes the measured positions $\tilde{x}$ uniformly distributed (right). Here, the positions η and $\tilde{x}$ are expressed in terms of the decimal places of the fractal strip number. Regions I and III (and the corresponding regions 1 and 3) contain events where the whole charge was collected by one strip and the signal was capacitively coupled to the neighbouring strip. Events in these regions do *not* contain any additional position information. Events in region II (2) show real charge sharing. This figure shows sample data from the beam test in 2012.

distributed between two strips, which means that the distribution of η should be uniform, too. In contrast, η is a random variable with a certain un-uniform distribution, and the left histogram in figure 4.10 is a measurement of the probability density function $f(\eta)$ of this distribution.

One can identify three regions in this histogram: two roughly gaussian peaks (I and III), and a smeared uniform region (II). Only region II is created by events showing real charge sharing, while the peaks I and III are created by events where the whole charge is collected by a single strip, and the signal is capacitively coupled to the neighbouring strip. These events lack any additional position information, and should be counted as 1-strip-clusters. However, the position of the peaks is a measure for the capacitive coupling and therefore for the interstrip capacitance, and the width of the peaks scales inversely with the signal-to-noise ratio. The amplitude difference depends on the incidence angle of the particles [38], and can further be influenced by asymmetries of the drift fields, provoked by e.g. misaligned photo masks during processing.

Due to the nonlinear relation between particle position and signal height the calculated positions x_{COG} are prone to a systematic shift, which has to be corrected even in region II. A (numerical) integral over the histogram $f(\eta)$ as function of the upper bound yields the corresponding distribution function $F(\eta) = {}^1\!/_N \sum_{\eta'=0}^{\eta} f(\eta')$, where N is the number of

data points in the histogram. To make the measured positions $\tilde{x}$ uniformly distributed, one replaces equation 4.19 with:

$$\tilde{x} = x_{i_{\min}} + p \cdot F(\eta) \qquad \text{with} \qquad \eta = \frac{\sum_{j=1}^{n-1} j S_{j+i_{\min}}}{\sum_{j=0}^{n-1} S_{j+i_{\min}}} \tag{4.20}$$

So, inserting the interpolated positions η from region II into the distribution function $F(\eta)$ yields the uniformly distributed measured positions $\tilde{x}$ in region 2, as is displayed in the middle and right plots of figure 4.10. This procedure is called "eta correction", and corrects for the systematic shift induced by nonlinear charge sharing. The position measurement improves considerably for particles traversing the sensor with close to normal incidence, which is of particular importance for beam tests. For particles with shallower incidence angles the region 2 grows due to simple geometry, and charge sharing becomes more and more linear. Therefore, these particles can be measured with good accuracy using the COG position x_{COG} directly [38]. In both cases one achieves a position resolution which scales with the signal-to-noise ratio (SNR):

$$\sigma_{n,\mathrm{pulse}}(\tilde{x}) \propto \frac{p}{SNR}, \qquad \sigma_{n,\mathrm{pulse}} < \sigma_{n,\mathrm{bin}} \tag{4.21}$$

4.5. Two-dimensional position measurement

Usually one wants to follow the three-dimensional track of a particle which is created at the IP to be able to conclude what happened in the collision of the particle beams. This requires a series of three-dimensional measurement points along the particle's trajectory. These three-dimensional points can be achieved by placing sensors with two-dimensional position measurement capabilities in several cylindrical layers around the IP with accurate knowledge about the exact position and alignment of each sensor. With silicon sensors, one has three possibilities to fulfil the requirement of two-dimensional position measurement, namely the use of:

1. Pixel sensors: these sensors offer a very precise and unambiguous two-dimensional position measurement. However, they are expensive both in manufacturing and operation due to the large number of readout channels. Moreover, it is complicated to manufacture them on thin wafers, and they show a low rate capability.

2. Two silicon microstrip sensors rotated by a stereo angle: This configuration can provide a two-dimensional position measurement with only a fraction of the readout channels of pixel sensors. As long as material budget is not a concern – i.e. when measuring high-energetic particles – this configuration allows large-scale instrumentation at reasonable cost and effort. However, the two-dimensional measurement can be prone to ambiguities when the sensors are hit by more than one particles at the same time. Two hit strips on either sensor side have four possible intersecting points,

only two of which are the real hits. The two additional intersections are the so-called "ghost hits" (see figure 4.11).

3. Double-sided silicon microstrip sensors (DSSDs): Segmenting the electrodes on both sides of the wafer yields a similar strip configuration as in case of two rotated silicon microstrip sensors. This allows the same two-dimensional measurement with only one sensor, thus minimising the material budget. However, fabrication is more complicated with a lot more processing steps and lower yield, thus increasing the cost per sensor. Moreover, the electrical insulation of n-type implanted strips requires additional measures, which are explained in detail in section 7. A DSSD is sensitive to ghost hits, too, so it can only be used at locations promising low occupancy.

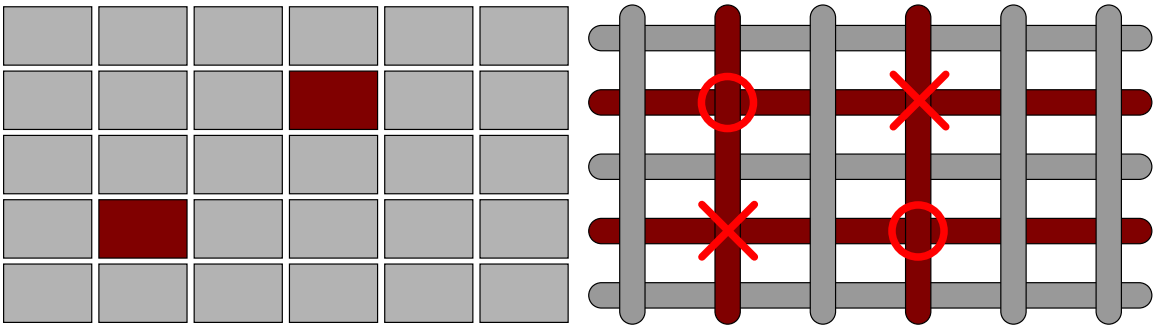

Figure 4.11.: When hit by two particles at the same time, a pixel sensor (left) is able to unambiguously tell the two hits apart. In silicon microstrip sensors these two hits lead to four combinatorial possibilities, two of them being the real hits (crosses), the other two being the so-called ghost hits (circles).

4.5.1. Dealing with ghost hits

A high occupancy increases the probability to have more than one simultaneous hits in the sensor which produce ghost hits. There are some methods to be able to tell real hits and ghost hits apart:

1. Pattern recognition and track reconstruction: Robust reconstruction algorithms are able to distinguish hits that are likely to belong to a physical particle track from outliers. However, these methods can only work if the real hits – and thus also the ghost hits – are separated by a certain distance.

2. Energy loss measurement: The signal seen by the readout chip is the total charge created by the energy loss of the traversing ionising particles. This energy loss is randomly distributed according to a Landau probability density function (see figure 4.2) and has to be exactly the same (see equation 4.5). Depending on the resolution of the signal measurement one can therefore determine which p-side hit corresponds to which n-side hit – provided the energy loss of the two traversing particles was different enough.

3. Stereo angle: Using a small stereo angle between the p-side and the n-side strips, one can shift the strip intersections producing ghost hits across the edge of the sensor, as is sketched in figure 4.12. This approach works as long as the the two real hits are a certain minimum distance apart, and can thus eliminate only a part of all possible ghost hits. The others have to be resolved by the methods mentioned above.

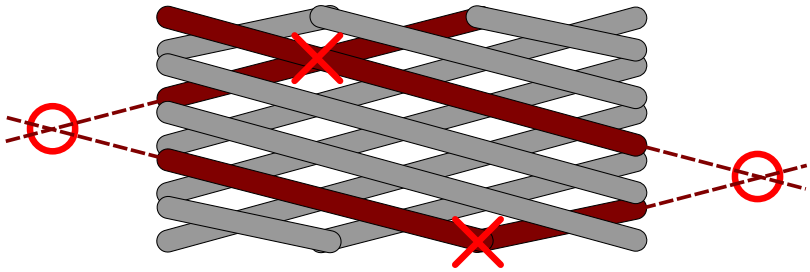

Figure 4.12.: When hit by two particles at the same time, a DSSD with a small stereo angle between opposed sides' strips is able to unambiguously tell the two hits apart. These two hits lead to four combinatorial possibilities for intersection points, two of them being the real hits (crosses), the other two being the so-called ghost hits (circles), which are shifted outside of the sensor.

In the Belle II SVD DSSDs are applied at a safe distance away from the IP, so that the occupancy is low enough for an acceptably small probability of ghost hits, even though the strips are perpendicular. The inner two layers are equipped with DEPFET pixel sensors, which can deliver unambiguous two-dimensional position measurements at high occupancy.

4.5.2. Lorentz angle and windmill structure

Most subdetectors of Belle II are operated inside a 1.5 T solenoidal magnetic field. The force acting on the charge carriers is the Lorentz force:

$$\vec{F} = q_{\mathrm{e,h}}(\vec{E} + \vec{v}_{\mathrm{e,h}} \times \vec{B}) \tag{4.22}$$

Therefore, the electrons and holes generated by a traversing charged particle don't drift exactly along the electric field lines anymore, but they are deflected by the magnetic field, as is displayed in figure 4.13.

The so-called "Lorentz angle" of the deflection is calculated according to:

$$\tan(\Theta) = r_{\mathrm{H}}\mu|\vec{B}|, \tag{4.23}$$

where the "Hall scattering factor" $r_{\mathrm{H}} = \mu_{\mathrm{H}}/\mu$ is the ratio between the mobility with magnetic field μ_{H} and the "normal" mobility without magnetic field μ. At room temperature the Hall scattering factor becomes $r_{\mathrm{H,n}} \approx 1.15$ and $r_{\mathrm{H,p}} \approx 0.7$ for electrons and holes, respectively.

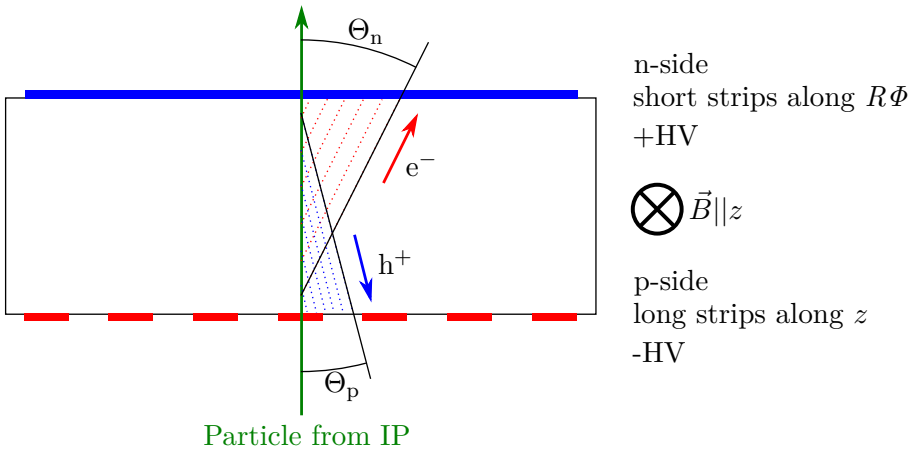

Figure 4.13.: The charge carriers are deflected from the electric field lines due to the magnetic field. Electrons are more prone to this deflection because of their higher mobility [39].

In the SVD, only the p-side strips are affected by the Lorentz angle, because these strips run parallel to the z-coordinate and the B field and measure the $R\Phi$-coordinate. To minimise the charge spreading one can now tilt the sensor counter-clockwise to compensate for the Lorentz angle of electrons or tilt it clockwise to compensate for the Lorentz angle of holes. As long as one assumes electrons and holes equally important for the final signal, one would choose to compensate for electrons because of their larger Lorentz angle. However, this assumption is only valid for a parallel-plate configuration, but not anymore for segmented electrodes. For separated electrode strips, the signal is dominated by the type of charge carriers that travel towards the strips in question, which are the holes for p-type implanted strips.

The signal induced in one arbitrarily chosen strip depends on the so-called "weighting field" E_v according to $i = E_v q_e v$ [33]. This field is the electric field which would exist at the charge carrier's instantaneous position under the following circumstances: the charge carrier is removed, the chosen strip is raised to unit potential, and all other strips are grounded. Figure 4.14 shows an example for the weighting field.

The weighting field is only high in the vicinity of the chosen strip. All charge carriers drifting *towards* this strip cross the region with high field, while only a small part of the departing charge carriers does so. Consequently, the signal induced in this p-side strip is dominated by holes, as is simulated in figure 4.15.

Knowing that in case of the SVD the Lorentz angle has to be compensated for holes yields the windmill structure already mentioned in section 2.2.2. This means a tilt in clockwise direction, as is displayed in figure 4.16.

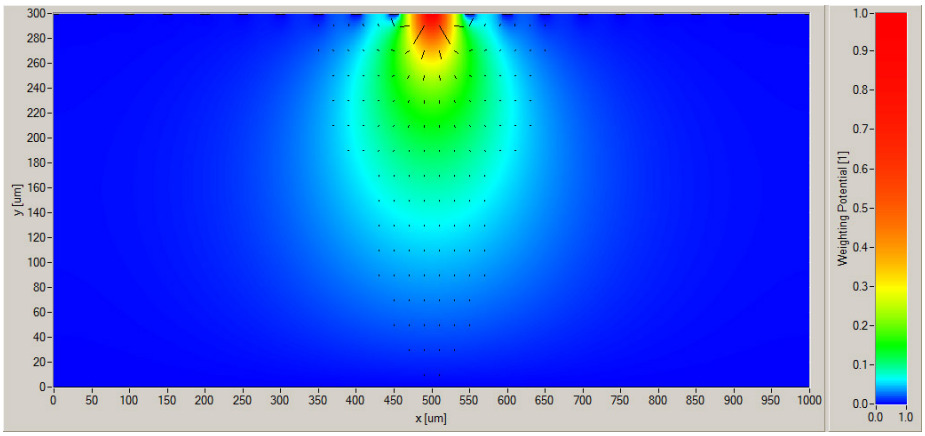

Figure 4.14.: The weighting field E_v displayed with a nonlinear color scale, for a silicon microstrip sensor with p-type strips at a pitch of 50 µm in 300 µm n-type material [39]. All charge carriers drifting to this strip traverse the high-field region, while only a fraction of the other charge carriers do so.

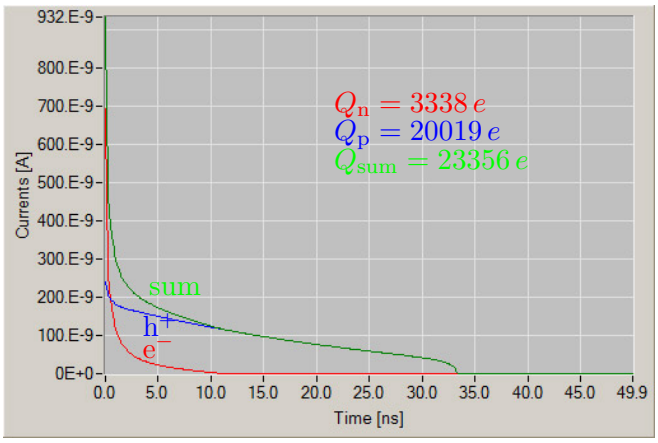

Figure 4.15.: The signal induced in a p-type strip is dominated by the holes' contribution, because the weighting field enhances their contribution in the vicinity of the readout strip. The surrounding strips see a higher contribution from electrons, so that in total both charge carrier types again contribute the same amount of charge to the final signal [39].

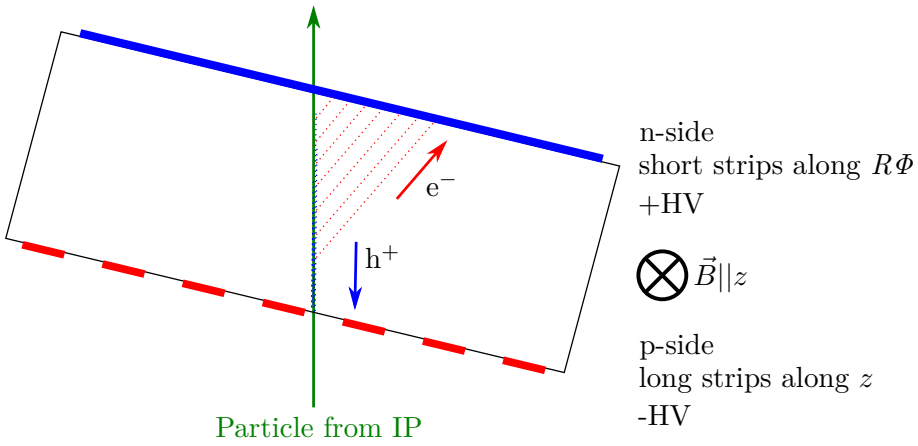

Figure 4.16.: A tilt in clockwise direction reduces the charge spreading of holes due to the Lorentz force. The actual windmill angle is determined by mechanical requirements and does not exactly match the Lorentz angle [39].

4.6. Design basics of a silicon microstrip sensor

Silicon microstrip sensors are composed of a few basic building blocks which can be found in any of them. The following section will shed light on the design basics of a single-sided silicon microstrip sensor as can be seen in figure 4.17, but all of them apply to the other side of a DSSD as well.

Figure 4.17 shows the principal components of a single-sided silicon microstrip sensor:

Strip implants: These are the segments of the electrode creating the electric field. Most of the field lines end at these strips, and the charge carriers drifting along the field lines induce their signal in the strips.

Backplane: The other side of a single-sided silicon microstrip sensor is an unstructured electrode consisting of an aluminium layer and an underlying heavily n-type doped area for preventing a Schottky contact. For a DSSD this electrode is segmented as well, and the strips consist of the same elements as on the other side, plus additional measures for strip insulation.

Aluminium strips: The induced signal is capacitively coupled to aluminium strips above the implanted strips to filter away the DC component of the dark current. A small part of the field lines ends at these aluminium strips.

Coupling oxide: This thin oxide layer is the dielectric between the implanted strips and the aluminium strips.

AC pad: These contact pads allow to connect the readout electronics to the aluminium strips, and serve as contact pads for sensor tests.

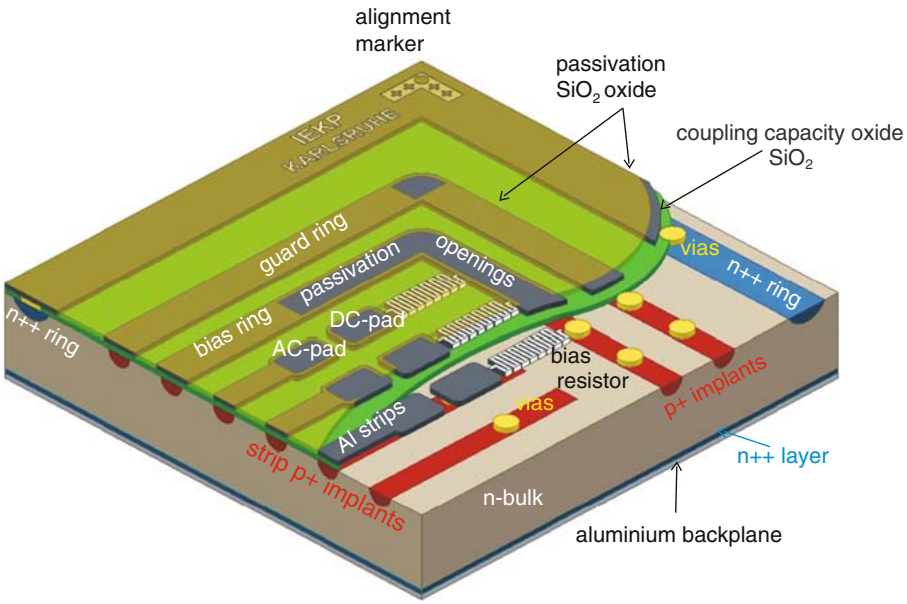

Figure 4.17.: Three-dimensional model of a single-sided silicon microstrip sensor as used by the CMS experiment. It uses AC-coupled strips with polysilicon resistors for biasing. The active area is protected from high-voltage breakdown by a single guard ring [40].

DC pad: These contact pads allow to contact the strip implants for sensor tests, and connect the bias resistors to the implanted strips.

Bias ring: This ring-like structure surrounds the active area (strip area) and connects all strips to the reverse bias voltage via the bias resistors.

Bias resistor: This polysilicon meander connects the implanted strips to the bias ring and insulates the strips from each other.

Guard ring: The reverse bias voltage creates a potential difference of up to several 100 V between the implanted strips and the backplane. The guard ring helps to protect the device from breakdown by lowering the electric field in a defined way towards he sensor edge.

Edge ring: This ring also acts as breakdown protection and isolates the active area from the cutting edges, which contain a lot of lattice imperfections due to dicing. Furthermore, its area is used to implement inscriptions in the metal layer.

Passivation and passivation openings: The passivation is a thick layer of silicon oxide to protect the surface of the device from the environment. This oxide layer has only openings at dedicated contact pads.

Oxide windows (vias): At some points the coupling oxide has to be opened to allow contact to the silicon substrate underneath. This is achieved by implementing the oxide

windows, which are often wrongly called “vias”.

4.6.1. Strip geometry

For single-sided silicon microstrip sensors only one electrode is segmented to form strips, while the other one is left in one piece, being called “backplane”. The strip pitch of the segmented electrode is driven by the requirements of spatial resolution and number of readout channels. The ratio between strip width and pitch (the so-called “width-to-pitch ratio” r_{wp}) is a subtle optimisation between field peaks at the implant edges and the interstrip capacitance.

One can increase the position resolution by implanting additional strips which are *not* read out. The drifting charge carriers induce a signal in these so-called intermediate strips, which is hereafter capacitively coupled to the neighbouring readout strips. Therefore, intermediate strips increase the number of events which share charge among two readout strips. Applying pulse height readout (see section 4.4) yields an improved spatial resolution.

DC- and AC-coupled strips

A p-n-junction in reverse bias operation shows a small dark current (see equation 3.50). Ideally, this dark current is divided evenly among the strips of the sensor, so that each strip sees a small DC current I_{strip} in the order of a few nA. With irradiation this current can reach several µA.

The integrating preamplifiers of the APV25 chips are very sensitive to DC currents at their inputs, and have to be protected from them. This can be done using current compensation circuits in the front-end electronics which remove the DC fraction of the current, only allowing the AC contribution of the signal pulse to reach the input. In this case, the strip implants are directly connected to the readout electronics, and are called “DC-coupled strips”.

The filtering of the signal’s DC component can also be integrated into the sensor itself. To do so, one creates a capacitor between the strip implant and the readout electronics which acts as a high pass filter. These readout capacitors are formed by the strip implant as one electrode, an aluminium strip of similar shape above it, separated by a thin layer of silicon dioxide SiO_2 and sometimes silicon nitride. This MOS structure forms a parallel-plate capacitor with a coupling capacitance of $C_{\mathrm{ac}} = \epsilon A_{\mathrm{strip}}/d_{\mathrm{ox}}$. Instead of the strip implant, now the aluminium strip is connected to the readout electronics. Strips featuring this built-in coupling capacitance are called “AC-coupled” strips.

Biasing of the strips

The reverse bias voltage for depleting the bulk has to be applied to every single strip. In case of single-sided silicon microstrip sensor only one electrode is segmented to form strips, the other one (the "backside") is fully covered with an aluminium layer to contact the bulk.

AC-coupled strips are biased via an additional structure on the sensor, the so-called "bias ring" or "bias line". This bias ring surrounds the segmented area, and all strips are connected to this ring, applying the same potential to all of them at once. However, this connection has to be made with some kind of bias resistor to ensure electrical insulation of the strips.

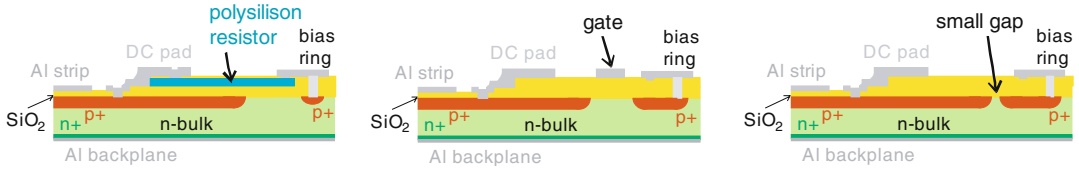

(a) Polysilicon bias resistor **(b)** FOXFET biasing **(c)** Punch through biasing

Figure 4.18.: The strips are connected to the bias ring via a resistor to ensure electrical insulation [26].

There are several ways to implement these resistors:

Polysilicon bias resistor: The connection between strip an bias ring is made via a meander of doped polysilicon (see figure 4.18a). This resistor has an ohmic behaviour and is very radiation tolerant. However, manufacturing such a resistor requires additional processing steps, which makes the sensor more expensive.

FOXFET[11] biasing: The bias ring and the strip implant are only separated by a small gap. A gate electrode is placed above this gap to make it a MOS structure. Similar to the behaviour of a MOSFET[12] one can now control the effective resistance of the gap by applying a small voltage to the metal gate (see figure 4.18b). It is cheaper than the bias resistor, but less radiation hard.

Punch through biasing: This uses a similar structure as the FOXFET biasing, with an even smaller gap and omitting the gate electrode. The resistance is defined by the size of the gap and by the electric properties of the silicon oxide, only (see figure 4.18c). It is again cheaper and less radiation hard than the bias resistor, and less flexible than the FOXFET biasing.

[11] FOXFET: Field OXide Field Effect Transistor
[12] MOSFET: Metal-Oxide-Semiconductor Field Effect Transistor

Insulation of n-side strips

The silicon oxide contains fixed positive oxide charges, which attract a conductive electron layer to the surface and shorts all n-type doped areas (see section 3.5.5 for details). This happens both in n-type and p-type bulk materials, and the occurring electron layer is called accumulation layer and inversion layer, respectively. One has to foresee a way to interrupt or compensate this electron layer, which can be done by three methods. In the following, we assume an n-type doped silicon substrate; the same methods are applied in p-type materials.

1: The p-stop blocking method: The accumulation layer can be interrupted by implanting dedicated p-type areas between the n-type strips, as is sketched in figure 4.19. These so-called "p-stop" areas introduce a p-n-junction in the n-type bulk, which is surrounded by a small space charge region free of charge carriers. The p-n-junction bends the energy bands locally opposite to the bending introduced by the oxide charges, driving the charge carriers away from the local space charge region and into the bulk.

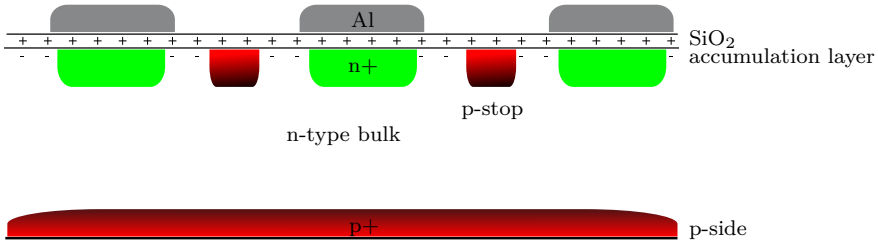

Figure 4.19.: The conductive layer can be interrupted by implantation of "p-stop" structures.

The p-stop blocking method requires an additional photolithography step during manufacturing, and therefore makes the sensor more expensive. The depth of the p-stop doping profile is usually similar to the depth of the strip implants. The exact geometry of the p-stop implants can be optimised to make the sensor efficient and radiation hard, as is done in section 7. Using the SRP[13] measurement method [41], we measured the sheet resistance of the p-stop implantation to be 200 kΩ/□ on DSSDs processed by Micron Semiconductor Ltd.

2: The p-spray blocking method: The accumulation layer can be removed from the strip area by completely converting the bulk to p-type near the surface. This is done by a large-scale and unstructured p-type implantation, as is sketched in figure 4.20. Fluence and energy of this implantation have to be chosen carefully to supply just as many acceptor atoms needed to compensate for the accumulated electrons. Irradiation with ionising particles and gamma rays changes the density of the oxide charges and therefore the density of accumulated electrons, and therefore this blocking method suffers from strong irradiation. This is shown experimentally in section 7.

[13]SRP: Spreading Resistance Profiling

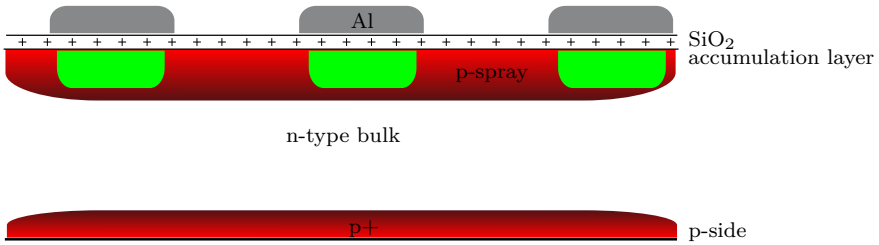

Figure 4.20.: The conductive layer can be dissolved completely by a large-area and deep p-spray implantation.

The p-spray blocking method is cheap and easy to manufacture, because it doesn't require a dedicated photolithography step. In case of Micron Semiconductor Ltd., the doping concentration is two orders of magnitude lower than for the p-stop blocking method, but with doubled implantation energy. This results in a doping profile about twice as deep as the doping profile of the n-type strips, which therefore are completely embedded in p-type material. Using the SRP measurement method [41], we measured the sheet resistance of the p-spray implantation to be 600 kΩ/□ on DSSDs processed by Micron Semiconductor Ltd.

3: The MOS blocking method (field plate method): The accumulation layer can be locally compensated by a suitably biased MOS structure between the strips, the so-called "field plate". For a moderate negative potential w.r.t. the strips, the electron layer is repelled, leaving the area under the MOS structure free of charge carriers. This is the case when the potential difference between the MOS gate and the n-type strips equals the flat-band voltage. For higher biasing, holes are attracted to the surface.

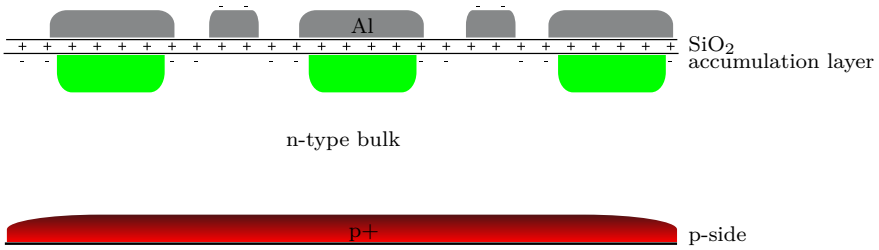

Figure 4.21.: The conductive layer can be compensated locally by MOS structures negatively biased w.r.t. the potential of the n-type strips.

The MOS blocking method requires an additional power supply to provide the bias voltage of the MOS structures, and is therefore more elaborate in operation. However, this provides the versatility to adjust the strip insulation to the changing sensor properties in a harsh radiation environment.

A variant of this method uses the overhang of the aluminium strips as gate for the MOS structure. Biasing these aluminium strips requires the readout electronics to be able to cope with the shifted operation potential. In this variant the bias voltage of the aluminium strips can also be provided by the readout electronics directly.

4.6.2. Breakdown protection

During operation, the two sensor sides are held at a potential difference of up to several hundreds of Volts to ensure full depletion. This potential difference has to be securely handled on a small distance, or it may cause breakdown of the sensor, rendering it inoperable or even destroying it. The most common methods of breakdown protection implement additional ringlike structure surrounding the strip area, and aim to avoid field spikes:

Edge ring: The edge of the sensor is an area with a high density of lattice imperfections and contamination due to dicing, and if the space charge region reaches this area a high amount of unwanted dark current can be expected. As calculated in equation 3.47, the space charge region of a p-n-junction extends predominantly into the lower doped area. So, heavily doping the edge of the sensor will keep the space charge region away from the imperfections, thus reducing the number of impurities in the space charge region which introduce dark current. Moreover this heavy doping ensures that the so-called "edge ring" is at the potential of the backplane, which confines the bias voltage drop to a defined area.

Guard ring: The main voltage drop occurs in the inactive area between the outer edge of the bias ring and the edge ring, at a distance of a millimeter or less. This small distance translates into high electric fields, where lattice imperfections due to dicing are likely to induce field spikes. One can ease this effect by implanting one or more concentric ringlike structures outside of the bias ring. These additional "guard rings" are electrically floating, i.e. they are not held at a defined potential, and thus ensure an undefined but homogeneous and soft voltage drop which is spread out over a larger distance.

Metal overhang: The aluminium strips above the implanted strips are made wider by a few micrometers. Hence, some of the field lines end in the aluminium strips rather than in the implanted ones. This reduces the electric field strength at the edges of the strip implants and makes use of the much higher breakdown voltage of the silicon oxide.

Round corners: In the design of a silicon microstrip sensor – as in the design of any IC – one should generally avoid sharp corners. The electric field strength scales quadratically with the radius of the used structures, so designing structures with comfortably rounded corners improves the high voltage stability a lot.

4.6.3. Contact pads

The strips of a silicon microstrip sensor have to be electrically connected to the readout electronics and power supplies, and electrical characterisation in the laboratory also needs

some means to connect structures on the sensor to the measurement equipment. This is done by foreseeing small dedicated areas for electrical contact.

On sensors with AC-coupled strips on can distinguish two different kinds of pads to contact the strips:

DC pads allow to contact the implanted strip directly, and are used for electrical characterisation. These pads are usually located at either end of the strips, because as much of the strip as possible should be covered by the aluminium strip, which is not to touch the implanted silicon. The DC pad connects the implant through an oxide window in the coupling oxide. When the strip is biased with a polysilicon bias resistor, the DC pad also connects to the strip-side end of the resistor, connecting it to the strip implant.

AC pads allow to contact the aluminium strips located above the strip implants. These pads can be placed anywhere along the strip, allowing them to be larger than the DC pads. While the AC pads are used for sensor testing as well, their main task is to connect the strips to the readout electronics. Usual sensor designs implement several AC pads per strip, to increase the flexibility of testing and wire bonding.

4.7. Manufacturing of silicon sensors

The production of silicon microstrip sensors makes use of well established procedures developed in the semiconductor and microelectronics industries. Most of the production and manufacturing processes can be applied as-is, but silicon microstrip sensors pose some requirements which are not common in the production of "normal" ICs.

4.7.1. Production of pure silicon

Silicon is one of the most common elements on earth, it accounts for a quarter of the mass of the earth's crust. There, it is predominantly found in form of silicon dioxide SiO_2, also known as "quarz sand". It is purified by various chemical and physical processes to qualify as "electronic grade silicon" (EGS[14]), which is pure to better than $^1/_{100}$ ppb[15]. This prepares the EGS in polycrystalline form, which has hereafter to be transformed to a single crystal. Among many others, two main methods are used to produce single-crystalline silicon on a macroscopic scale:

Czochralski (CZ[16]) silicon: Polycrystalline silicon is melted inside a quartz crucible. To create a macroscopic single crystal from it, a small single-crystalline seed crystal is dipped into the melt. It is slowly retraced, while the liquid silicon crystallises,

[14] EGS: Electronic Grade Silicon
[15] ppb: parts per billion
[16] CZ: CZochralski

following the single-crystalline structure of the seed crystal. A perfect macroscopic single crystal is grown by carefully controlling the rotation and pull rate of the seed crystal, and the temperature of the liquid silicon. The Czochralski method is sketched in figure 4.22a.

Float Zone (FZ[17]) silicon: This procedure uses a rod of polycrystalline silicon as base material. Again, it is brought in contact with a small single-crystalline seed. The polycrystalline rod is locally melted by RF[18] heating, while the RF coil is slowly moved along the rod. Due to the seed crystal the solidifying silicon crystallises as single crystal, following the crystal orientation of the seed. The solubility of contaminations is higher in liquid silicon, so that they stay in the melt and follow the RF coil to the end of the rod. The process parameters are the temperature of the melt (controlled by the RF power), the rotation of the rod and the exact movement of the RF coil. The Float Zone method is sketched in figure 4.22b.

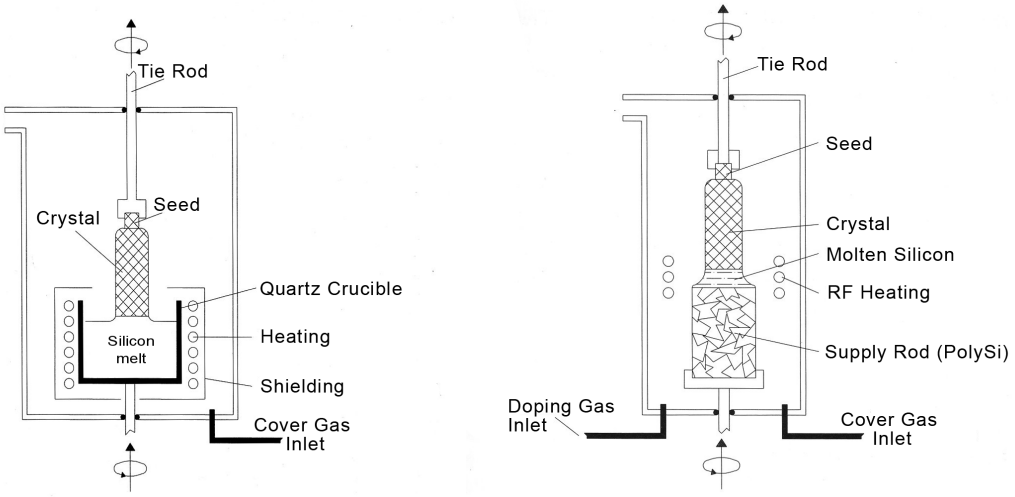

(a) Czochralski method **(b)** Float zone method

Figure 4.22.: The main methods for producing EGS on a macroscopic scale [42].

During production of the macroscopic single crystal (the "ingot"), dopants are added to adjust the resistivity of the final material. In case of the CZ method the dopants are added to the melt directly, while for the FZ method they are diffused in the cover gas. The dopant concentration defines the type of the majority charge carriers and the full depletion voltage of the sensor (see equation 3.57). FZ silicon proves very suitable for the production of silicon microstrip sensors due to the very low impurity concentration, while CZ silicon is more radiation hard due to its inherently higher oxygen concentration.

The ingots can be produced in various diameters from four to twelve inch and growing, and are hereafter cut into small discs (wafers) with a thickness between 100 and several hundreds of micrometers.

[17]FZ: Float Zone
[18]RF: Radio Frequency

Figure 4.23.: A single-crystalline silicon ingot.

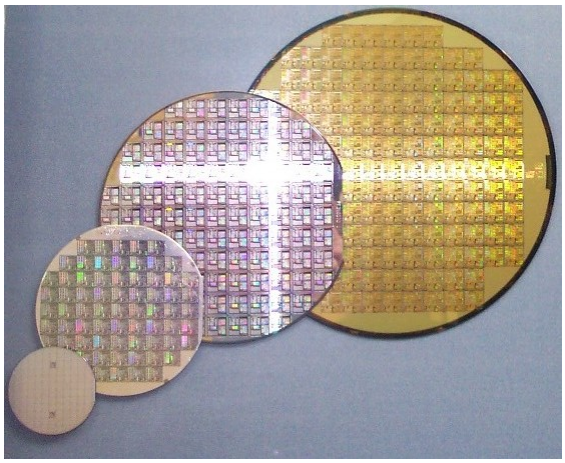

Figure 4.24.: Wafers of different diameters housing processed ICs.

4.7.2. General processing steps in microelectronics industry

The production of silicon microstrip sensors takes advantage of the same so-called "planar processes" used in traditional microelectronics industry, which are described in the following sections. However, there are some differences in the requirements:

- Lower contamination of the base material: Low contamination leads to low dark current and determines the full depletion voltage.
- Higher quality of oxides: A low oxide charge concentration increases the radiation hardness of the sensors.
- Higher homogeneity: Sensors are large-scale devices compared to traditional ICs. Consequently, the base material and the deposited materials have to be homogeneous and free of defects over the scale of several tens of square centimeters. Hundreds of traditional ICs with a size of less than a fingernail fit on the same wafer, and the ones processed on a faulty area of the wafer can simply be discarded. Usually there is only *one* main sensor per wafer, hence a single defect can render the product of a whole wafer dysfunctional.

Please refer to [42] for more in-depth information about the technologies used in microelectronics industry.

Thermal oxidation

When silicon comes in contact with oxygen, the surface is oxidised and establishes a layer of silicon oxide SiO_2 (also called silica). This is one of the main reasons why silicon is such a successful material in microelectronics industry. The natural oxide is chemically inert and mechanically hard, it is a dielectric ($\epsilon_r = 3.9$) and can be produced easily in uniform and thin layers of a few nanometers to a few micrometers. These layers are grown by

exposing silicon to an oxygen enriched environment while heating it up to between 800 °C and 1200 °C. This "high temperature oxidation" (HTO[19]) can be performed using a dry or humid gaseous atmosphere:

Dry oxidation: The oxidation is performed by exposing the silicon to gaseous molecular oxygen, which invokes the following reaction:

$$\mathrm{Si} + \mathrm{O_2} \rightarrow SiO_2 \tag{4.24}$$

The solubility of molecular oxygen in SiO_2 is low, hence the growth rate is slow, which results in very homogeneous oxide layers of high quality.

Wet oxidation: The oxidation is performed by exposing the silicon to water vapour, which invokes the following reaction:

$$\mathrm{Si} + 2\mathrm{H_2O} \rightarrow SiO_2 + 2\mathrm{H_2} \tag{4.25}$$

The solubility of water vapour in SiO_2 is higher than for oxygen, so wet oxidation creates oxide layers with large growth rate and reduced quality.

During the reaction, surface silicon is consumed and converted to SiO_2, moving the interface between silicon and oxide deeper into the wafer. SiO_2 has a larger volume than pure silicon, for each unit of consumed silicon about 2.27 units of SiO_2 are grown [42] (see figure 4.25).

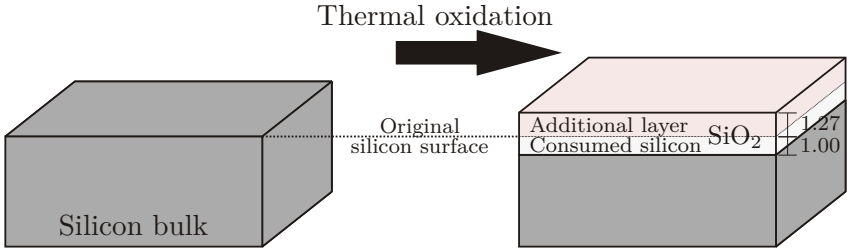

Figure 4.25.: The interface between silicon and oxide moves into the bulk during oxide growth [26].

Deposition

A whole range of materials can be attached to the silicon surface by deposition:

Metals – usually in form of aluminium alloys – are deposited to form electrodes, conductive lines, contact pads and to fill oxide windows to establish interconnections.

Polysilicon is used to form resistors, and sometimes serves as high resistivity readout lines which allow some degree of additional position sensitivity.

[19] HTO: High Temperature Oxidation

Silicon oxide can not only be grown by HTO, but can also be deposited at considerably lower temperatures down to 300 °C. This has the advantage that a protective passivation layer can be formed on other materials than only bare silicon. However, the quality is lower than for HTO. This type of oxide is often doped to form BPSG[20], which is softer and allows to level uneven surfaces.

Silicon nitride Si_3N_4 is a dielectric with excellent electrical and mechanical properties. It often serves as an additional layer in the coupling capacitance layer, and its high diffusion barrier for water molecules makes it the preferred material for top layer passivation.

The most common deposition methods are:

Chemical vapour deposition (CVD[21]): This is the umbrella term for a number of chemical deposition methods to create layers of oxide, polysilicon and silicon nitride. The materials to be deposited are dissolved in a cover gas, to which the wafer is hereafter exposed. Some of the variants include APCVD[22], LPCVD[23] and PECVD[24], which differ in usable deposition materials, layer quality and operation temperature.

Epitaxy is the deposition of a crystalline overlayer on a crystalline substrate, where the deposited (or grown) layer inherits the crystal orientation of the substrate. Its main application is the production of pure or doped silicon layers of high quality on a silicon substrate.

Sputtering, in contrast to CVD, is a physical method of deposition. The substrate is exposed to atoms coming from a target material in its vicinity, which is bombarded with an ion beam. With this method, one can deposit a whole range of materials which are not eligible for chemical methods due to missing appropriate chemical reactions. A combination of chemical and physical methods is the "reactive sputtering", where a reactive gas is added to the cover gas. The sputtered target atoms react with this gas, and the reaction product is deposited on the silicon substrate.

Doping

The process of steering the conductivity of a semiconductor is called doping. It is the most important ingredient of semiconductor technology, as it allows to controllably alter the electrical properties of semiconductors over several orders of magnitude (see section 3.2). The main methods for doping a semiconductor are:

[20] BPSG: BoroPhosphoSilicate Glass
[21] CVD: Chemical Vapour Deposition
[22] APCVD: Atmospheric Pressure Chemical Vapour Deposition
[23] LPCVD: Low Pressure Chemical Vapour Deposition
[24] PECVD: Plasma Enhanced Chemical Vapour Deposition

Implantation: Dopant ions are implanted in the semiconductor by bombarding it with an ion beam. The dopant ions face considerably less scattering when the beam is directed parallel to one of the main crystallographic axes of the substrate due to the "channelling effect", which results in much deeper implantation. To avoid this, one has to tilt the beam by a few degrees or perform the implantation through a thin layer of amorphous oxide. By manipulating the energy of the beam one can choose the depth where the majority of the dopant ions come to rest. Hence, one can create doping profiles which have a maximum inside the substrate rather than at the surface. The implantation leaves the crystal lattice shattered and the dopant ions orphaned. Both is cured in a subsequent temperature treatment at around 900 °C, which reorders the crystal and activates the dopants, i.e. integrates them in the lattice.

Diffusion: The substrate is exposed to a gas containing the dopants, or it is coated with a material like highly doped polysilicon, from which the dopant atoms can diffuse into a thin layer at the surface of the substrate. This is done at around 900 °C. A subsequent high temperature step of around 1100 – 1250 °C drives the dopants into the bulk and activates them. With this method one can only create doping profiles that have the maximum concentration at the surface of the substrate.

Photolithography

Photolithography is the process of transferring geometrical structures into the silicon substrate, the oxide, or other layers on the surface of the wafer. These geometrical structures are designed using a CAD software framework, as is used for designing the trapezoidal sensor for the Belle II SVD (see section 5.1).

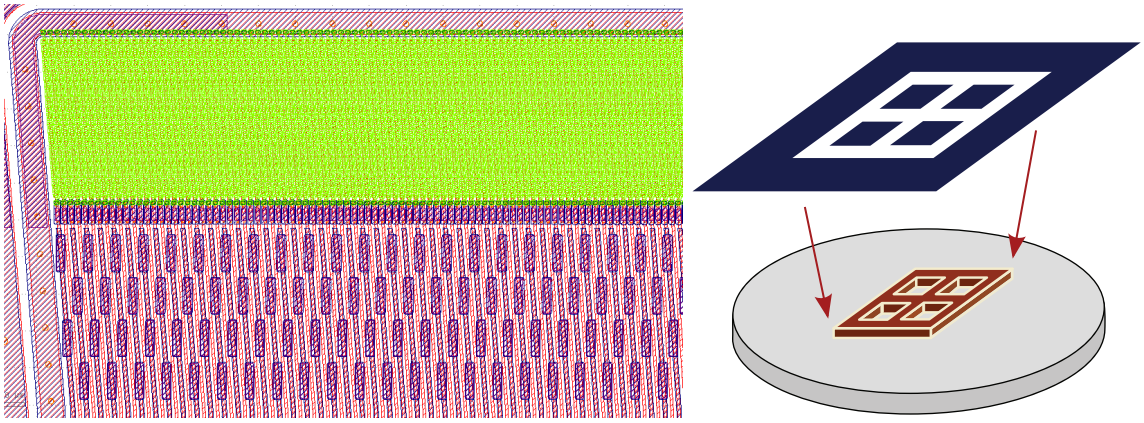

(a) Screenshot of a sensor's CAD layout. The different colours each represent different photo masks.

(b) Exposure of the photo resist through the photo mask [26].

Figure 4.26.: The structures on the photo mask (left) allow exposure of the photo resist only in selected areas (right), which are hereafter chemically altered. The structure is transferred to the photo resist by a subsequent etching step.

The main steps of transferring a computer design onto the wafer are:

1. Photo mask: The design is imprinted to the chrome layer on a glass substrate. Figure 4.26a shows a sensor design with several different photo mask layouts on top of each other.

2. Oxidation of the wafer (optional): For some processing steps a layer of silicon oxide is prepared, into which the structures are transferred.

3. Photo resist: The wafer is coated with a light sensitive material using a technology called "spin coating". While rotating around its axis at 1000 – 5000 RPM[25], the wafer is applied with a small amount of photo resist, which due to the fast rotation is homogeneously spread over the whole surface.

4. Exposure: The photo resist is exposed to light through the photo mask (see figure 4.26), which invokes a chemical reaction of the exposed parts of the photo resist.

5. Development: In this step either the exposed parts or the shaded parts of the photo resist are made soluble for a subsequent etching, depending on the used resist type.

6. Etching: The soluble parts of the photo resist are removed, leaving the geometrical structure imprinted in the resist layer.

7. Oxide etching (optional): The structure in the photo resist can be further transferred to a underlying oxide layer by another (different) etching step.

8. Treatment: The above steps created a mask on the surface of the wafer, which selectively protects some areas from subsequent treatments like implantation, deposition and etching.

Etching

Deposition of material can only be done on the wafer as a whole, and not selectively on dedicated areas. The structuring of these layers has to be performed in a subsequent step, usually by etching of the needless material.

When etching structures into a material layer, the areas selected to remain untouched have to be covered by a layer of structured photo resist. The unprotected structures are transferred into the underlying layer by etching. The etchants are chemicals which predominantly etch a certain material species due to vastly different etch rates in different materials. The so-called "selectivity" is a measure for how well an etchant etches a given material and to what extent other materials remain untouched, as is shown in figure 4.27a.

[25] RPM: Revolutions Per Minute

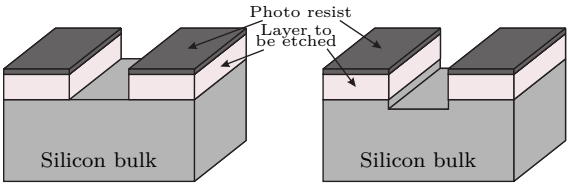

(a) Left: Good selectivity, the etching process stops at the underlying material. Right: Poor selectivity, the etching also affects the underlying material [26].

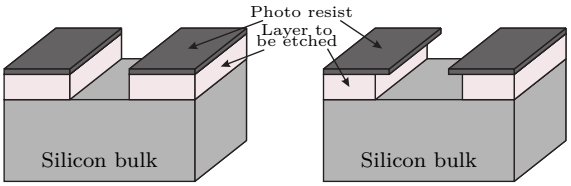

(b) Left: A high anisotropy preserves the material under the protecting photo resist. Right: Isotropic etching affects also the material under the protective layer [26].

The etch rate can also depend on the etching direction, due to anisotropies of the material to be etched, or due to the etching method. Figure 4.27b shows the following limit cases:

Isotrop etching: The etch rate is the same in all directions. This leads to the effect of "under-etching", where a part of the material protected by the photo resist is etched away. One can correct for this effect by adapting the photo masks accordingly.

Anisotrop etching: The etch rate is vastly different in different directions. This is preferable, as long as the etching method maintains enough selectivity.

One distinguishes two main etching methods:

Wet etching: The etchants are liquid chemicals which etch the material, dissolve it, and transport it away from the surface. Generally speaking, wet etchants mostly are highly selective but isotropic. However, some etchants show a high anisotropy due to the crystallographic structures of e.g. silicon. The (111) plane of the crystal is denser than others, reducing the etching rate considerably. Wet etching is comparably cheap, so that it is used in small companies and research institutions.

Dry etching: The etching is performed by physical removal of the material using an ion beam. Careful tuning yields acceptable selectivity while allowing both anisotropic and isotropic etching. The expensive equipment is outweighed by the versatility, the low consumption of additional chemicals, and the high quality of the etching process, making dry etching the preferred method in the large-scale microelectronics industry. Variants of dry etching involve reactive ion etching and plasma etching.

Dicing

The last step after completing a process sequence of planar processes is separating the sensor from the rest of the wafer. This process is called "dicing". The wafer is mounted on a metal plate using a special sticky tape and cut along predefined dicing lines using a diamond saw or a laser with a width of typically 75 µm. The diced sensor remains safely on the sticky tape after dicing.

Part II.

Sensor development and production

Computer-aided design (CAD) is the use of computer systems to assist in the creation, modification, analysis, or optimisation of a design.

Wikipedia on **CAD**

5

CAD Framework and Design Rules

The final silicon microstrip sensor product is defined both by the depth profile of the implemented layers and the two-dimensional geometric layout of the planar processes. The former usually is chosen by the manufacturer to comply with the electric specifications defined by the customer, and often contains a lot of company secrets. The latter, however, is defined by the photo masks used in the photolithography, and can often be defined in detail by the customer. For a scientific institute, the design of the photo masks therefore marks the central tool in defining the sensor's properties and performance.

5.1. The CAD framework SiDDaTA

Commercially available software frameworks for photo mask design mainly focus on IC development, and there is no CAD software specifically made for designing silicon microstrip sensors. However, these commercial software frameworks can be adapted to meet the needs of sensor design. The adaptation done in-house is called "SiDDaTA[1]", which is based on the component "IC station" from the Electronic Design Automation software suite by Mentor Graphics [43]. The CAD layout is not drawn by hand, the IC station framework is rather steered by commands from the C-like scripting language AMPLE[3]. So, the layout is drawn automatically based on a set of parameters read from a parameter file. When a parameter is changed, e.g. the strip pitch, the whole sensor design is redrawn and adapted to the new geometry.

[1] SiDDaTA: Silicon Detector Design and Teststructures using AMPLE[2]
[3] AMPLE: Advanced Multi-Purpose LanguagE

The SiDDaTA framework defines the recurring elements of a silicon microstrip sensor – like the contact pads – as readily available objects, and is implemented as a design framework with a tree-like architecture (see figure 5.1):

Functions: These are the drawing routines, which create the basic shapes like circles, rectangles, trapeze, etc. Functions take their parameters only at runtime from the calling routine.

Structures: A Structure is a composite object which fulfils a certain task in the silicon microstrip sensor, like a single strip or the bias ring. It can be assembled using the Functions defined before or using other Structures. Structures are mostly defined by external parameters, and only some aspects are defined at runtime to adapt to the surroundings.

Devices: A Device is a whole silicon microstrip sensor or a test structure assembled from the Structures defined before. It is entirely defined by external parameters.

The external parameters used for defining Structures and Devices are collected in the so-called "global" files. The SiDDaTA framework is described in more detail in [26].

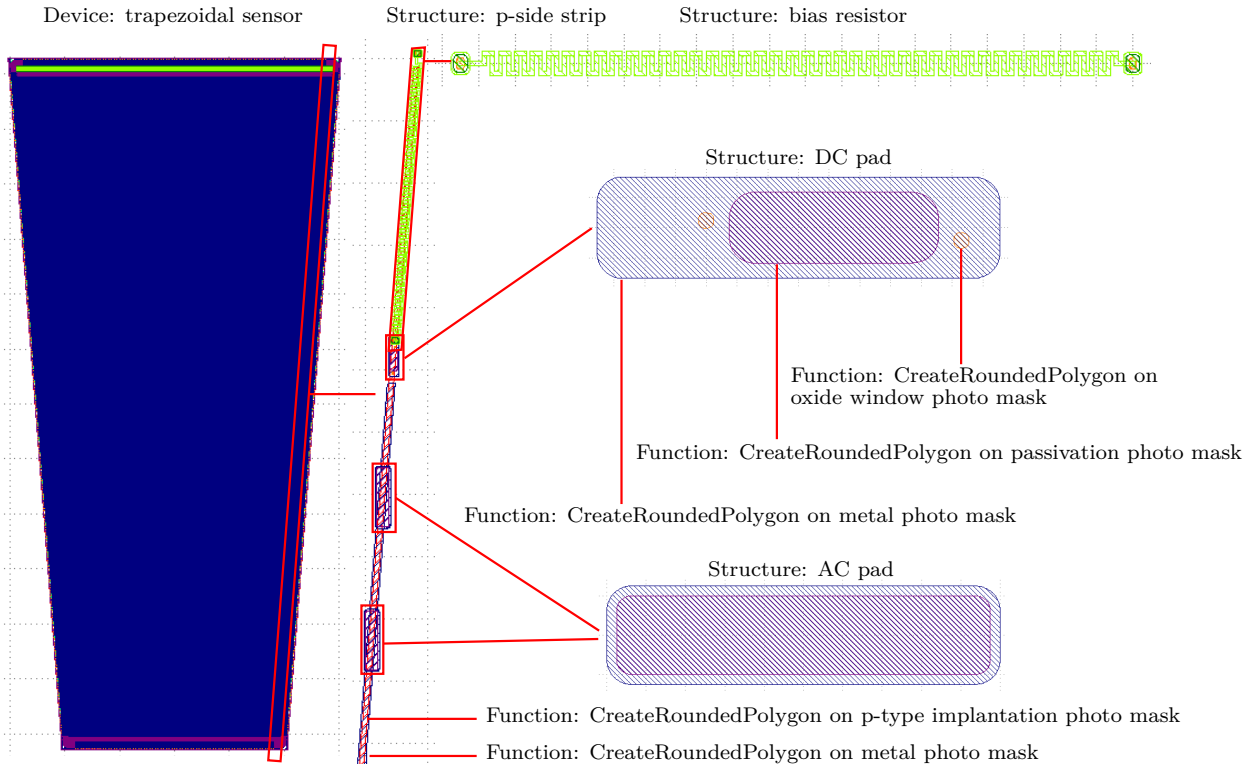

Figure 5.1.: The tree structure of SiDDaTA: Devices (like a sensor) are composed of Structures, which can be assembled using Functions and other Structures. The source code of the basic Function "CreateRoundedPolygon" can be found in Addendum 10.2. The screenshots are taken with the layout viewer "KLayout" [44].

5.1.1. Extension of SiDDaTA to trapezoidal DSSDs

The original SiDDaTA framework was developed to design single-sided rectangular silicon microstrip sensors. The design of a trapezoidal double-sided silicon microstrip sensor requires a thorough overhaul of the complete framework:

- The fundamental shape of a rectangular silicon microstrip sensor design is a rectangle with rounded corners. In contrast, a trapezoidal sensor needs trapeze and rhombuses with rounded corners as basic shapes. Consequently, the extension of SiDDaTA needs to start at the most fundamental functions. Addendum 10.2 displays the source code of the function "CreateRoundedPolygon", which draws an arbitrary polygon with rounded corners.
- A trapezoidal silicon microstrip sensor shows reduced symmetry compared to a rectangular one. For rectangular sensors each strip (or each second strip, depending on the implementation) is identical, so once it is drawn, it can simply be copied automatically to the different target locations. For a trapezoidal sensor, each strip is unique. In case of the trapezoidal DSSD for the Belle II SVD, the p-side strips have a varying pitch, and each strip has a different inclination angle and a different length. The strips of the n-side have a constant pitch and no inclination, but still different lengths.
- The production of a DSSD requires a whole lot of additional photo masks for the layout of the n-side. However, the designs of p-side and n-side are not independent from each other. The SiDDaTA framework has to be reprogrammed in such a way, that e.g. the bias rings of the two sensor sides are congruent (see figure 5.2).

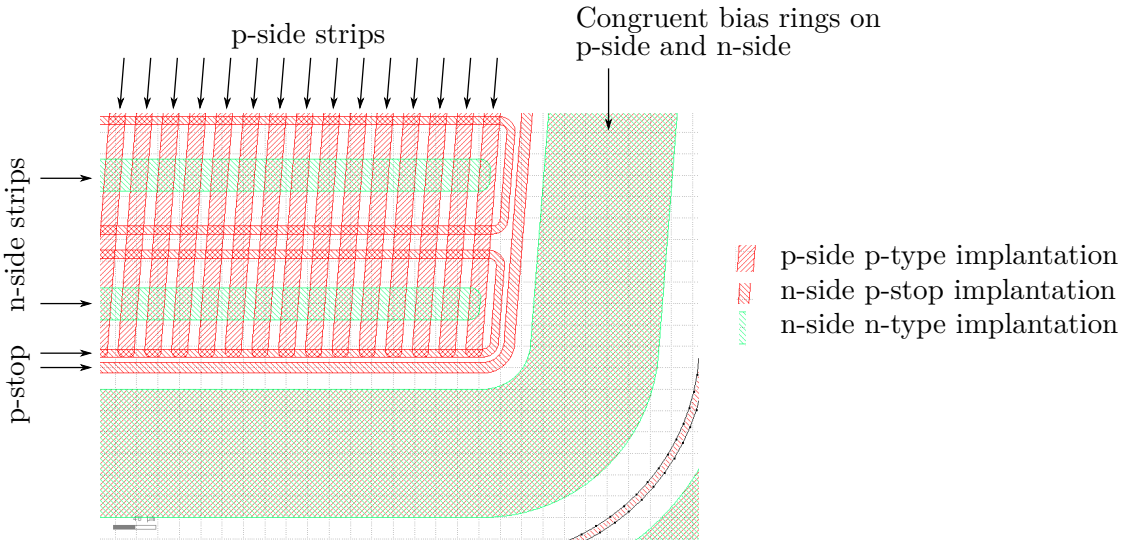

Figure 5.2.: A trapezoidal DSSD needs individual and unique strips built from rhombuses, and the common structures like the bias rings on both sides must be congruent.

5.2. Design rules

Micron Semiconductor Ltd. [19] provided so-called "design rules" to which the design of the trapezoidal DSSD must comply. This ensures that the design is compatible with the manufacturing process sequence, and that the photo mask misalignment of about 1 µm can be tolerated. Note that the photo masks provided by the customer are used as-is in the processing, they are *not* changed to compensate over- or underetching. The process steps are rather carried out in such a way that on average the geometric dimensions defined in the photo masks are met.

5.2.1. Wafer design rules

Excluded areas: Some areas on the wafer must be kept free of devices by the customer, as is shown in figure 5.3.

- For the outer 5 mm the homogeneity of the wafer material cannot be guaranteed, so this so-called "fiducial circle" has to be avoided.
- There are four quadratic areas excluded from processing to preserve secure handling areas. These areas are affected by the etching steps as well, and serve for optical end point inspection, allowing to visually see when the layer to be etched is completely removed.
- In addition, the vendor puts own test structures in a large area on the left side of the wafer, and on four small spots in each quadrant.

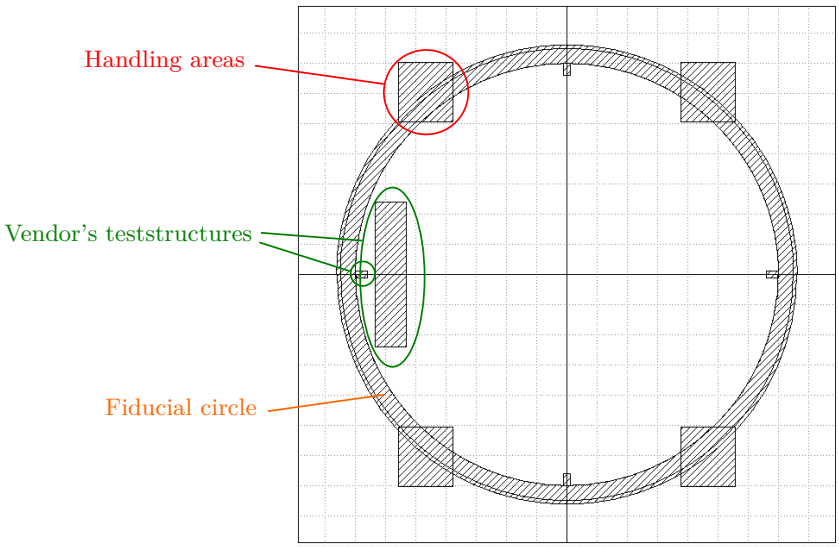

Figure 5.3.: Only a part of a wafer's area can be equipped with devices by the customer. The grey areas are excluded from processing to leave space for handling, test structures by the vendor, and the fiducial circle. View at the p-side.

Mirroring of n-side photo masks: All photo masks have to show the wafer as seen from the p-side. Consequently, the n-side photo masks have to be mirrored in the design to be congruent with the p-side photo masks. In words of Micron Semiconductor Ltd.: "All the p-side masks are shown chrome side down, while all the n-side masks are displayed chrome side up." Figure 5.4 shows the mirrored inscriptions on the n-side metallisation photo mask.

5.2.2. Sensor design rules

Guard ring structure: Micron Semiconductor Ltd. implements a commercially sensitive multi-guard ring structure consisting of ten different guard rings, which is not to be disclosed publicly. The exact geometry was supplied after a NDA[4] was signed.

Dicing line: As already shown in section 6.1, the outline of the sensor is defined by the so-called "dicing line", along which the sensor is diced out of the wafer. In the sensor design, one has to make sure that there is no oxide along this line. So, the dicing line has to be included in the photo masks for p-type and n-type implantation (which remove the thick field oxide, 50 µm wide), in the oxide window photo masks (which remove the thin coupling oxide, 30 µm wide), and in the passivation photo masks (30 µm wide). In addition, the dicing line is coated with aluminium to avoid splitting.

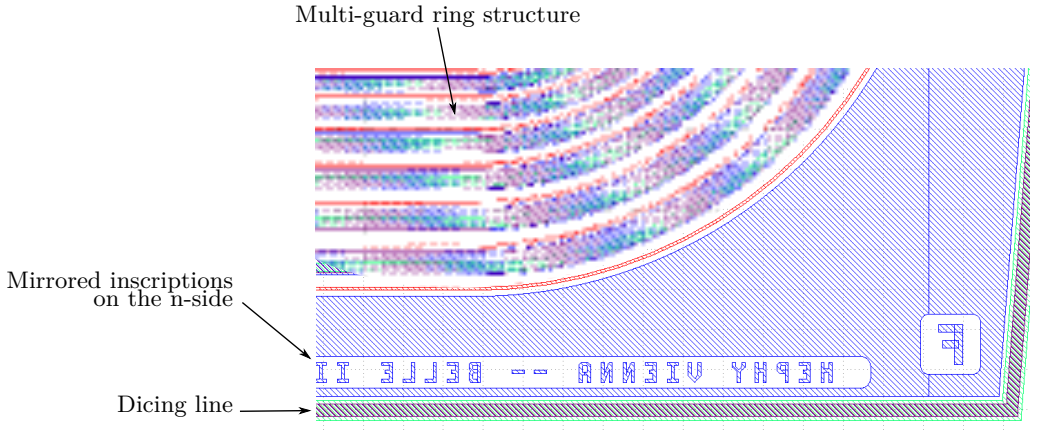

Figure 5.4.: The photo masks of the n-side are mirrored. Micron Semiconductor Ltd. implements a custom multi-guard ring structure which is not to be disclosed. The dicing line surrounding the sensor removes all oxide layers, leaving only a metal line for splinter-proof dicing.

5.2.3. Strip design rules

Bias resistor value: The sheet resistance obtained after doping the polysilicon is not known in detail. However, to achieve a resistor value of 10 MΩ the polysilicon meander should

[4]NDA: Non Disclosure Agreement

contain at least 350 squares, ideally 500. The meander should be 6 µm wide[5], and the arcs of the meander should be separated by 5 µm (see figure 5.5).

Bias resistor end: The connection point of the bias resistor to the bias ring should be placed on a planar surface, i.e. well inside the boundary of the bias ring implant. The oxide window of the bias resistor end should be 7.5 µm per side smaller than the polysilicon part.

Strip geometry: The separation between the end of the implanted strip and the bias ring implant is typically no smaller than the pitch of the implanted strips (see figure 5.5). The metal strip is 5 µm on each side wider than the implanted strip (metal overhang, see figure 5.6).

p-stop geometry: The isolated parts of the p-stop implantation are fixed to a width of 7.5 µm, and the common part is 10 µm wide, the unimplanted gap is 5 µm wide (see figure 5.6). For more details about n-side strip insulation refer to section 7.

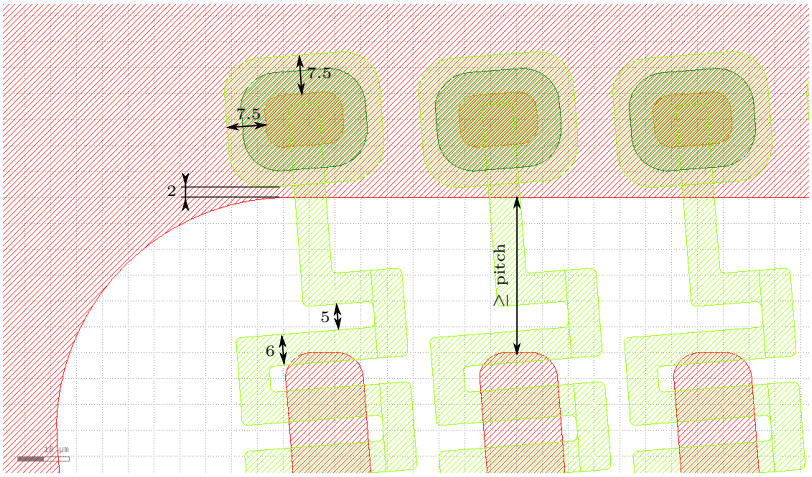

Figure 5.5.: Design rules for the bias resistor and implanted strip ends, values in µm. Red is p-type implantation, light green is polysilicon, dark green is polysilicon head implantation, orange is oxide windows.

5.2.4. Contact pad design rules

Passivation openings: The distance between passivation openings and metal boundaries should be at least 5 µm.

DC pad oxide windows: The oxide windows should have a minimum diameter of 5 µm, and should be no less than 10 µm away from any metal boundary and no less than 5 µm away from any implant boundary (see figure 5.6).

[5]With a width of 6 µm, a polysilicon meander of 500 squares results in a length of $500\,\square \times 6\,\mu m = 3000\,\mu m$

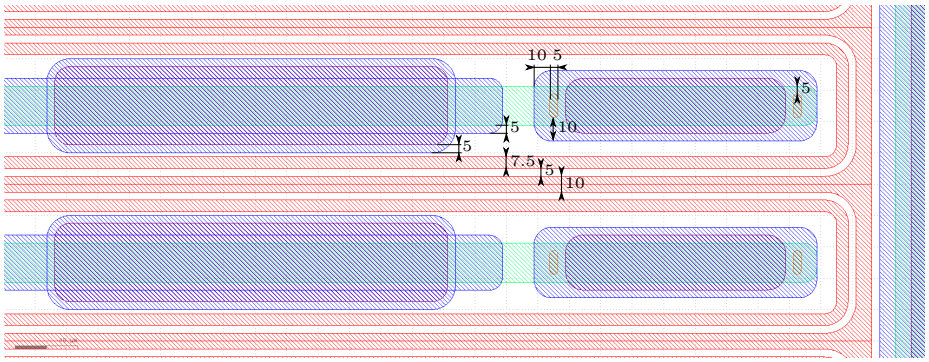

Figure 5.6.: Design rules for the p-stop implantation and the contact pads, values in µm. Red is p-type implantation, green is n-type implantation, blue is metallisation, purple is passivation openings, orange is oxide windows.

5.2.5. Wafer layout

The wafer is roughly divided in the main trapezoidal sensor in the middle, and four cut-offs, which remain after dicing the main sensor, as is shown in figure 5.7. All devices have to fit in the processing areas defined in figure 5.3. The right and left cut-offs are further diced to separate the baby sensors; the test structures remain on one common wafer slice.

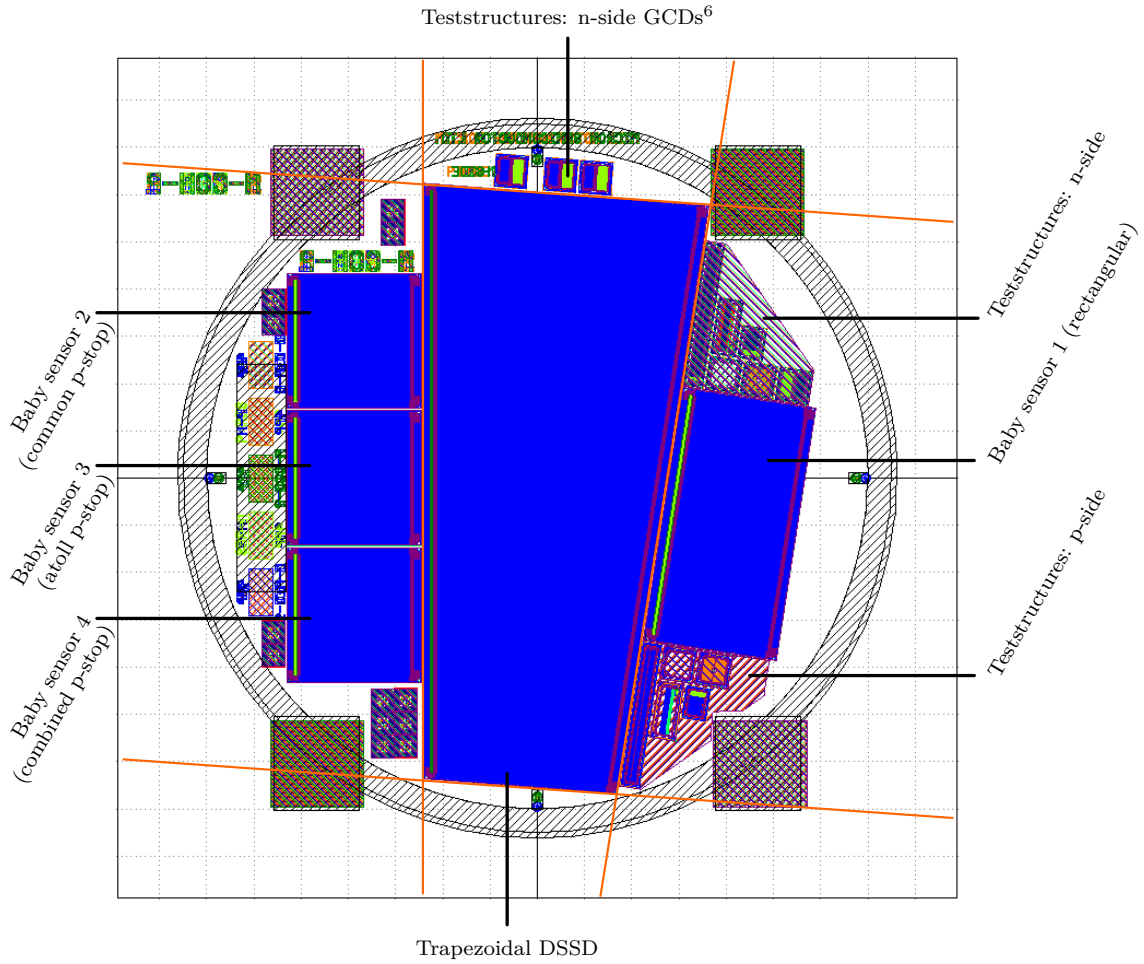

Figure 5.7.: The wafer layout as processed by Micron Semiconductor Ltd. Apart from the main trapezoidal sensor there are four baby sensors and test structures for p-side and n-side. The orange lines mark the main dicing lines, which separate the main sensor from four cut-offs, three of which containing further sensors and test structures.

Semiconductor device fabrication is the process used to create the integrated circuits that are present in everyday electrical and electronic devices. It is a multiple-step sequence of photolithographic and chemical processing steps during which electronic circuits are gradually created on a wafer made of pure semiconducting material.

Wikipedia on **Semiconductor device fabrication**

6

Production of the trapezoidal DSSD

The following sections review details about the sensor production at Micron Semiconductor Ltd. The process sequence presented in section 6.1 resembles how a DSSD is processed in-house at Micron Semiconductor Ltd., but can be regarded an example of the generally necessary processing steps. Section 6.2 describes the produced devices in detail.

6.1. The process sequence by Micron Semiconductor Ltd.

The basic process steps described in section 4.7.2 have to be combined and repeated to form a process sequence yielding a working single-sided or double-sided silicon microstrip sensor. In this process sequence one has to pay special attention to the temperature budget. Every processing step carried out at elevated temperature influences the wafer as a whole, and alters the results of the preceding steps. Therefore, the process sequence has to start with the high temperature processes and end with the low temperature ones.

The wafer carriers used by Micron Semiconductor Ltd. can hold up to 25 wafers, but only six wafers are processed simultaneously to allow optical inspections during processing. Micron Semiconductor Ltd. is capable of starting the processing of 50 wafers per week, a DSSD can theoretical be finished within six weeks when there is nothing else to do. Under normal circumstances, however, completion takes about 5 months, and reaches a yield of 60%.

This section presents a principal showcase process sequence, to outline the main steps in manufacturing a DSSD in qualitative, but not to scale diagrams. These diagrams are cut-away views along a p-side strip, as is sketched in figure 6.1. The detailed process parameters like temperature, duration and ambient pressure are usually company secrets of the vendor. However, this process sequence resembles the basic steps implemented by Micron Semiconductor Ltd. [19] used to manufacture the trapezoidal DSSDs for the Belle II SVD, omitting some intermediate temperature treatments. The production of a DSSD includes a total of about 400 individual processing steps, all of which are carried out in-house at Micron Semiconductor Ltd..

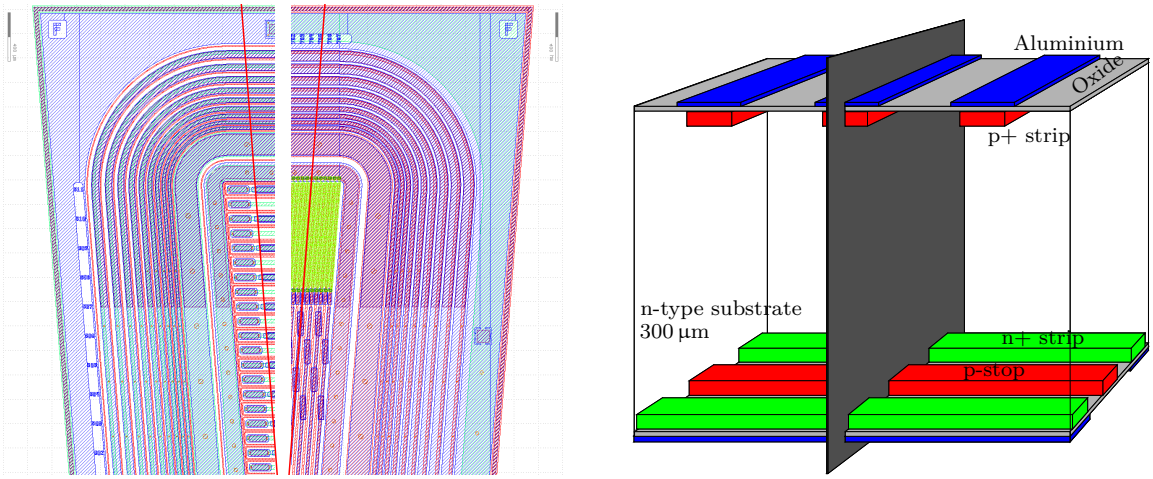

Figure 6.1.: The process sequence is explained with help of a series of cut-away views along the p-side strip of the trapezoidal DSSD.

Step 1: Plain silicon wafer

The processing starts with a n-type wafer (grey), which is thinned and polished by third-party wafer suppliers. An eventual p-spray implantation is carried out first, if n-side strip insulation is not achieved via the p-stop method. See section 7 for more information about these insulation methods.

Step 2: Oxidation, photo resist, photolithography for strip and ring implants

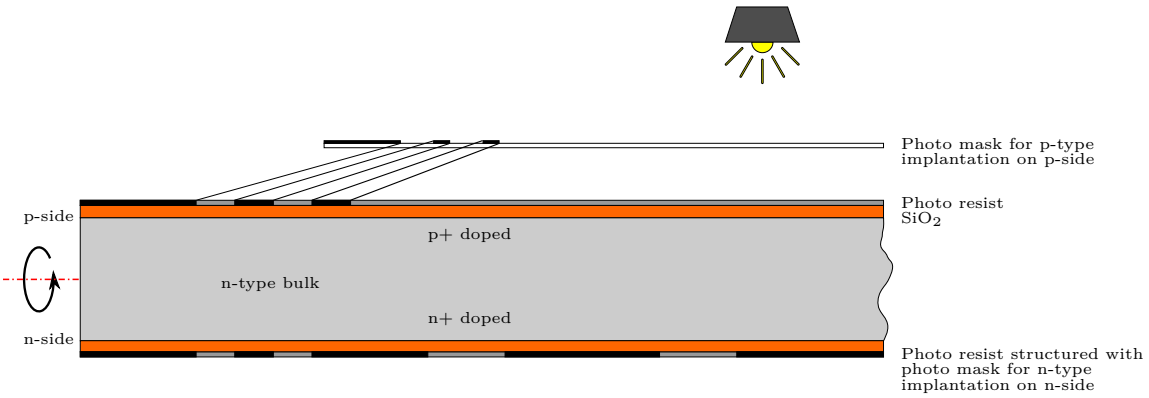

First, a layer of thermal oxide (orange) is grown simultaneously on both sides, which will be formed to be the mask for the implantation of strips and bias and guard rings. The real design includes multiple guard rings, while in the simplified cut views only one is drawn. The oxide layer on one side is coated with photo resist (black) and illuminated (dark grey) through the corresponding photo mask (e.g. p-side, red). Afterwards, the wafer is turned, and the other side is coated with photo resist and illuminated through its own photo mask (n-side, green). The oxide created in this step is called "field oxide". Note that the area outlining the sensor's shape in the mask layout marks the dicing line and is not part of the actual sensor design.

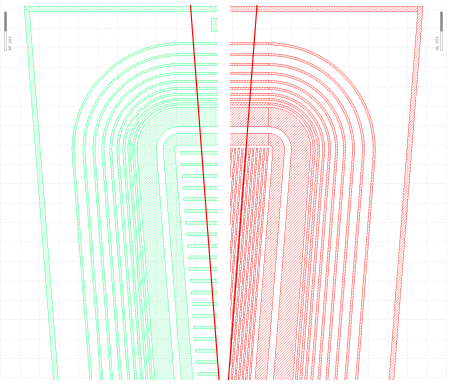

Step 3: Etching of oxide mask for strip and ring implants

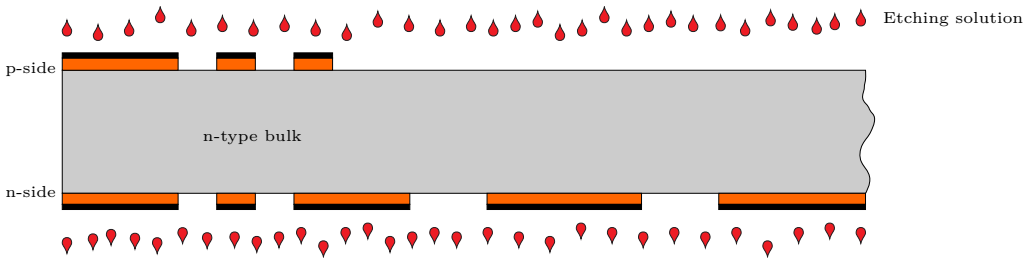

The structure in the photo resist is transferred to the underlying field oxide by exposing the wafer to an etching solution which affects illuminated photo resist and silicon oxide, but not bare silicon. Afterwards, the rest of the photo resist is removed as well.

Step 4: Thermal growth of the thin coupling oxide

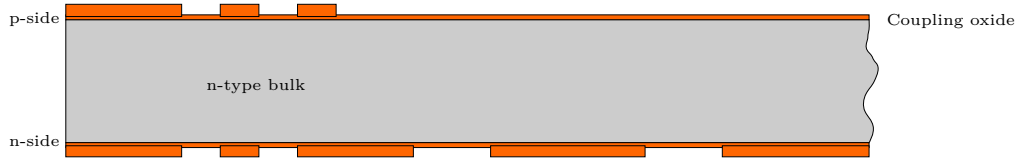

In a thermal step a 220 nm thin and pure oxide layer is grown, which serves as coupling oxide to build the capacitor between the implanted strips and the aluminium strips. In the field of silicon microstrip sensors, this oxide layer is also called “readout oxide”, while in the traditional microelectronics industry it is known as “gate oxide”, because it is similar to the oxide found in a MOSFET’s gate. Note that the coupling oxide grows *under* the field oxide, but with a lower growth rate.

Step 5: Implantation of strips and rings

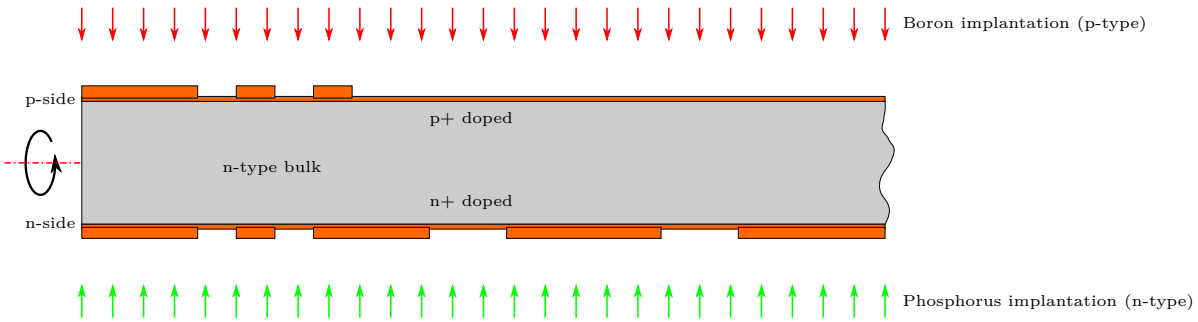

The p-type (red) and n-type (green) areas are implanted *through the coupling oxide*, turning the wafer in between. After implantation, the crystal lattice is cured with a temperature treatment, also activating the dopants. Because the process step creating the coupling oxide already happened before, the created doping profiles are altered by one subsequent temperature step less.

Step 6: Creation of n-side strip insulation (p-stop)

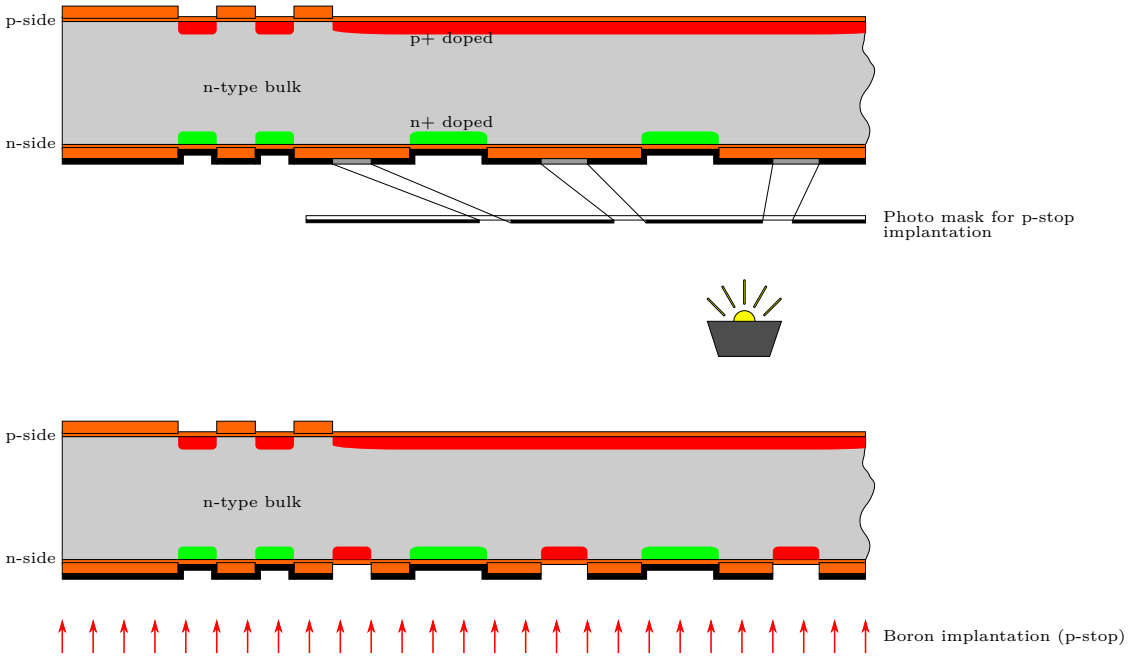

This step is only carried out if the p-spray implantation in step 1 is not applied. The insulation of the n-side strips needs implantation of dedicated "p-stop" structures (red) to interrupt the accumulation layer. The etching step in between is not shown. After implantation, the photo resist is again removed. A subsequent temperature treatment anneals the crystal lattice and activates the dopants. See section 3.5.4 for the theoretical background about the accumulation layer, and section 7 on how the geometry of the p-stop implantation influences the sensor performance. After this step, an additional thermal oxide of 250 nm is grown to protect the bare silicon areas created in this etching step. This increases the the coupling oxide to 320 nm.

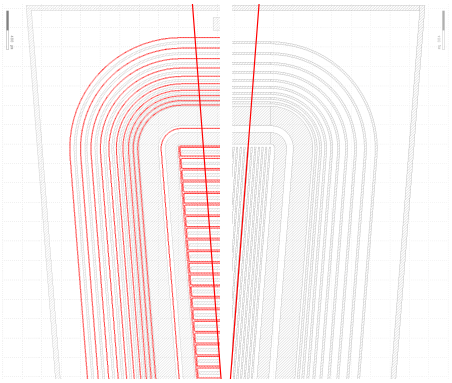

Step 7: Polysilicon deposition and implantation

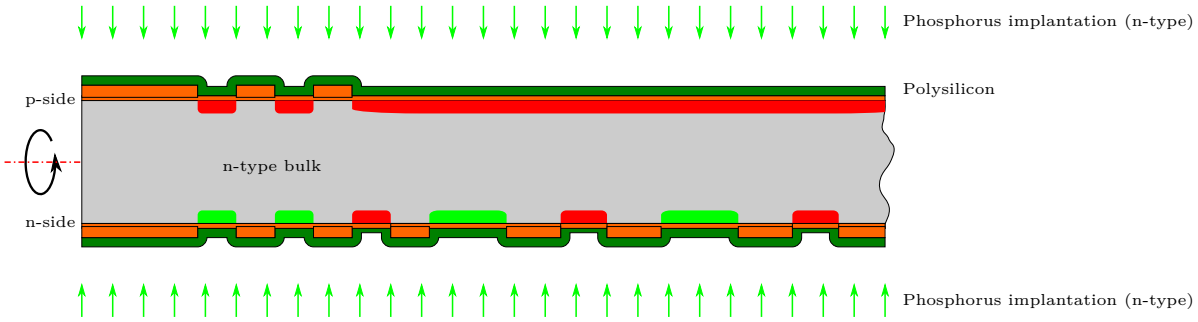

To build the bias resistor, a layer of polysilicon (dark green) is deposited with PECVD on both sides simultaneously. Afterwards, the resistance value is adjusted by implantation on one side after the other.

Step 8: Polysilicon head implantation

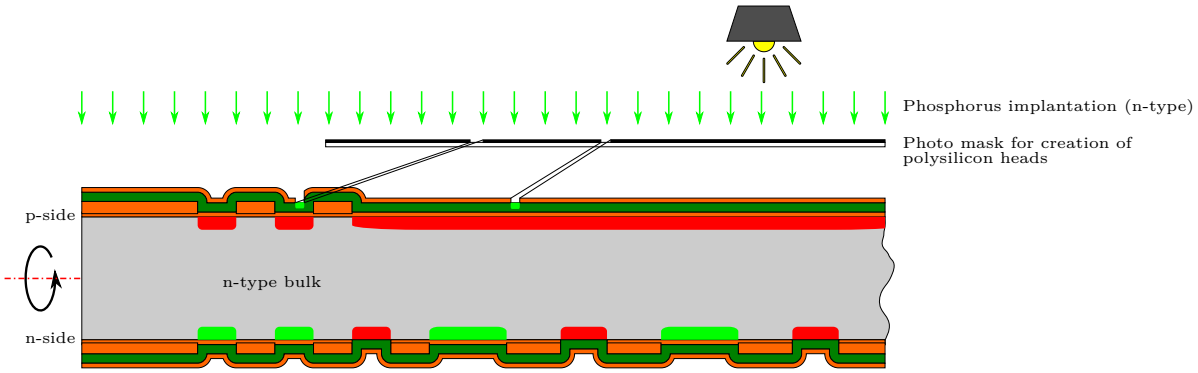

Another special implantation is needed on both wafer sides at the spots where the bias resistors will be connected to the metal of bias ring and DC pads (green spots). This implantation increases the conductivity of the polysilicon considerably and prevents a Schottky contact. The implants are only shown for the p-side, because the cut view does not cross any areas with this implant on the n-side.

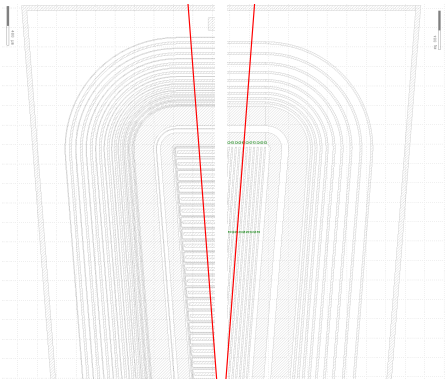

Step 9: Structuring of the bias resistor

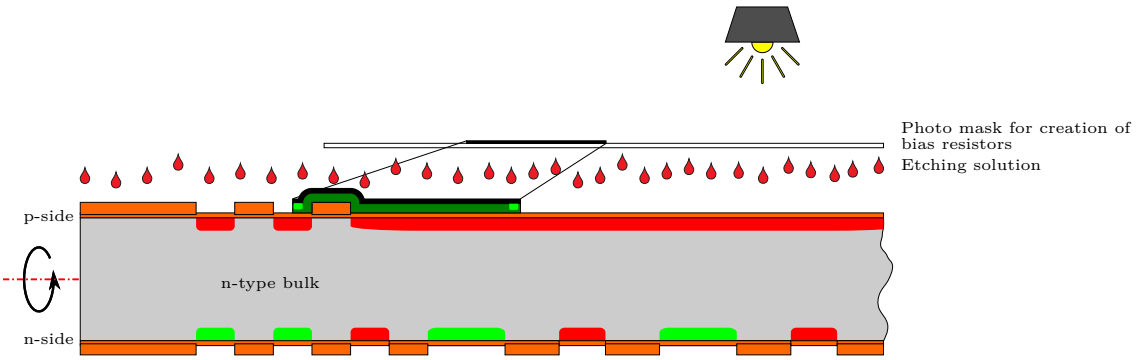

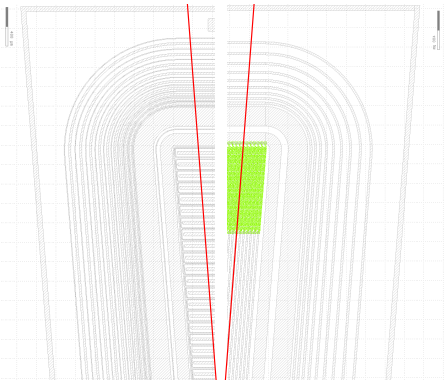

The next steps perform photo resist coating, photolithography of the bias resistors' shapes and their etching, as well as subsequent removal of the photo resist. This is done on both sides successively, but it is only shown on the p-side, because the chosen cut view does not cross the bias resistors of the n-side.

Step 10: Formation of the edge ring

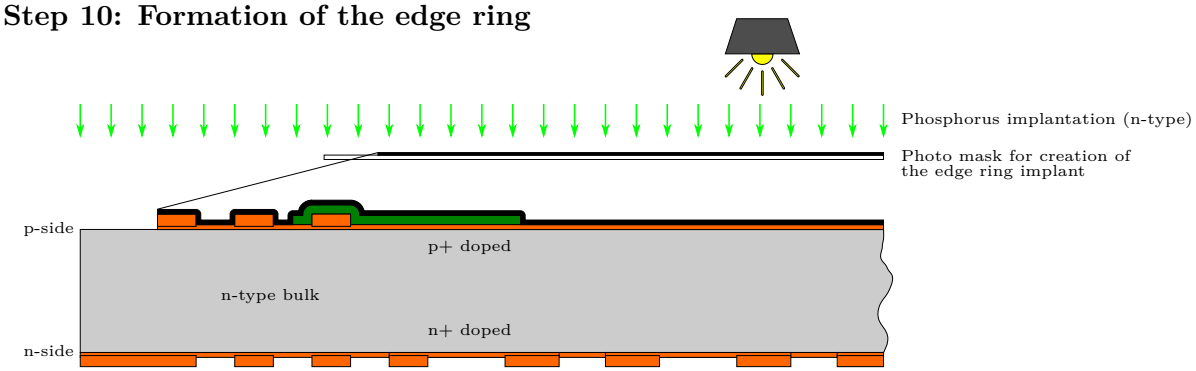

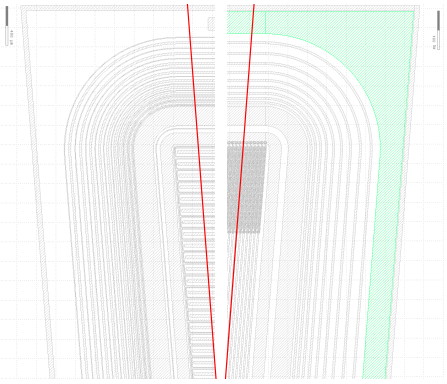

The edge ring (green) is formed by using photo resist and the already available field oxide at the edge of the wafer as mask for implantation. The edge ring implant is only done on the p-side. After this step, a temperature treatment is carried out to anneal the implants of edge ring, polysilicon and polysilicon heads in one step.

Step 11: Etching of oxide windows

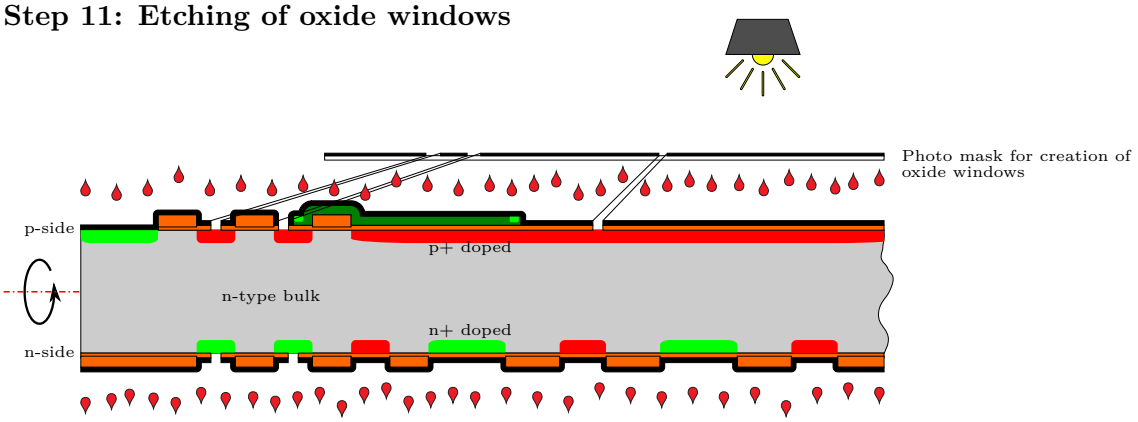

The next step forms the oxide windows (orange) through the coupling capacitance, which will serve as a connection between the implanted silicon substrate and the upcoming metal layer. The photolithography is performed on both sides separately using the corresponding photo masks, the etching step is performed for both sides at once. Note that the photo mask contains oxide windows at the ends of the bias resistor as well, and that there is a separate photo mask holding oxide windows in the edge ring. Both are only effective if the process sequence implements an additional oxide layer after implantation of the edge ring, which is not the case for our sensor order.

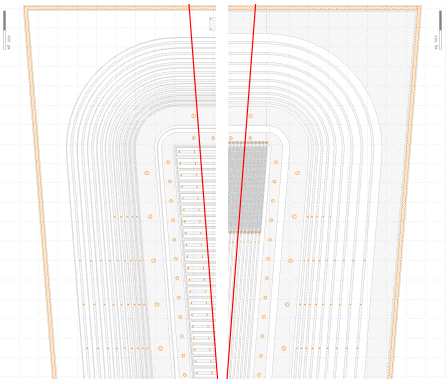

Step 12: Creation of the metal layer

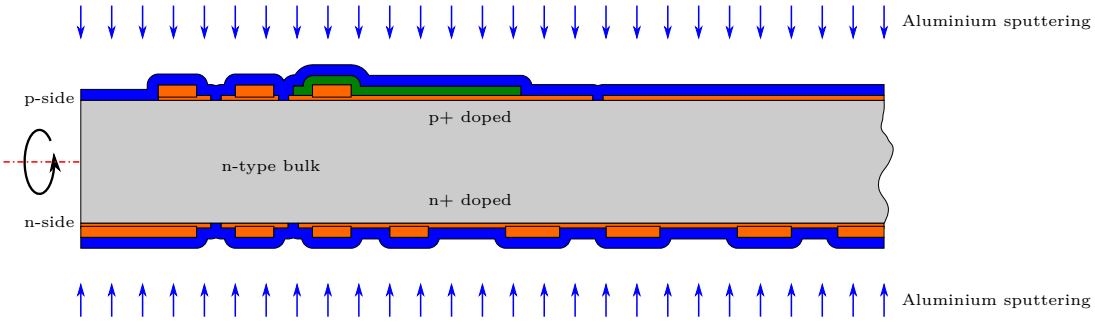

An aluminium metallisation (blue) of 1.2 - 1.4 µm is deposited by sputtering, one side after the other. Note that this layer also fills the oxide windows created in the previous step, and has a contact to the underlying doped silicon substrate.

Step 13: Structuring of the metal layer

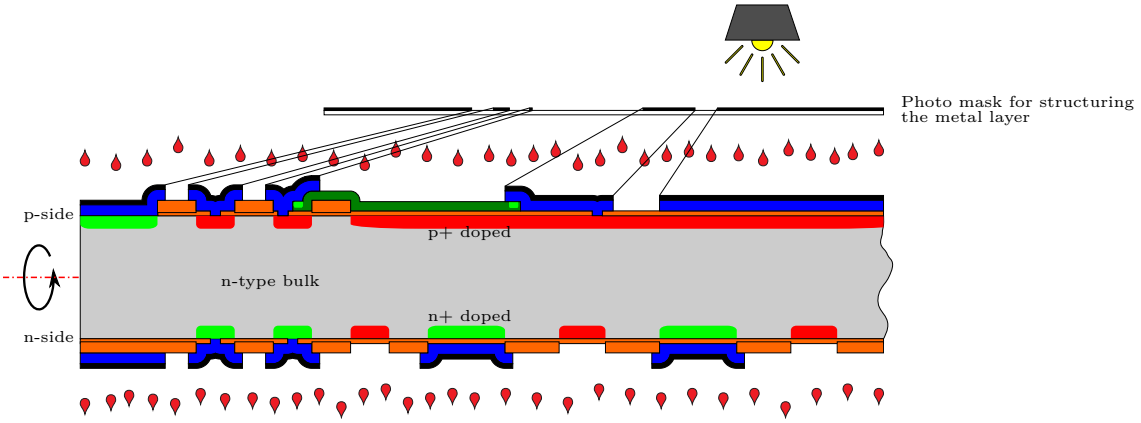

The metal layer is structured to form the aluminium strips above the implanted ones, the pads on strips, the metallisation of the rings, and the inscriptions in the edge ring. Photo resist coating, photolithography and etching is finished on one side, then the wafer is turned. Afterwards the rest of the photo resist is removed. The connection between the right end of the bias resistor and the implanted strip will later form the DC pad. Note that the width of the metal strips is larger than the width of the implanted strips for breakdown protection (metal overhang), best visible on the n-side.

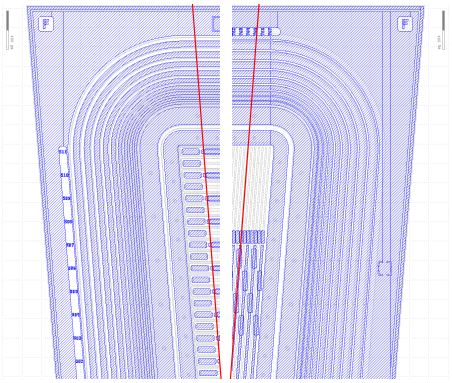

Step 14: Deposition of passivation oxide

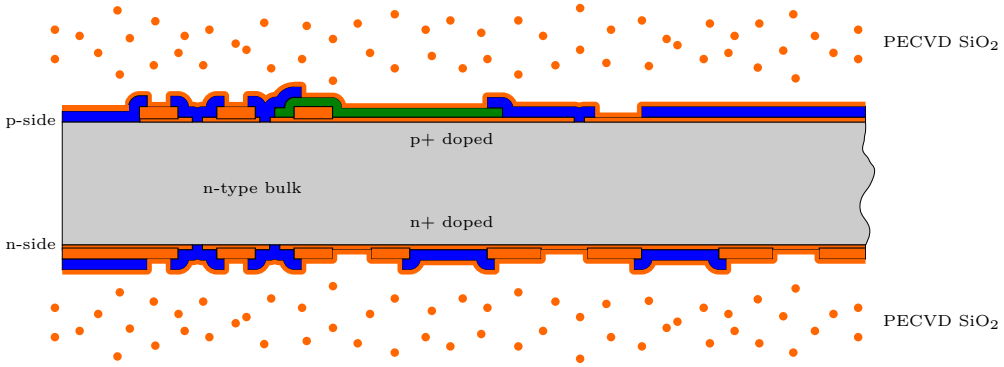

A protective layer of pure silicon oxide SiO_2 (orange) is deposited using the PECVD method, with a thickness of 500 nm. Thermal growth of SiO_2 can not be used in this step, because the oxide layer has to be *above* the existing layers, while thermal oxide could only grow at the surface of the bare silicon substrate, under the existing structures.

Step 15: Passivation openings

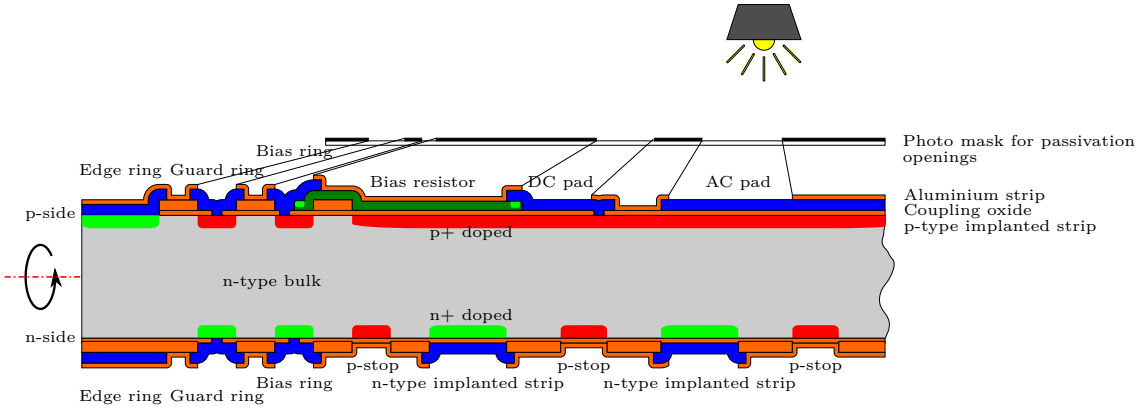

A last photolithography and etching step is performed on both sides of the wafer to create openings in the passivation layer in order to allow access to the contact pads (purple). While for the other photo masks the coloured areas mark the regions where material is kept or an implantation is carried out, the coloured areas of this mask mark the regions where the passivation is *removed*. This concludes the showcase process sequence, which is followed by dicing along the dicing line surrounding the sensor.

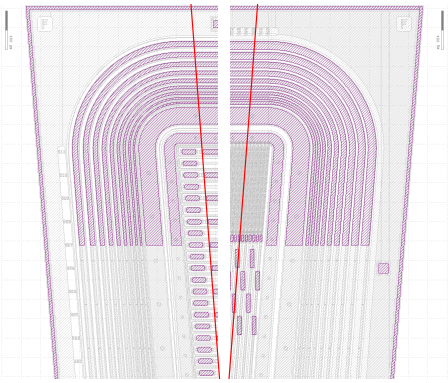

6.2. The produced devices

The order at Micron Semiconductor Ltd. contained the following electrical specifications for the trapezoidal sensor:

Table 6.1.: Electrical specifications for the trapezoidal sensor

Quantity	Value
Base material	300 µm n-type Si, 8 kΩcm
Full depletion voltage V_{FD}	40 V (typ.), 70 V (max)
Operation voltage	$V_{FD} \ldots 2 \times V_{FD}$
Breakdown voltage	$\geq 2.5 \times V_{FD}$
Polysilicon resistor	10 MΩ (min.), 15 ± 5 MΩ (max.)
Interstrip resistance, p-side	100 MΩ (min.), 1 GΩ (typ.)
Interstrip resistance, n-side	10 MΩ (min.), 100 MΩ (typ.)

Unless otherwise noted, these values apply to all produced devices. Up to now, Micron Semiconductor Ltd. processed four different batches of prototype wafers:

1. Batch number 2826: n-type material with p-stop implantation: For these first prototypes the bias resistor value was wrongly adjusted to 50 MΩ. The coupling capacitance on the n-side is 0.94 pF/cm µm per strip length and width.

2. Batch number 2825: n-type material with p-spray implantation: The n-side strip insulation implements the p-spray blocking method. The polysilicon was left unimplanted, yielding a bias resistor value in the order of 120 MΩ. The coupling capacitance on the n-side is approximately 1.9 pF/cm µm per strip length and width, which suggests a reduced thickness of the coupling oxide.

3. Batch number 2815: p-type material with p-stop implantation: In this experimental processing run, Micron Semiconductor Ltd. used a p-type base material, the properties of which are not exactly known.

4. Batch number 2965: n-type material with p-stop implantation and final design: Testing of the sensors with the initial design revealed some shortcomings, which were removed in a design update (see section 7.3 for beam test results motivating the changes). The changed photo masks are the p-stop implantation mask on the n-side as well as the metallisation and passivation masks on the p-side. The bias resistor value is now corrected to 15 MΩ. The coupling capacitance on the n-side is 0.94 pF/cm µm per strip length and width.

6.2.1. Main trapezoidal sensor

The trapezoidal sensor is introduced already in section 2.3.2, the final geometric layout is documented in detail in the data sheet in Addendum 11.3. The main parameters are:

- Active area: 58.9 cm^2
- Total area: 63.83 cm^2
- Number of readout strips on p-side: 768, with one intermediate strip between two readout strips
- Number of readout strips on n-side: 512, with one intermediate strip between two readout strips
- Readout pitch on p-side: 50-75 µm
- Readout pitch on n-side: 240 µm
- Strip implant area on p-side: 12.27-12.31 cm × 15 µm
- Strip implant area on n-side: 38.36-57.52 mm × 30 µm
- n-side strip insulation: atoll p-stop, width $a = 7.5$ µm, distance from implanted strip $d = 15$ µm

The initial contact pad configuration on the p-side introduced difficulties when testing the sensor in the laboratory. In the initial layout (figure 6.2, left) all pads were centred on the

inclined strips. Consequently, DC pads and AC pads were not aligned. While this poses no problem for wire bonding[1], testing in the laboratory is affected. When performing a strip scan (i.e. carrying out a number of measurements on every strip), the relative alignment of the current strip's DC pad and AC pad must remain the same. This is because one usually moves the sensor as a whole to place the needles on the pads of the next strip; the needles can't be moved automatically and individually. Therefore, the pads of the final design (figure 6.2, right) were shifted in order to establish this alignment. Moreover, all AC pads for needle testing are in the same row in the final design, while they were staggered in the initial one.

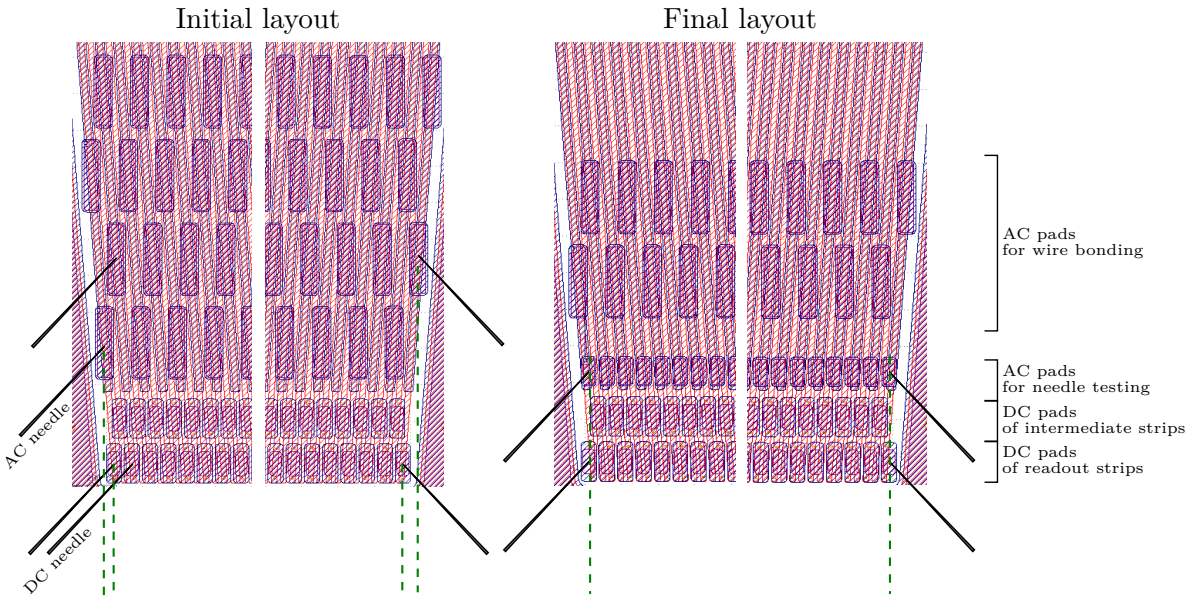

Figure 6.2.: The initial pad layout (left) features staggered AC pads, which are not aligned with the corresponding DC pads. In the final design (right), the DC pads of the readout strips and one row of AC pads are shifted to be aligned, introducing a linear AC pad row for needle testing.

Moreover, the first sensor design implemented the so-called "combined p-stop" pattern for n-side strip insulation, as suggested by references [45] and [46]. However, our own optimisation measurements (section 7) showed that the "atoll p-stop" pattern works best on our devices.

6.2.2. Baby sensors

Baby sensors are small but fully functional silicon microstrip sensors, often with a special purpose. On the wafer processed by Micron Semiconductor Ltd. we implemented four different baby sensors:

[1] On an automated wire bonding machine, connections between two pad rows with different pitch can easily be programmed

The rectangular baby sensor 1

The baby sensor 1 is a generic rectangular DSSD with the following parameters:

- Active area: $13.14\,\mathrm{cm}^2$
- Total area: $15.35\,\mathrm{cm}^2$
- Number of readout strips on p-side: 512, with one intermediate strip between two readout strips
- Number of readout strips on n-side: 512, with one intermediate strip between two readout strips
- Readout pitch on p-side: $50\,\mu\mathrm{m}$
- Readout pitch on n-side: $100\,\mu\mathrm{m}$
- Strip implant area on p-side: $5.12\,\mathrm{cm} \times 15\,\mu\mathrm{m}$
- Strip implant area on n-side: $2.56\,\mathrm{cm} \times 15\,\mu\mathrm{m}$
- n-side strip insulation: atoll p-stop, width $a = 7.5\,\mu\mathrm{m}$, distance from implanted strip $d = 7.5\,\mu\mathrm{m}$

The quadratic baby sensors 2 – 4

The baby sensors 2, 3 and 4 are designed specifically to investigate different geometrical patterns of the p-stop blocking method for n-side strip insulation (see sections 3.5.5 and 4.6.1 for further information). In every other aspect, the sensors are completely identical:

- Active area: $6.76\,\mathrm{cm}^2$
- Total area: $8.12\,\mathrm{cm}^2$
- Number of strips on p-side: 512, no intermediate strips
- Number of strips on n-side: 256, no intermediate strips
- Pitch on p-side: $50\,\mu\mathrm{m}$
- Pitch on n-side: $100\,\mu\mathrm{m}$
- Strip implant area on p-side: $2.56\,\mathrm{cm} \times 15\,\mu\mathrm{m}$
- Strip implant area on n-side: $2.56\,\mathrm{cm} \times 25\,\mu\mathrm{m}$

Each sensor implements a different p-stop pattern for strip insulation on the n-side. Figure 6.3 shows sketches of these patterns, where p-type implantation is shown in red, n-type implantation in green.

Common p-stop pattern (figure 6.3a): The n-type doped strips are surrounded by a p-type doped area covering the whole sensor. Only small regions around the strips are left unimplanted. This interrupts the accumulation layer which hence cannot short the n-type strips. The p-stop implant itself is on the same floating potential all over

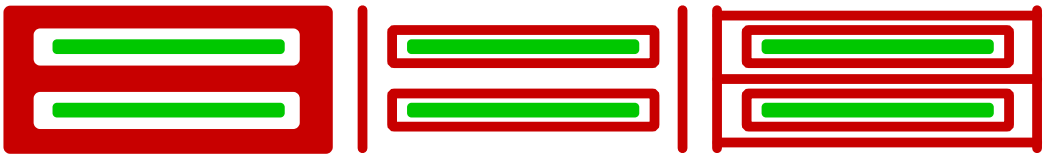

(a) The common p-stop (baby sensor 2)

(b) The atoll p-stop (baby sensor 3)

(c) The combined p-stop (baby sensor 4)

Figure 6.3.: The p-stop patterns. p-stop implant is red, n-type strip implant is green (Drawings inspired by [45])

the sensor and could therefore distribute any charge introduced in the implant. This pattern has been used for a long time and is well known.

Atoll p-stop pattern (figure 6.3b): The n-type doped strips are embedded in isolated ring-like p-type implants. Here, the accumulation layer between the strips is interrupted, but remains intact outside the atoll implants and spreads all over the sensor. This pattern is the standard p-stop pattern nowadays.

Combined p-stop pattern (figure 6.3c): The n-type doped strips are surrounded by atoll p-stop implants. In addition to that, both strip and atoll implants are embedded in a p-type doped area covering the whole sensor, like in case of the common pattern. Only small regions around the strip and the atoll are left unimplanted. This pattern tries to combine the benefits of the common pattern and the atoll pattern, and was favoured by the studies [45] and [46].

The geometry variants of the p-stop patterns: On every sensor type there are four zones of 64 strips each, which implements a different variant of its p-stop pattern. So in total, there are twelve different p-stop geometries. The geometry variant is defined by the distance between the n-type strip implant and the p-stop implant. Hence, the geometries are called “wide”, “half-wide”, “half-narrow” and “narrow”, where for the “wide” geometry the p-stop implant is far away from the strip, and for the “narrow” geometry it is close. Figure 6.4 illustrates of these designs.

Details of the geometries can be found in table 6.2. Here, “atoll width” denotes the width of the ring-like p-type implant. “Bar width” is the width of the p-type implant part of the common structure, which is between the strips. “Distance” denotes the width of the unimplanted region between strip implant and p-stop implant. These dimensions are shown in the sketch next to the table. Note that the geometry variation is finer in the final design. “Strips” displays the strip numbers which belong to the respective geometry zone.

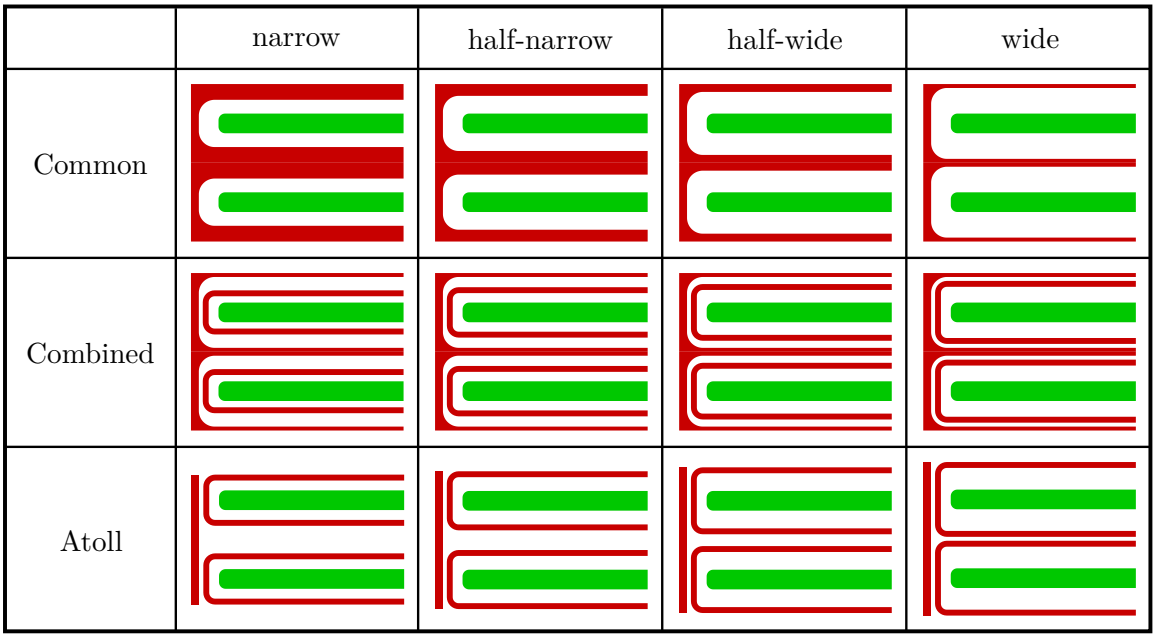

Figure 6.4.: The different p-stop patterns and geometries. Green: n-type implants (strips); red: p-stop implants

Table 6.2.: Dimensions of the p-stop geometries in µm. The first values are from the initial design, the others from the final design. Note that the sequence of zones is different for the common p-stop.

		narrow	half-narrow	half-wide	wide
Common	bar width (b)	40/25	30/20	20/15	10/10
	distance (d)	17.5/25	22.5/27.5	27.5/30	32.5/32.5
	strips	0 – 63	64 – 127	128 – 191	192 – 255
Combined	bar width (b)	10	10	10	10
	atoll width (a)	7.5	7.5	7.5	7.5
	distance (d)	8/14	12/16	16/18	20/20
	strips	192 – 255	128 – 191	64 – 127	0 – 63
Atoll	atoll width (a)	7.5	7.5	7.5	7.5
	distance (d)	12.5/20	17.5/22.5	22.5/25	27.5/27.5
	strips	192 – 255	128 – 191	64 – 127	0 – 63

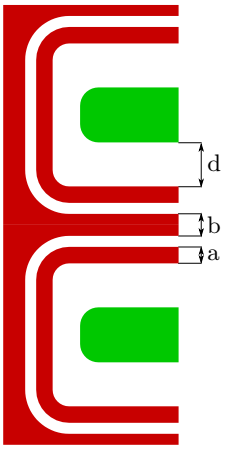

6.2.3. Test structures

The wafer design implements a standard set of test structures, which were already used for the quality control of the single-sided silicon microstrip sensors of the CMS experiment. However, this set was extended to work on the n-side of DSSDs as well.

All relevant tests have been carried out on the sensors themselves, so the test structures presented here have not been studied in detail.

p-side test structures

The standard set of test structures for p-in-n silicon microstrip sensors is described in detail in [26] and [47]. It contains the following devices (see figure 6.5):

Diode: The diode is used to measure the full depletion voltage and determine the bulk resistivity.

MOS: The MOS structure is dedicated to measuring the flat-band voltage and allows to determine the amount of oxide charges in the thick field oxide.

GCD: The GCD[2] is used to individually measure the bulk current and the surface current contributions to the total dark current. The two variants use aluminium and polysilicon as gate materials between a comb-shaped p-type electrode.

Sheet: The sheet structure contains meanders made of aluminium, p-type implantation, n-type implantation and polysilicon to measure the resistivity of these layers. Note that the n-type meander is not part of the standard set of CMS test structures.

TS Cap: The TS Cap structure allows direct measurement of the capacitance value and the breakdown voltage of the coupling capacitance.

TS Cap DC: The TS Cap DC structure is dedicated to measuring the interstrip resistance.

The opposite side of the wafer is n-type doped and coated with aluminium, which resembles the situation of a single-sided p-in-n silicon microstrip sensor.

[2]GCD: Gate Controlled Diode

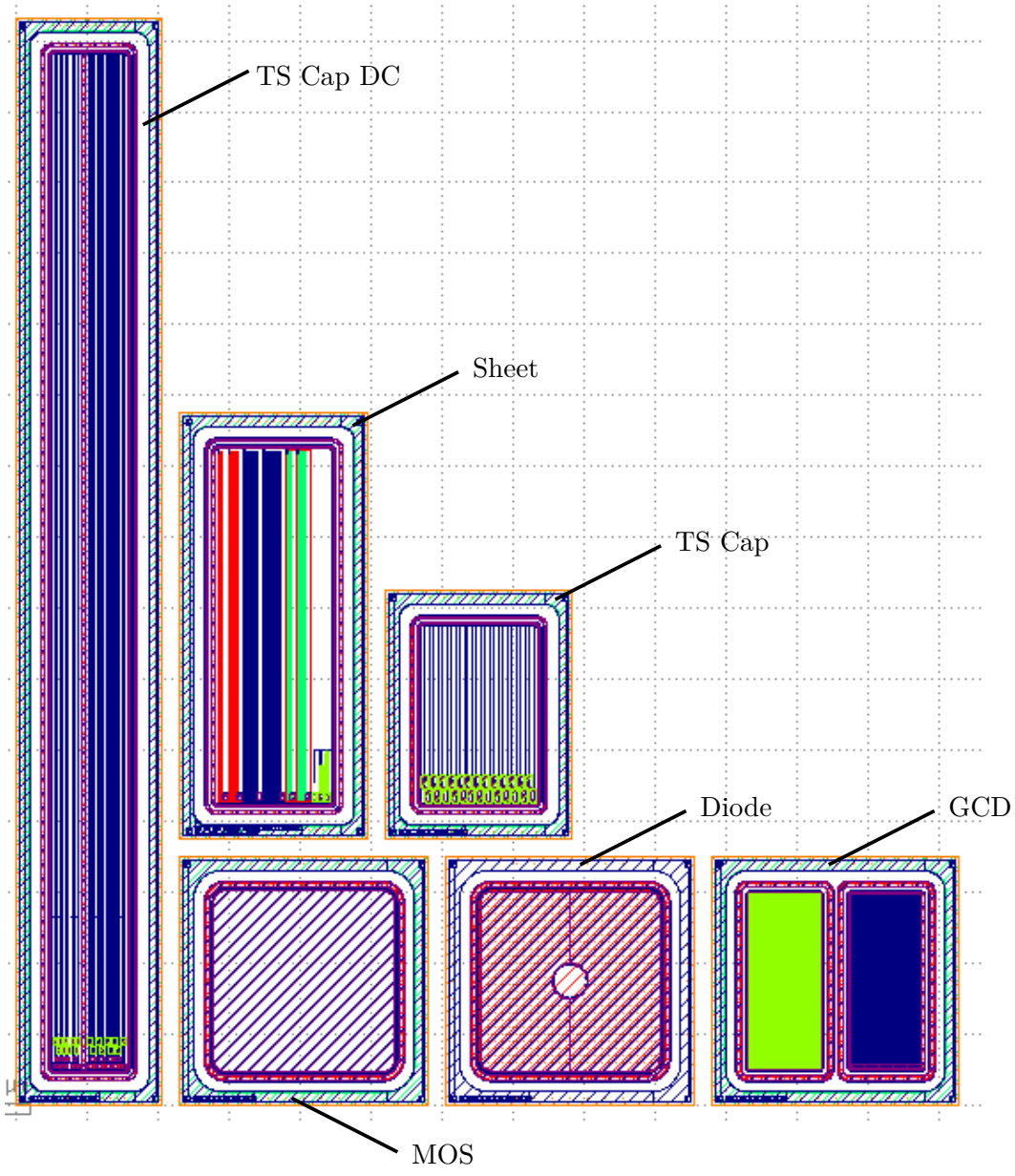

Figure 6.5.: The test structures on the p-side correspond to the ones used in the quality assurance of the CMS experiment.

n-side test structures

The test structures on the n-side implement the same functionality as on the p-side, but with switched front- and backside implantations (see figure 6.6). The structured side is now the n-side, while the opposite side of the wafer is p-type doped and coated with aluminium, which resembles the situation of a single-sided n-in-n silicon microstrip sensor. Note that there are some subtle differences between the initial wafer design and the final design:

Diode: The diode electrode, the guard ring and the edge ring all are implemented as n-type implantation. The initial design foresees p-stop rings to separate them, in the final design the p-stop is omitted.

MOS: Similar to the diode, also for the MOS structure all areas are n-type implanted. Again, the initial design implements p-stops, while the final design doesn't.

Sheet: In the initial design, the sheet structure implements the same meanders as on the p-side, with additional p-stop implants to insulate active area, guard ring, edge ring and the n-type meanders. The final design omits the p-stops and the p-type meanders.

TS Cap: The strips and rings of the TS Cap structure are now n-type and surrounded by p-stop implants. There is no difference between initial and final design.

TS Cap DC: Like for the TS Cap structure, also here strips and rings are n-type, insulated by p-stop implants. Again, initial and final design are identical.

The GCDs on the n-side all use n-type rings and are identical for initial and final design. They are implemented in three different variants:

GCD1: The first variant implements an n-type electrode gated by polysilicon. There is an additional p-type implantation under the polysilicon gate. The second variant uses the same implants, but aluminium as gate material. The rings are insulated by p-stop implantations.

GCD2: The GCD2 structure is identical to the GCD1 structure but omits the p-type implantation under the gate material.

GCD_Inverse: This inverted GCD uses p-type implantation for electrode and guard ring, leaving out the p-stop implantation. The two variants again use polysilicon and aluminium as gate materials.

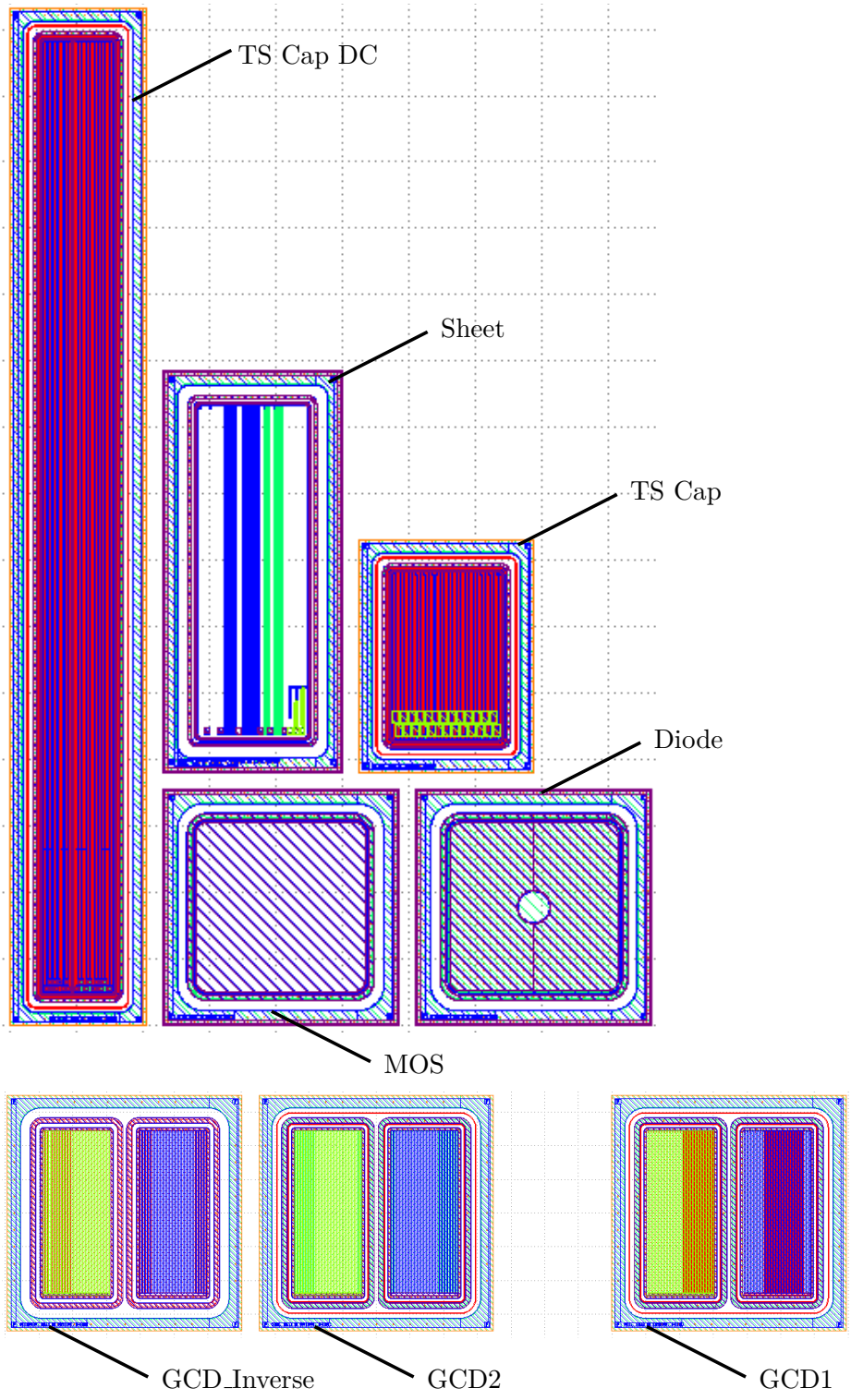

Figure 6.6.: The test structures on the n-side show the same functionality as on the p-side. However, there are small differences between the initial and the final design (shown here), and the GCD is implemented in three different ways.

Part III.

Measurements and test results

In semiconductor device fabrication, channel-stopper or channel-stop (p-stop) is an area in semiconductor devices produced by implantation or diffusion of ions, by growing or patterning the silicon oxide, or other isolation methods in semiconductor material with the primary function to limit the spread of the channel area or to prevent the formation of parasitic channels (inversion layers).

Wikipedia on **Channel-stopper**

7

Optimisation of n-side strip insulation

Whenever n-type implanted areas in silicon are next to areas with a silicon-oxide interface, one has to take special care of the insulation of the n-type structures. As outlined in section 3.5.5, the fixed positive oxide charges attract an electron layer to the surface, which connects to the majority charge carriers in the n-type areas. This electron layer has to be interrupted using one of the methods described in section 4.6.1. On the wafer processed by Micron Semiconductor Ltd. we placed baby sensors specifically designed to investigate different variants of strip insulation methods. We tested baby sensors from three different batches:

1. Batch number 2826: initial p-stop design with coarse geometry variations.
2. Batch number 2825: p-spray blocking method
3. Batch number 2965: updated p-stop design with fine geometry variations

All used sensors are listed in table 7.1. See section 6.2.2 for details about the different implementations of the p-stop blocking method.

Table 7.1.: The tested baby sensors and the module names used in the respective beam tests. The sensor names follow the convention of the Belle II construction database. The batch 2826 implements the initial p-stop design, batch 2825 uses the p-spray blocking method, and batch 2965 features the updated p-stop design. The modules with a capital "I" in the name have only every second strip bonded, yielding a device which resembles a sensor with doubled readout pitch and intermediate strips.

Sensor name	Module name 2010	Module name 2011	Module name 2012
2826-01_BabyQ_comm	TRK1		
2826-01_BabyQ_atoll	TRK2		
2826-01_BabyQ_comb	TRK6	COMB-I-1	
2826-07_BabyQ_comm	DUT3	COMM-IRRAD	
2826-07_BabyQ_atoll		ATOLL-I-1	
2826-07_BabyQ_comb	GEW		
2826-17_BabyQ_comm		COMM-I-2	
2826-17_BabyQ_atoll		ATOLL-I-2	
2826-17_BabyQ_comb		COMB-I-2	
2826-19_BabyQ_comm	TRK7	COMM-I-1	
2826-19_BabyQ_atoll	DUT5		
2826-19_BabyQ_comb	DUT4	COMB-IRRAD	
2825-05_BabyQ_baby3		SPRAY-1	SPRAY-1
2825-05_BabyQ_baby4		SPRAY-2	SPRAY-2
2825-15_BabyQ_baby2		SPRAY-I-1	SPRAY-I-1
2825-15_BabyQ_baby3		SPRAY-I-2	SPRAY-I-2
2965-10_BabyQ_comm			COMM-1
2965-10_BabyQ_atoll			ATOLL-I-1
2965-10_BabyQ_comb			COMB-1
2965-13_BabyQ_atoll			ATOLL-I-2
2965-14_BabyQ_comm			COMM-2
2965-14_BabyQ_atoll			ATOLL-1
2965-14_BabyQ_comb			COMB-2
2965-16_BabyQ_comm			COMM-I-1
2965-16_BabyQ_comb			COMB-I-1
2965-17_BabyQ_comm			COMM-I-2
2965-17_BabyQ_atoll			ATOLL-2
2965-17_BabyQ_comb			COMB-I-2

7.1. Electrical characterisation of the test sensors

7.1.1. Measurement equipment and setup

The electrical characterisation took place in the QTC[1] at the Institute of High Energy Physics in Vienna [37], using the following equipment (see figure 7.1):

- SMU[2] 1: Keithley 237
- SMU 2: Keithley 2410
- Electrometer: Keithley 6514
- Matrix Switching System: Keithley 7001 with two 7153 matrix cards with 5×4 contacts each (see figure 7.4)
- LCR[3] meter: Agilent 4284A, decoupled from high DC voltages by a decoupling box
- Temperature and humidity monitoring: TRHX[4] system
- Light tight measurement box made in-house, equipped with an xyz-table, a microscope, a cold light source, and feedthroughs for vacuum and dry air (see figure 7.2)
- Jig for contacting the bottom-side bias ring (see figure 7.3)
- Measurement control is done using LabView communicating through a IEEE488 (GPIB[5]) interface bus.
- The air condition keeps the clean room temperature and humidity at 23 °C and 30%.

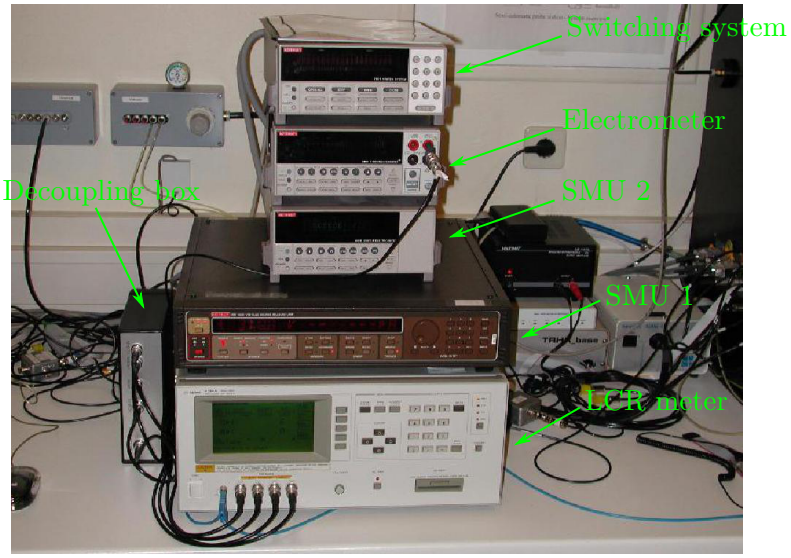

Figure 7.1.: The laboratory equipment consists of a switching system, two SMUs, an electrometer and an LCR meter protected by a decoupling box.

[1] QTC: Quality Test Center
[2] SMU: Source Measurement Unit
[3] LCR: Inductance (L), capacitance (C), resistance (R)
[4] TRHX: Temperature and Relative Humidity eXtended [48]
[5] GPIB: General Purpose Interface Bus

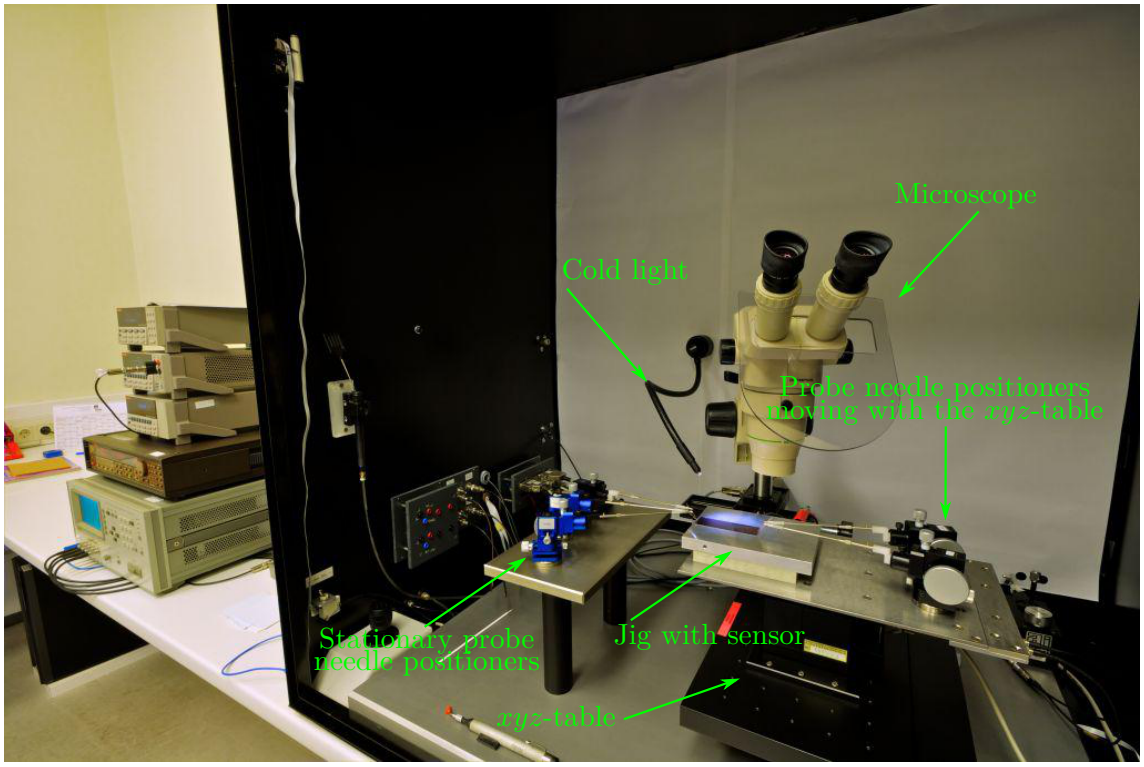

Figure 7.2.: The QTC consists of a light-tight box housing an xyz-table for jigs and probe needle positioners, a microscope, a cold light source, a fixed table for stationary positioners, and feedthroughs for cables, vacuum and dry air.

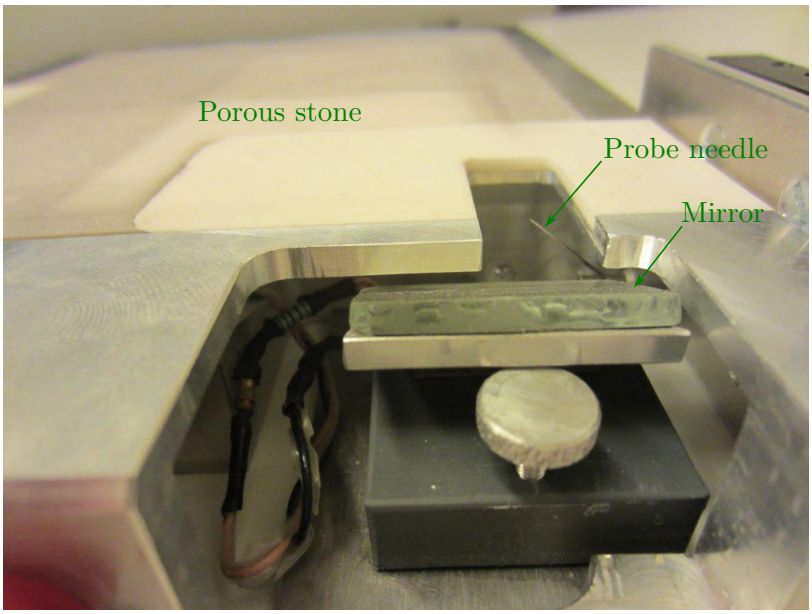

Figure 7.3.: The jig for testing DSSDs features an embedded needle, which can be moved in 3D using micrometer screws. The positioning of this needle is monitored through the microscope via a mirror and illuminated by a white LED. The DSSD is held in place by vacuum applied to a reservoir under a surface of porous stone.

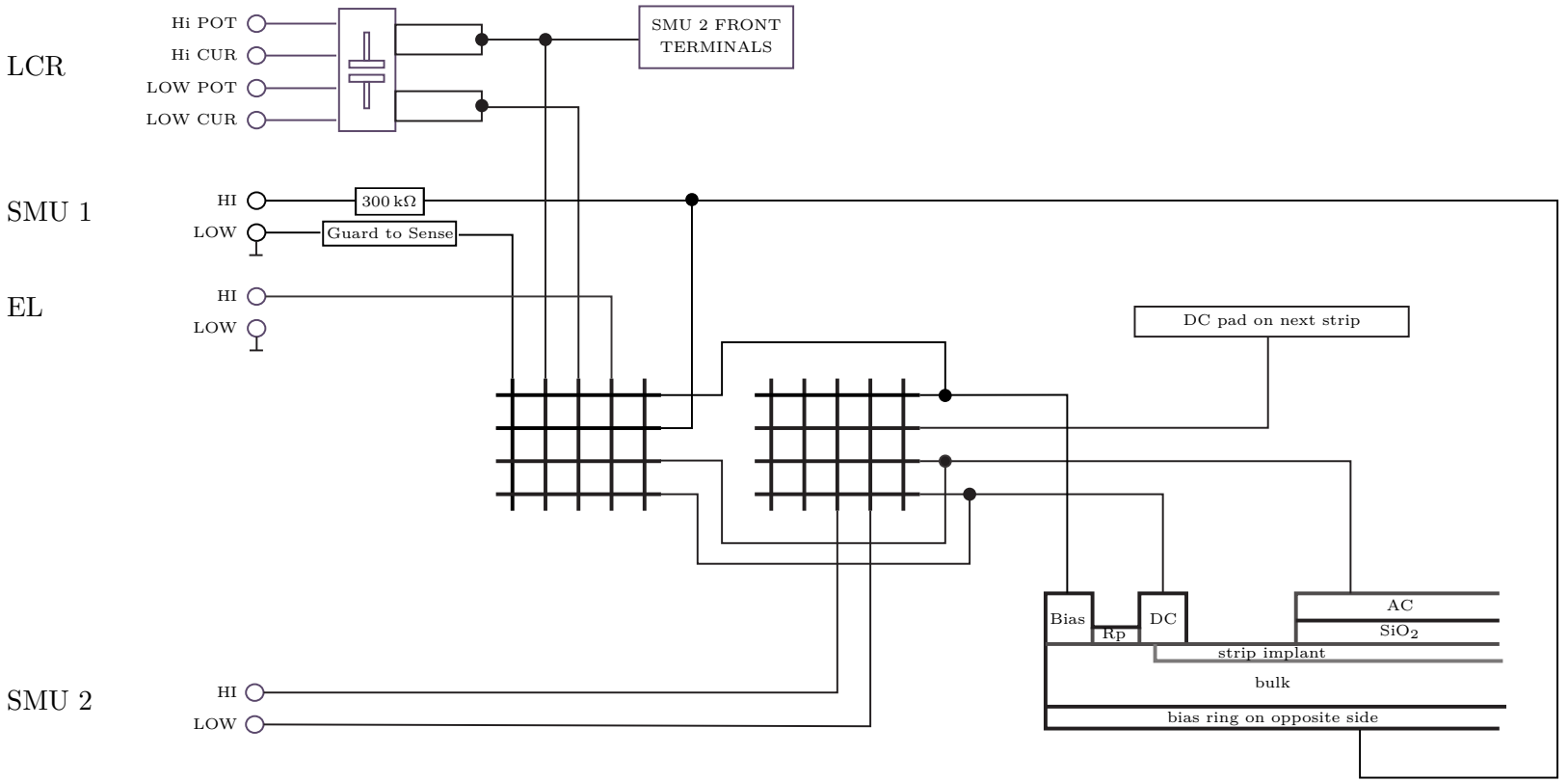

Figure 7.4.: The matrix switching system connects the measurement devices (left) to the probe needles contacting the contact pads on the DSSD (right) in a flexible and automatically controllable way.

7.1.2. Global measurements

The most fundamental quality characteristics of a silicon microstrip sensor are the IV- and CV-curves. As derived in section 3.5.1 these curves allow the determination of the full depletion voltage and the total dark current at the operating point. For these measurements, the SMU 1 applies a reverse bias voltage ramp between the bias rings of p-side and n-side while measuring the total dark current. The LCR meter measures the total capacitance in parallel. Figures 7.5 and 7.6 show these curves for all baby sensors used in this study.

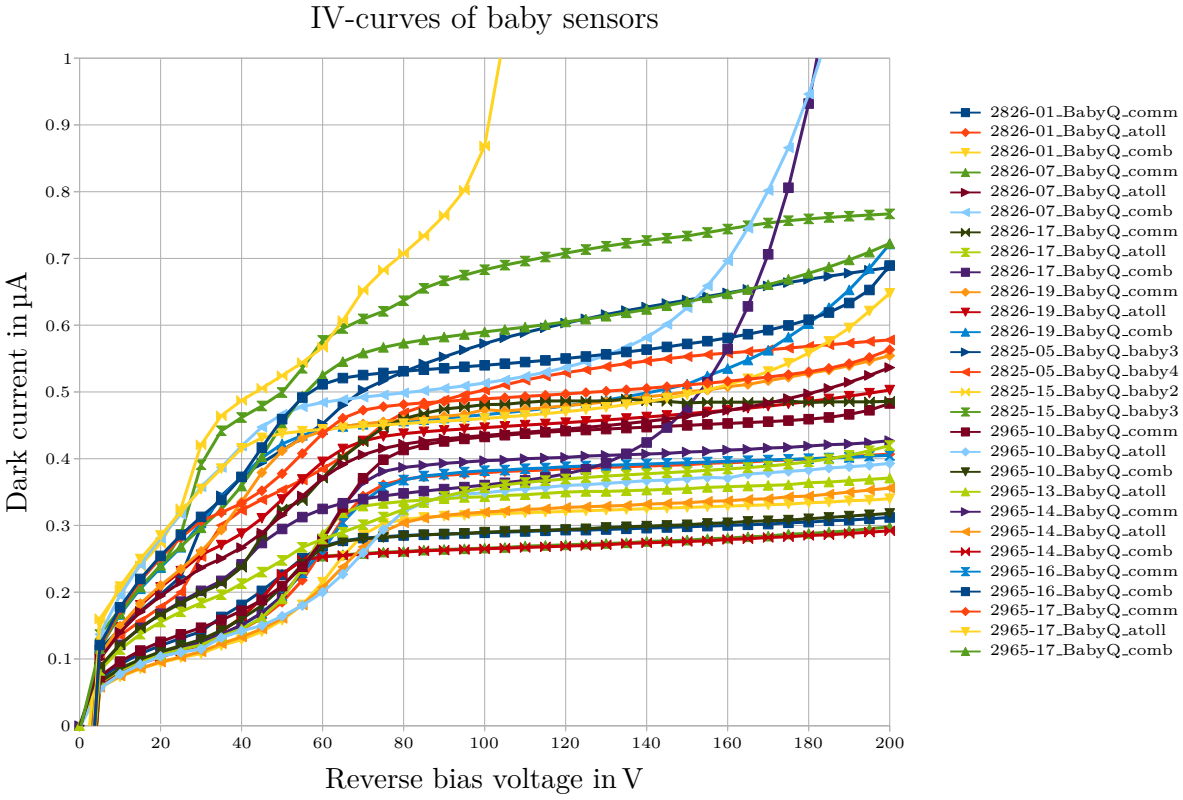

Figure 7.5.: Summary of IV-curves of all used baby sensors. The p-spray sensor 2825-15_BabyQ_baby2 (yellow, steep inclination) shows imperfect high-voltage stability, but was used anyway due to the small number of available p-spray sensors.

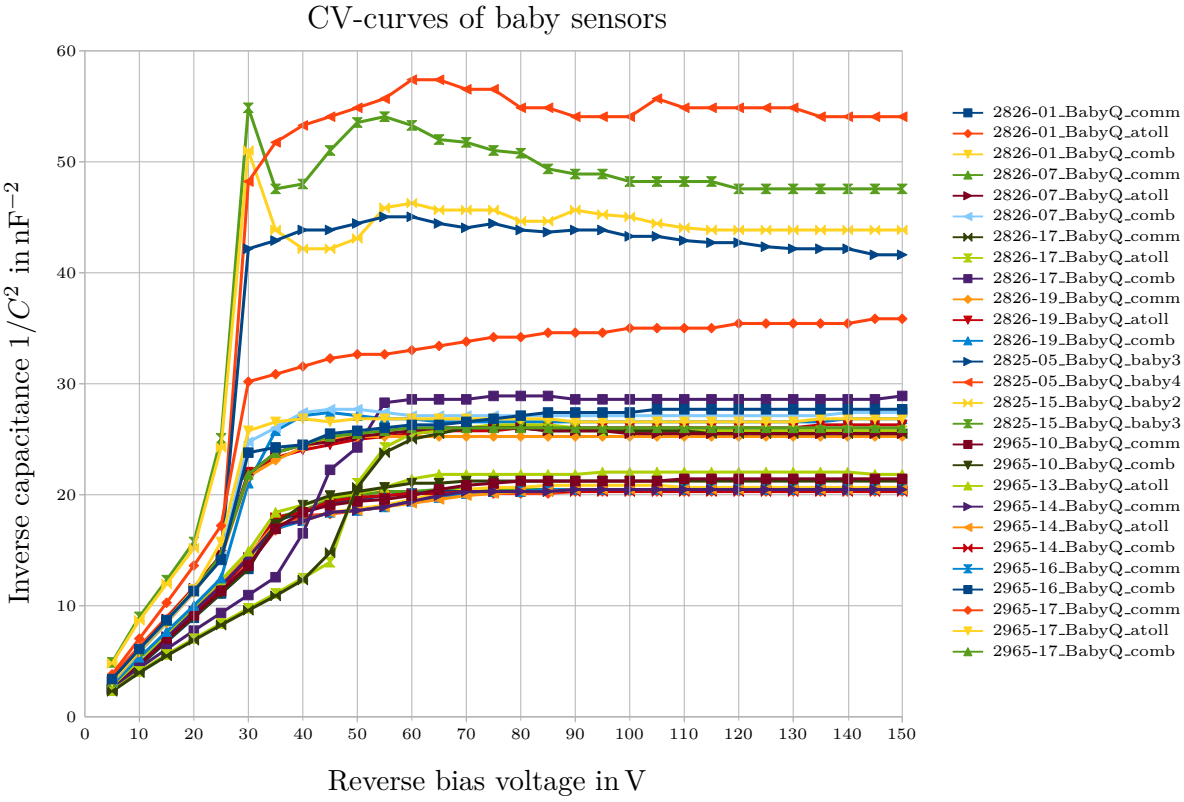

Figure 7.6.: Summary of CV-curves of all used baby sensors. The LCR meter measures the total capacitance of the p-n-junction at a frequency of 1 kHz. The capacitance measurement of the sensor 2965-10_BabyQ_atoll failed and is not shown here. Note that the capacitance of the p-spray sensors from batch 2825 is smaller resulting in a larger $1/C^2$ value (upper four curves). This indicates a slightly reduced active thickness due to the deep p-spray implantation. Also the sensors from the initial prototype batch 2826 and the updated prototype batch 2965 are grouped at slightly different capacitance values. The calculated nominal capacitance assuming a depletion thickness of 300 µm is 0.233 nF, corresponding to $1/C^2 = 18.4\,\mathrm{nF}^{-2}$.

7.1.3. Strip scans

For detailed investigation of silicon microstrip sensors a number of quantities is measured on every single strip of the sensor. To do so, the sensor is placed on the automatic xyz-table and the sensor's coordinate system is aligned to the table's coordinate system by software. After alignment, the pads of each strip can be contacted by the probe needles by first lowering the table, moving to the desired strip, and raising the table again. By default, the following quantities are measured on each strip:

- Dark current I_{strip} (figure 7.7): Each strip receives a portion of the sensor's total bulk dark current. The probe needle contacted to the strip's DC pad is connected to the electrometer. A high value of I_{strip} suggests a faulty strip.

- Bias resistor R_{poly} (figure 7.8): The specified value of the bias resistor is tested by the electrometer using the DC pad contact and the bias ring contact, while correcting the measurement for high strip currents.
- Coupling capacitance C_{ac} (figure 7.9): The value of the coupling capacitance is measured with three needles: one on the strip's AC pad, and two on the strip's and its neighbour's DC pads, connected together. Both contacts are connected to the LCR meter, which performs the capacitance measurement at a frequency of 100 Hz. A pinhole manifests itself in a very low capacitance value (i.e. a short), while the contact to the neighbouring strip's DC pad allows detection of a short between the aluminium strips, which produces a doubled capacitance value.
- Current across the coupling dielectric I_{diel} (figure 7.10): The SMU 2 applies a potential difference of 10 V between the strip's DC pad and AC pad, while the current is monitored. A high current again points to a pinhole.

See [37] for a more thorough description of the default measurements. The strip scans are only carried out on the n-side of the baby sensors. Note that only one sensor from batch 2826 was measured on a strip-by-strip basis.

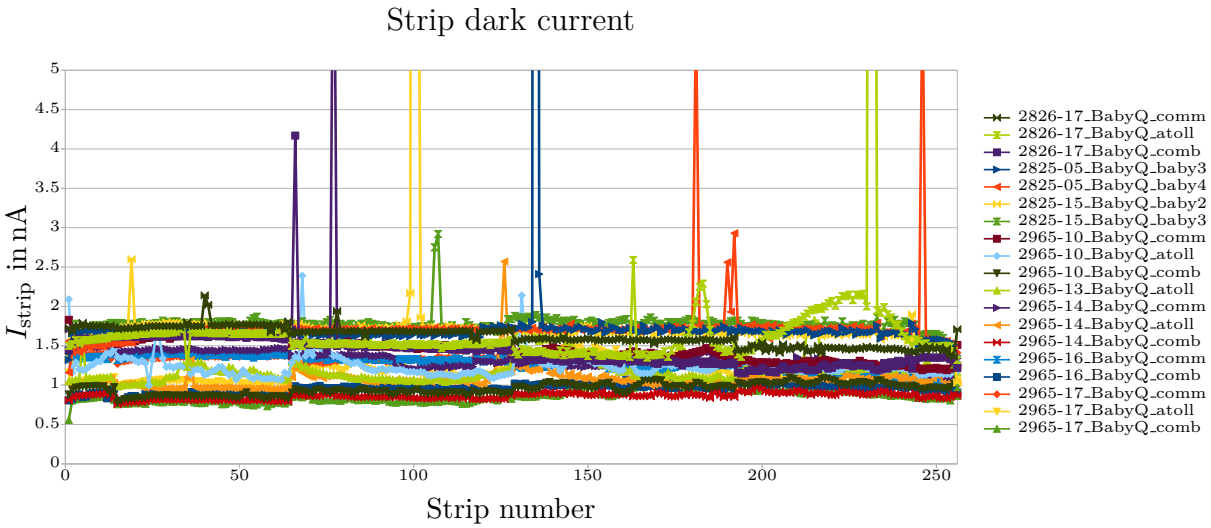

Figure 7.7.: Dark current I_{strip} as function of the strip number for the baby sensors. One can easily see a few divergent measurements (small spikes) and a few faulty strips (large spikes above the displayed range). The sensors from all batches have similar strip dark currents, and the p-stop sensors (batches 2826 and 2965) show steps at the edges of the different p-stop geometries (see section 6.2.2) at the strip numbers 64, 128 and 192.

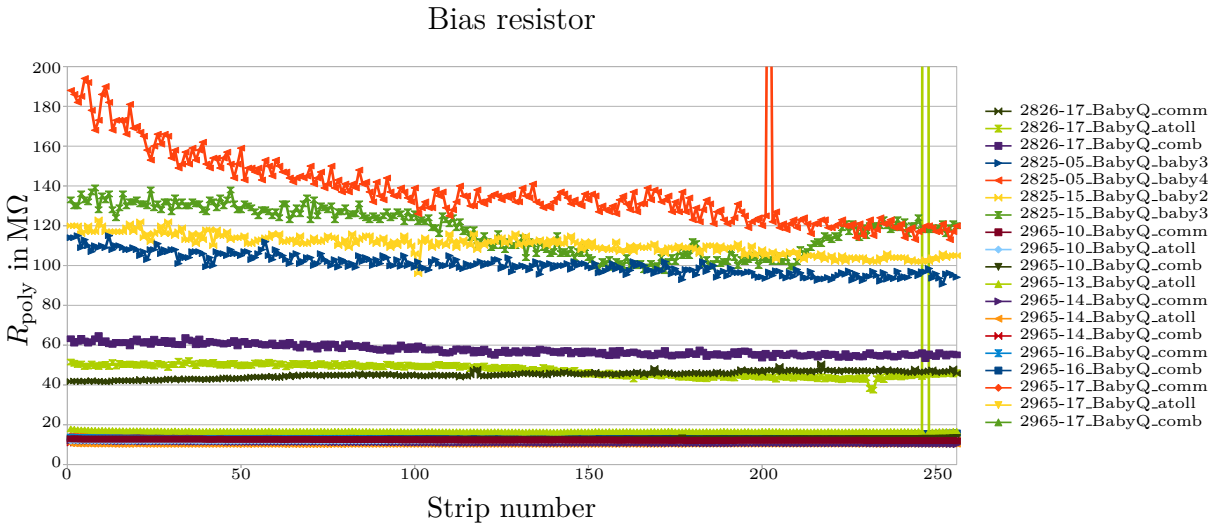

Figure 7.8.: Bias resistor R_{poly} as function of the strip number for the baby sensors, corrected for high strip currents I_{strip}. One can easily see two interrupted resistors. The three batches show different values for the bias resistor: batch 2826 has $R_{poly} \approx 40\,\mathrm{M\Omega}$, batch 2825 shows $R_{poly} \approx 120\,\mathrm{M\Omega}$, and the final prototype batch 2965 implements the required value of $R_{poly} \approx 15\,\mathrm{M\Omega}$.

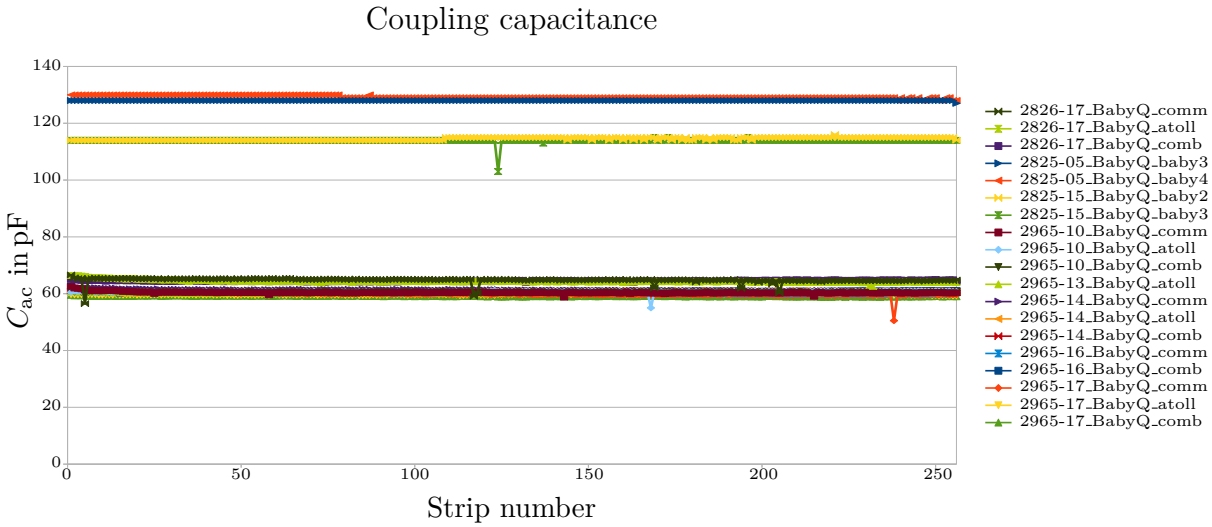

Figure 7.9.: Coupling capacitance C_{ac} as function of the strip number for the baby sensors, measured at a frequency of 100 Hz. One can easily see that the capacitance i.e. the thickness of the coupling oxide is different for the p-spray sensors from batch 2825, but equivalent for the sensors from the same wafer. The course of the capacitance shows no abnormalities apart from a few slightly divergent measurements. The measurements correspond to an average coupling oxide thickness of around 360 nm.

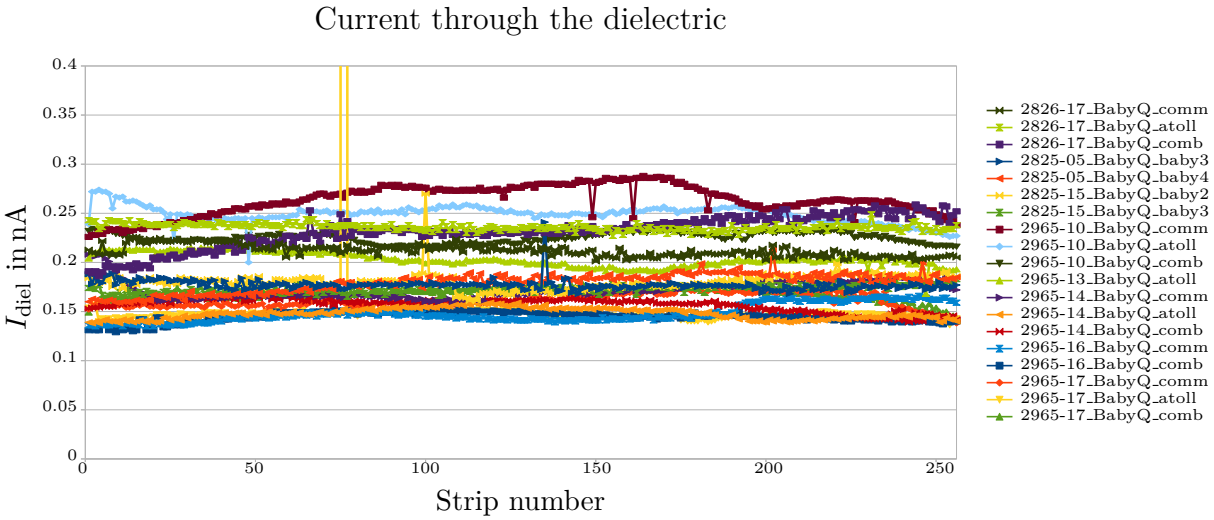

Figure 7.10.: Current through the dielectric I_{diel} as function of the strip number for the baby sensors, when applying a potential difference of 10 V to the coupling capacitance. One can easily see that one strip shows a pinhole.

7.2. Beam test setup

The baby sensors listed in table 7.1 were assembled in module frames (see figure 7.11 for a picture) and taken to CERN to be tested in the particle beam. These beam tests were conducted in three consecutive years from 2010 to 2012, but always with the same beam setup:

- Accelerator: CERN SPS[6]
- Experimental hall: North Area Experimental Hall, building 887 (EHN1), Prevéssin site
- Beam line: H6
- Beam momentum: 120 GeV/c
- Beam composition: Hadrons, with pions being the major component
- Beam spot dimensions: approximately 1 cm high and 2 cm wide

Table 7.1 gives an overview over which sensors were used in the different beam tests:

2010: Only sensors from the first batch 2826 were used. Three modules (one per p-stop pattern) were chosen to act as DUT[7]s. The other modules were used as a kind of beam telescope to monitor the position of the beam spot. The DUTs were irradiated with a ^{60}Co gamma source (see section 7.2.1). The DUTs were tested before and after irradiation in the exact same setup. See section 7.3 for details and results.

2011: Some of the modules from 2010 were reused, while some new ones were added to have two modules per p-stop pattern for redundancy. For all p-stop modules only every

[6]SPS: Super Proton Synchrotron
[7]DUT: Device Under Test

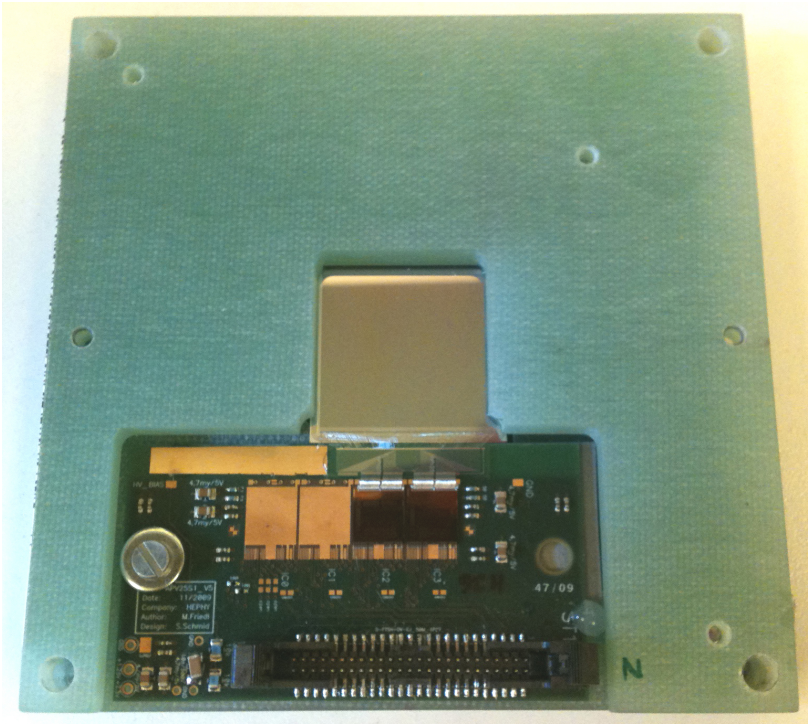

Figure 7.11.: A beam test module holding a baby sensor is opened to reveal the sensor's n-side and the front-end readout electronics (i.e. the hybrid board housing the APV25 chips). The strips of the sensor are connected to the APV25 chips via a glass pitch adapter.

second strip was connected to the readout electronics. This yields a device which resembles a sensor with doubled readout pitch and intermediate strips. Moreover, four modules with p-spray sensors from batch 2825 were constructed, two of which had only every second strip bonded. That year no irradiation was performed. All used modules were DUTs. See section 7.3 for details and results.

2012: The measurements performed with the sensors from the initial batch were repeated with the sensors from the updated prototype batch 2965. For this batch, the geometry variations within the p-stop patterns are finer than for the initial batch 2826 (see section 6.2.2). We prepared four modules per p-stop pattern, for two of which again only every second strip was bonded. In addition, the four p-spray modules from the year before were reused. All modules were taken to a gamma irradiation (see section 7.2.1) and tested before and after irradiation in the exact same setup. All used modules were DUTs. See section 7.4 for details and results.

Unless otherwise noted, all sensors are operated uncooled at ambient temperature of about 23 °C, and under a reverse bias voltage of 100 V.

7.2.1. Gamma irradiation

For gamma irradiation we took the sensor modules to SCK•CEN[8] in Mol, Belgium [49]. This facility provides different underwater ^{60}Co gamma sources:

- BRIGITTE[9]: This small but high intensity source was used for irradiation in 2010. Figure 7.12a shows the DUTs (and other items) at the point of being inserted into BRIGITTE's waterproof container. We irradiated the sensors during one night with the high dose rate of 25 kGy/h to a total dose of about 700 kGy. This heated the modules up to about 100 °C.
- RITA[10]: This large and low intensity source was used for irradiation in 2012. Figure 7.12b shows the DUTs (and other items) at the point of being inserted into RITA's waterproof container. We irradiated the sensors during one week with the low dose rate of 0.6 kGy/h to a total dose of about 100 kGy. This ensures that the sensors essentially remain at ambient temperature, and the induced effects are due to irradiation only.

While being irradiated, all devices were held under a reverse bias voltage of 100 V to avoid chargeup. We did not perform dosimetry, so the total doses are estimates based on the dose rate values provided by SCK•CEN and the time of exposure.

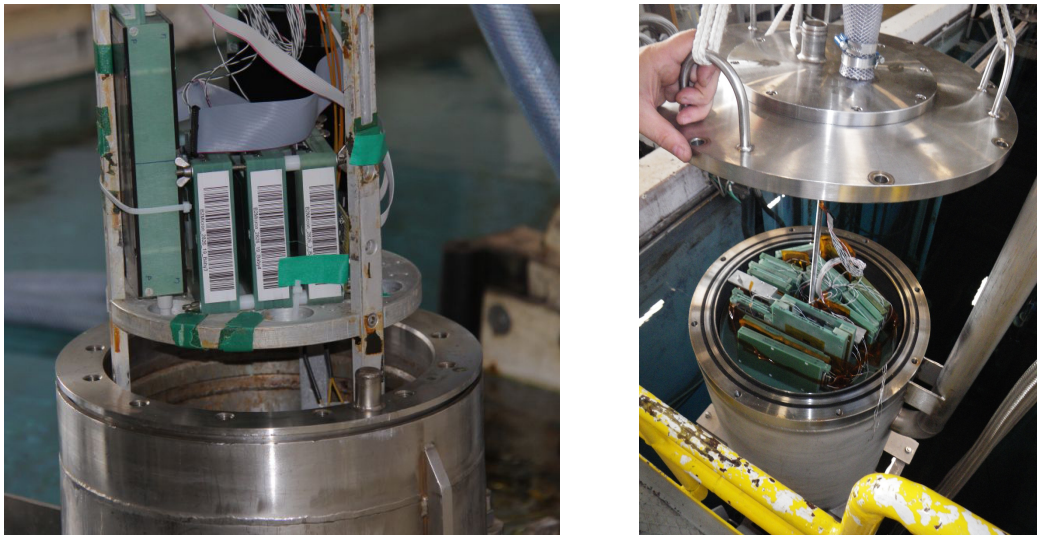

(a) BRIGITTE, used in 2010, is small, but provides high dose rates.

(b) RITA, used in 2012, is large and provides low dose rates.

Figure 7.12.: SCK•CEN in Mol, Belgium provides several underwater ^{60}Co gamma sources.

[8] SCK•CEN: StudieCentrum voor Kernenergie • Centre d'Etude de l'énergie Nucléaire
[9] BRIGITTE: Big Radius Installation under Gamma Irradiation for Tailoring and Testing Experiments
[10] RITA: Radio Isotope Test Arrangement

7.2.2. Readout system and triggering

The readout system used in the beam tests is a prototype of the Belle II SVD readout system described in section 2.4.3, which was intended for an intermediate upgrade from the old SVD2 to the never-realised SVD3. The front-end hybrid boards read out the APV25 chips and send the data to the "dock box", which contains one MAMBO[11] and two REBOs[12], each of which can read the data of four hybrid boards. This dock box differs from the junction box of the real readout system in its active components; the junction box will only contain passive electronics to be radiation hard. The data is hereafter sent to the FADC boards housed in a 9U VME crate. At this point the readout chain differs from the one presented in section 2.4.3, because the data are directly sent to a prototype DAQ software instead of the FTB and DATCON units.

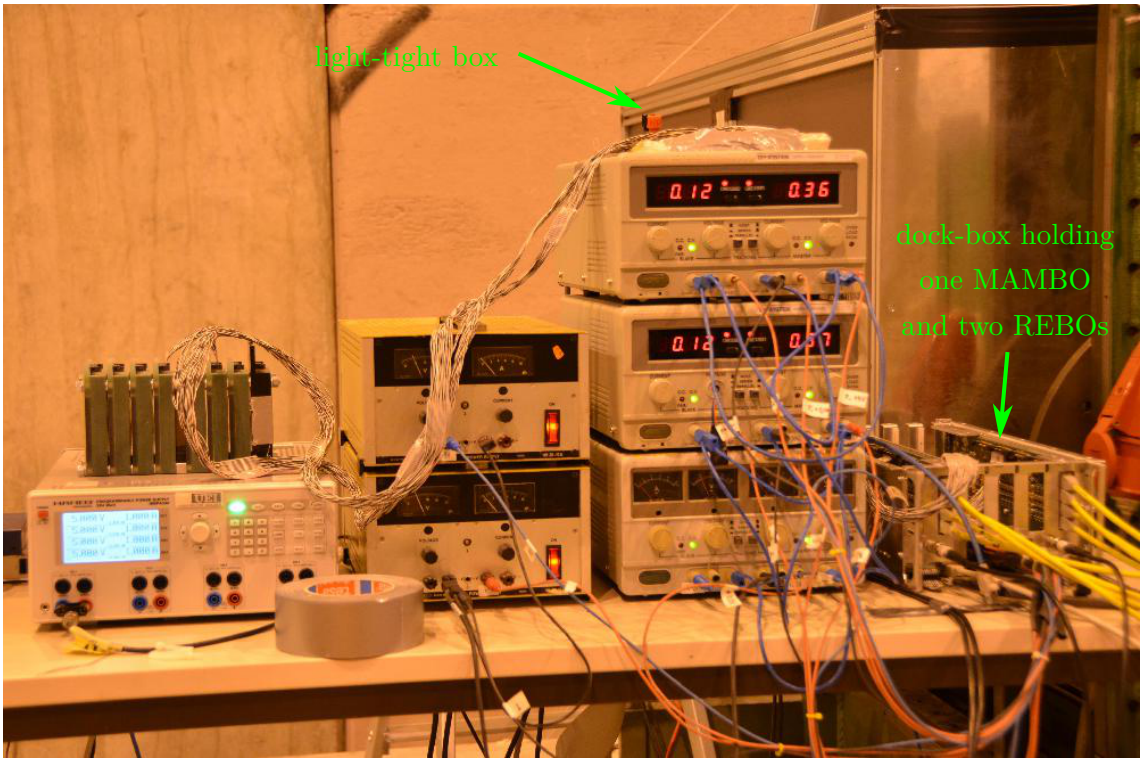

Figure 7.13.: The readout system preprocesses the data from the front-end hybrids (inside the light-tight box) in the dock box and transfers them further to the FADC unit. The power supplies feed power to the dock box and to the front-end electronics.

In 2010, we used the EUDET[13] telescope's TLU[14] for triggering, which picks up signals from two scintillators (see figure 7.17b). From 2011 on, we generated the triggers ourselves. To do so, we used a single scintillator with two attached photomultipliers in a light-tight

[11] MAMBO: Mother (MAMa) BOard
[12] REBO: REpeater BOards
[13] EUDET: Detector R&D towards the International Linear Collider, a project supported by the European Union in the 6^{th} Framework Programme (FP6) structuring the European Research Area
[14] TLU: Trigger Logic Unit

box (see figure 7.14a) and a coincidence and shaping wiring realised with NIM[15] units (see figure 7.14b).

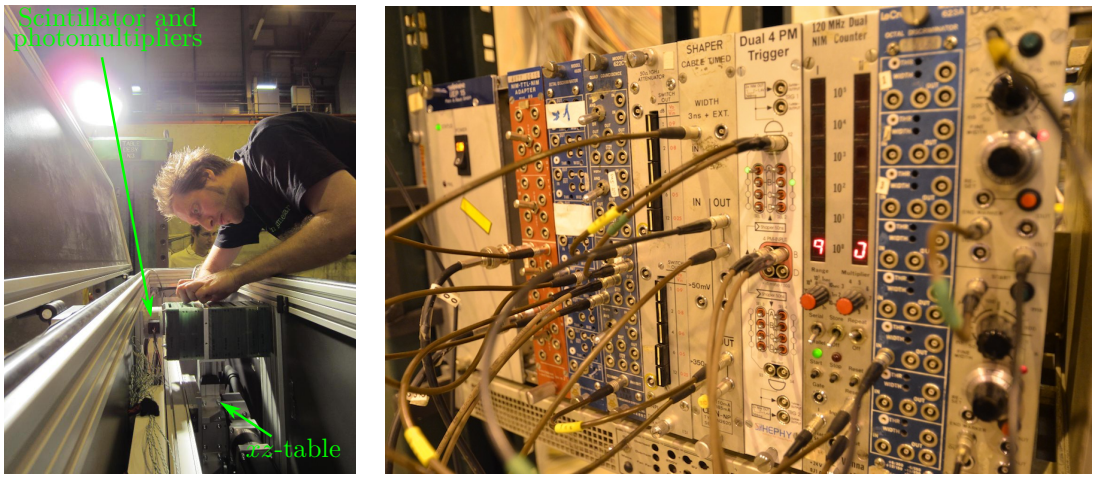

(a) Light-tight box. **(b)** The trigger logic is implemented in form of NIM units.

Figure 7.14.: In the beam tests 2011 and 2012 we used a triggering system built in-house. The light-tight box contains an xz-table onto which the modules are mounted, and a scintillator with photomultipliers for triggering.

With the maximum number of connected front-end hybrids the VME bus can handle a data rate in the order of 200 triggers per second. According to the SPS supercycle the north area experimental hall is served with beam for about ten seconds every minute. Acquiring 100000 events therefore takes about an hour.

7.2.3. Definition of the measured observables

Clustering

A strip counts as "hit" and contributes to a cluster if the following criteria are met:

- Seed strip threshold: One strip needs a minimum signal of five times its single strip noise.
- Neighbour strip threshold: Adjacent strips contribute to the cluster as long as their signals are at least three times as high as their respective single strip noises.
- Cluster threshold: The total cluster signal has to be at least five times as high as the total cluster noise. This eliminates wide-spread clusters originating from particles hitting the sensor under a very large incident angle.

The number of strips contributing to a cluster is called cluster width, abbreviated as CLW[16]. In our analysis we focus on events with CLW 2 for the following reasons:

[15] NIM: Nuclear Instrumentation Module
[16] CLW: CLuster Width

- Events with CLW 1 are rare in real-life detectors, because they only are created by particles hitting the sensor under normal incidence. This, however, is the standard case for a beam test, as is already outlined in section 4.4.
- With the baby sensors we investigate the strip insulation from one strip to its neighbours. It is therefore natural to consider events with more than one hit strips.

Cluster signal

When readout is triggered, the APV25 chip takes six samples of every readout channel's shaped waveform (see figure 4.5) to determine the peak signal and the precise hit time. The cluster signal for each sample is calculated by summing up the respective samples of all neighbouring strips above threshold (i.e. strips contributing to the cluster). This procedure gives the cluster signal, which enters the calculation of the SNR, and not the single strip signal! These samples are fitted with a reference waveform, yielding amplitude and timing (see figure 7.15).

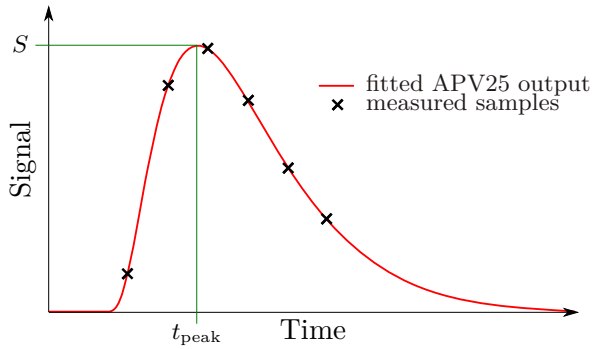

Figure 7.15.: The shaped signal curve is rastered in time by taking six samples, and is hereafter fitted with a reference waveform, yielding the exact time t_{peak} of the maximum in ns. The amplitude of this peak is the signal S seen by the strip in ADC counts.

The reference waveform is obtained by performing an internal calibration scan of the APV25 chip. The cluster signal values (i.e. the amplitudes of the waveforms) are distributed according to a Landau probability density function convoluted with a Gaussian probability density function. The Landau part describes the distribution of energy deposition by ionisation, whereas the Gaussian part accounts for fluctuations of the charge cloud by diffusion as well as for electronic noise. We fit a convolution of a Landau PDF[17] with a Gaussian PDF to a histogram filled with the cluster signal values of sets of interesting strips. There is a separate histogram with its own fit for every cluster width. The free parameters of the fit are the MPV and the width of the Landau PDF, the width of the Gaussian PDF and the amplitude of the overall (convoluted) PDF. For comparisons of signal levels we use the MPV given by this fit. The MPV is estimated with a typical fit accuracy of 50 electrons.

[17] PDF: Probability Density Function

Strip noise and cluster noise

When starting a data taking run, we first acquire 600 readings with random triggers and no beam. This is to ensure that the sensor sees no physical signal at the time of the trigger. The mean value of the first 200 readings of each strip gives the pedestal offset of the individual strips, which is hereafter subtracted from all following readings ("pedestal subtraction"). For each one of the next 200 readings the mean value of blocks of 32 strips is calculated, which gives the common mode noise of the considered reading. For each strip a first approximate noise value is calculated as the RMS[18] value of these 200 readings, after subtracting from each reading the respective common mode noise ("common mode correction"). From now on, strips with a high value of this approximate noise are omitted when calculating common mode noise. Finally, the last 200 readings are histogrammed for each strip after pedestal subtraction and common mode correction, and the resulting distribution is fitted with a Gaussian PDF. The standard deviation of this Gaussian is the single strip noise, whereas the cluster noise is hereafter calculated according to the denominator in equation 7.1.

For comparisons of the noise levels we histogram the single strip noise values of the set of strips in question, and determine the mean value with a Gaussian fit. This averaged strip noise can be determined with a typical fit accuracy of 10 electrons, which accounts to about 15 electrons for the average cluster noise of 2-strip-clusters.

Signal-to-noise ratio

For judging the detector performance we mainly use the SNR, which directly affects the position accuracy, as is outlined in section 4.4. The SNR for a cluster consisting of n strips reads

$$SNR_n = \frac{S_{\text{cluster}}}{N_{\text{cluster}}} = \frac{\Sigma_{i=1}^{n} S_i}{\sqrt{\Sigma_{i=1}^{n} N_i^2}}, \tag{7.1}$$

where S_i and N_i are signal and noise of strip i inside the cluster, respectively. We only take into account events that created a cluster of exactly two strips, because for these events the effect of charge sharing is clearly visible. For clusters consisting of two strips the SNR is reduced to

$$SNR_{n=2} = \frac{S_1 + S_2}{\sqrt{N_1^2 + N_2^2}}. \tag{7.2}$$

Once cluster signal and cluster noise of a cluster are determined, the SNR is calculated according to equation 7.1. Like the cluster signal values, also the SNR values follow a Landau probability density function convoluted with a Gaussian PDF. An eventual improper sensor design would lower the cluster signal, and/or it would raise the cluster noise. Both effects translate into a shift of the peak of the SNR distribution. That's why we are not

[18] RMS: Root Mean Square

interested in the width of the SNR distribution, but only in its MPV. We fit a convolution of a Landau PDF with a Gaussian PDF to a histogram filled with the cluster SNR values of sets of interesting strips. There is a separate histogram with its own fit for every cluster width. The fit parameters are again the MPV and width of the Landau PDF, the width of the Gaussian PDF and the amplitude. For comparing the detector performance we use the fit results for the MPV of the distribution. All possible fluctuations that would widen the Gaussian part of the distribution are irrelevant for the comparison, because they don't affect the average behaviour of the sensor, i.e. the most probable SNR. The MPV is estimated with a typical fit accuracy of below 0.1.

Relative signal

The most probable signals are usually different for events which create clusters of different widths, as is sketched in figure 7.16. This difference is a measure of the charge collection efficiency CCE. To be independent of the calibration of the signal measurement (see next section) the relative signal is defined as the ratio of the most probable signals of 2-strip-clusters (numerator) and 1-strip-clusters (denominator). Using error propagation we can assume an accuracy of about 1%.

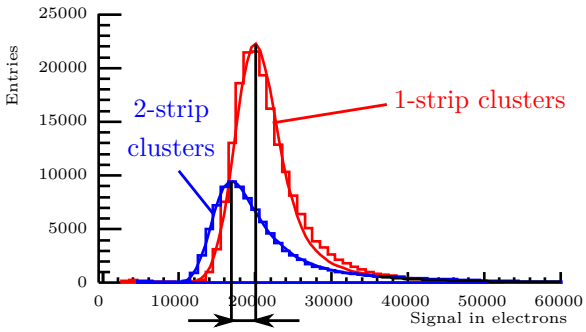

Figure 7.16.: Definition of the relative signal: The signal distribution follows a Landau probability density function convoluted with a Gaussian PDF, with different values of the most probable signal for events with one and two strips. The relative signal is the ratio between the 2-strip-cluster most probable signal and the 1-strip-cluster most probable signal, expressed in %.

Calibration of the signal measurement

When triggered, the readout system reads the levels of its input channels in ADC counts. One has to perform a calibration to match these numbers to the physical signal charge. The readout chip injects a calibration pulse on selected strips and measures the system response, which is then used to calculate the number of electrons per ADC count. The calibration pulse nominally corresponds to an injected charge of 22500 electrons [50], which is equivalent to 1 MIP (see section 4.1). This calibration procedure has to deal with some sources of inaccuracy. The height of the calibration pulse can differ from chip to chip, moreover the system response to the calibration pulse can change from channel to channel

due to small differences of the charge injection capacitors and the preamplifiers. Both effects influence the calibrated value of the cluster signal and of the strip noise. The uncertainties of the charge injection capacitors do not carry much weight for the final most probable cluster signal values, because the MPVs represent an average over many input channels. However, the amplitude of the calibration pulse applies to the chip as a whole and does change the MPV of the signal. In contrast, for the SNR all these effects cancel out on an event-by-event basis, making the results comparable. For the relative signal the calibration also cancels out, but not on an event-by-event basis. So, the choice of SNR and relative signal for our comparison is not only a practical one. All effects that alter the gain (and thus calibration) of the readout electronics cancel out for the SNR and the relative signal, so that these quantities can serve properly for judging the sensor performance.

7.3. Beam tests 2010 & 2011

In the beam test 2010 we used baby sensors from the first batch 2826 only. These sensors feature the coarse geometry variations of the p-stop patterns, as is noted in table 6.2. We prepared eight modules, the best working three of them were selected to serve as DUTs. These modules were read out on the n-side. Four others were read out on the p-side and served as beam monitors. One additional badly working module was included as counterweight and read out on the n-side. The exact stack configuration can be found in figure 7.17a. The module stack was placed inside the EUDET telescope (figure 7.17b), which provides precise particle tracking using a total of six planes of silicon pixel sensors. However, we did not use the EUDET data in our analysis. The DUTs were tested in the beam, irradiated to 700 kGy (see section 7.2.1), and tested again in the exact same beam test setup as before. All sensors were operated uncooled at ambient temperature of about 23 °C, with a reverse bias voltage of 100 V applied. In each measurement run we acquired 100000 events and selected events with exactly one 2-strip-cluster, individually for each sensor. This suppresses ambiguous events like particle splashes. The beam spot serves two p-stop geometry zones at once, therefore the results of the geometry zones are based on a data sample of about 10000 events.

In 2011 we expanded these tests to include sensors with the p-spray blocking technique from batch 2825. We prepared four modules in total, two of which had sensors with only every second strip connected to the readout. This mimics a sensor with doubled readout pitch and intermediate strips. Some p-stop modules from 2010 were reused, disconnecting every second strip from the readout electronics, others were newly built, also with only every second strip bonded. Table 7.1 gives an overview of the sensors and modules used in the individual beam tests. The p-stop sensors are assembled to form the so-called “p-stop stack” (see figure 7.18), the p-spray and two remaining irradiated DUTs from 2010 form the “p-spray stack” (see figure 7.19). The p-spray sensors with every strip connected to the readout have been tested in 2011, but are compared to the results of the p-stop sensors from 2010. Although these tests weren’t carried out at the same time, they still were done at the same place with the same readout electronics and the same beam setup, thus establishing comparability.

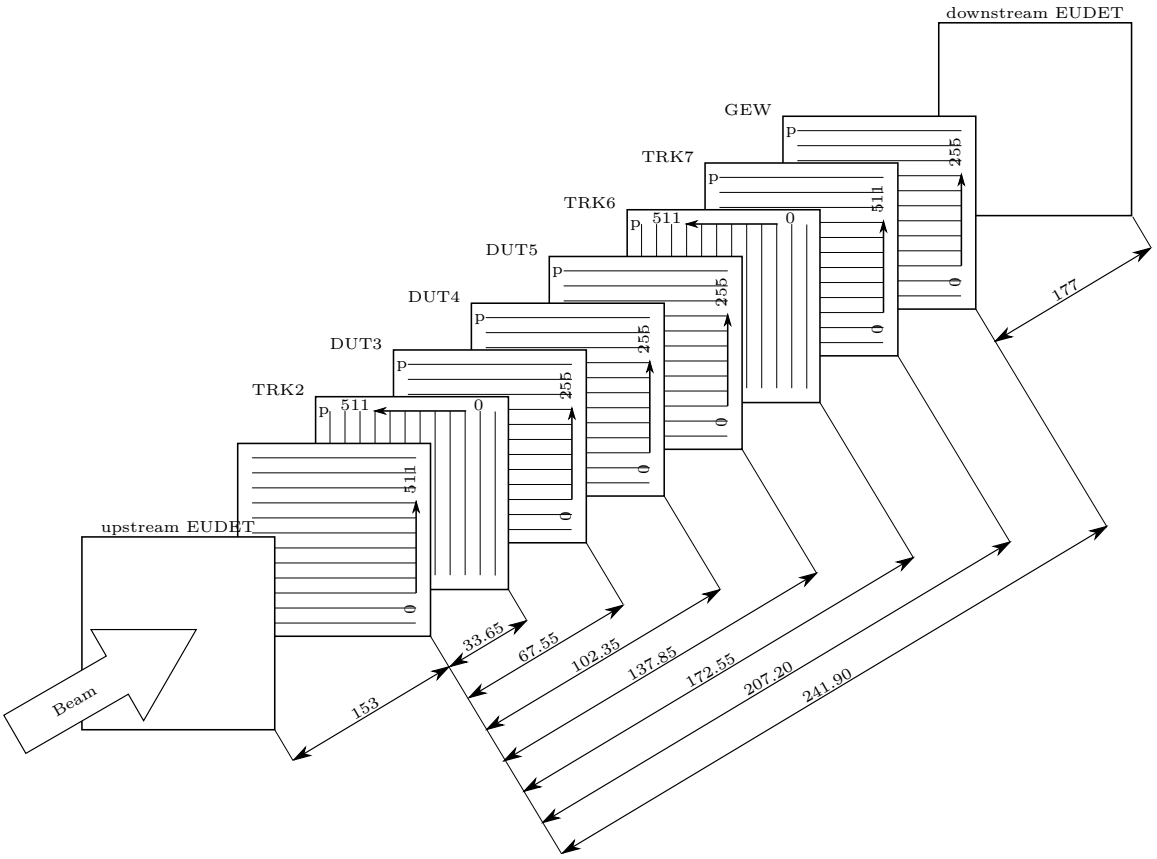

(a) Configuration of the beam test module stack 2010.

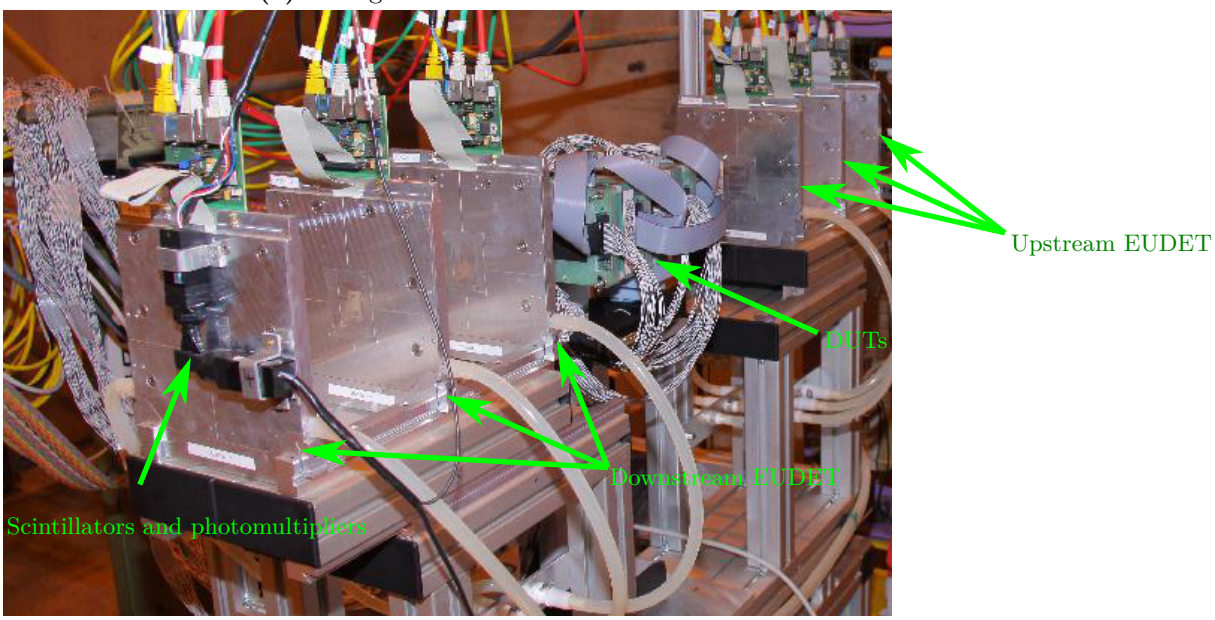

(b) Photo of the stack inside the EUDET telescope. The beam comes from the right

Figure 7.17.: The beam test module stack of 2010 consists of eight modules housing p-stop sensors from batch 2826 with the coarse geometry variations. The stack is placed inside the EUDET telescope. The modules DUT3, DUT4, DUT5 and GEW are read out on the n-side, the others are read out on the p-side to serve as beam monitoring devices. The strip direction of the DUTs is chosen so that the beam spot hits one half of the sensors at a time, serving two p-stop geometry zones at once. All modules face the beam with the p-side, as is indicated by the small "p" in the upper left corner.

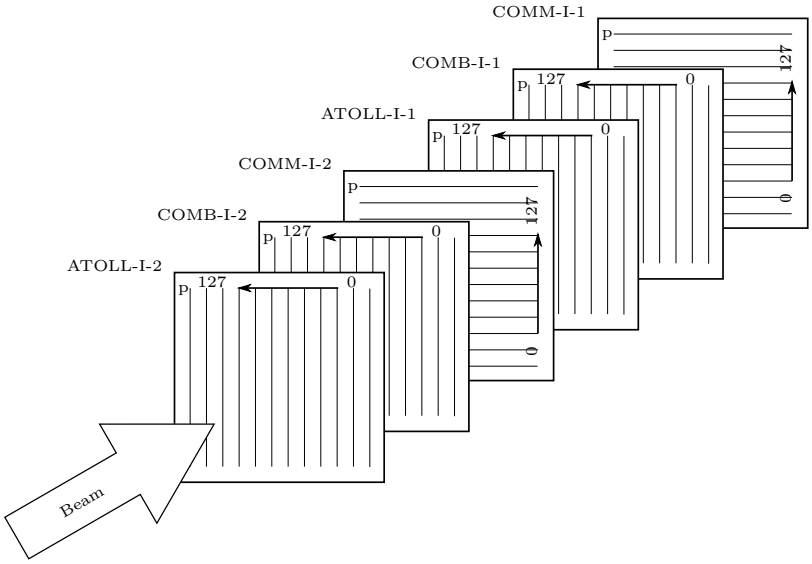

Figure 7.18.: The p-stop module stack of 2011 consists of six modules housing p-stop sensors from batch 2826 with the coarse geometry variations, two modules per p-stop pattern (common, atoll, combined). The strip direction of the DUTs is chosen so that the beam spot serves the same two p-stop geometry zones on all sensors. Note that for the common p-stop sensor the order of p-stop geometry zones is inverted, see table 6.2 for details. All modules have only every second strip of the n-side connected to the readout electronics and face the beam with the p-side.

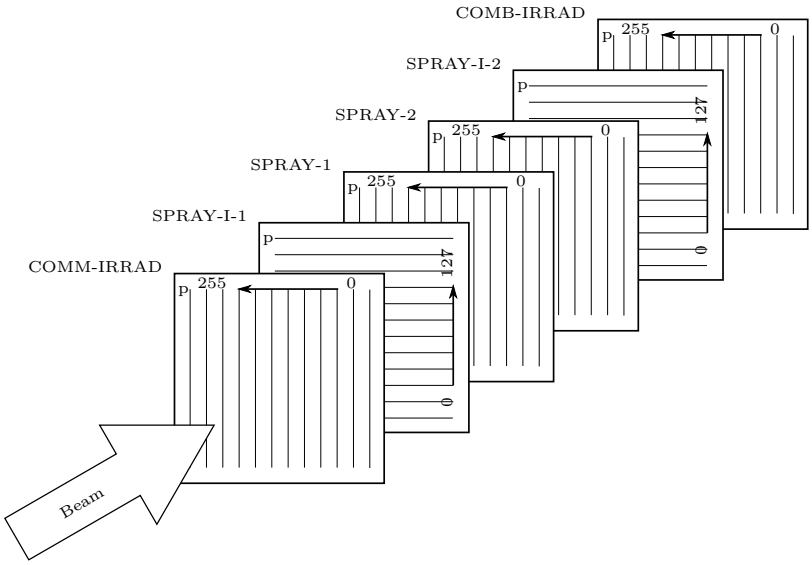

Figure 7.19.: The p-spray module stack of 2011 consists of six modules. The two outer modules are the remaining irradiated ones from the previous beam test, the inner four feature the p-spray blocking method (batch 2825) lacking any geometry variations. Two of the p-spray modules have only every second strip bonded. All modules face the beam with the p-side and are read out on the n-side only.

7.3.1. Results of sensors with every strip connected to the readout

We first inspect the performance of the baby sensors with every strip connected to the readout electronics (100 µm readout pitch, no intermediate strips). Note that the results of the p-stop methods are drawn from one single sensor module per p-stop pattern tested in 2010, while the results of the p-spray method are from the better working module out of two, and averaged among the data from two measurement runs carried out in 2011. Focussing on the better working module minimises the influence of electronic noise of the periphery, inefficient wire bonding, bad strips, etc. The selected module is SPRAY-2.

Comparison of the cluster signal

The top two plots of figure 7.20 show the most probable cluster signal of baby sensors with every strip connected to the readout electronics for clusters of exactly two strips, where the values found in the left plot are before irradiation to 700 kGy and those in the right plot are after irradiation.

We observe that in the unirradiated case the most probable cluster signal of the combined and atoll p-stop geometries are comparable and show little dependence on the geometry dimensions, while for the common p-stop the signal changes significantly with the geometry. In general, a part of the signal is lost when electric field lines do not arrive at the strip implant [46]. For the common p-stop pattern the total p-type implanted area differs depending on the geometry, pushing the field lines towards the strip implant, while for the other p-stop patterns a change in the geometry opens up unimplanted regions between the p-stop implants where field lines can end up. This qualitatively explains the geometry dependence of the cluster signal. The p-spray method shows a performance comparable to the p-stop patterns.

After irradiation the common p-stop shows a very equalized and high cluster signal for all geometries, while the other p-stop patterns show a clear tendency for higher cluster signals when going to the wide geometry. The highest cluster signal is found for the wide atoll p-stop. Note that the p-spray sensors were not irradiated and consequently don't show up in this comparison.

Due to uncertainties of the calibration one has to be careful when comparing the absolute values of the signals. Each p-stop pattern resides on a different sensor, and each sensor is read out by two APV25 chips. Strictly speaking one can only compare p-stop geometries read out by the same chip, i.e. the wide and half-wide geometries and the narrow and half-narrow geometries separately. One can *not* directly compare narrow and wide geometries, nor different p-stop patterns. Especially values before and after irradiation can not be compared due to different readout chip settings. For a direct comparison consider the SNR and the relative signal *only*!

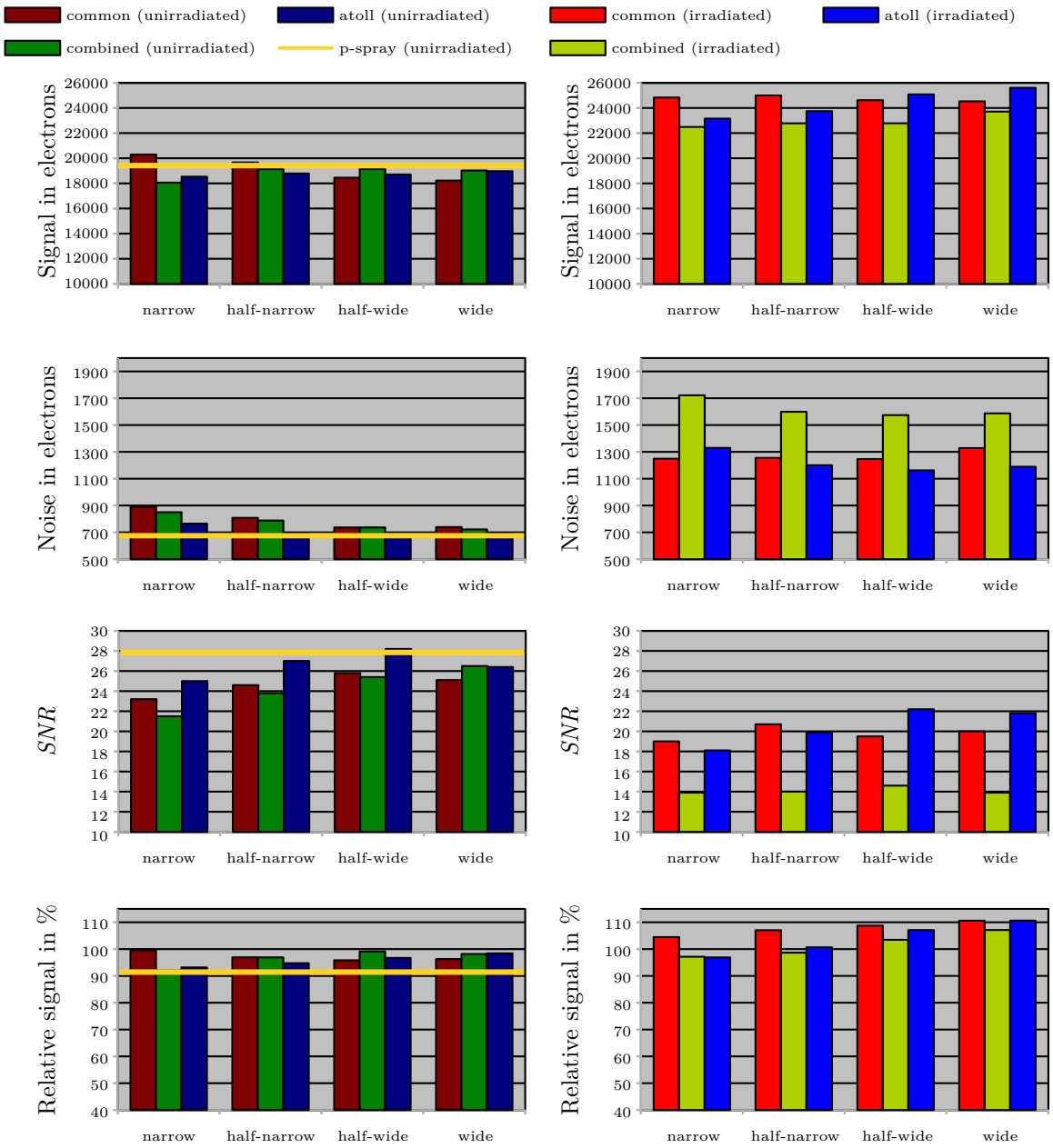

Figure 7.20.: Cluster signal, cluster noise and SNR for 2-strip-clusters, and relative signal of 2-strip-clusters w.r.t. 1-strip-clusters, for sensors from batches 2826 and 2825 with coarse p-stop geometry variations and every strip connected to the readout electronics (100 µm readout pitch, no intermediate strips).
The left plots are before irradiation to 700 kGy, the right ones are after irradiation. The data of the p-stop sensors have been taken in 2010, the data of the p-spray sensors are from 2011, when no irradiation was carried out.
Each measured quantity is the result of a fit to a histogram with about 10000 entries. The data of the p-spray method are the results of the better working module (i.e. the one with lower noise and higher SNR), and the average of two data taking runs. The numerical values can be found in table 7.2.

Table 7.2.: Cluster signal, cluster noise and SNR for 2-strip-clusters, and relative signal of 2-strip-clusters w.r.t. 1-strip-clusters, for sensors from batches 2826 and 2825 with coarse p-stop geometry variations and every strip connected to the readout electronics (100 µm readout pitch, no intermediate strips). Green: best value within one p-stop pattern; Red: overall best value.

		narrow	half-narrow	half-wide	wide
Cluster signal in electrons, $\sigma(S) < 50$ electrons					
Common p-stop	unirradiated	20292	19663	18450	18222
	irradiated	24830	24996	24617	24530
Combined p-stop	unirradiated	18055	19128	19136	19021
	irradiated	22487	22780	22782	23710
Atoll p-stop	unirradiated	18529	18783	18706	18967
	irradiated	23155	23751	25081	25608
p-spray	unirradiated		19543		
Cluster noise in electrons, $\sigma(N) < 15$ electrons					
Common p-stop	unirradiated	891	808	737	739
	irradiated	1249	1255	1246	1328
Combined p-stop	unirradiated	850	788	737	722
	irradiated	1722	1598	1574	1587
Atoll p-stop	unirradiated	765	692	670	696
	irradiated	1330	1200	1162	1189
p-spray	unirradiated		683		
Cluster SNR, $\sigma(SNR) < 0.1$					
Common p-stop	unirradiated	23.2	24.6	25.8	25.1
	irradiated	19.0	20.7	19.5	20.0
Combined p-stop	unirradiated	21.5	23.8	25.4	26.5
	irradiated	13.9	14.0	14.6	13.9
Atoll p-stop	unirradiated	25.0	27.0	28.2	26.4
	irradiated	18.1	19.9	22.2	21.8
p-spray	unirradiated		27.3		
Relative signal in %, $\sigma(S_{\text{rel}}) < 1\%$					
Common p-stop	unirradiated	99.5	96.9	95.8	96.3
	irradiated	104.5	107.0	108.8	110.6
Combined p-stop	unirradiated	92.0	96.9	99.1	98.2
	irradiated	97.1	98.7	103.5	107.1
Atoll p-stop	unirradiated	93.2	94.7	96.7	98.4
	irradiated	96.9	100.7	107.1	110.6
p-spray	unirradiated		92.0		

Comparison of the cluster noise

The second row of plots in figure 7.20 shows the average cluster noise for clusters of exactly two strips $\bar{N}_{n=2} = \sqrt{2}\bar{N}_{\text{strip}}$, where $\bar{N}_{\text{strip}}$ is the noise averaged over all strips of the same group. Again, the left plot is before irradiation to 700 kGy and the right one is after irradiation.

We observe that in the unirradiated case the average cluster noise gets better when increasing the distance between strip implant and p-stop implant, i.e. going to the wide geometries. Here, the common and combined p-stop geometries behave similarly, while the atoll p-stop performs slightly better, by a factor of about 10%. The p-spray method shows a similarly low noise as the atoll p-stop. Note that the bias resistor of the p-spray sensors from batch 2825 have a resistance twice as large as the p-stop sensors from batch 2826, leading to a reduced noise contribution of the parallel resistor (see section 4.3). Using the equations from section 4.3, however, one finds that this reduction amounts to less than a percent of the total noise.

After irradiation the combined p-stop suffers strongly, while again the atoll p-stop shows the lowest cluster noise. Again, for comparison of noise levels the same restrictions apply as for the cluster signal levels!

Comparison of the cluster signal-to-noise ratio

The third row of plots in figure 7.20 shows the SNR for clusters[19] of exactly two strips before and after irradiation. The effect of the different calibrations cancels out for the SNR – this is true even for measurements taken before and after irradiation – so that we can compare the values directly.

Before irradiation (left plot) the half-wide atoll p-stop clearly beats all other p-stop patterns with a maximum SNR value of 28.2. This is due to a decent signal height and a very low noise. For the common p-stop the high signals of the narrow geometries are counteracted by high noise levels, causing it to fall back behind the atoll p-stop for all geometries. The combined p-stop shows high signal levels for the wide geometries, but also higher noise levels. This leads to the best performance for the wide geometry with a SNR of 26.5, for all other geometries it is surpassed by the atoll p-stop and the common p-stop. The p-spray reaches a very high SNR of 27.3, which is outperformed by the half-wide atoll p-stop only. Similar to the atoll p-stop, this is due to a decent signal and a very low noise.

After irradiation (right plot) the atoll p-stop performs best for the wide geometries, again reaching the best SNR of 22.2 for the half-wide geometry. This is mainly due to very high signal levels and low noise compared to the other patterns. The common pattern beats the

[19] Note that the computation of the cluster SNR ratio uses the individual strip noise values of the strips involved in the cluster, according to the definition in equation 7.2, and not the averaged cluster noise displayed in the second-row plots of figure 7.20.

other patterns for the narrow geometries with a SNR of 20.7, where it shows high signals and low noise on its part. Compared to the other patterns, the combined pattern loses some signal while its noise is larger by almost 30% after irradiation, so its SNR suffers strongly from irradiation and drops to values around 14.

Comparison of the relative signal

The bottom two plots of figure 7.20 show the relative signal, i.e. the division of the MPV of the 2-strip-cluster signal by the MPV of the 1-strip-cluster signal. Like for the SNR, the effect of the potentially different calibration of signal levels cancels out here as well, making the results directly comparable.

Before irradiation (left plot) all p-stop patterns show a comparable relative signal around 95%. One can observe a slight decline when going to wide common geometries, while the atoll geometries increase. The p-spray method performs worst of all blocking methods.

After irradiation (right plot) the relative signal generally increases, partly to values above 100%. This doesn't imply an amplification of the signal, it just means that for 1-strip-clusters more signal is lost than for 2-strip-clusters. This increase is less pronounced for the combined p-stop. One can clearly see an increasing tendency when going to wide geometries. This increase is strongest for the atoll p-stop, which starts at the level of the combined p-stop for the narrow geometry, and reaches the level of the common p-stop for the wide geometry.

7.3.2. Results of sensors with every second strip connected to the readout

We now take a look at the baby sensors with every second strip connected to the readout electronics (200 µm readout pitch with intermediate strips) for clusters of exactly two strips. For these sensors no irradiation was carried out. All data of the p-spray module stack (figure 7.19) were taken immediately after testing the p-stop module stack (figure 7.18), at the same beam test in 2011. For each strip insulation method (common, atoll, combined p-stop, p-spray) we tested two modules and present the results of the better working one in terms of SNR. This minimises the influence of electronic noise of the periphery, inefficient wire bonding, bad strips, etc. The selected modules are COMM-I-2, COMB-I-2, ATOLL-I-1 and SPRAY-I-1.

Comparison of the cluster signal

The top plot in figure 7.21 shows the most probable cluster signal of the baby sensors with every second strip connected to the readout. We observe that the atoll p-stop and the p-spray methods are almost tied for the best cluster signal, with slight advantages for the

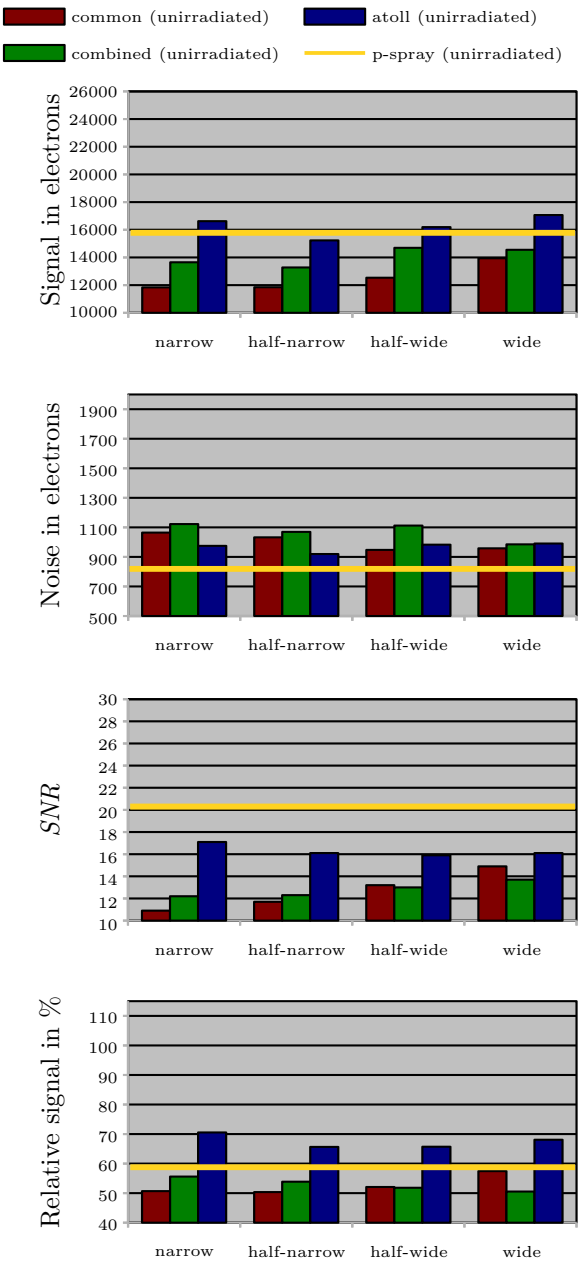

Figure 7.21.: Cluster signal, cluster noise and SNR for 2-strip-clusters, and relative signal of 2-strip-clusters w.r.t. 1-strip-clusters, for sensors from batches 2826 and 2825 with coarse p-stop geometry variations and every second strip connected to the readout electronics (200 µm readout pitch, with intermediate strips). These data have been recorded in 2011, where no irradiation was performed.
Each measured quantity is the result of a fit to a histogram with about 10000 entries. We plot the results of the better working module (i.e. the one with lower noise and higher SNR). The numerical values can be found in table 7.3.

Table 7.3.: Cluster signal, cluster noise and SNR for 2-strip-clusters, and relative signal of 2-strip-clusters w.r.t. 1-strip-clusters, for sensors from batches 2826 and 2825 with coarse p-stop geometry variations and every second strip connected to the readout electronics (200 µm readout pitch, with intermediate strips). Green: best value within one p-stop pattern; Red: overall best value.

Cluster signal in electrons, $\sigma(S) < 50$ electrons				
	narrow	half-narrow	half-wide	wide
Common p-stop	11834	11847	13649	13944
Combined p-stop	13649	13277	14694	14552
Atoll p-stop	16621	15233	16194	17064
p-spray		15778		
Cluster noise in electrons, $\sigma(N) < 15$ electrons				
Common p-stop	1065	1033	948	958
Combined p-stop	1122	1069	1112	985
Atoll p-stop	975	920	983	991
p-spray		819		
Cluster SNR, $\sigma(SNR) < 0.1$				
Common p-stop	10.9	11.7	13.2	14.9
Combined p-stop	12.2	12.3	13.0	13.7
Atoll p-stop	17.1	16.1	15.9	16.1
p-spray		20.3		
Relative signal in %, $\sigma(S_{\text{rel}}) < 1\%$				
Common p-stop	50.7	50.4	52.1	57.5
Combined p-stop	55.6	53.9	51.8	50.5
Atoll p-stop	70.5	65.7	65.7	68.1
p-spray		58.8		

atoll p-stop. While for the common p-stop and the combined p-stop an increasing tendency towards wide geometries is visible, the atoll p-stop doesn't show such distinct behaviour. Again, one has to be careful when comparing bare signal levels, because they are subject to calibration.

Comparison of the cluster noise

The second plot in figure 7.21 shows the most probable cluster noise of the baby sensors with every second strip connected to the readout. The p-spray method clearly shows the lowest noise figure. For the narrow geometries, the atoll p-stop works best, while for the wide geometries the common p-stop has the lowest noise figure. Except for the wide geometry the combined p-stop is the worst option. Again, one has to be careful when comparing bare noise levels, because they are subject to calibration.

Comparison of the cluster signal-to-noise ratio

The third plot in figure 7.21 shows the SNR for clusters[20] of exactly two strips. The effect of the different calibrations cancels out for the SNR so that we can compare the values directly.

The high signal and the unbeatably low noise leads to the best SNR of 20.3 for the p-spray method. Among the p-stop patterns the atoll p-stop clearly stands out with a SNR of 17.1. It shows a slightly falling tendency towards wide geometries. In contrast, both the common and the combined p-stops show an increasing tendency, which is more pronounced for the common p-stop.

Comparison of the relative signal

The bottom plot of figure 7.21 shows the relative signal, i.e. the division of the MPV of the 2-strip-cluster signal by the MPV of the 1-strip-cluster signal. Like for the SNR, the effect of the potentially different calibration of signal levels cancels out here as well, making the results directly comparable.

The atoll p-stop clearly beats all other options in terms of the relative signal, without showing a distinct tendency w.r.t. the geometry variants. The p-spray reaches a not-so-close second. Common and combined p-stop are battling for the third place, showing opposed tendencies in terms of geometry variants.

[20] Note that the computation of the cluster SNR ratio uses the individual strip noise values of the strips involved in the cluster, according to the definition in equation 7.2, and not the averaged cluster noise displayed in the second plot of figure 7.21.

It is eye-catching that the relative signal of sensors with doubled readout pitch and intermediate strips is drastically reduced w.r.t. the normal ones, check against the bottom left plot of figure 7.20. Consequently, a considerable part of the signal is lost when sharing the charge among two strips which are far apart, and the capacitive coupling of the intermediate strip can not recover all of it.

When comparing the relative signal to the one of the full-scale sensors tested in section 8.3 we observe that it is slightly lower for the baby sensors presented here, although the full-scale sensors have an even larger readout pitch of 240 µm. It suggests itself that this discrepancy originates in the aluminium trace which resides above the non-connected strips of the baby sensors, while a real intermediate strip lacks this metallisation, as is sketched in figure 7.22.

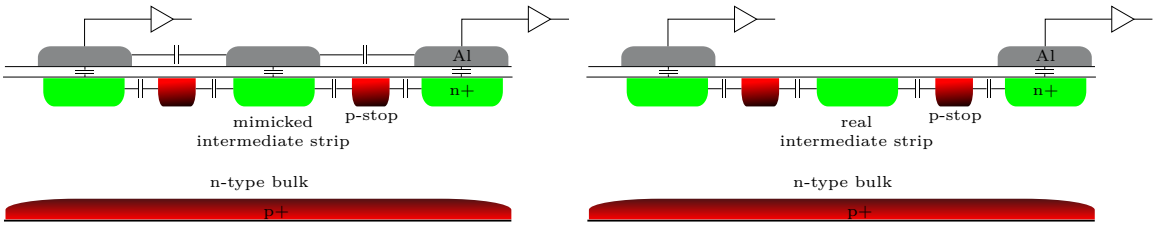

Figure 7.22.: The mimicked intermediate strip (left) is still covered by an aluminium trace, to which a part of the signal arriving at the intermediate strip is coupled. Not all of it is recovered by the coupling to the aluminium traces of the readout strips. In contrast, for a real intermediate strip (right) this kind of signal drain is drastically reduced.

The measurements suggest that a part of the signal is coupled to the aluminium trace instead of to the implants of the neighbouring readout strips. Only a part of this lost signal is coupled to the aluminium lines of the readout strips and can be recovered.

7.3.3. Enhanced conductivity in unimplanted areas

One possibility of exploring the behaviour of a sensor in the area between the strips is taking a look at the η distribution. The quantity η is the center of gravity of the signals given by all strips in a cluster (see also section 4.4):

$$\eta_n = \frac{\Sigma_{i=1}^{n}(i-1)S_i}{\Sigma_{i=1}^{n}S_i}, \tag{7.3}$$

where n is the cluster width and S_i is the signal of strip i. In case of clusters consisting of two strips η is reduced to

$$\eta_{n=2} = \frac{S_2}{S_1 + S_2} \tag{7.4}$$

and can assume values of $\eta \in (0,1)$[21]. 0 means that the whole signal is collected by the left strip, whereas 1 means that the whole signal is collected by the right strip. In general the signal will be distributed among the two neighbouring strips, but not evenly. When a particle hits a detector near one strip, the charges are more likely to travel to the closer strip than to the other, and this likelihood is *not* linearly proportional to the difference in geometric distance to the two strips. When histogramming the quantity η for many events, the distribution will therefore not be flat, but rather shaped like a bath tub.

Figure 7.23 shows a comparison of the η distribution of the atoll p-stop geometries, before and after irradiation. The top row shows the η distribution before irradiation, the middle row after irradiation, and the bottom row shows a closeup of the corresponding sensor design. The columns show the four different geometries of the atoll p-stop pattern, starting with the narrow geometry on the left, and going to the wide geometry on the right.

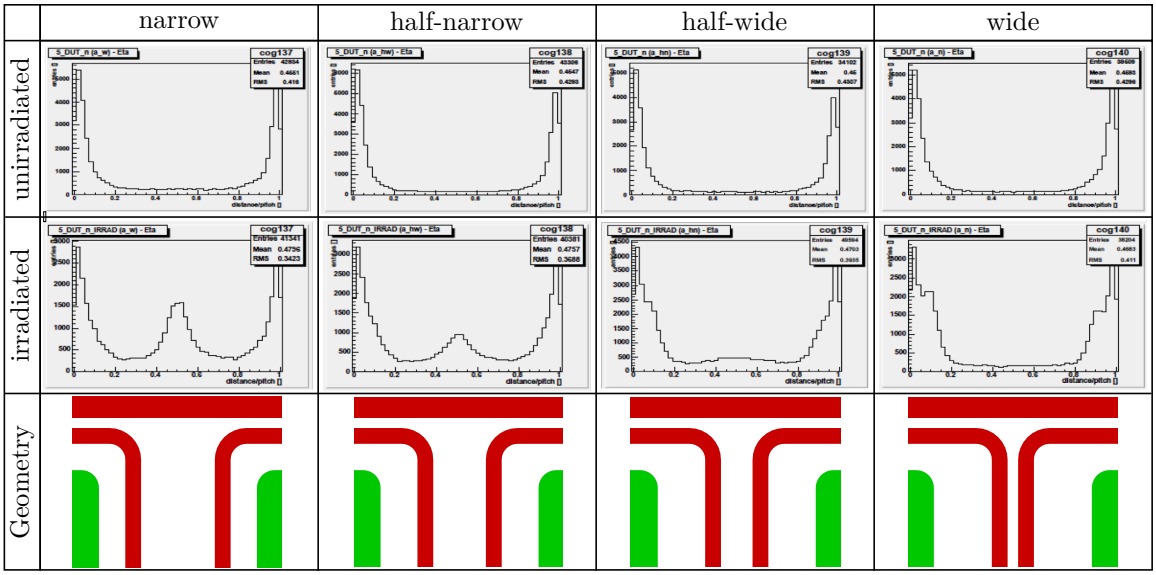

Figure 7.23.: Distributions of η for the atoll p-stop. After irradiation to 700 kGy additional peaks develop in unimplanted regions, which for the narrow geometry resemble the behaviour on an intermediate strip. For the wide geometry, additional shoulders occur.

While in the unirradiated case (figure 7.23, top row) all geometries show the expected bath tub shape of the η distribution, we see quite some differences in the irradiated case. Best visible in the narrow geometry (figure 7.23, middle row, left column), the η distribution shows enhancements in unimplanted regions. This shape of the η distribution looks very similar the one of sensors with one intermediate strip. These sensors also show an additional peak in the middle of the η distribution, where the charge is mainly collected by the intermediate strip and distributed evenly among the neighbouring readout strips by capacitive coupling. This produces more events where the signals of the two readout strips are similar,

[21] For clusters with more than two strips η can assume values $\eta > 1$. In this case, only the digits after the comma are filled into the histogram.

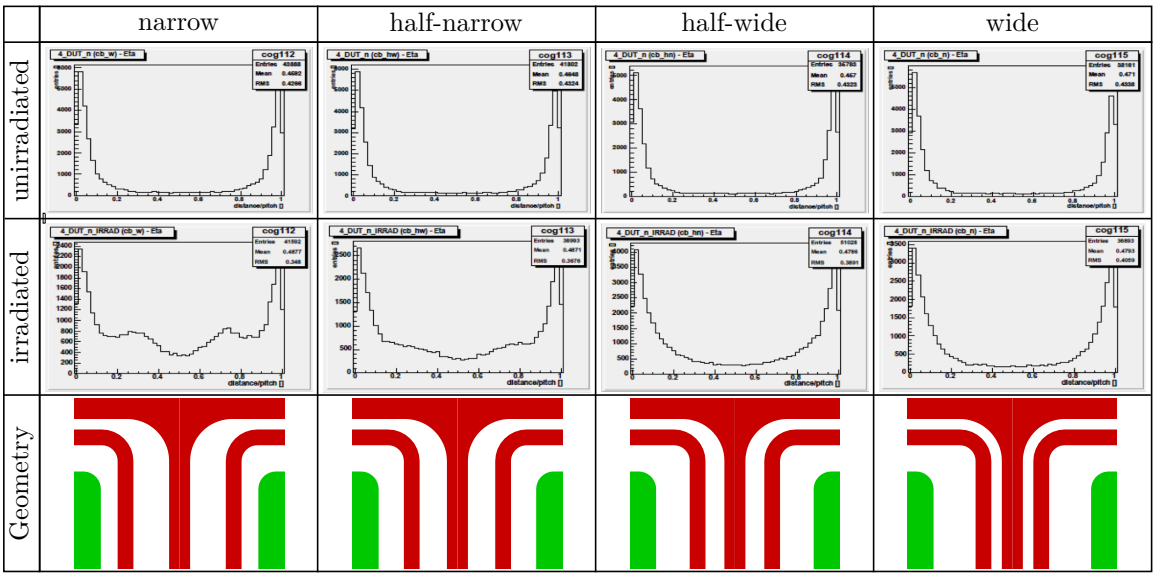

Figure 7.24.: Distributions of η for the combined p-stop. After irradiation to 700 kGy additional peaks and shoulders develop, following the structure of unimplanted regions.

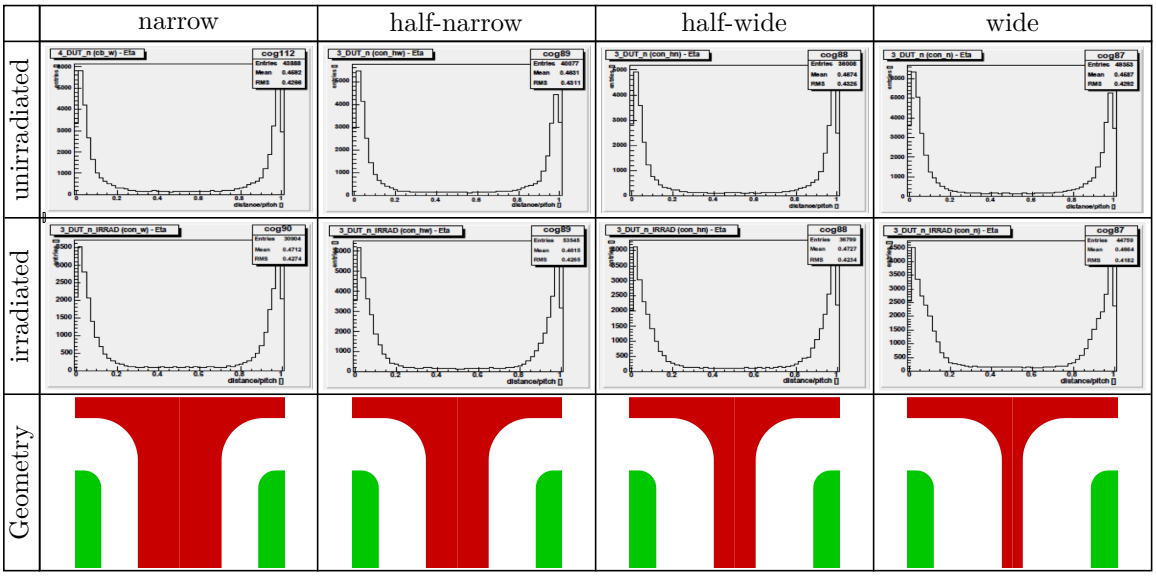

Figure 7.25.: Distributions of η for the common p-stop. After irradiation to 700 kGy additional shoulders develop in unimplanted regions, which become wider when going to the wide geometry.

i.e. in the center of the η distribution. The enhancements in the irradiated η distributions suggest an enhanced conductivity in unimplanted regions.

The η distributions of the irradiated combined p-stop sensor (figure 7.24) and of the common p-stop sensor (figure 7.25) show the similar enhancements, always in regions free of implantations.

Spreading Resistance Profiling measurement

We performed an SRP measurement [51] on the surface of the narrow atoll p-stop region of the irradiated sensor to further investigate the suspected regions with enhanced conductivity.

In this destructive measurement method all passivation and metalization is removed, leaving the sensor substrate naked. Then, two needles are placed on the surface (with a defined distance between each other, and a defined contact force), and the resistance between the needles is measured. Implanted areas will show a lower resistance than unimplanted ones. From the resistance one can calculate the charge carrier concentration of the underlying substrate. When stepping those needles across the surface, one can record a profile of the charge carrier concentration.

Figure 7.26 shows an SRP measurement of the narrow atoll p-stop geometry, stepping the needles perpendicular to the strip direction. The bottom part shows a microscope picture of the investigated region, with the marks of the needles clearly visible. One can identify the wide strip implants and the narrow p-stop implants. The top part shows the corresponding SRP measurement results. We plot the charge carrier concentration against the position covered by stepping the needles. One can easily identify the strip implant (wide, high charge carrier concentration), bordered by the p-stop implants (narrow, lower charge carrier concentration).

The region between the p-stop implants shows no peak whatsoever. So, no enhanced conductivity of the substrate could be identified. The most probable explanation is that a chargeup takes place in the oxide, which hereafter accumulates majority charge carriers to the surface which form the conductive region. This cannot happen in implanted regions. The same effect is used when implanting p-stop structures to interrupt the intrinsic accumulation layer at the interface of the substrate and the oxide, as is explained in section 4.6.1.

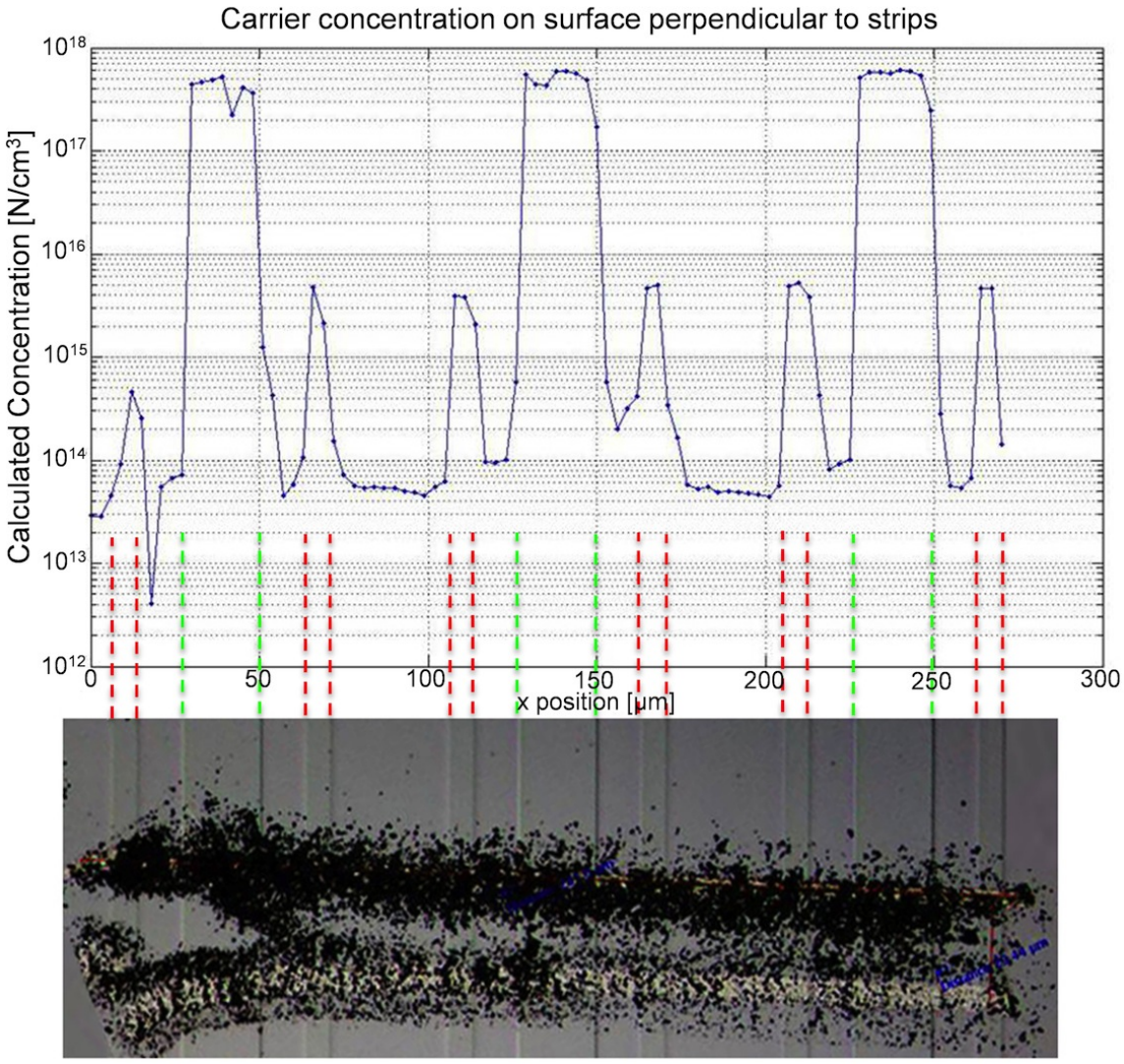

Figure 7.26.: SRP measured carrier concentration of the narrow atoll p-stop geometry. The enhanced conductivity seen in the η distribution (figure 7.23, middle row, left plot) is not visible in the SRP measurement.

7.3.4. Connection to the interstrip capacitance

As can be seen in equation 4.8, the sensor performance depends on the interstrip capacitance C_{int}. The measurement of the interstrip capacitance was carried out in the semiconductor laboratory with the QTC setup, using additional baby sensors left from batch 2826 with the coarse p-stop geometry variations. For each p-stop geometry zone the interstrip capacitance was measured on three different strips, connecting to the DC pads of the strip to be measured and to the shorted four neighbour strips. The values of C_{int} presented here are the average of these three measurements. The LCR meter was set to a measurement frequency of 1 MHz. Note that the used frequency is a convention, and that the measurement of such a small capacitance is a delicate procedure with low accuracy. Please refer to [52] for details.

Figure 7.27 shows the results from the beam test 2010 (unirradiated p-stop sensors with initial design, no intermediate strips) and 2011 (unirradiated p-spray sensors, no intermediate strips) as function of the interstrip capacitance C_{int}. It can generally be observed that the interstrip capacitance increases when the p-stop implant comes closer to the strip implant, i.e. going to narrow geometries. This is true for all p-stop patterns. The p-spray method reaches the lowest interstrip capacitance.

Signal and noise levels have to be compared with caution, because these quantities are subject to calibration and can differ for different readout chips. Figure 7.27 allows the following observations:

Most probable signal of 1-strip-clusters (top plot): The signal slightly increases with increasing interstrip capacitance, where the common p-stop shows the strongest inclination. This, however, could also be the effect of the calibration, because there is an unnatural step between the wide geometries (left two points) and the narrow geometries (right two points). These geometry pairs were read out with two different readout chips.

Most probable signal of 2-strip-clusters (second plot): Here, no general tendency can be observed. The common p-stop still increases, while the atoll p-stop shows a slight decrease. The signals of the combined p-stop don't even show a clear tendency.

Single strip noise (middle plot): The theory states that the noise increases linearly with the interstrip capacitance. This is roughly true for the common and combined p-stop, the atoll p-stop shows a non-monotonous behaviour. This may be due to the non-ideal calibration of signal and noise levels.

Cluster SNR for 2-strip-clusters (penultimate plot): The signal-to-noise ratio shows quite a clear decrease with increasing interstrip capacitance, as can be expected from the theory. Only the wide geometries of the atoll and common p-stop (leftmost points) seem to be outliers. Note that the SNR is independent from the calibration of the readout chip.

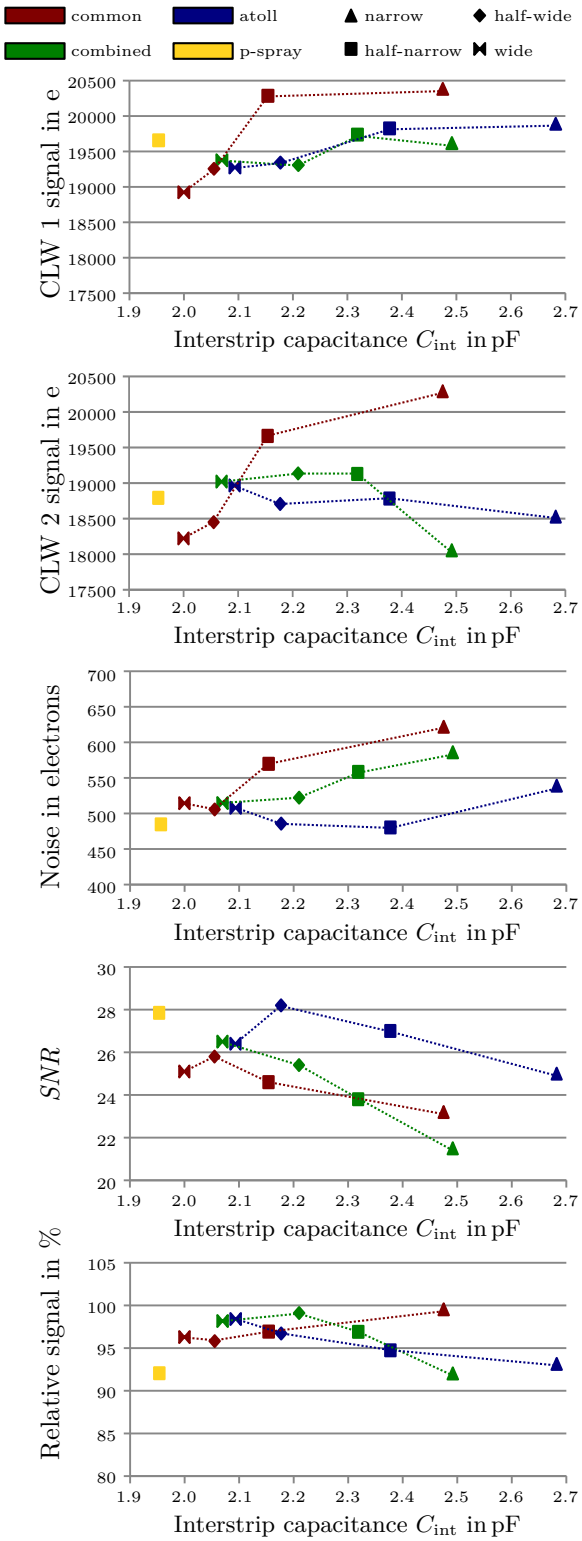

Figure 7.27.: Cluster signal for 1-strip-clusters and 2-strip-clusters, single-strip noise, SNR for 2-strip-clusters and relative signal of 2-strip-clusters w.r.t. 1-strip-clusters as function of the interstrip capacitance C_{int}.

Relative signal (bottom plot): The relative signal seems to be quite independent from the interstrip capacitance. There seems to be a slight increase for the common p-stop and a slight decrease for the atoll and combined p-stop. Like the SNR, also the relative signal is independent of the calibration.

7.3.5. Conclusions of the beam tests 2010 and 2011

The results from the beam test 2010 provided vital input for the design of the trapezoidal sensor to be installed in the forward part of the Belle II SVD. The n-side strip insulation of the trapezoidal sensor was originally implemented as combined p-stop, as suggested by [45] and [46]. However, the SNR values before and after irradiation (figure 7.20, third row) clearly show that the combined p-stop is the worst option in our case, especially as it strongly suffers from irradiation. Therefore, we chose to update the design of the trapezoidal sensor to implement the half-wide atoll p-stop pattern, which proved to be the best option both before and after irradiation. This p-stop design is similar to the one Hamamatsu Photonics K.K. implements on the full-scale rectangular sensors, as can be seen in the data sheet in Addendum 11.1.

The p-spray method showed a very good performance in the beam test 2011, making it a real competitor of the atoll p-stop, the more so because it saves one photo mask and several processing steps, making the production cheaper. However, a complete picture can only be gained once the p-spray sensors have been subjected to an irradiation campaign. This was done for the beam test in 2012, see section 7.4.

In the beam test 2011 we learned that it is of utmost importance to prepare more than one module per sensor type to be tested. In the beam test one tries to draw conclusions about the sensor itself from the performance of the module as a whole, i.e. including the electronic periphery. It is impossible to disentangle e.g. the noise contributions coming from the sensor from the ones coming from the readout electronics. In 2011, for example, we prepared two modules with p-spray sensors from the *same* wafer, in the exact same electrical configuration, and we measured different performances of these two modules. Therefore it is advisable to prepare at least two modules per sensor type and electrical configuration, and only consider the results of the better working ones. This minimises the influence of electronic noise of the periphery, inefficient wire bonding, bad strips, etc.

7.4. Beam test 2012

In 2012 we tried to ensure direct comparability of all data taken, in order to improve on the shortcomings revealed by the beam tests of the years before. This time, two stacks of modules were put on the beam one directly after the other, to ensure similar environmental conditions. We used baby sensors from the last prototype batch 2965, as well as reused the four p-spray modules already tested in the beam test 2011. The p-stop sensors from batch 2965 feature the fine geometry variations of the p-stop patterns, as is noted in table 6.2. Table 7.1 gives an overview of the sensors and modules used in the individual beam tests.

We newly prepared twelve modules, four per p-stop pattern. For half of the modules only every second strip was connected to the readout electronics. This mimics a sensor with doubled readout pitch and intermediate strips. The eight modules with normal readout (six with p-stop and two with p-spray from the year before) were assembled to form the "normal" stack (figure 7.28a), the eight remaining modules with every second strip connected form their own "intermediate" stack (figure 7.28b). The stacks are arranged to deliver eight measurements of the vertical coordinate, which is sufficient to allow particle tracking and resolution estimation without the need for a beam telescope. The DUTs were tested in the beam, irradiated to 100 kGy (see section 7.2.1), and tested again in the same beam test setup as before. Note that for irradiation the protective covers were taken off and replaced by smaller ones. After irradiation the modules were reassembled with randomly picked original lids, leading to slightly different dimensions of the stacks after irradiation. All sensors were operated uncooled at ambient temperature of about 23 °C, with a reverse bias voltage of 100 V applied. The readout system and triggering scheme was the same as in 2011, see section 7.2.2, and the same observables as described in section 7.2.3 were measured. In each measurement run we acquired 300000 events and selected events with exactly one 2-strip-cluster, individually for each sensor. This suppresses ambiguous events like particle splashes. The beam spot serves two geometry zones at once, therefore the results of the p-stop geometry variants are based on a data sample of about 30000 events. For the p-stop modules we present the results of the better working one in terms of noise and SNR. This reduces the influence of electronic noise of the periphery, inefficient wire bonding, bad strips, etc. The selected modules are COMM-1, SPRAY-1, COMB-1, and ATOLL-2, COMM-I-1, SPRAY-I-1, COMB-I-1 and ATOLL-I-2. For the p-spray modules we present the averaged results from two measurement runs.

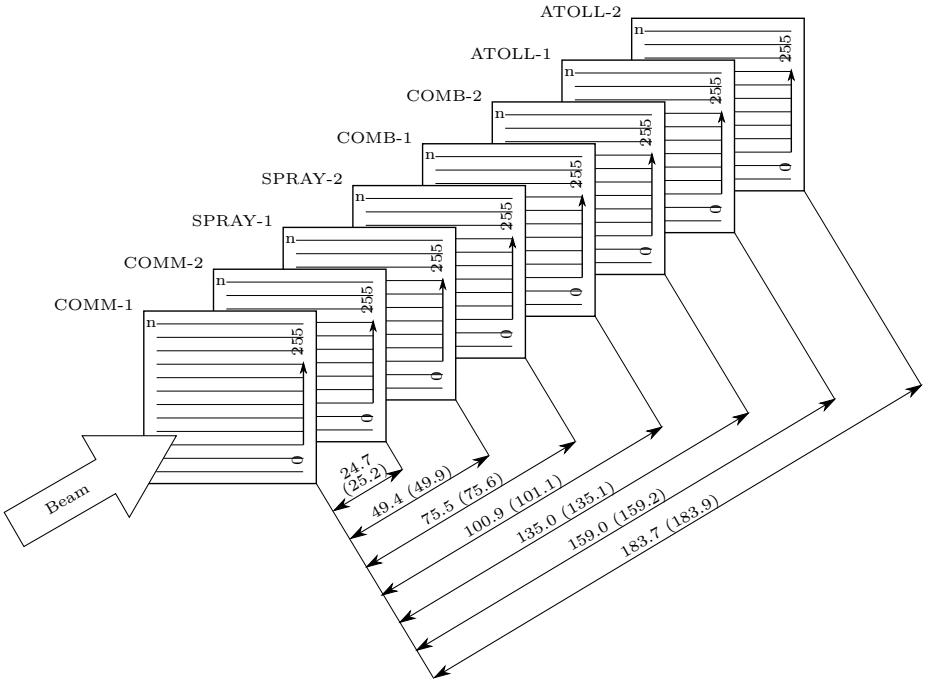

(a) The "normal" module stack contains eight sensors with every strip connected to the readout, yielding devices with a readout pitch of 100 µm without intermediate strips.

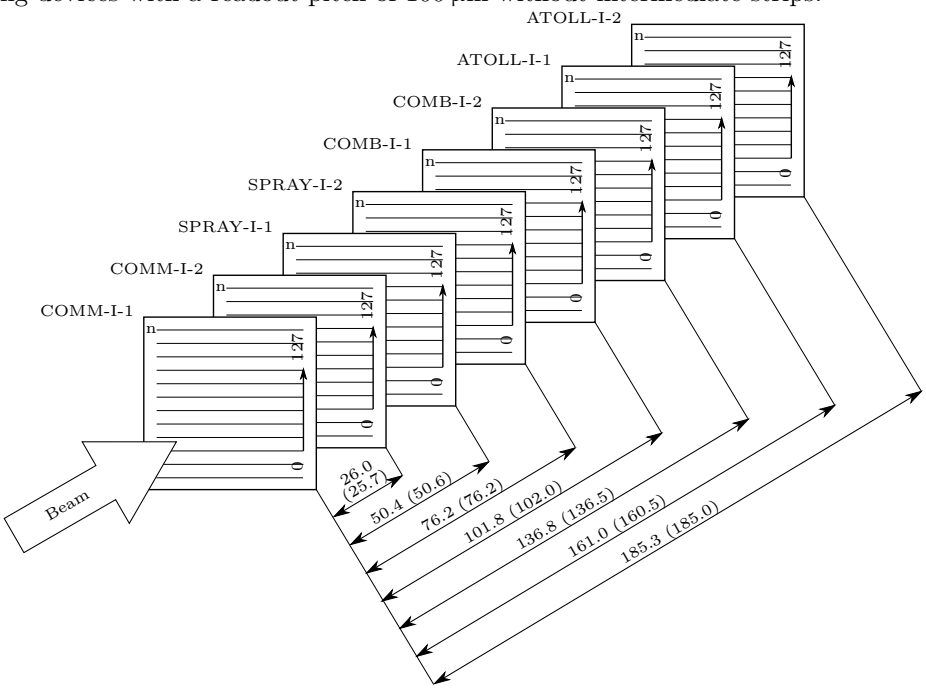

(b) The "intermediate" module stack contains eight sensors with every second strip connected to the readout, yielding devices with a readout pitch of 200 µm and intermediate strips.

Figure 7.28.: The module stacks from 2012 consist of six modules holding sensors from batch 2965 with the updated (finer) p-stop geometry variations, and two p-spray modules from 2011, two modules per strip insulation method (common, atoll combined p-stop, p-spray). All modules have the same strip direction and face the beam with the n-side. Only the n-side is read out. The dimensions in brackets are after irradiation.

7.4.1. Results of sensors with every strip connected to the readout

Comparison of the cluster signal

The top two plots of figure 7.29 show the most probable cluster signal of baby sensors with every strip connected to the readout electronics for clusters of exactly two strips, where the values found in the left plot are before irradiation to 100 kGy and those in the right plot are after irradiation. Note that in contrast to the results from 2010 and 2011 the geometry variants (narrow, half-narrow, half-wide, wide) now refer to the updated design with finer variation, as is listed in table 6.2.

We observe that in the unirradiated case the most probable cluster signal of the combined and atoll p-stop geometries are comparable and show a small increasing tendency towards wide geometries, if any. The common p-stop shows an unnatural step between the wide and narrow geometries which might be due to calibration. The p-spray method shows a significantly lower signal level compared to the p-stop patterns.

After irradiation the common p-stop still shows the characteristic step between narrow and wide geometries, while the other ones show a tendency for higher cluster signals when going to the wide geometry. The p-spray catches up to the p-stop patterns.

Comparison of the cluster noise

The second row of plots in figure 7.29 shows the average cluster noise for clusters of exactly two strips $\bar{N}_{n=2} = \sqrt{2}\bar{N}_{\text{strip}}$, where $\bar{N}_{\text{strip}}$ is the noise averaged over all strips of the same group. Again, the left plot is before irradiation to 100 kGy and the right one is after irradiation.

We observe that in the unirradiated case the average cluster noise gets slightly higher for the atoll and combined p-stop when increasing the distance between strip implant and p-stop implant, i.e. going to the wide geometries. The common p-stop geometries again show the characteristic step. Without that step, it would show an increasing tendency as well. The p-spray method shows a significantly lower noise than the p-stop patterns.

After irradiation the relative behaviour of the p-stop patterns stays the same at an elevated noise level, only the p-spray method suffers strongly. The atoll and combined p-stop are tied for the lowest noise after irradiation.

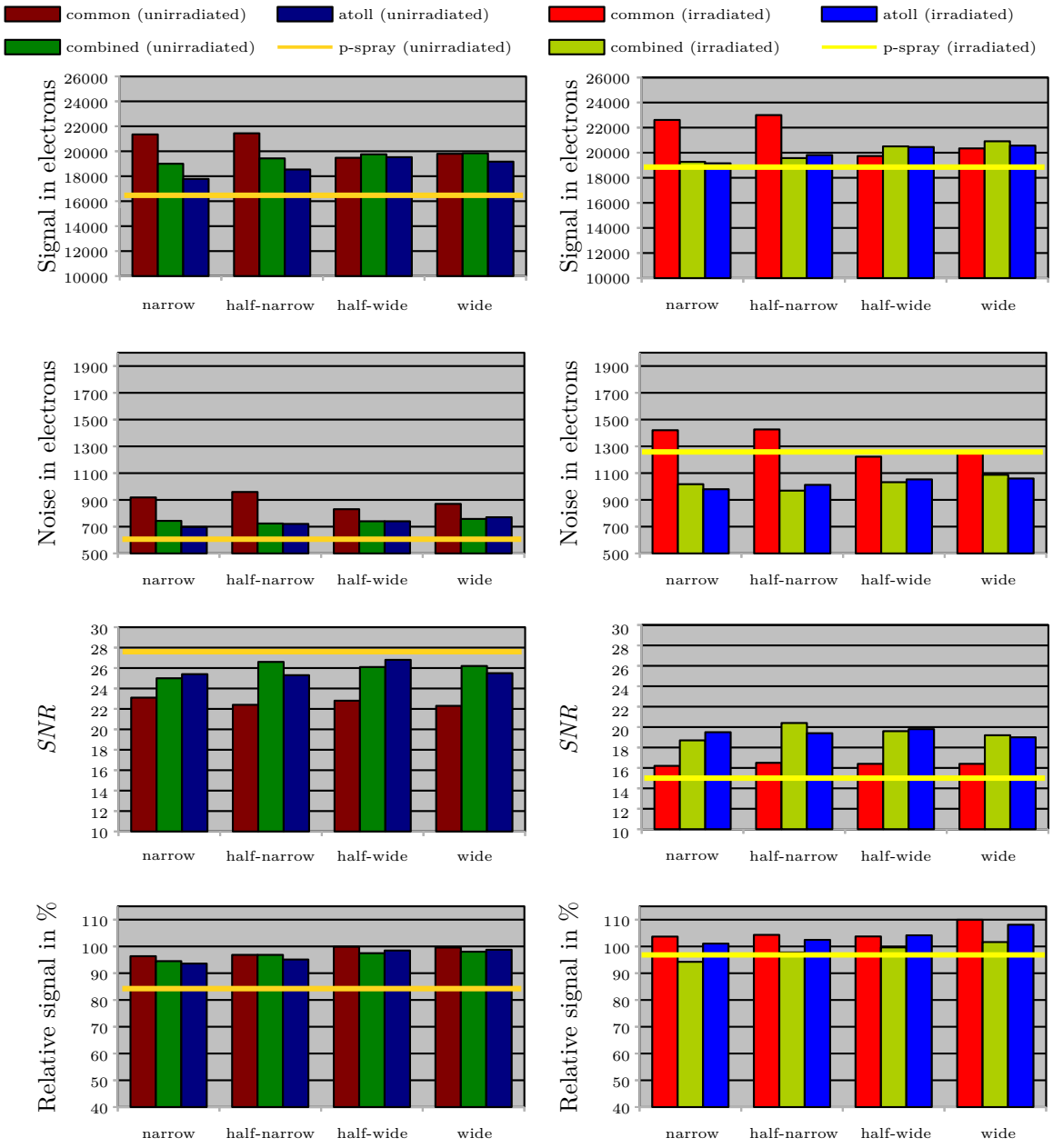

Figure 7.29.: Cluster signal, cluster noise and SNR for 2-strip-clusters, and relative signal of 2-strip-clusters w.r.t. 1-strip-clusters, data taken in 2012 for sensors with finer p-stop geometry variations and every strip connected to the readout electronics (100 µm readout pitch, no intermediate strips).
The left plots are before irradiation to 100 kGy, the right ones are after irradiation. Each measured quantity is the result of a fit to a histogram with about 30000 entries, taken from the better working one of two modules (i.e. the one with lower noise and higher SNR). The data of the p-spray method are the average of two data taking runs.

Table 7.4.: Cluster signal, cluster noise and SNR for 2-strip-clusters, and relative signal of 2-strip-clusters w.r.t. 1-strip-clusters, data taken in 2012 for sensors with finer p-stop geometry variations and every strip connected to the readout electronics (100 µm readout pitch, no intermediate strips). Green: best value within one p-stop pattern; Red: overall best value.

		narrow	half-narrow	half-wide	wide
Cluster signal in electrons, $\sigma(S) < 50$ electrons					
Common p-stop	unirradiated	21348	21439	19475	19799
	irradiated	22612	22999	19735	20342
Combined p-stop	unirradiated	19011	19430	19755	19841
	irradiated	19270	19570	20505	20566
Atoll p-stop	unirradiated	17782	18540	19526	19167
	irradiated	19155	19813	20450	20566
p-spray	unirradiated		16470		
	irradiated		18850		
Cluster noise in electrons, $\sigma(N) < 15$ electrons					
Common p-stop	unirradiated	918	959	831	870
	irradiated	1420	1426	1223	1248
Combined p-stop	unirradiated	744	724	740	758
	irradiated	1017	969	1032	1088
Atoll p-stop	unirradiated	697	721	740	771
	irradiated	980	1012	1053	1060
p-spray	unirradiated		606		
	irradiated		1258		
Cluster SNR, $\sigma(SNR) < 0.1$					
Common p-stop	unirradiated	23.1	22.4	22.8	22.3
	irradiated	16.2	16.5	16.4	16.4
Combined p-stop	unirradiated	25.0	26.6	26.1	26.2
	irradiated	18.7	20.4	19.6	19.2
Atoll p-stop	unirradiated	25.4	25.3	26.8	25.5
	irradiated	19.5	19.4	19.8	19.0
p-spray	unirradiated		27.6		
	irradiated		15.0		
Relative signal in %, $\sigma(S_{\text{rel}}) < 1\%$					
Common p-stop	unirradiated	96.3	96.8	99.9	99.6
	irradiated	103.7	104.3	103.7	110.0
Combined p-stop	unirradiated	94.5	96.8	97.5	98.7
	irradiated	94.3	97.8	99.6	101.6
Atoll p-stop	unirradiated	93.6	95.1	98.5	98.7
	irradiated	101.1	102.5	104.2	108.1
p-spray	unirradiated		84.2		
	irradiated		96.8		

Comparison of the cluster signal-to-noise ratio

The third row of plots in figure 7.29 shows the SNR for clusters[22] of exactly two strips before and after irradiation. The effect of the different calibrations cancels out for the SNR – this is true even for measurements taken before and after irradiation – so that we can compare the values directly.

Before irradiation (left plot) the half-wide atoll p-stop and the half-narrow combined p-stop are tied for the best SNR among the p-stop geometries, with SNR values of 26.8 and 26.6, respectively. The common p-stop is caused to fall back behind the other p-stop patterns by its high noise levels. The p-spray reaches the overall best SNR of 27.6. This is mainly due to its unequaled low noise.

After irradiation (right plot) the atoll p-stop and the combined p-stop show similar performance with SNR values around 19, while the common p-stop pattern still plays no role. The p-spray method suffers severely from irradiation and is busted to the last place with a SNR of 15.0.

Comparison of the relative signal

The bottom two plots of figure 7.29 show the relative signal, i.e. the division of the MPV of the 2-strip-cluster signal by the MPV of the 1-strip-cluster signal. Like for the SNR also here the effect of the potentially different calibration of signal levels cancels out, making the results directly comparable.

Before irradiation (left plot) all p-stop patterns show a comparable relative signal around 95%. One can observe a slight incline for all p-stop patterns when going to wide geometries. The p-spray method shows a significantly lower relative signal of around 85%.

After irradiation (right plot) the relative signal generally increases, partly to values above 100%. This means that for 1-strip-clusters more signal is lost than for 2-strip-clusters. This increase is less pronounced for the combined p-stop. One can again see an increasing tendency when going to wide geometries. The p-spray method could catch up and reaches a similar relative signal level as the combined p-stop.

[22] Note that the computation of the cluster SNR ratio uses the individual strip noise values of the strips involved in the cluster, according to the definition in equation 7.2, and not the averaged cluster noise displayed in the second-row plots of figure 7.29.

7.4.2. Results of sensors with every second strip connected to the readout

Comparison of the cluster signal

The top two plots of figure 7.30 show the most probable cluster signal of baby sensors with every second strip connected to the readout electronics for clusters of exactly two strips, where the values found in the left plot are before irradiation to 100 kGy and those in the right plot are after irradiation. Note that in contrast to the results from 2010 and 2011 the geometry variants (narrow, half-narrow, half-wide, wide) now refer to the updated design with finer variation, as is listed in table 6.2.

We observe that in the unirradiated case the most probable cluster signal of the atoll p-stop is outstanding, the other p-stop patterns only play an underpart. The common p-stop shows advances for the wide geometries. The p-spray method is the only one coming close to the atoll p-stop.

After irradiation the picture basically stays the same at elevated signal levels. Still the atoll p-stop shows the best cluster signal, the wide common p-stop managed to catch up to the p-spray method.

Comparison of the cluster noise

The second row of plots in figure 7.30 shows the average cluster noise for clusters of exactly two strips $\bar{N}_{n=2} = \sqrt{2}\bar{N}_{\text{strip}}$, where $\bar{N}_{\text{strip}}$ is the noise averaged over all strips of the same group. Again, the left plot is before irradiation to 100 kGy and the right one is after irradiation.

We observe that in the unirradiated case the average cluster noise shows no significant dependence on the geometry variant. The worst noise is found for the common p-stop, the atoll is the best p-stop pattern, only surpassed by the p-spray method. Note that the bias resistor of the p-spray sensors from batch 2825 have a resistance eight times as large as the p-stop sensors from batch 2965, leading to a reduced noise contribution of the parallel resistor (see section 4.3).

After irradiation the combined p-stop, the atoll p-stop and the p-spray method all show comparable noise levels, only the common p-stop stands out. The p-spray method lost the good performance it showed before irradiation.

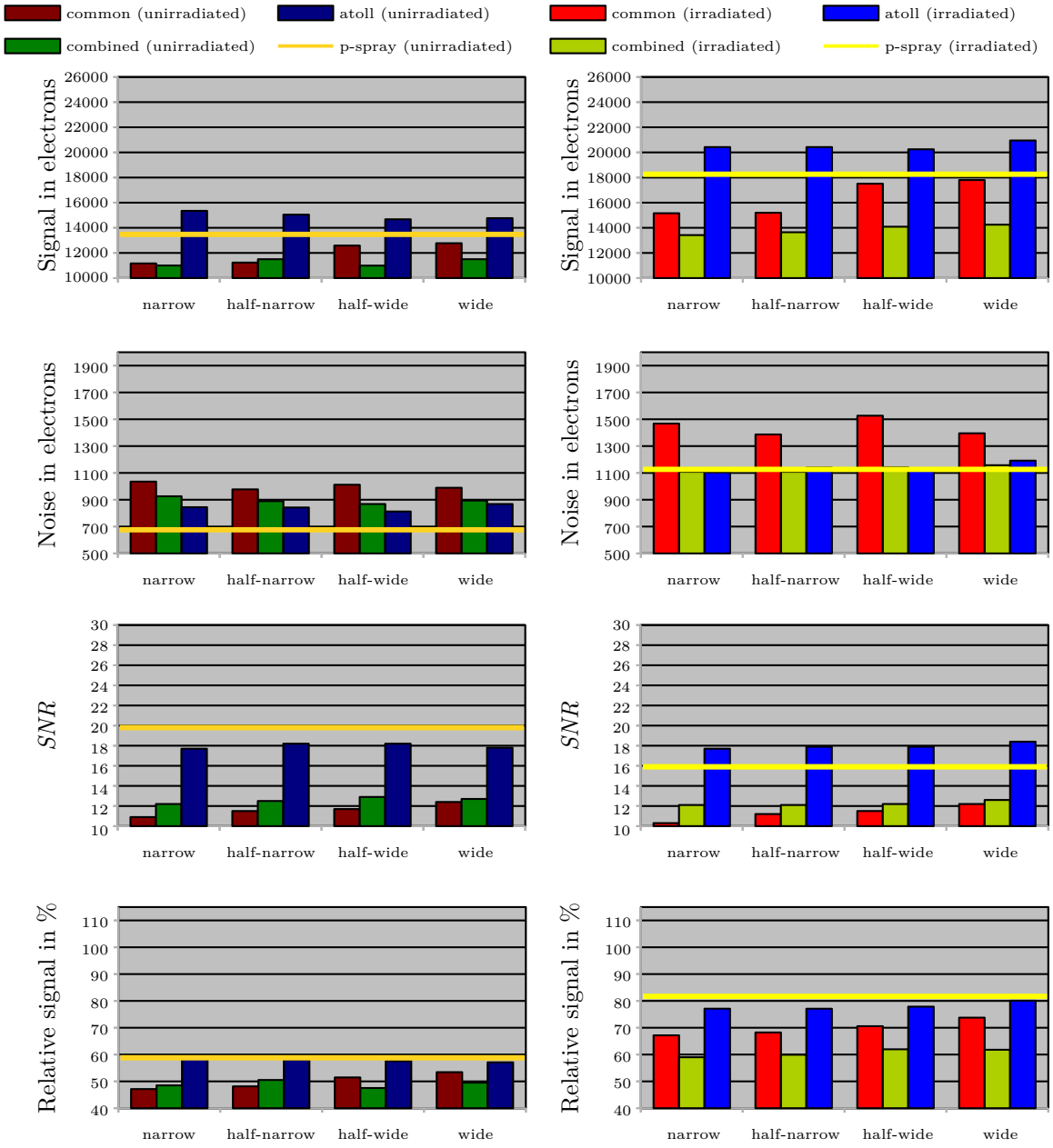

Figure 7.30.: Cluster signal, cluster noise and SNR for 2-strip-clusters, and relative signal of 2-strip-clusters w.r.t. 1-strip-clusters, data taken in 2012 for sensors with finer p-stop geometry variations and every second strip connected to the readout electronics (200 µm readout pitch with intermediate strips).
The left plots are before irradiation to 100 kGy, the right ones are after irradiation. Each measured quantity is the result of a fit to a histogram with about 30000 entries, taken from the better working one of two modules (i.e. the one with lower noise and higher SNR). The data of the p-spray method are the average of two data taking runs.

Table 7.5.: Cluster signal, cluster noise and SNR for 2-strip-clusters, and relative signal of 2-strip-clusters w.r.t. 1-strip-clusters, data taken in 2012 for sensors with finer p-stop geometry variations and every second strip connected to the readout electronics (200 µm readout pitch with intermediate strips). Green: best value within one p-stop pattern; Red: overall best value.

		narrow	half-narrow	half-wide	wide
Cluster signal in electrons, $\sigma(S) < 50$ electrons					
Common p-stop	unirradiated	11165	11234	12586	12774
	irradiated	15158	15196	17508	18800
Combined p-stop	unirradiated	11011	11503	10990	11507
	irradiated	13419	13645	14085	14247
Atoll p-stop	unirradiated	15349	15047	14677	14769
	irradiated	20423	20422	20248	20947
p-spray	unirradiated		13477		
	irradiated		18262		
Cluster noise in electrons, $\sigma(N) < 15$ electrons					
Common p-stop	unirradiated	1035	977	1012	989
	irradiated	1468	1387	1527	1396
Combined p-stop	unirradiated	926	890	868	894
	irradiated	1109	1108	1143	1168
Atoll p-stop	unirradiated	845	842	812	894
	irradiated	1104	1140	1119	1192
p-spray	unirradiated		676		
	irradiated		1126		
Cluster SNR, $\sigma(SNR) < 0.1$					
Common p-stop	unirradiated	10.9	11.5	11.7	12.4
	irradiated	10.3	11.2	11.5	12.2
Combined p-stop	unirradiated	12.2	12.5	12.9	12.7
	irradiated	12.1	12.1	12.2.	12.6
Atoll p-stop	unirradiated	17.7	18.2	18.2	17.8
	irradiated	17.7	17.9	17.9	18.4
p-spray	unirradiated		19.8		
	irradiated		15.9		
Relative signal in %, $\sigma(S_{\text{rel}}) < 1\%$					
Common p-stop	unirradiated	47.1	48.1	51.5	53.4
	irradiated	67.2	68.2	70.6	73.8
Combined p-stop	unirradiated	48.5	50.5	47.5	49.5
	irradiated	59.0	59.9	62.0	61.8
Atoll p-stop	unirradiated	59.2	58.1	57.6	57.1
	irradiated	77.1	77.1	77.9	80.1
p-spray	unirradiated		58.8		
	irradiated		81.7		

Comparison of the cluster signal-to-noise ratio

The third row of plots in figure 7.30 shows the SNR for clusters[23] of exactly two strips before and after irradiation. The effect of the different calibrations cancels out for the SNR – this is true even for measurements taken before and after irradiation – so that we can compare the values directly.

Before irradiation (left plot) the atoll p-stop proves unequaled performance among the p-stop patterns with SNR values around 18, without showing any significant dependence on the geometry variant. The combined and the common p-stop only play an underpart. The p-spray method surpasses the atoll p-stop with a SNR of 19.8 due to its very good performance in terms of cluster noise.

After irradiation (right plot) the p-stop patterns show no significant change relative to the performance before irradiation, which is surprising in its own right. Only the p-spray method suffers severely from irradiation and is busted to the second place with a SNR of 15.9, leaving the atoll p-stop to be the best option in terms of radiation hardness.

Comparison of the relative signal

The bottom two plots of figure 7.30 show the relative signal, i.e. the division of the MPV of the 2-strip-cluster signal by the MPV of the 1-strip-cluster signal. Like for the SNR also here the effect of the potentially different calibration of signal levels cancels out, making the results directly comparable.

The picture before irradiation (left plot) is similar to the one of the SNR: the atoll p-stop and the p-spray method are on top, the other p-stop patterns do not play a significant role.

After irradiation (right plot) the relative signal generally increases, where this increase is less pronounced for the combined p-stop. There is a faint increasing tendency when going to wide geometries for the common p-stop. The p-spray method was able to slightly break away from the atoll p-stop.

7.4.3. Irradiation effects on the SNR

The noise seen by a readout channel strongly depends on the capacitive load, which is the sum of the backplane capacitance ($C_{\text{back}} \approx C_{\text{total}}/\text{number of readout strips}$) and the interstrip capacitance C_{int}. Only C_{int} increases with irradiation [29]. For the sensors with every strip connected (i.e. with a small readout pitch) C_{int} is large, and so these sensors are

[23] Note that the computation of the cluster SNR ratio uses the individual strip noise values of the strips involved in the cluster, according to the definition in equation 7.2, and not the averaged cluster noise displayed in the second-row plots of figure 7.29.

very sensitive to radiation-induced changes. In contrast, the sensors with every second strip connected (i.e. with a large readout pitch) have halved C_{int} and doubled C_{back} per readout channel. Thus the increase of C_{int} after irradiation is less significant and counteracted by the signal increase.

7.4.4. Irradiation effects on the relative signal

The primary charge deposited in the detector material does not change with irradiation. However, the cluster signal of 2-strip-clusters measured by the readout electronics depends on the charge sharing between two readout strips, and is thus sensitive to irradiation effects. The relative signal increased after irradiation, thus suggesting reduced signal loss w.r.t. 1-strip-clusters. Already in the previous beam test we observed the effect of enhanced conductivity in the unimplanted regions between the strips after irradiation to 700 kGy (see section 7.3.3, figures 7.23, 7.24 and 7.25), which acts like an intermediate strip and improves capacitive coupling of the signal to the neighbouring readout strip. A small area of p-stop implantation is beneficial, and thus the relative signal improvement after irradiation is less pronounced for the combined p-stop.

7.4.5. Tracking and resolution estimation

We tried to estimate the resolutions of the baby sensors in order to find further differences between the strip insulation techniques. To do so, we processed the data of one measurement run with the unirradiated, normally read-out sensors (see figure 7.28a) with a standalone tool for alignment, tracking and resolution estimation of sensors in a beam test setup [53].

Due to the normal angle of beam incidence, there is a high percentage of clusters of size 1, between 62% and 73%. Because of the small distance between layers and the fact that all strips are parallel, there are strong correlations between hits with cluster width 1. Clusters of width > 1 are assumed to be uncorrelated. The high beam momentum of 120 GeV/c leads to negligible multiple scattering, which therefore cannot destroy the correlations. The alignment converges very quickly, as it is not affected by correlations between the hit position errors. The estimation of the resolutions, on the other hand, is affected by the correlations.

Unfortunately, it is not possible to estimate the full correlation matrix from the residuals of the linear least-squares fit, as the latter are confined to a subspace of lower dimension. A feasible solution is to use a nonlinear fit instead, for example an L_1 fit, which minimises the sum of the absolute residuals. As the tracks are nearly parallel, the L_1 fit can be approximated very well by the median of the hit coordinates of every track. We therefore estimate the correlation matrix from the residuals with respect to the track median. The results of the resolution estimation can be found in table 7.6.

Table 7.6.: Estimated point resolutions of the wide common p-stop, the narrow combined and atoll p-stop, and the p-spray method from unirradiated sensors with every strip connected to the readout electronics (100 µm readout pitch, no intermediate strips). The results of modules in parenthesis are not used in the beam test analysis.

Cluster width	COMM-1	(COMM-2)	SPRAY-1	(SPRAY-2)	COMB-1	(COMB-2)	(ATOLL-1)	ATOLL-2
1	23	(x)	24	(23)	27	(x)	(32)	23
2	15	(x)	17	(17)	24	(x)	(26)	19

Actually the resulting resolutions look very reasonable: SPRAY-1 and SPRAY-2 are identical and indeed have the same resolution; ATOLL-1 – known to have a noise problem – has the worst resolution. The resolution of COMM-1 seems to be somewhat underestimated, which is a consequence of the strong correlations. The distribution of the P-values of the total χ^2 is not uniform [53], which is a further indication that the estimated correlations are not the true ones. Clearly more work is needed on the problem of correlated errors. The results presented here can not be used to judge the insulation options.

7.4.6. Conclusions of the beam test 2012

In the previous beam test 2010 we identified the atoll p-stop to be the best strip insulation method for n-type strips. However, in the beam test 2011 the p-spray method proved to be a real competitor, but we had no results after irradiation. With the data from the beam test 2012 we can now confirm that the atoll p-stop indeed is the best match for our needs. This is best visible in the SNR values for the sensors with every second strip connected to the readout electronics, as displayed in the third row of figure 7.30. These sensors have a readout pitch of 200 µm and intermediate strips, which is a configuration close to the one of the full-scale sensors with their readout pitch of 240 µm with intermediate strips. While before irradiation we have a close call between the atoll p-stop and and the p-spray method, after irradiation the atoll p-stop is the clear favourite, as it turns out to be more radiation tolerant. With this finding we chose to equip the full-scale trapezoidal sensor with the atoll p-stop blocking method for the series production, keeping the photo masks which were redesigned after the beam test in 2010.

When trying to do particle tracking and resolution estimation *without* beam telescope we ran into problems with correlated measurement errors, which caused the reconstruction algorithm to deliver biased results. We prepared a module stack configuration which proved to be especially suboptimal for particle tracking: all sensors with the same strip direction and small distance to each other, in a high energetic beam at normal incidence. Future beam tests have to foresee measures to avoid these correlations.

7.5. Beam test experience - lessons learned

For successfully running a beam test, one should consider the following suggestions:

- Redundancy: Prepare more than one module per sensor type under test. This not only helps in the event of failure, it also opens the possibility to disentangle e.g. noise contributions from sensor and readout electronics.

- Irradiation: An irradiation campaign will usually take place at a different location than the beam test. This threatens the comparability and credibility of the results, but can usually not be avoided. However, one can strive for comparable and meaningful results by considering the following:

  - Dosimetry: The dose rate of a gamma source may not be constant in space but show a profile. Include dosimetry in close vicinity of the DUTs to know the exact amount of dose the DUTs were exposed to.
  - Dose rate: Choose a gamma source with low dose rate. This takes longer to irradiate, but the target dose is better controllable, and the DUTs won't heat up. So, you can be sure that the observed effects are due to irradiation only.
  - Testing after irradiation: It is beneficial to have the possibility to return the irradiated DUTs to the exact same setup they were tested in before irradiation. This ensures direct comparability of the results.

- Particle tracking: Position measurements from a beam test setup may be prone to strong correlations. To avoid those, one can either increase the number of 2-strip-clusters - which are uncorrelated - or one can try to decorrelate the position measurements themselves. These strategies can be implemented by adopting one of the following options:

  - A beam telescope provides well-known and accurate position measurements, which allow to estimate position resolutions even if the position measurements of the DUTs are correlated.
  - Rotation of the modules w.r.t. each other causes the coordinate directions to be different, uncorrelating the position measurements.
  - Inclination of the modules w.r.t. the beam diminishes the number of problematic 1-strip-clusters.
  - Extension of the distance between the modules will allow multiple scattering to decorrelate the position measurements.
  - A reduced beam energy causes multiple scattering to be more dominant, which in turn can decorrelate the position measurements.
  - Inclusion of additional passive material next to the modules also increases multiple scattering.

- Data analysis: When data is taken one can make an effort to extract meaningful results. It may be helpful to consider the following:

  - Event selection: Focus on events with cluster width 2. In a real detector normal incidence of a particle is a rare event, but it is the standard case in a beam test. Consequently, one will find a lot of 1-strip-clusters in beam test data, which doesn't reflect the situation in a real collider environment. To make things worse, the properties of 1-strip-clusters are vastly different from clusters with two or more strips, as is outlined in section 4.4. Therefore, 1-strip-cluster events and events with more strips have to be analysed separately *in any case*. For a sensor with 100 µm pitch about 25% of the events create 2-strip-clusters, so make sure to take enough data.
  - Observables: Keep in mind that signal and noise levels are subject to a calibration procedure, which may have some sources of inaccuracy. It is therefore advisable to focus on observables for which the calibration cancels out, like the SNR and the relative signal, when comparing sensor performances.

- Remote control of the beam test setup is a great help in making the beam test comfortable. A few computers with a screen sharing software installed do the trick, and one can keep an eye on the measurements even at night, without the need to pull an all-nighter inside the experimental hall. It also helps to be able to adjust things without the need of entering the beam zone, which always involves a lengthy procedure to switch off and turn on the beam. Of course, one still has to comply with the security regulations, which in some cases demand the counting rooms in the experimental hall to be always manned, as long as the measurement is carried out.

In Euclidean geometry, a convex quadrilateral with at least one pair of parallel sides is referred to as a trapezoid in American English and as a trapezium in English outside North America. The parallel sides are called the bases of the trapezoid and the other two sides are called the legs or the lateral sides (if they are not parallel; otherwise there are two pairs of bases).

Wikipedia on **Trapezoid**

8

Quality assurance of the trapezoidal DSSD

This section focuses on the measurements and tests performed on the full-scale trapezoidal DSSDs, which will be installed in the Belle II SVD's forward part. The sensors are described in further detail in section 6.2.1, the exact geometric layout for the mass production can be found in addendum 11.3.

While the baby sensors investigated in section 7 were designed for doing sensor R&D[1], the aim of the following studies is to demonstrate the capabilities of the full-scale sensor and to derive the expected performance when installed in the SVD. This has been done using electrical characterisation in the laboratory, beam tests including gamma irradiation and a long-term thermal cycling campaign.

[1] R&D: Research and Development

8.1. Electrical characterisation

The electrical characterisation took place in the QTC at HEPHY[2] Vienna [37], using the same equipment as was used for testing the baby sensors (see section 7.1.1).

8.1.1. Global measurements

The most fundamental quality characteristics of a silicon microstrip sensor are the IV- and CV-curves. As derived in section 3.5.1 these curves allow the determination of the full depletion voltage and the total dark current at full depletion, i.e. at the operating point. For these measurements, the SMU 1 applies a reverse bias voltage ramp between the bias rings of p-side and n-side while measuring the total dark current. The LCR meter measures the total capacitance in parallel. Figures 8.1 and 8.2 show these curves for all tested trapezoidal sensors. Note that the larger area of the full-scale trapezoidal sensors leads to a dark current one order of magnitude higher when compared to the baby sensors. Also, the total capacitance scales with the sensor area.

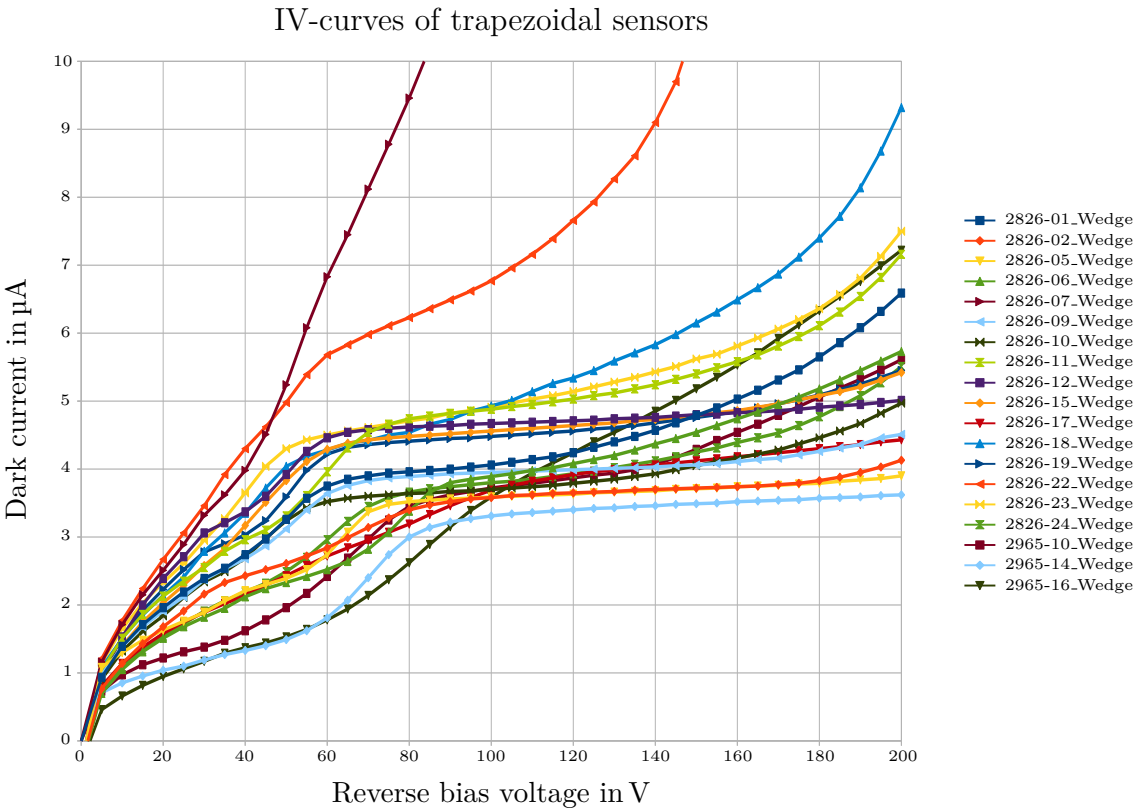

Figure 8.1.: Summary of IV-curves of all measured trapezoidal sensors. The sensor 2826-07_Wedge was dropped after unpacking, leading to interrupted guard rings and basically non-existent high-voltage stability.

[2]HEPHY: Institute of High Energy PHYsics

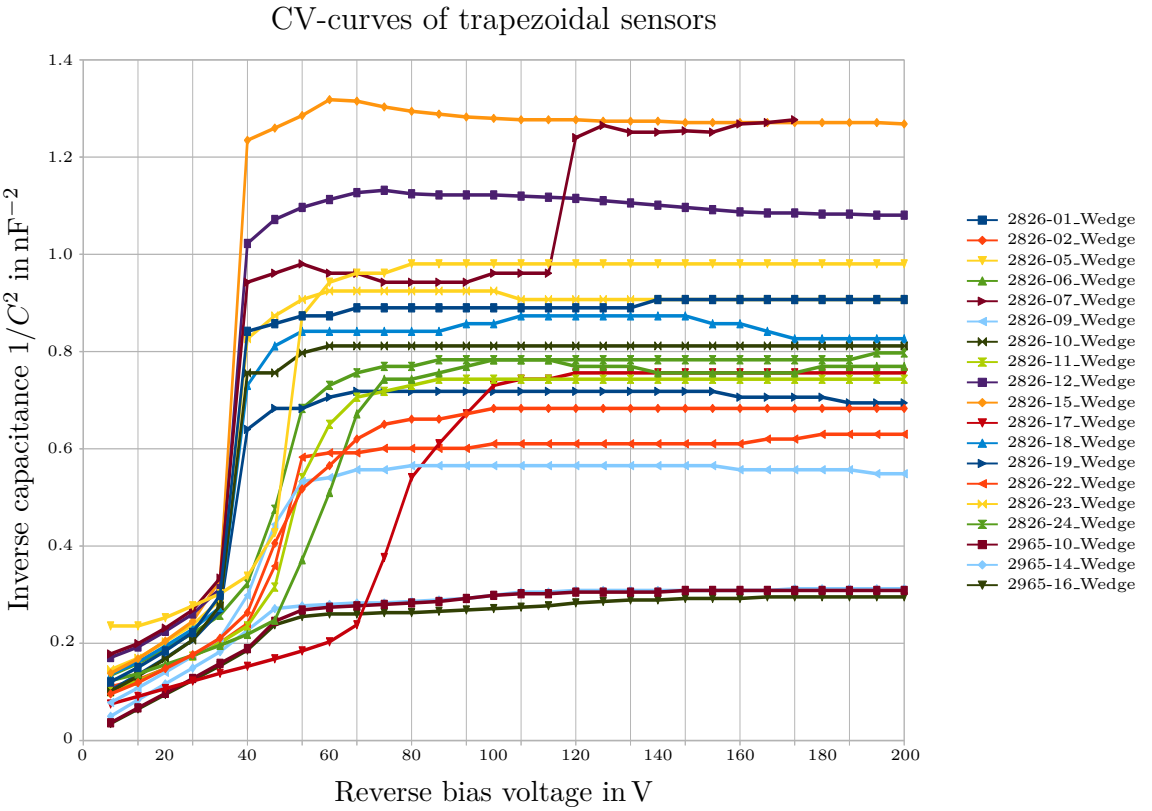

Figure 8.2.: Summary of CV-curves of all measured trapezoidal sensors. The LCR meter measures the total capacitance of the p-n-junction at a frequency of 1 kHz. Note that the capacitance of the sensors from the updated prototype batch 2965 is larger and more uniform, resulting in a smaller $1/C^2$ value (bottom three curves). The calculated nominal capacitance assuming a depletion thickness of 300 µm is 2.03 nF, corresponding to $1/C^2 = 0.24\,\mathrm{nF}^{-2}$.

8.1.2. Strip scans p-side

On the full-scale trapezoidal DSSDs the same quantities are measured as on the baby sensors (see section 7.1.3), but on both sides of the sensor. For the sensors with the initial design (batch 2826) the strip scans on the p-side are carried out on strips 1, 3, 5, etc. first and hereafter in the reverse direction on strips 767, 765, 763, etc. This is due to the staggered AC pads (see section 6.2.1). Slightly changing environmental conditions and sensor heating can therefore cause neighbouring strips to show differing measurements especially of the strip dark current I_{strip}. Moreover, the different pitches of the DC pads and the AC pads require repositioning of the probe needles about five times along the width of the sensor. In contrast, the sensors from batch 2965 with the updated design feature non-staggered AC pads with the same pitch as the DC pads. The strips of these sensors can be measured consecutively. Note that no strip scans were carried out for the sensors 2826_01_Wedge and 2826_19_Wedge.

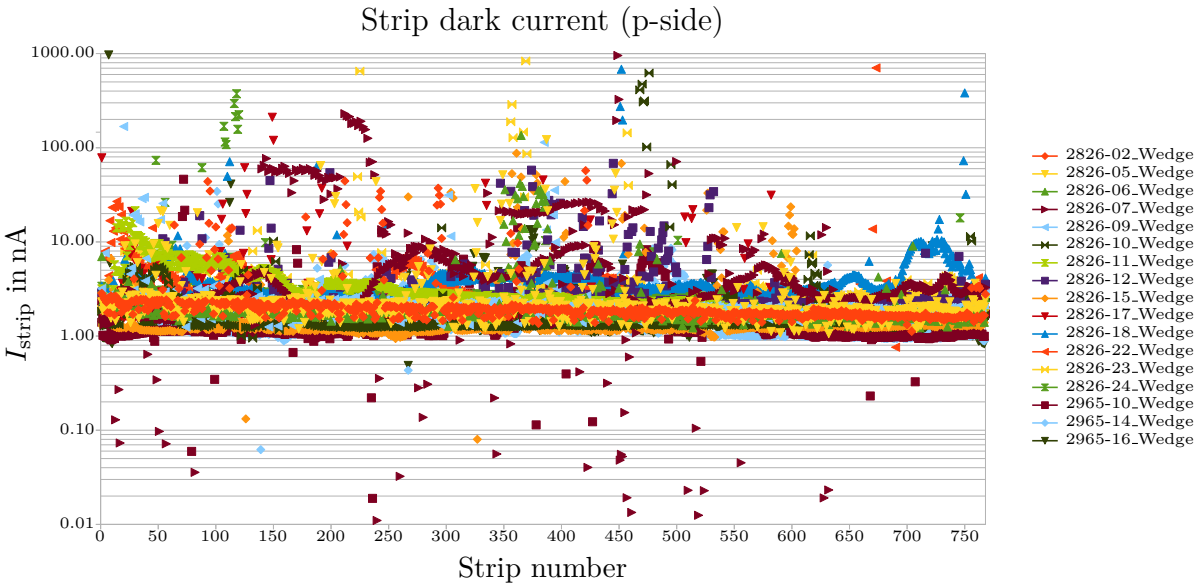

Figure 8.3.: Dark current I_{strip} as function of the strip number for the trapezoidal sensors' p-sides. Note the logarithmic scale of the y-axis. The sensors from all batches have similar strip dark currents in the order of a few nA. The damaged sensor 2826_07_Wedge shows regions with considerably elevated dark current. Also the sensors 2826_11_Wedge and 2826_18_Wedge display some non-conform regions.

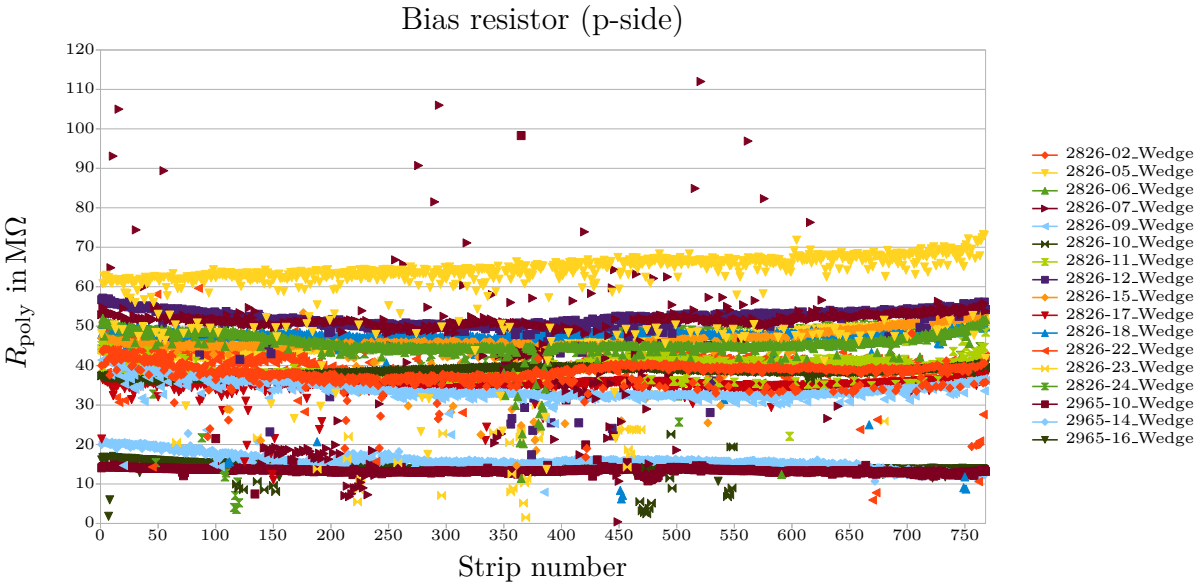

Figure 8.4.: Bias resistor R_{poly} as function of the strip number for the trapezoidal sensors' p-sides. The two batches show different values for the bias resistor: batch 2826 has $R_{\text{poly}} \approx 40 \ldots 60\,\text{M}\Omega$, the updated prototype batch 2965 implements the required value of $R_{\text{poly}} \approx 15\,\text{M}\Omega$.

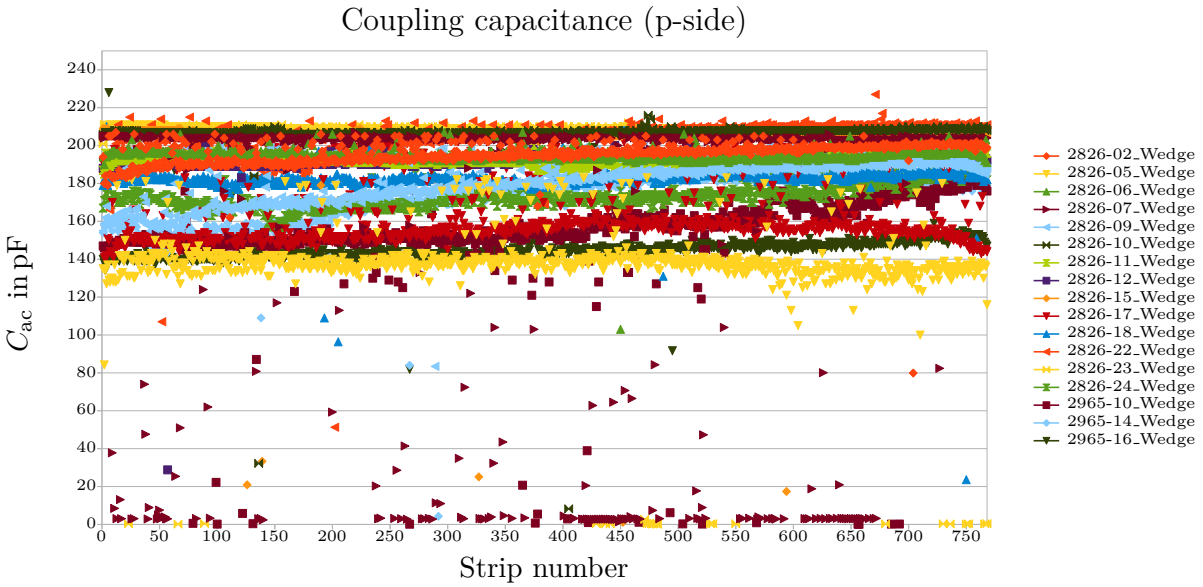

Figure 8.5.: Coupling capacitance C_{ac} as function of the strip number for the trapezoidal sensors' p-sides, measured at a frequency of 100 Hz. One can easily see that the capacitance i.e. the thickness of the coupling oxide slightly differs for different sensors in a range of about 60 pF. Especially the damaged sensor 2826_07_Wedge shows a lot of failed measurements. The measurements correspond to an average coupling oxide thickness of around 360 nm.

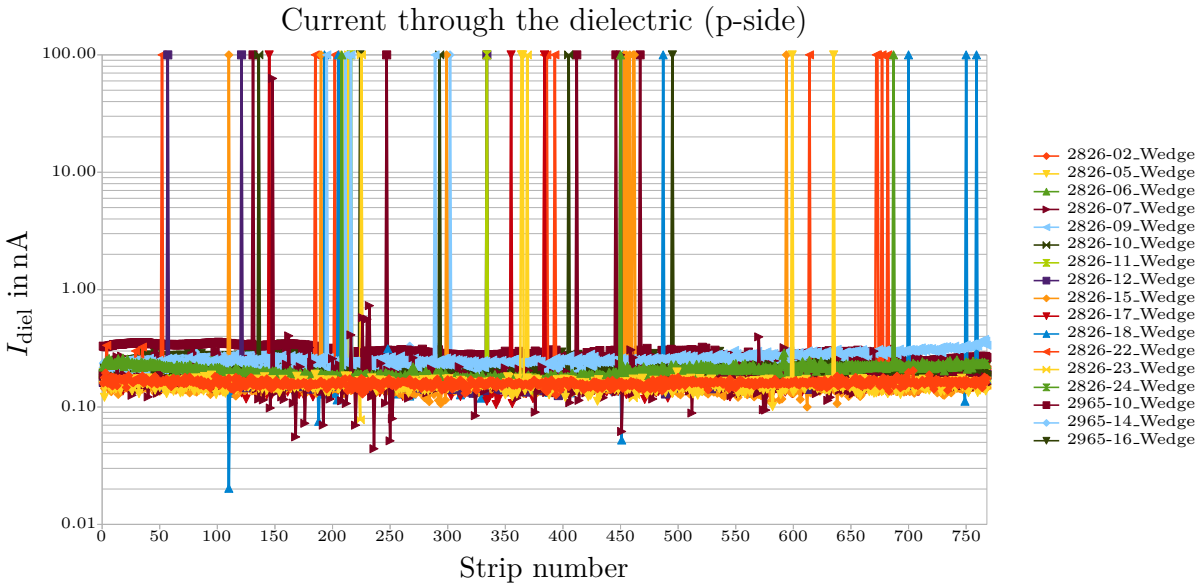

Figure 8.6.: Current through the dielectric I_{diel} as function of the strip number for the trapezoidal sensors' p-sides, when applying a potential difference of 10 V to the coupling capacitance. Note the logarithmic scale of the y-axis. The large spikes mark pinholes.

8.1.3. Strip scans n-side

The design of the trapezoidal sensors' n-sides is the same for the initial design (batch 2826) and the updated design (batch 2965), except for the strip insulation method. Batch 2826 implements the combined p-stop pattern, whereas batch 2965 uses the optimised atoll p-stop pattern (see also sections 6.2.1 and 7). However, this difference doesn't require different treatments for the strip scan, all n-side strips were measured consecutively in one go. Again, no strip scans were carried out for the sensors 2826_01_Wedge and 2826_19_Wedge.

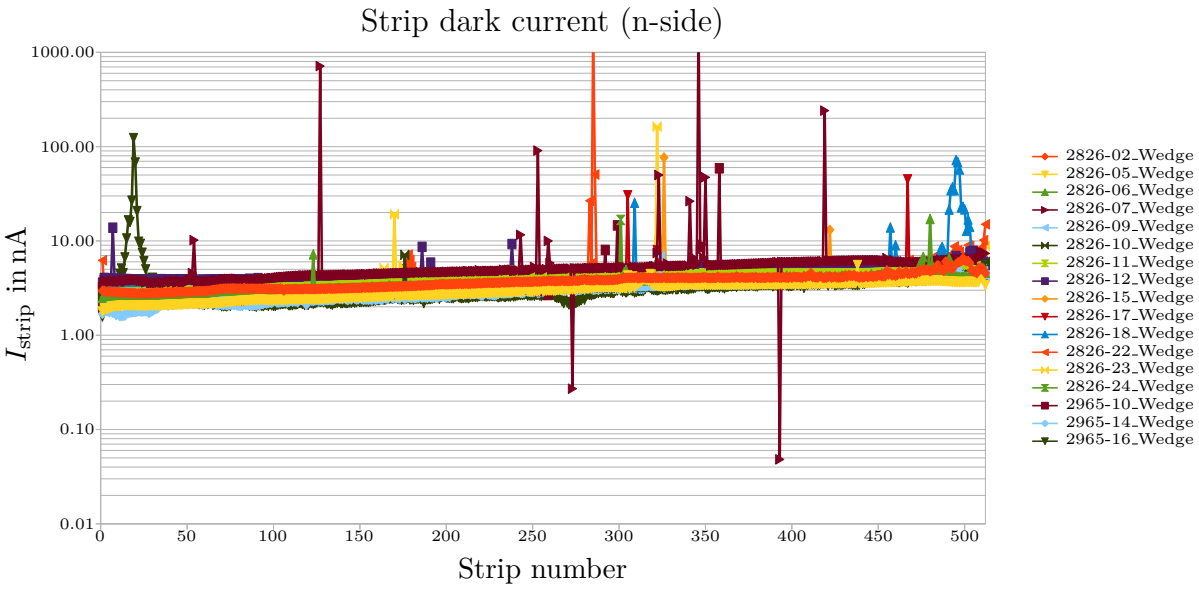

Figure 8.7.: Dark current I_{strip} as function of the strip number for the trapezoidal sensors' n-sides. Note the logarithmic scale of the y-axis. The sensors from all batches have similar strip dark currents in the order of a few nA. One can easily see an increase of the dark current for longer strips. The sensors 2826_18_Wedge and 2965_16_Wedge show some non-conform regions at the edges.

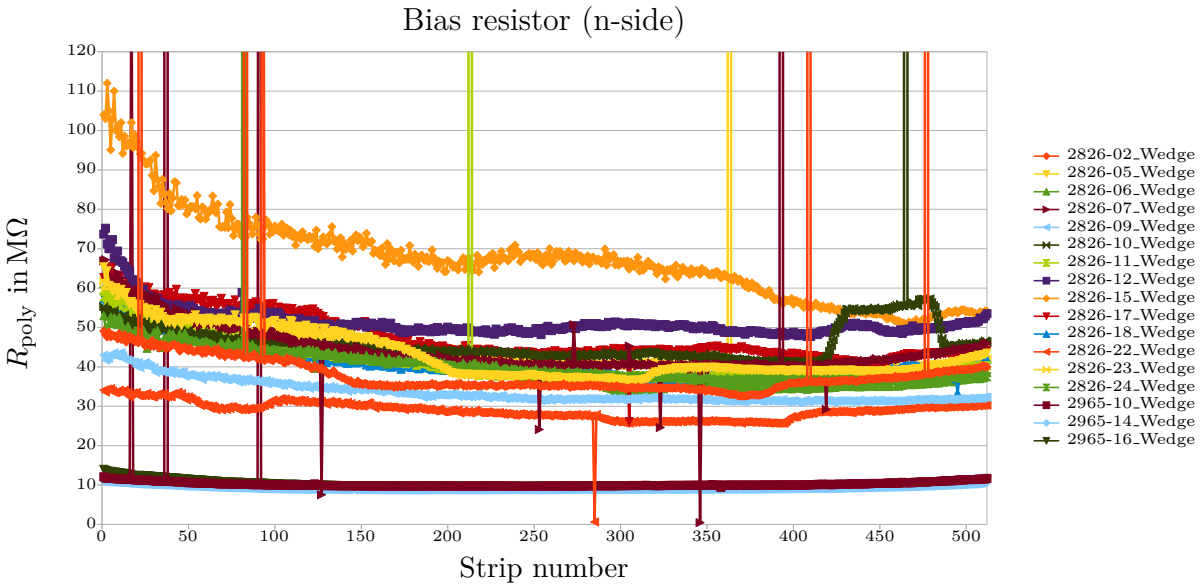

Figure 8.8.: Bias resistor R_{poly} as function of the strip number for the trapezoidal sensors' n-sides. The two batches show different values for the bias resistor: batch 2826 has $R_{poly} \approx 40 \ldots 60\,\mathrm{M\Omega}$, the updated prototype batch 2965 implements the required value of $R_{poly} \approx 15\,\mathrm{M\Omega}$. Some sensors of the initial prototype batch 2826 show quite adventurous curve shapes.

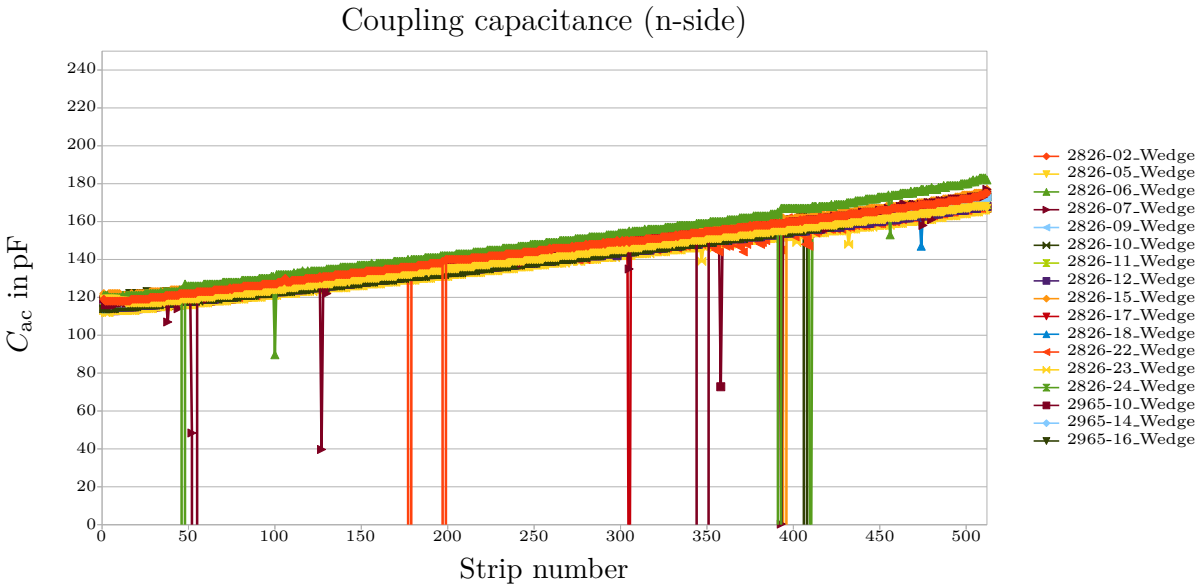

Figure 8.9.: Coupling capacitance C_{ac} as function of the strip number for the trapezoidal sensors' n-sides, measured at a frequency of 100 Hz. The capacitance i.e. the thickness of the coupling oxide is considerably more uniform for different sensors than on the p-side. One can clearly see the expected increase of the coupling capacitance for longer strips. The measurements correspond to an average coupling oxide thickness of around 360 nm.

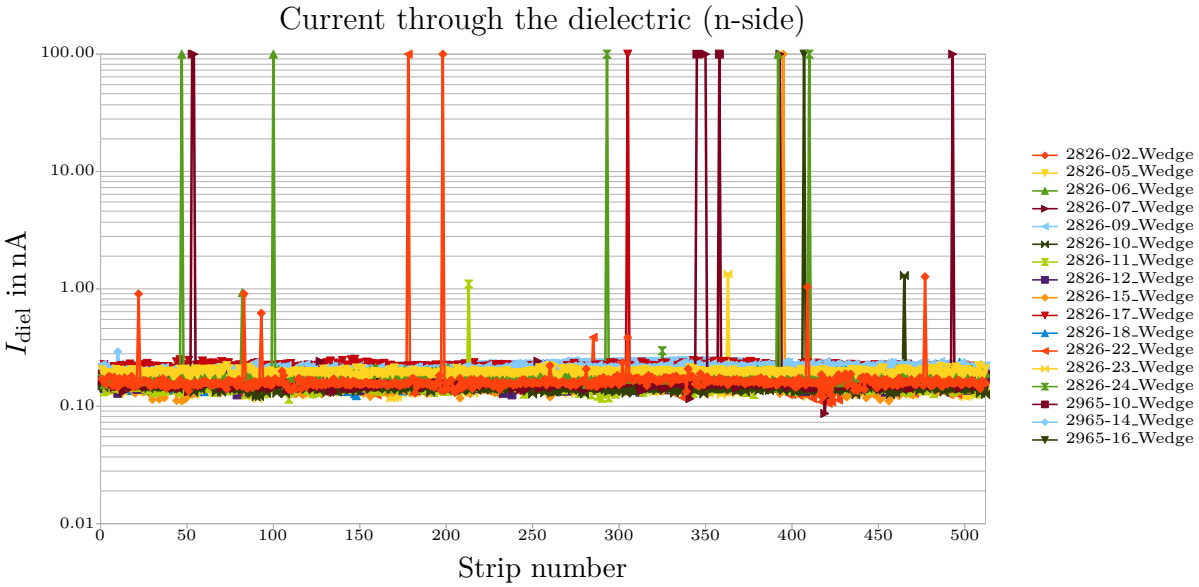

Figure 8.10.: Current through the dielectric I_{diel} as function of the strip number for the trapezoidal sensors' n-sides, when applying a potential difference of 10 V to the coupling capacitance. Note the logarithmic scale of the y-axis. The large spikes mark pinholes.

8.1.4. Conclusions

A thorough quality assurance analysis is given in [54]. Summing up, the sensors show less than 2 % faulty strips, where a faulty strip is defined as outside of the specifications given in table 2.5. The wrongly adjusted bias resistors of batch 2826 were not taken into account; the bias resistor is considered as faulty if it differs considerably from the average value of the individual sensor. Table 8.1 gives an averaged overview of the measured quantities and the percentage of faulty strips.

Table 8.1.: Summary of averaged stripscan results [54]. The coupling capacitance C_{ac} is normalized to a unit strip length of 1 cm.

	Observable	I_{strip}	R_{poly}	C_{ac}	I_{diel}
p-side	mean value	2.46 nA	43.5 MΩ	15.3 pF/cm	0.182 nA
	standard deviation	0.54 nA	4.31 MΩ	0.5 pF/cm	0.016 nA
	bad strips	1.50 %	1.95 %	0.66 %	0.53 %
n-side	mean value	3.75 nA	43.1 MΩ	29.7 pF/cm	0.168 nA
	standard deviation	0.72 nA	4.84 MΩ	0.27 pF/cm	0.011 nA
	bad strips	0.27 %	1.05 %	0.12 %	0.27 %

8.2. Long term measurement and thermal cycling

To determine the long term stability and ageing behaviour of the Belle II DSSDs, we performed a thermal cycling campaign testing two full-scale trapezoidal DSSDs and two large HPK DSSDs at the IISS[3] in Wiener Neustadt, which provided the possibility to use their climate chamber for three weeks. The measurement equipment included the following instruments:

- Climate chamber: CTS 200l, cycling the temperature between −20 °C and 100 °C, at the lowest possible relative humidity of about 1%. One full cycle took about two hours; we performed 286 cycles in total.
- SMU: Keithley 2410, applying a reverse bias voltage of 100 V to two sensors.
- Scanning Multimeter: Keithley K2700, taking readings every six seconds.
- PCB with shunt resistors.
- Readout: LabView via GPIB.
- Temperature and humidity monitoring: TRHX with two sensors. The presented readings are the average of the two sensors.

The sensors were glued to a base plate, one per vendor with the p-side up, and one per vendor with the n-side up (see figure 8.11). The sensors with p-side up were held under a reverse bias voltage of 100 V, and were connected to the SMU via the bias ring contacts and the n-sub pads. These pads are low-resistance contacts to the n-type substrate residing on the p-side, which allow to operate the sensor even if the bias ring contact pads of the n-side are not accessible. For these sensors the dark current was monitored by repeatedly measuring the voltage drop at well-known shunt resistors. Note that the sensors with n-side up were *not* biased. On all sensors every fourth aluminium strip was daisy-chained and the resistance of this long aluminium line was monitored. See table 8.2 for details.

Table 8.2.: The sensors used for the thermal cycling campaign, and the dimensions of the daisy-chained aluminium lines in µm. Note that the length and width values are calculated using the geometrical specifications given in the data sheets in addendum 11.1 and 11.3, whereas the thickness of the aluminium layer was determined by electron microscopy on *different* sensors from the same batch [55].

Sensor	side up	length	width	thickness	# squares
2826-18_Wedge	n-side	6022464	40	1.41	150561.6
2826-24_Wedge	p-side	11435899	25	1.34	457436.0
B2HPK_10938-9239_04	n-side	7183260	40	1.52	179581.5
B2HPK_10938-9239_17	p-side	11445440	20	1.47	572272.0

[3] IISS: Institute for Integrated Sensor Systems

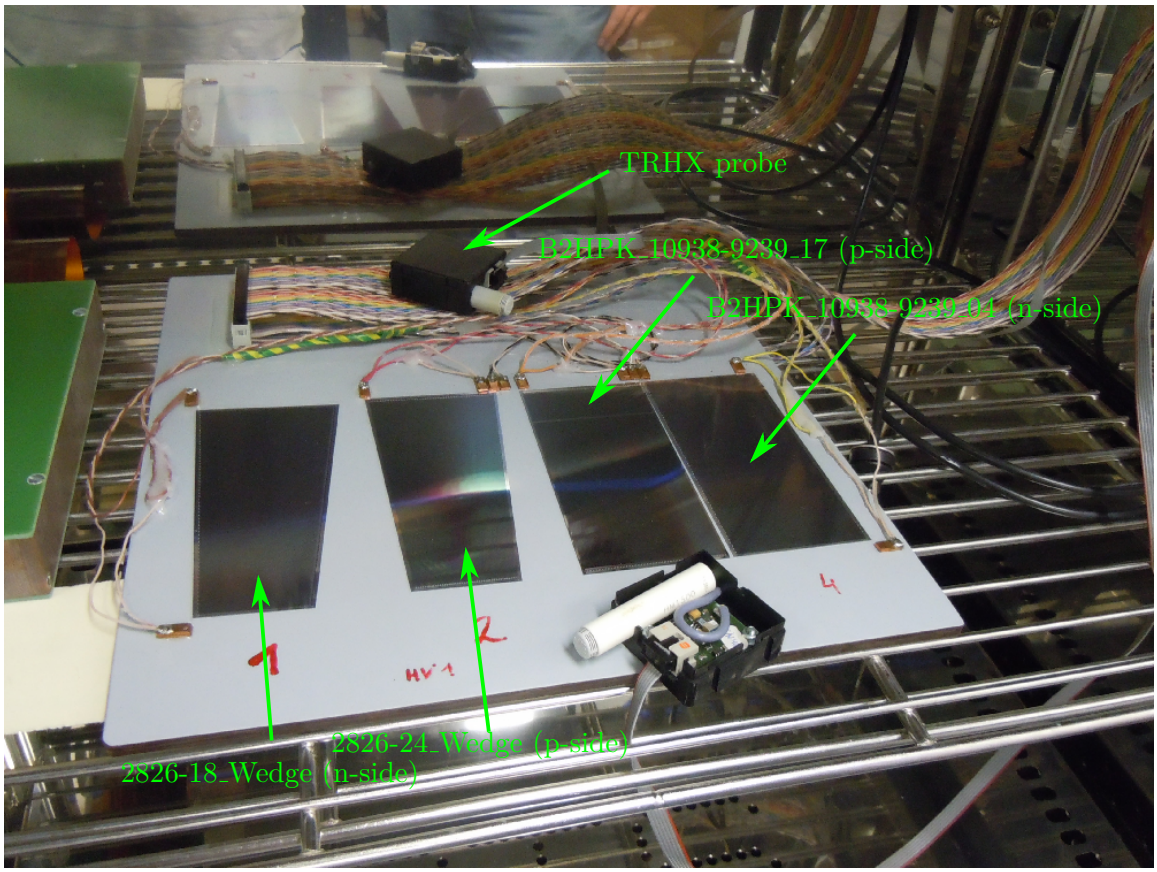

Figure 8.11.: The sensors used in the thermal cycling campaign were mounted on a base plate and connected to the periphery using copper pads glued to the base plate. Only the sensors with p-side facing up were biased and their dark current was measured. The actual temperature and relative humidity were monitored using two TRHX sensors. The cables were guided through a sealable feedthrough on the right side, the window in the door was shaded by a light-proof tissue.

8.2.1. Dark current

As mentioned before, the dark current was monitored on the sensors 2826-24_Wedge and B2HPK_10938-9239_17 only. Figure 8.12 shows the course of the dark currents over the whole time of measurement. The dark current changes from 0.2 µA at −20 °C to about 210 µA at 100 °C. The upper value corresponds to the current limit set by the SMU. While the HPK sensor was very stable during the whole period of data taking, the Micron sensor showed some kind of initial transient response, during which the low-temperature dark current limit dropped from 8 µA to 0.2 µA. After this phase, it showed the same stability as the HPK sensor.

There were two glitches during the data taking, during which the dark current measurement failed. These glitches occurred on Saturday at 12 am and on Sunday at 3 pm, thus ruling out interruptions by working people. Figure 8.13 shows a zoom to the second glitch, and also visualises the course of temperature and relative humidity. The temperature profile was

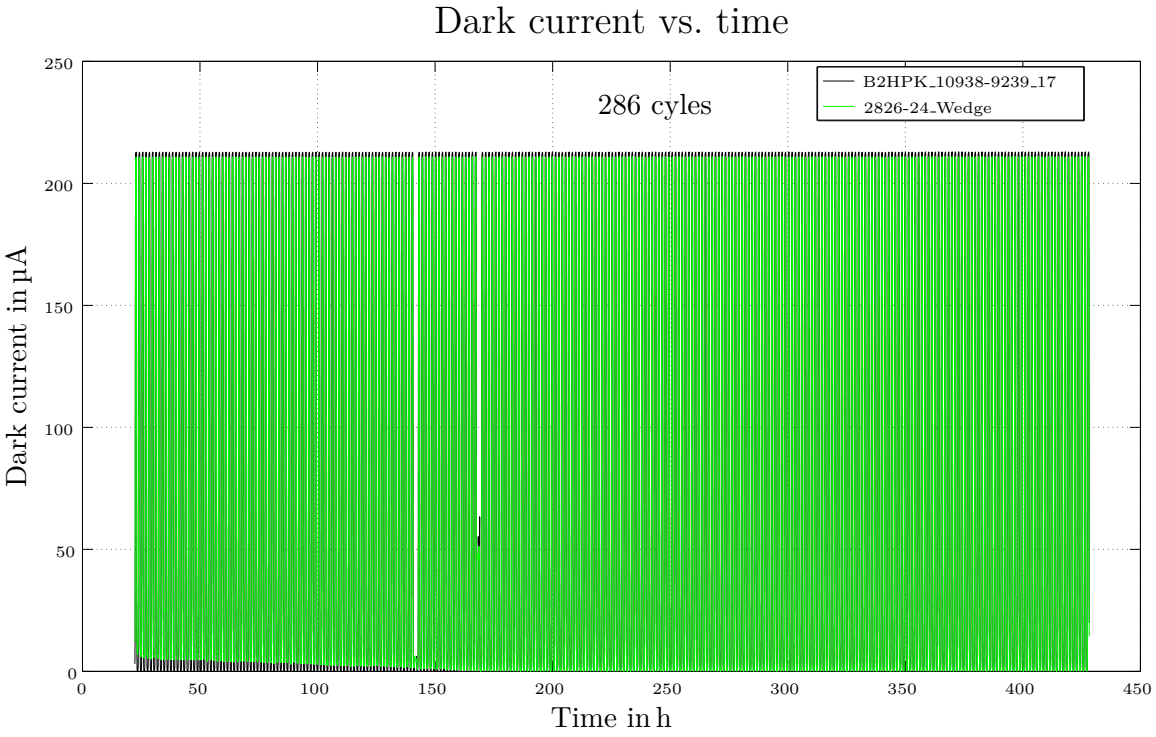

Figure 8.12.: Dark current as function of the whole measurement time. We monitored 286 temperature cycles during three weeks. The HPK sensor (black) was perfectly stable, while the Micron sensor (green) showed some kind of initial transient behaviour. The two measurement glitches occurred during the weekend, suggesting a purely equipment-related interruption.

set to form plateaus at −20 °C and 100 °C lasting for 20 minutes to allow the inside of the climate chamber to settle at the target temperature. The form of the measured temperature shows the chamber's thermal inertia due to the thermal mass. Note that the SMU limits the dark current to about 210 µA to protect the sensors.

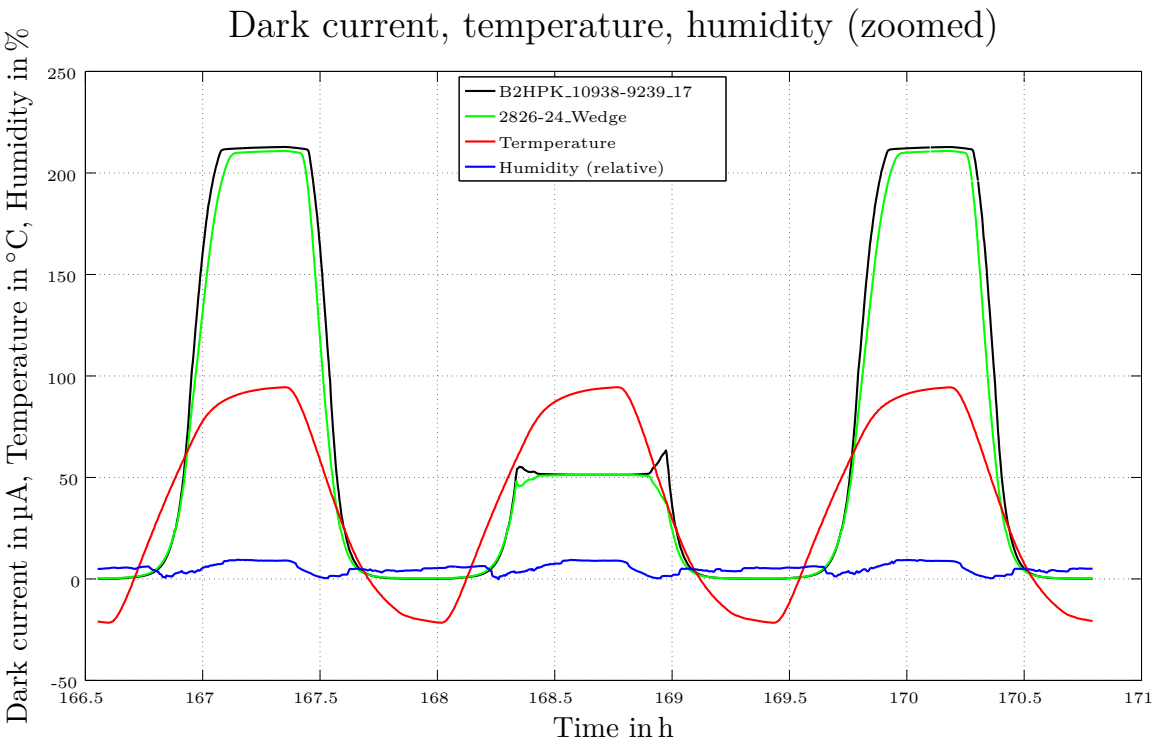

Figure 8.13.: Dark current, temperature and relative humidity as function of time, zoomed to the second measurement glitch. The sensors's dark currents are limited by the SMU. Note that the measurement glitch occurred for the current measurement only.

Figures 8.14 and 8.15 show the dark current as function of the temperature for the HPK sensor and the Micron sensor, respectively. One can clearly see the hysteresis resulting from the thermal mass of the sensor. Note the logarithmic scale of the y-axis. The measurement glitches manifest themselves as horizontal outliers. Keep in mind that the hysteresis is warped at the high temperature limit due to the SMU's current limit setting.

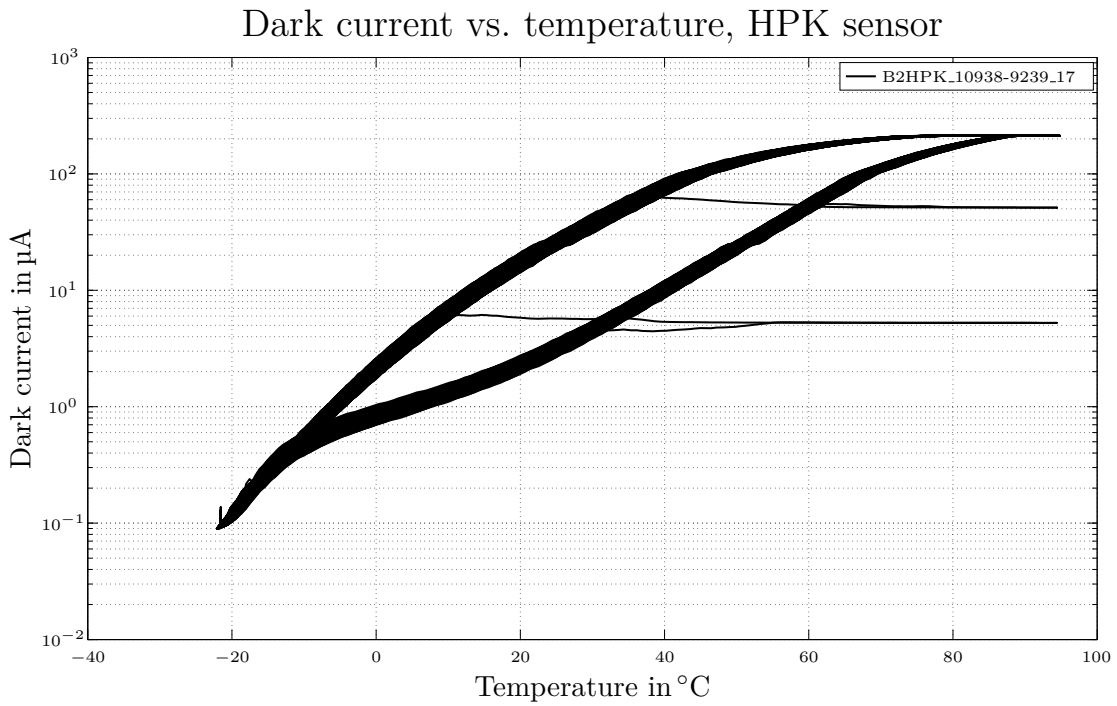

Figure 8.14.: Dark current as function of the temperature for the HPK sensor. One can clearly see that – apart from the measurement glitches – the HPK sensor worked very stably during the whole thermal cycling campaign.

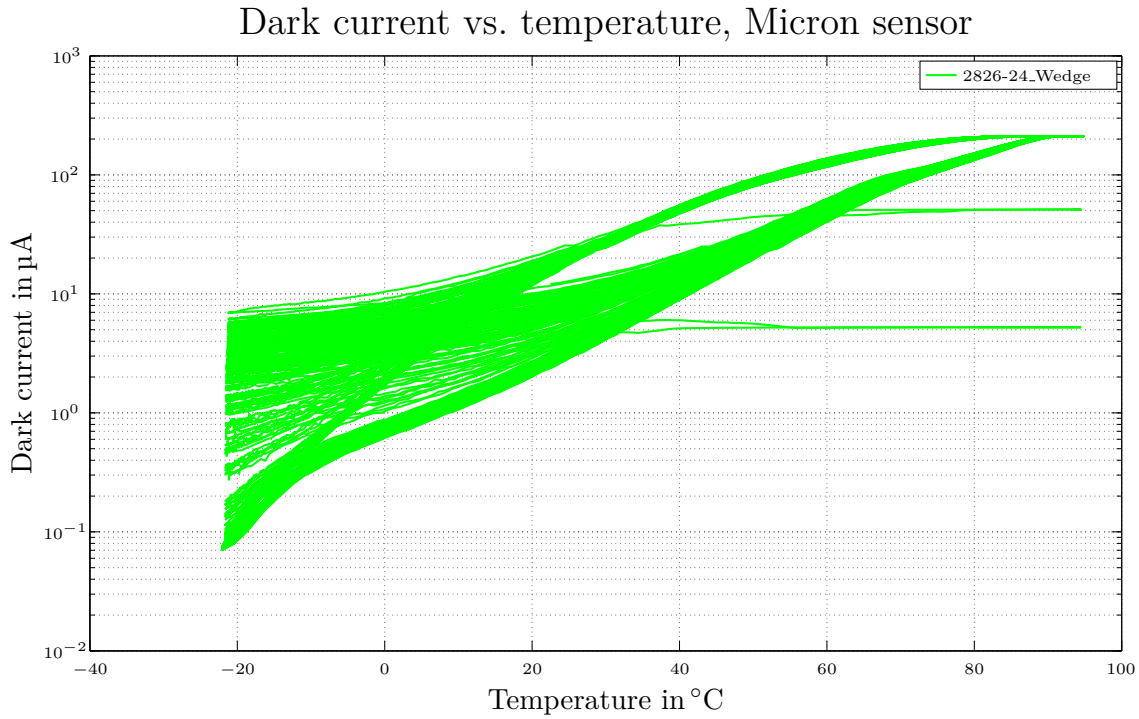

Figure 8.15.: Dark current as function of the temperature for the Micron sensor. The initial transient behaviour of the low-temperature current is clearly visible in form of fanned-out curves in the left part of the diagram.

8.2.2. Aluminium resistance

The resistance of the aluminium layer was monitored on all sensors, regardless of whether it was biased or not. The dimensions of the daisy-chained aluminium lines can be found in table 8.2. The scanning multimeter measured the total resistance of each connected aluminium line every time when also dark current, temperature and humidity were measured. Figure 8.16 shows a zoom to the normalised resistance as function of the time. The total (measured) resistance is divided by the number of squares and the thickness of the aluminium layer. Note that the thickness was measured on *different* sensors from the same batch using electron microscopy.

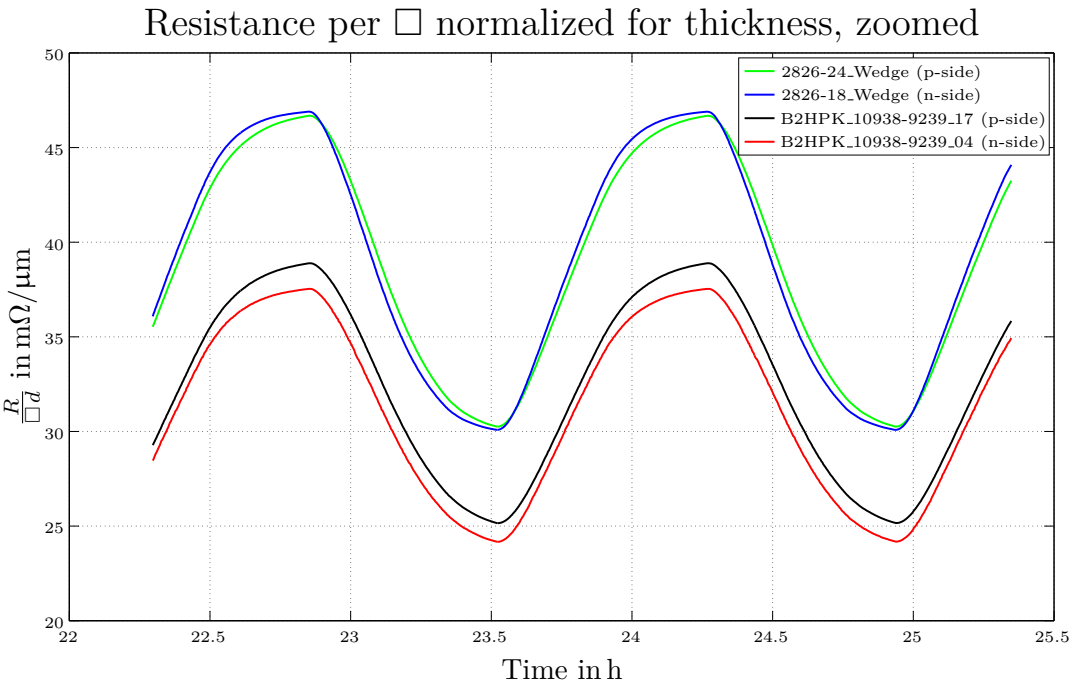

Figure 8.16.: Resistance per square as function of time, normalised to unit thickness. Micron (green and blue) uses an aluminium alloy with higher specific resistance than HPK (black and red), the thickness normalisation indeed makes the curves of p-side and n-side congruent. The readings from the HPK sensors show some difference even after thickness normalisation, suggesting that the sensor used here has a slightly different aluminium thickness than the sensor used for the electron microscopy.

It is obvious that Micron uses an aluminium alloy with higher specific resistivity than HPK. It furthermore catches the eye that for the Micron sensors the thickness normalisation indeed makes the resistance curves of both sensor sides practically congruent, while some discrepancy remains for the HPK sensors. This is due to the fact that the actual thickness of the aluminium layer may vary slightly from wafer to wafer, even if they come from the same batch.

Figures 8.17 and 8.18 show the normalised resistance as function of the temperature for the HPK sensor and the Micron sensor, respectively. One can observe that the hysteresis is more pronounced for the p-side measurements, which have a higher thermal mass due to

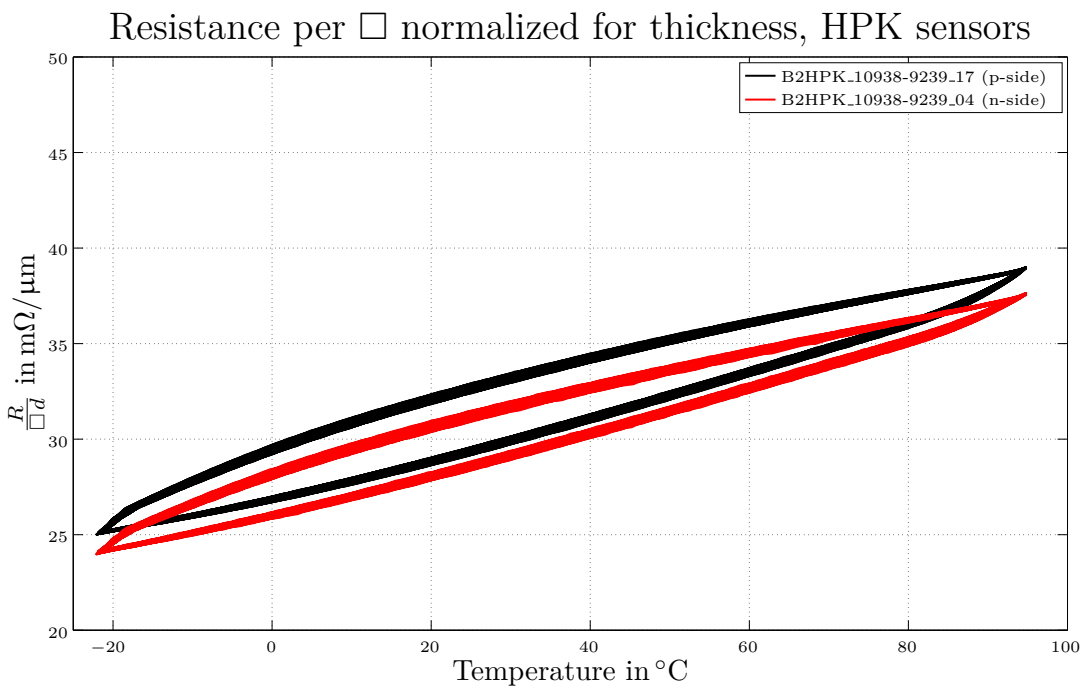

Figure 8.17.: Resistance per square as function of temperature for the HPK sensors, normalised to unit thickness. No sign of ageing is visible, the measurements indicate perfectly stable behaviour.

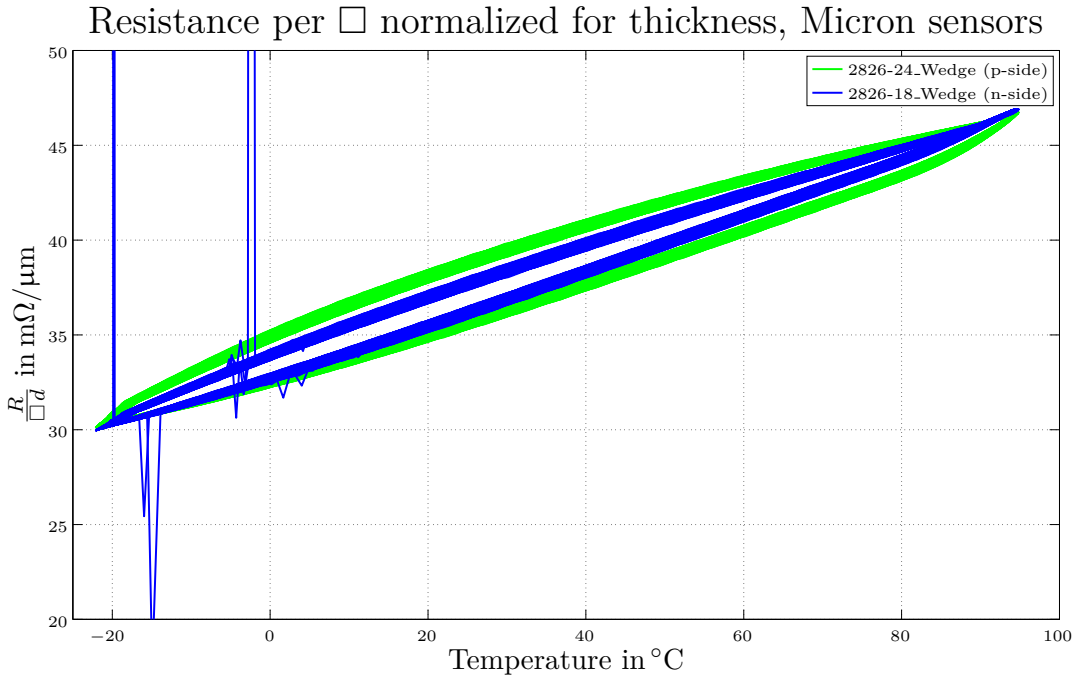

Figure 8.18.: Resistance per square as function of temperature for the Micron sensors, normalised to unit thickness. No sign of ageing is visible, the measurements indicate perfectly stable behaviour – apart from a few failed measurements. The initial transient behaviour seen in the dark current measurement has no influence on the aluminium resistance.

the larger number of squares of the aluminium line (refer to table 8.2). It is furthermore noteworthy that the measurement glitches of the dark current measurement don't show up for the resistance measurement, ruling out a malfunction of the scanning multimeter. These glitches therefore must have been caused by the SMU. The normalised resistance shows no sign of ageing.

8.2.3. Conclusions

The sensors used in the thermal cycling campaign showed a high degree of long-term stability. For the sensor 2826-24_Wedge an initial transient behaviour of the dark current was observed, which had no impact on the excellent ageing behaviour. The resistance measurement was constant over the whole time of measurement, leaving no clue for possible changes in the aluminium layer. Summing up, the sensors both from HPK and from Micron proved to be capable to withstand temperature oscillations between $-20\,^{\circ}\mathrm{C}$ and $100\,^{\circ}\mathrm{C}$ over an extended period of time without changing their behaviour, which makes them applicable to the use-case of the Belle II SVD.

8.3. Beam test results

The full-scale trapezoidal sensors have been tested in all beam tests from 2010 to 2012 to ensure operability of the first prototypes and to determine their performance. However, here we present only results from the beam test 2012, where we put a sensor from the initial batch 2826 and one from the updated batch 2965 on the beam together, applying realistic cooling and close-to-final readout electronics.

Table 8.3.: The tested full-scale trapezoidal and rectangular sensors and the module names used in the beam test 2012. The sensor names follow the convention of the Belle II construction database.

Sensor name	Module name	Comment
2826-09_Wedge	Wedge_Old	combined p-stop
2965-14_Wedge	Wedge_New_1	atoll p-stop, 1 faulty n-side APV25
2965-16_Wedge	Wedge_New_2	damaged during transport
B2HPK_202012007048	Origami_3	*not* taken to the irradiation
B2HPK_202012007046	Origami_4	taken to the irradiation

Table 8.3 shows the full-scale DSSDs which were assembled to beam test modules. Apart from two Origami modules (see section 2.4 for details about the Origami chip-on-sensor concept) we prepared three modules holding trapezoidal sensors. We could not build more because of a lack of pitch adapters. These three modules held one sensor from the initial batch 2826 with the combined p-stop pattern as n-side strip insulation, and two sensors from the updated batch 2965 with atoll p-stop and updated p-side pad layout. Please refer to section 6.2.1 for details about the layout differences, and see Addendum 11.3 for a complete data sheet detailing the updated layout of the trapezoidal sensor.

Figures 8.19a and 8.19b show an opened beam test module as seen from p-side and n-side, respectively. Please pay special attention to the vastly different lengths of p-side and n-side pitch adapters. The hybrid boards are prototypes of the ones to be used in the Belle II SVD, and are mounted back-to-back separated by a thin sheet of electrically insulating and thermally conductive Sil-Pad.

The DUTs were tested in the beam, the two trapezoidal modules and one of the Origami modules were irradiated to 100 kGy (see section 7.2.1), and tested again in the same beam test setup as before, with a split reverse bias voltage of $\pm 50\,\mathrm{V}$ applied. The module Wedge_New_2 suffered transportation damage and could not be used for tests.

To achieve conditions as close as possible to the real use case, the readout chips of all modules were cooled using the open CO_2 system described in section 2.5. The coolant temperature was set to $-20\,^{\circ}\mathrm{C}$, whereas temperature sensors mounted to the cooling pipes in direct vicinity to the readout electronics indicated actual temperatures of $-33\,^{\circ}\mathrm{C}$ for the Origami modules and $-15\,^{\circ}\mathrm{C}$ for the trapezoidal ones. Note that the coolant temperature depends strongly on the pressure inside the cooling pipe and can vary due the cooling pipe

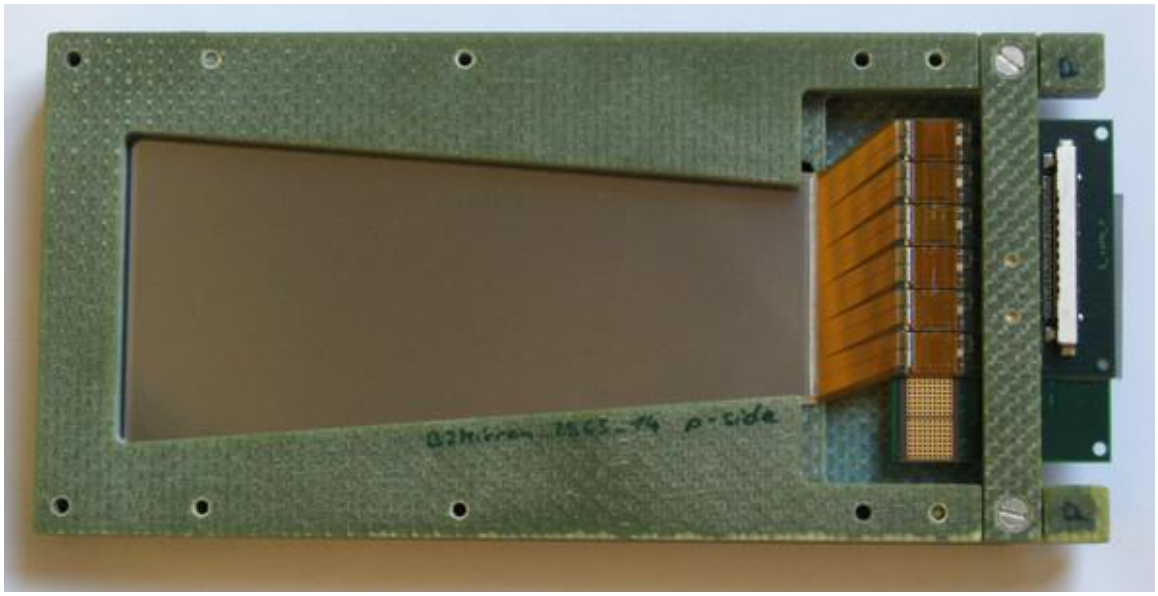

(a) p-side

(b) n-side

Figure 8.19.: A beam test module holding a trapezoidal sensor is opened to reveal the sensor's p-side (a) and n-side (b). Note that the pitch adapters have considerably different lengths. The p-side hybrid board houses six APV25 chips (only four of which were read out) and is mounted back-to-back to the n-side hybrid board. The APV25 chips of both sides are in thermal contact, cooling is done on the p-side only. The used pitch adapters stem from an early prototype production, with the final design the hybrid boards will be congruent.

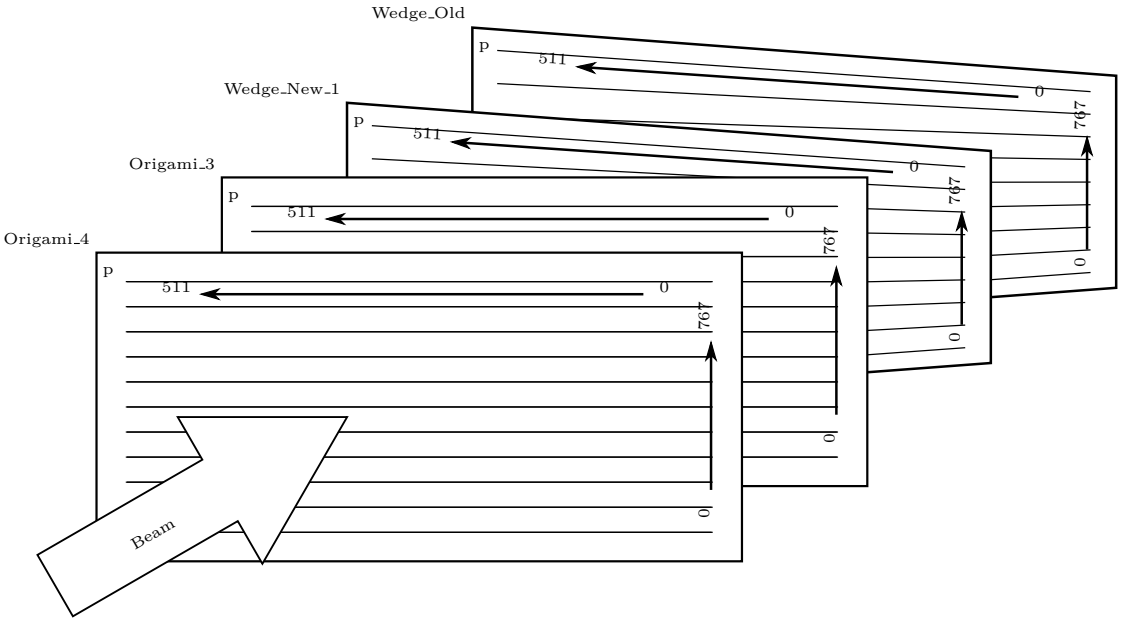

Figure 8.20.: The full-scale module stack from 2012 consists of four modules housing two large rectangular sensors from HPK and two trapezoidal sensors from Micron, one from batch 2826 with common p-stop strip insulation on the n-side, and one from batch 2965 with updated design and atoll p-stop. All sensors face the beam with the p-side.

routing and connectors. A cooling block makes contact to the p-side APV25 chips via a sheet of thermally conductive gap pad, the n-side readout chips are cooled by thermal contact of the back-to-back hybrid boards.

The readout system and triggering scheme is the same as in 2011, see section 7.2.2, and the same observables as described in section 7.2.3 were measured. In the analysis we selected events with exactly one 2-strip-cluster, individually for each sensor. This suppresses ambiguous events like particle splashes. Figure 8.20 shows details about the stack configuration. A photo of the stack can be found in figure 8.21, also showing the cooling tubes.

We aimed the beam at three different positions on the sensors, as is sketched in figure 8.22. Note that the p-side of the sensors needs six APV25 chips for reading out all strips, but the readout system allowed only for four APV25 chips to be read out. Therefore, the beam was directed to the lower two-thirds of the sensors. The module Wedge_New_1 showed one faulty APV25 chip on the n-side, so that the very narrow side of the trapezoidal sensors could not be read out. We recorded 150000 triggers at the wide and narrow positions, and 60000 triggers at the central position, both before and after irradiation.

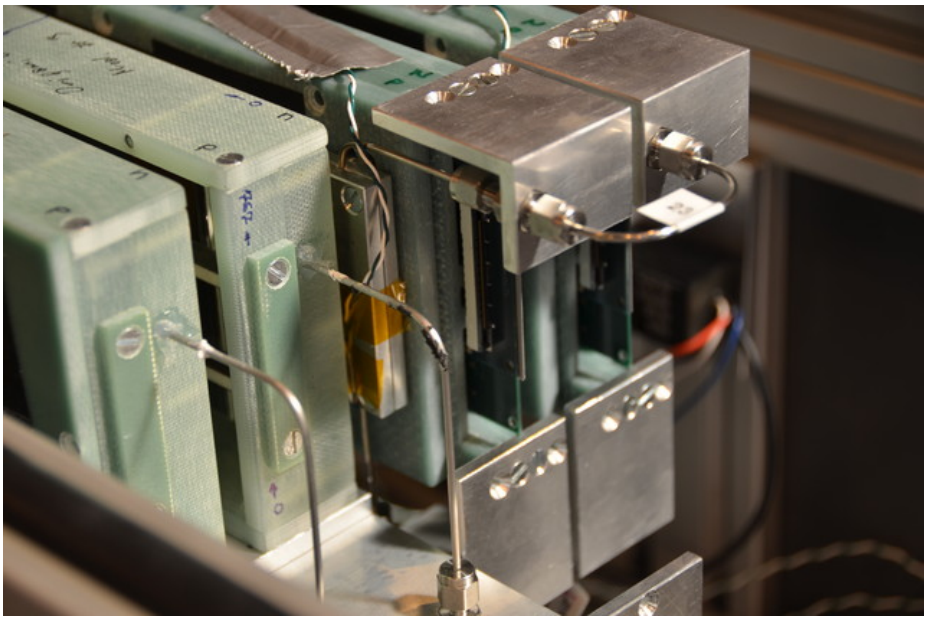

Figure 8.21.: The full-scale modules are cooled using the prototype open CO_2 cooling system.

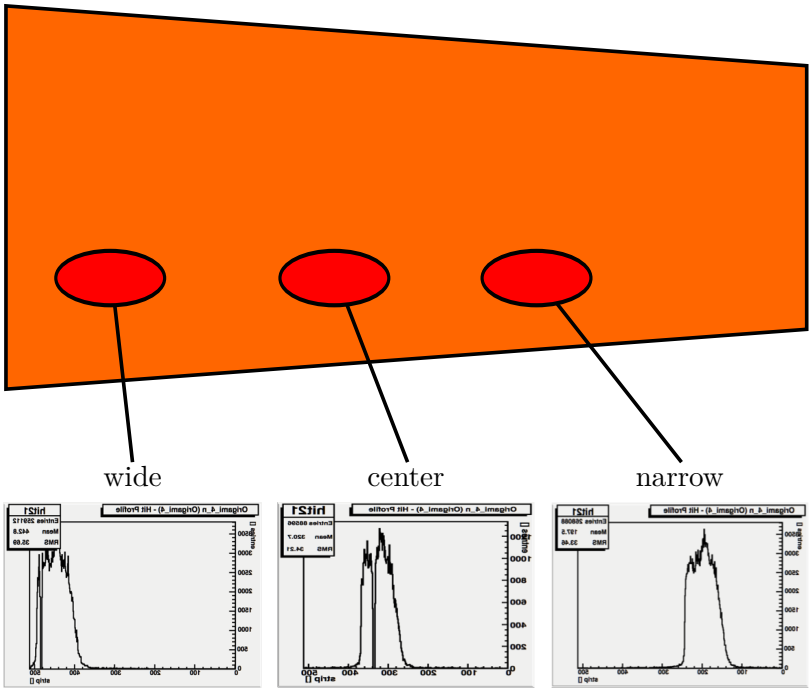

Figure 8.22.: The beam was directed to three different positions in terms of n-side strip number. Note that the upper third of the sensors was not read out due to the limited number of readout channels of the readout system. One module showed a faulty n-side APV25 chip, so that the very narrow side of the trapezoidal sensors could not be read out. The counting direction of the n-side strips is from right to left, consequently the beam spot diagrams appear mirrored.

8.3.1. Performance of the p-side

Comparison of the cluster signal

The top two plots of figure 8.23 show the most probable cluster signal of the full-scale DSSDs, where the values found in the left plot are before irradiation to 100 kGy and those in the right plot are after irradiation.

We observe that in the unirradiated case the most probable cluster signal of the Origami module is highest, while the trapezoidal sensor with the old design has some advance over the updated design.

After irradiation the trapezoidal sensor with the initial design shows a clear dependence of the cluster signal on the beam position, while the sensor with updated design still behaves levelled. Still the Origami module shows the best signal.

Due to uncertainties of the calibration one has to be careful when comparing the absolute values of the signals. Each beam position is read out by a different APV25 chip, and strictly speaking one can only compare signal values read out by the same chip. Especially values before and after irradiation can not be compared due to different readout chip settings. For a direct comparison consider the SNR and the relative signal *only*!

Comparison of the cluster noise

The second row of plots in figure 8.23 shows the average cluster noise for clusters of exactly two strips $\bar{N}_{n=2} = \sqrt{2}\bar{N}_{\text{strip}}$, where $\bar{N}_{\text{strip}}$ is the noise averaged over all strips of the whole sensor. Again, the left plot is before irradiation to 100 kGy and the right one is after irradiation.

We observe that in the unirradiated case the average cluster noise is very flat, as can be expected, because the full-scale sensors have no zones for which the noise would be calculated individually. It is clearly visible that the Origami module has a noise figure considerably larger than the two trapezoidal modules. This is mainly due to the long pitch adapters wrapped around the sensor edge to connect to the p-side strips (see figure 2.12 for details).

After irradiation the old trapezoidal module shows a considerable noise increase, setting it apart from the new trapezoidal module. The Origami module still displays the worst noise figure.

Again, for comparison of noise levels the same restrictions apply as for the cluster signal levels!

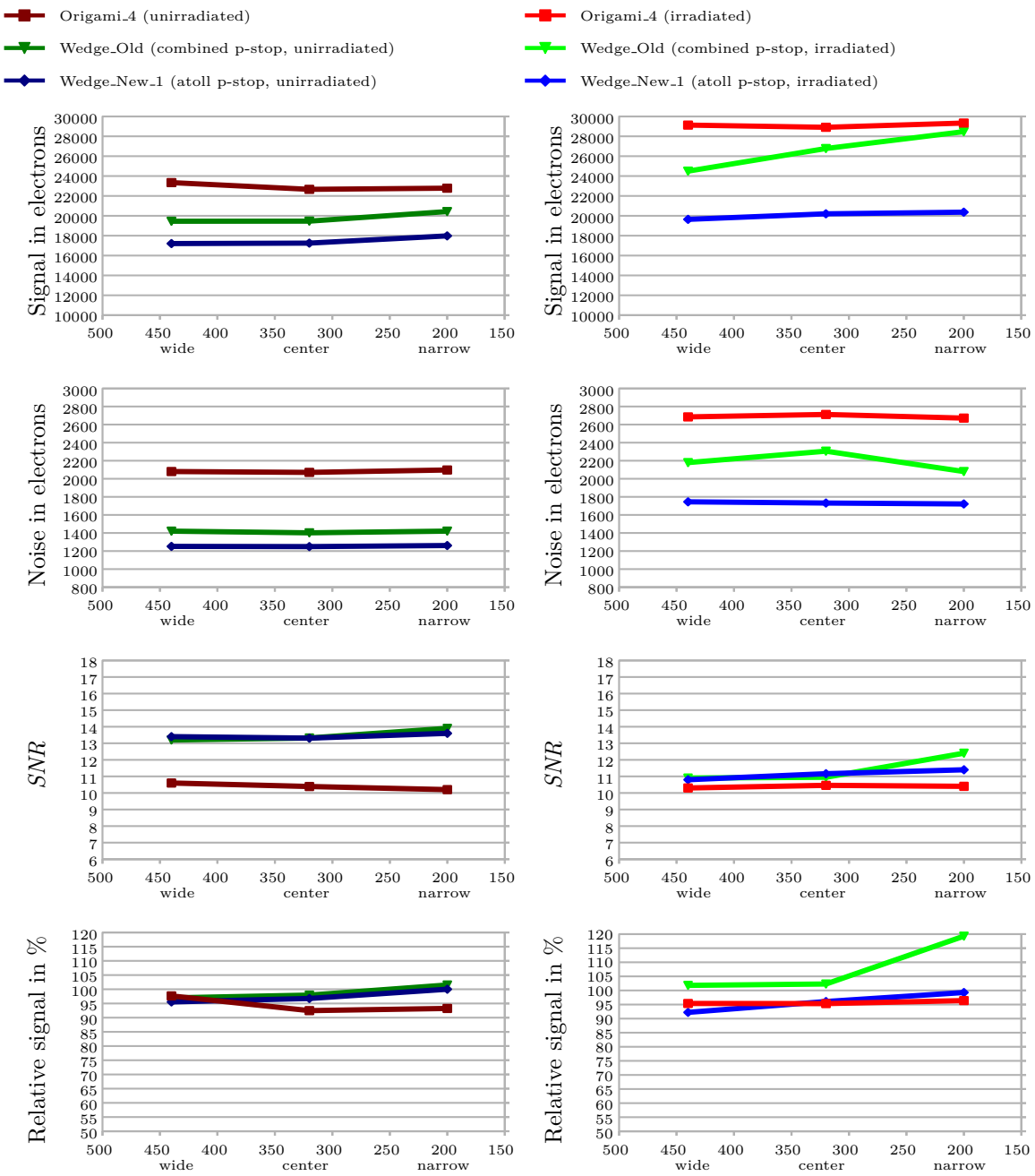

Figure 8.23.: Cluster signal, cluster noise and SNR for 2-strip-clusters, and relative signal of 2-strip-clusters w.r.t. 1-strip-clusters, for the full-scale sensors' p-sides, data taken in 2012. The observables are plotted as function of the beam spot position in terms of n-side strip number, for the three beam positions aiming at the wide side, center and narrow side of the trapezoidal sensors. The left plots are before irradiation to 100 kGy, the right ones are after irradiation. The values can also be found in table 8.4.

Table 8.4.: Cluster signal, cluster noise and SNR for 2-strip-clusters, and relative signal of 2-strip-clusters w.r.t. 1-strip-clusters, for the full-scale sensors' p-sides.

Cluster signal in electrons, $\sigma(S) < 50\,\text{electrons}$				
		wide	center	narrow
Origami_4	unirradiated	23340	22663	22779
	irradiated	29128	28906	29332
Wedge_Old	unirradiated	19450	19463	20426
	irradiated	22494	26770	28467
Wedge_New_1	unirradiated	18529	18783	18706
	irradiated	19642	20200	20363
Cluster noise in electrons, $\sigma(N) < 15\,\text{electrons}$				
Origami_4	unirradiated	2080	2071	2097
	irradiated	2685	2712	2672
Wedge_Old	unirradiated	1420	1402	1421
	irradiated	2179	2306	2080
Wedge_New_1	unirradiated	1252	1250	1261
	irradiated	1745	1732	1722
Cluster SNR, $\sigma(SNR) < 0.1$				
Origami_4	unirradiated	10.6	10.4	10.2
	irradiated	10.3	10.5	10.4
Wedge_Old	unirradiated	13.2	13.3	13.9
	irradiated	10.9	11.0	12.4
Wedge_New_1	unirradiated	13.4	13.3	13.6
	irradiated	10.8	11.2	11.4
Relative signal in %, $\sigma(S_{\text{rel}}) < 1\%$				
Origami_4	unirradiated	97.7	92.5	93.3
	irradiated	95.4	95.3	96.4
Wedge_Old	unirradiated	97.0	98.0	101.5
	irradiated	101.8	102.3	119.3
Wedge_New_1	unirradiated	95.6	96.8	100.0
	irradiated	92.2	96.1	99.3

Comparison of the cluster signal-to-noise ratio

The third row of plots in figure 8.23 shows the SNR for clusters[4] of exactly two strips before and after irradiation. The effect of the different calibrations cancels out for the SNR – this is true even for measurements taken before and after irradiation – so that we can compare the values directly.

Before irradiation (left plot) the two trapezoidal modules are on a par, while the Origami module shows worse performance. This can be explained by the vastly different pitch adapter lengths: The Origami module features long pitch adapters on the p-side – being a considerable noise source – whereas the trapezoidal modules have very short p-side pitch adapters.

After irradiation (right plot) the trapezoidal modules suffered from radiation damage, while the performance of the Origami module basically stayed the same. It seems that for the Origami module the noise is mainly determined by the pitch adapter, and the radiation-induced change is negligible. For the trapezoidal modules, however, the irradiation effect is clearly visible.

Comparison of the relative signal

The bottom two plots of figure 8.23 show the relative signal, i.e. the division of the MPV of the 2-strip-cluster signal by the MPV of the 1-strip-cluster signal. Like for the SNR also here the effect of the potentially different calibration of signal levels cancels out, making the results directly comparable.

Before irradiation (left plot) all modules show a similar relative signal in the order of 95%. Due to the small pitch of the sensor's p-sides hardly any signal is lost when shared among two strips. One can see a slight increase of about 5% when going to the trapezoidal sensors' narrow sides, where the pitch gets smaller.

After irradiation (right plot) the relative signal generally stays the same as before, only the old trapezoidal module looks a bit like an outlier here. For the new trapezoidal module one can still see the relative signal increase for the smaller pitch.

[4]Note that the computation of the cluster SNR ratio uses the individual strip noise values of the strips involved in the cluster, according to the definition in equation 7.2, and not the averaged cluster noise displayed in the second-row plots of figure 8.23.

8.3.2. Performance of the n-side

Comparison of the cluster signal

The top two plots of figure 8.24 show the most probable cluster signal of the full-scale DSSDs, where the values found in the left plot are before irradiation to 100 kGy and those in the right plot are after irradiation.

We observe that in the unirradiated case the most probable cluster signal of the Origami module is highest, while the trapezoidal modules show similar performance.

After irradiation the relative behaviour of the modules basically stayed the same, but at a different absolute signal level.

Comparison of the cluster noise

The second row of plots in figure 8.24 shows the average cluster noise for clusters of exactly two strips $\bar{N}_{n=2} = \sqrt{2}\bar{N}_{\text{strip}}$, where $\bar{N}_{\text{strip}}$ is the noise averaged over all strips of the whole sensor. Again, the left plot is before irradiation to 100 kGy and the right one is after irradiation.

We observe that in the unirradiated case the Origami module shows a better noise figure than the trapezoidal modules. This is mainly due to the extremely short pitch adapters of the Origami's n-side (see figure 2.12 for details), in contrast to the very long pitch adapters used for the trapezoidal module's n-sides (see figure 8.19).

After irradiation the Origami module shows a considerable noise increase and catches up to the noise levels of the trapezoidal modules.

Comparison of the cluster signal-to-noise ratio

The third row of plots in figure 8.24 shows the SNR for clusters[5] of exactly two strips before and after irradiation. The effect of the different calibrations cancels out for the SNR – this is true even for measurements taken before and after irradiation – so that we can compare the values directly.

Before irradiation (left plot) the two trapezoidal modules are on a par, while the Origami module shows considerably better performance. This can be explained by the vastly different pitch adapter lengths: The Origami module features a tiny pitch adapter on the n-side, whereas the trapezoidal modules have very long n-side pitch adapters.

[5]Note that the computation of the cluster SNR ratio uses the individual strip noise values of the strips involved in the cluster, according to the definition in equation 7.2, and not the averaged cluster noise displayed in the second-row plots of figure 8.24.

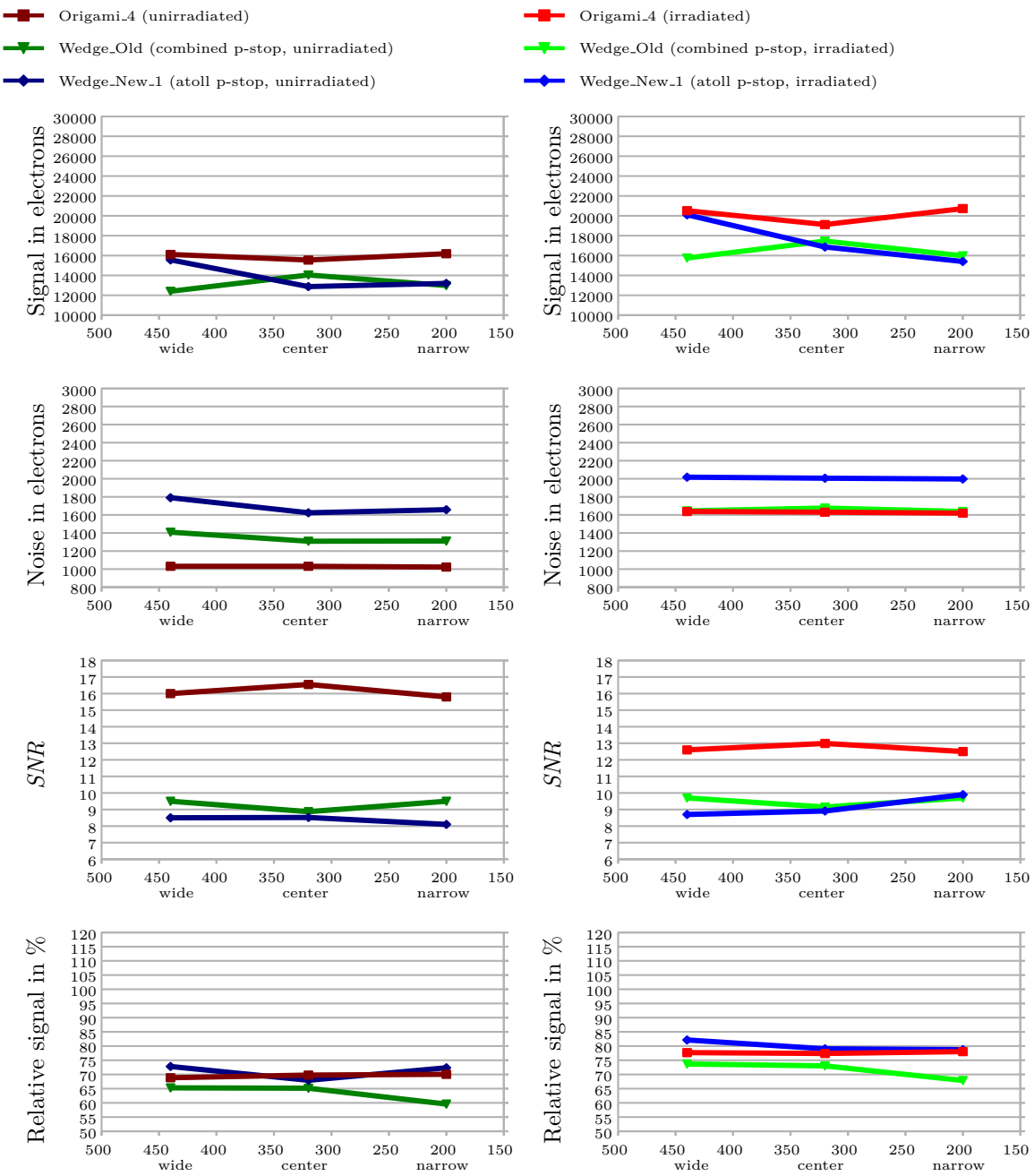

Figure 8.24.: Cluster signal, cluster noise and SNR for 2-strip-clusters, and relative signal of 2-strip-clusters w.r.t. 1-strip-clusters, for the full-scale sensors' n-sides, data taken in 2012. The observables are plotted as function of the beam spot position in terms of n-side strip number, for the three beam positions aiming at the wide side, center and narrow side of the trapezoidal sensors. The left plots are before irradiation to 100 kGy, the right ones are after irradiation. The values can also be found in table 8.5.

Table 8.5.: Cluster signal, cluster noise and SNR for 2-strip-clusters, and relative signal of 2-strip-clusters w.r.t. 1-strip-clusters, for the full-scale sensors' n-sides.

Cluster signal in electrons, $\sigma(S) < 50\,\text{electrons}$				
		wide	center	narrow
Origami_4	unirradiated	16111	15548	16187
	irradiated	20517	19119	20725
Wedge_Old	unirradiated	12404	14045	12985
	irradiated	15754	17457	15974
Wedge_New_1	unirradiated	15563	12876	13199
	irradiated	20101	16860	15401
Cluster noise in electrons, $\sigma(N) < 15\,\text{electrons}$				
Origami_4	unirradiated	1032	1032	1023
	irradiated	1638	1631	1620
Wedge_Old	unirradiated	1409	1309	1311
	irradiated	1645	1676	1638
Wedge_New_1	unirradiated	1791	1624	1658
	irradiated	2017	2006	1998
Cluster SNR, $\sigma(SNR) < 0.1$				
Origami_4	unirradiated	16.0	16.6	16.7
	irradiated	12.6	13.0	12.5
Wedge_Old	unirradiated	9.5	8.9	9.5
	irradiated	9.7	9.2	9.7
Wedge_New_1	unirradiated	8.5	8.5	8.1
	irradiated	8.7	8.9	9.9
Relative signal in %, $\sigma(S_{\text{rel}}) < 1\%$				
Origami_4	unirradiated	68.9	69.8	70.1
	irradiated	77.7	71.4	78.0
Wedge_Old	unirradiated	65.3	65.2	59.6
	irradiated	73.7	73.0	67.9
Wedge_New_1	unirradiated	72.8	68.0	72.4
	irradiated	82.2	79.0	78.7

After irradiation (right plot) the Origami module suffered from radiation damage, while the performance of the trapezoidal modules basically stayed the same. It seems that for the trapezoidal modules the noise is mainly determined by the pitch adapter, and the radiation-induced change is negligible. For the Origami module, however, the irradiation effect is clearly visible.

Comparison of the relative signal

The bottom two plots of figure 8.24 show the relative signal, i.e. the division of the MPV of the 2-strip-cluster signal by the MPV of the 1-strip-cluster signal. Like for the SNR also here the effect of the potentially different calibration of signal levels cancels out, making the results directly comparable.

Before irradiation (left plot) all modules show a similar relative signal in the order of 70%, with the old trapezoidal module being slightly worse. Due to the large pitch of the sensor's n-sides a considerable amount of signal is lost when shareing it among two strips. The relative signal of the full-scale sensors' n-sides is slightly higher than the one of the baby sensors (see section 7.4), despite the slightly larger pitch. A possible explanation is given at the end of section 7.3.2, in the paragraph about the relative signal.

After irradiation (right plot) the relative signal generally increases, whereas the relative positioning of the modules basically stays the same. Still, the old trapezoidal module with combined p-stop performs slightly worse than the other modules, which both feature the atoll p-stop with similar geometry.

8.4. Conclusions

The beam test 2012 offered the possibility to test both versions of the full-scale trapezoidal sensors in a realistic environment in terms of cooling and irradiation, and allowed the direct comparison to an Origami module. We observed that the module performance is considerably influenced by the length of the pitch adapters, which makes the n-side of the trapezoidal modules largely independent of irradiation. The clear difference between the combined p-stop pattern – as used in the initial design – and the atoll p-stop pattern – as used in the updated design – is not as pronounced as for the baby sensors. The combined p-stop showed slightly better SNR, but this observable can still be influenced by the readout electronics. The relative signal, on the other hand, is widely independent of the periphery, and this observable indeed shows advances for the atoll p-stop. Unfortunately we could only test one module per sensor version due to a limited number of available pitch adapters. Nevertheless, we could show that the sensors produced by Micron Semiconductor Ltd. perform just as well as the ones produced by HPK, as far as the vastly different periphery allowed judgement. On average, the final unirradiated full-scale trapezoidal sensor achieved a SNR of 13.4 on the p-side and 8.4 on the n-side, after irradiation we measured SNR values of 11.1 on the p-side and 9.1 on the n-side.

8.4.1. Sensor design experience - lessons learned

The possibilities for thoroughly testing a prototype sensor are greatly enhanced by including sufficient contact pads to a large number of different areas on the sensor. The most important lessons regarding the sensor design were the following:

- For the initial layout the p-side AC pads were not aligned to the corresponding DC pads, which is no problem for wire bonding, but poses a significant challenge when trying to perform a strip scan with fixed needles (see section 6.2.1). When designing a non-rectangular sensor, always try to keep the strips' contact pads aligned.
- The so-called "n-sub pad" proved very useful for the thermal cycling campaign (section 8.2), where the bottom side of the sensor was inaccessible. Using this connection to the n-type bulk and to the n-side, we were able to deplete the sensor although we had access to the p-side only. Note that this works on the junction side of DSSDs only, not on the ohmic side. At first, Micron Semiconductor Ltd. was reluctant to include the necessary n-type implantation on the p-side edge ring, without which the n-sub pad doesn't work. However, this implantation was proven to be beneficial by the sensor R&D group for the CMS experiment already, so be sure to implement it.
- For some tests we would have liked to make contact to the p-stop implantations, which was not foreseen in the initial design. Unfortunately we could not afford to change even more photo masks in the updated design to introduce proper p-stop contact pads. Furthermore, these contact pads have to be planned in advance, as the p-stop implantations are usually very small and one has to foresee the space to put the pads.

Steak? ... Steak. Steak. Steak. Steak. Steak! ... Steeeeaaaaak!
And DUTs...

Erik Huemer, MSc.

9

Conclusion and outlook

The upgrade of the KEKB collider to the high luminosity SuperKEKB will put strong demands on the SVD of the Belle II experiment. The increase in particle interactions requires a completely new readout scheme with specifically designed DSSDs. The introduction of a slanted forward part saves material budget, sensors, readout channels and money at the cost of increased mechanical complexity.

For the first time a double-sided silicon microstrip sensor was developed in Austria, which introduced a lot of knowledge about this sensor type. Although I could build upon previous work [26, 37], I basically had to rewrite the framework from scratch to make more complex shapes possible than just rectangles. Nevertheless, the basic structure of the framework remained the same. At the moment my branch of SiDDaTA is independent from the original one, although in principle it covers the special case of rectangular single-sided sensors as well. It will be a work of the future to combine the two branches to a single framework covering all applications needed so far, and maybe it can be ported to a non-commercial, simple development environment like "KLayout" [44].

On DSSDs one has to take special care of the strip insulation on the n-side, because of the presence of an electron layer at the interface of silicon bulk and SiO_2. The interruption of this conductive layer can be done using several techniques, two of which have been evaluated in this thesis: the p-stop blocking method in the three variants atoll, common and combined, and the p-spray blocking method. The evaluations showed that the atoll p-stop yields the best sensor performance, especially for large readout pitch and intermediate strips, as is the case for the Belle II SVD. In that my results contradict previous studies [45, 46], which favoured the combined p-stop pattern. The p-spray blocking method proved to be very performant as long as irradiation with gamma radiation is low. It would be very interesting to reevaluate the baby sensor beam test data from 2010 and perform a tracking

and resolution study. In that beam test we tested one sensor per p-stop pattern both before and after irradiation, with the additional position information of the EUDET telescope. In principle everything is there, it just has to be done.

I learned a lot about how to prepare a successful beam test, the conclusions are presented in section 7.5. One has to take special care if particle tracking and a resolution study are foreseen. In the course of dealing with the position measurements I came across the fact that the signal generation can be highly nonlinear, and that 1-strip-clusters behave vastly different from clusters with more strips involved. The former can be cured with the η correction, which to the best of my knowledge has not yet been implemented in the calibration code of a full-scale collider experiment. The latter too is usually ignored in the full-scale tracking codes, one would have to assume different point resolutions and error distributions depending on the size of the clusters. I feel intrigued to look into this matter and find out if the tracking resolution can be improved by taking into account these effects.

Ultimately, my work fortunately led to a working full-scale trapezoidal DSSD, which is being produced at the moment. I feel excited and honoured that I could contribute a small part to the huge effort that is the construction of Belle II.

I thank all the people who supported my work by their presence or by their absence.

Unknown author

Acknowledgements

Many people supported my work, and helped a great deal to bring my thesis to a successful end. My sincere thanks go out to all of them, knowing that there are more than I can mention here:

First and foremost, I want to thank my supervisor **Manfred Krammer**, who gave me the opportunity to work in one of the most exciting and versatile fields of basic research. Being a part of this excellent institute really is an honour.

Many thanks go out to **Thomas Bergauer**, head of the semiconductor sensors group, who agreed to make me part of his exquisite team. He has grown to be a friend more than a supervisor!

Christoph Schwanda, leader of the Belle and Belle II project groups, had a key say in the decision to build the slanted forward part of the Belle II SVD, which made the trapezoidal sensor necessary in the first place. He always had an open door and took time to help me with any question I had. Many thanks for your support!

My officemate **Marko Dragicevic** receives special esteem for providing me with the elaborated SiDDaTA framework, which formed the basis of all the work I did. He had to patiently answer countless questions, and devoted a great deal of his time to help me out. Thanks for taking things with your own sense of humour, and for being a friend!

Special thanks go out to the colleagues from the electronics group, **Markus Friedl** and **Christian Irmler**. They had to suffer endless questions about the readout system, but endured the burden with a smile. You too became valuable friends!

I had a lot of fun with all the fellow students who went on beam tests with me. Many thanks to **Wolfgang Kiesenhofer**, **Georg Auzinger**, **Thomas Obermayer**, **Immanuel Gfall**, **Anne-Kathrin Frankenberger**, **Thomas Spielauer** and **Erik Huemer**, may the DUTs be with you!

My biggest gratitude goes to my girlfriend **Cornelia Oppitz**, who for months encountered the very same picture when coming home: me sitting in front of the computer, distracted and unresponsive. Thanks for your patience, your continued support, and your willingness to keep supporting me whatever may come next. I love you not only for how you are, but also for how I am when I'm with you!

Part IV.

Addendum

10

Further details

10.1. Geometrical definitions

10.1.1. The coordinate system

The Belle II global coordinate system is defined in [56] and displayed in figure 10.1. The x-axis is horizontal and points outside of the accelerator tunnel, the y-axis is vertical. The z-axis is the Belle II solenoid axis, which roughly points toward the direction of the electron beam. The direction of the solenoid magnetic field lines is from $-z$ to z. In the baseline design of machine and detector, the z-axis is also identical to the bisector of the two beams, and to the axis of the straight part of the beam pipe at the interaction point. With respect to the z-axis, Φ is the azimuthal angle and θ is the zenith (or polar) angle. $\Phi = 0$ is defined for $(x, y, z) = (1,0,0)$ and $\theta = 0$ is defined for $(x, y, z) = (0,0,1)$.

Due to the roughly cylindrical symmetry of the detector planes, it is more natural to use cylindrical coordinates. The radius R is defined as the radius in the x-y-plane ($R = \sqrt{x^2 + y^2}$) and ρ in three dimensions ($\rho = \sqrt{x^2 + y^2 + z^2}$). Points in the x-y-plane are often expressed in terms of the $R\Phi$-coordinate (see figure 10.2), and the x-y-plane is frequently referred to as $R\Phi$-plane. The coordinates are related with each other as follows:

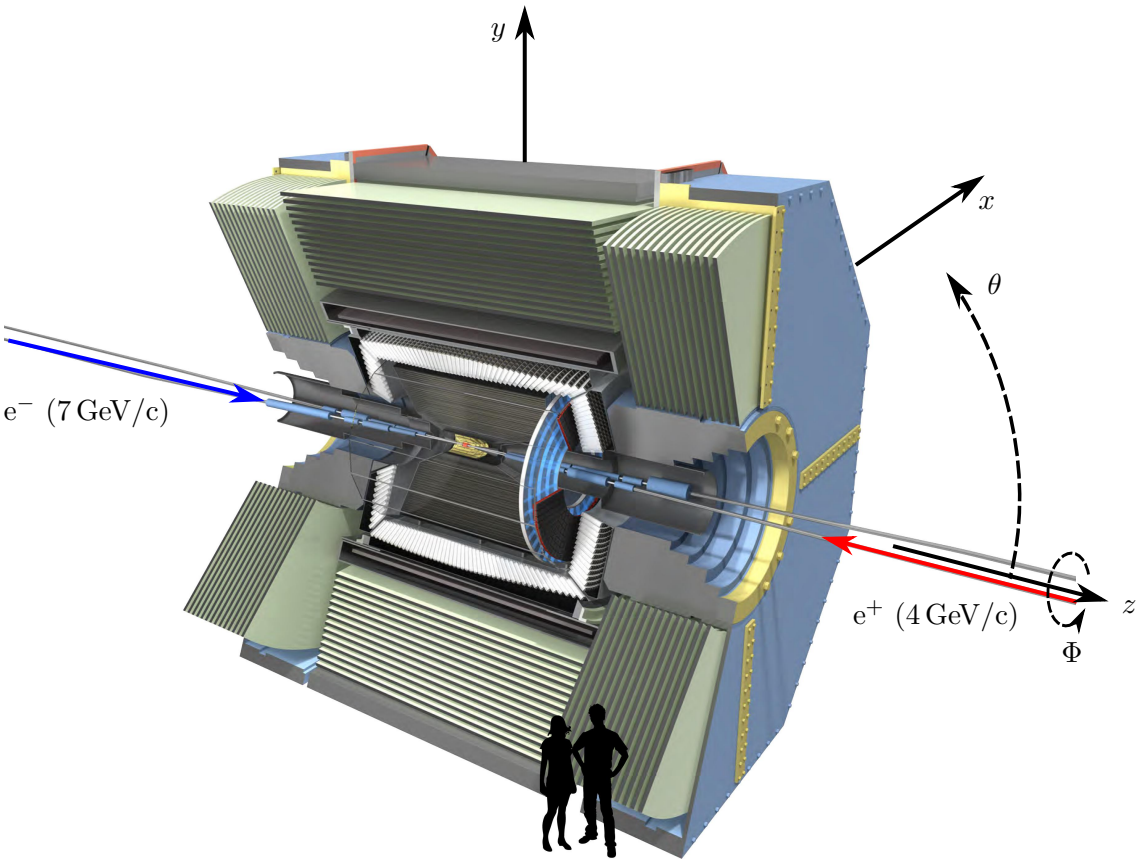

Figure 10.1.: The coordinate system of Belle II. The x-axis is horizontal and points outside of the accelerator tunnel, the y-axis is vertical. The z-axis is the Belle II solenoid axis, which roughly points toward the direction of the electron beam. Φ is the azimuthal angle around the z-axis. $\Phi = 0$ is defined for $(x, y, z) = (1,0,0)$. θ is the zenith (or polar) angle with respect to the z-axis. $\theta = 0$ is defined for $(x, y, z) = (0,0,1)$.

$$\sin\theta = R/\rho, \tag{10.1}$$
$$\cos\theta = z/\rho, \tag{10.2}$$
$$\sin\Phi = y/R, \tag{10.3}$$
$$\cos\Phi = x/R. \tag{10.4}$$

10.1.2. Acceptance region, barrel region, forward and backward region

The acceptance region is defined as the polar angle region $17° \leq \theta \leq 150°$ [15]. It is asymmetrical to take into account the inherent asymmetry of the experiment due to the different energies of the electron and positron beams. Everything inside these bounds is instrumented with particle-sensitive devices of all kinds. Especially the tracking detectors have to pay rigorous attention to this region, because the amount of material inside the

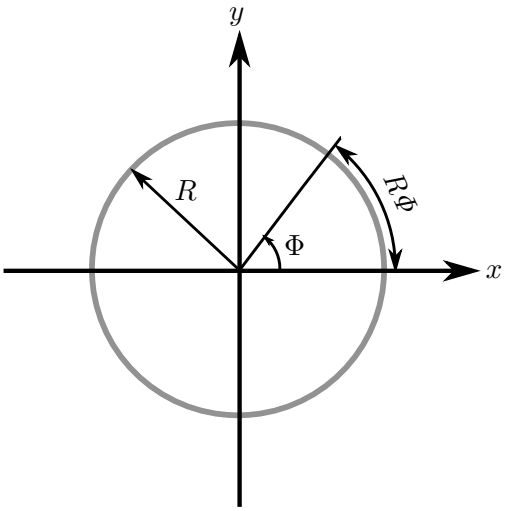

Figure 10.2.: Points in the x-y-plane are often denoted in terms of the arc length $R\Phi$.

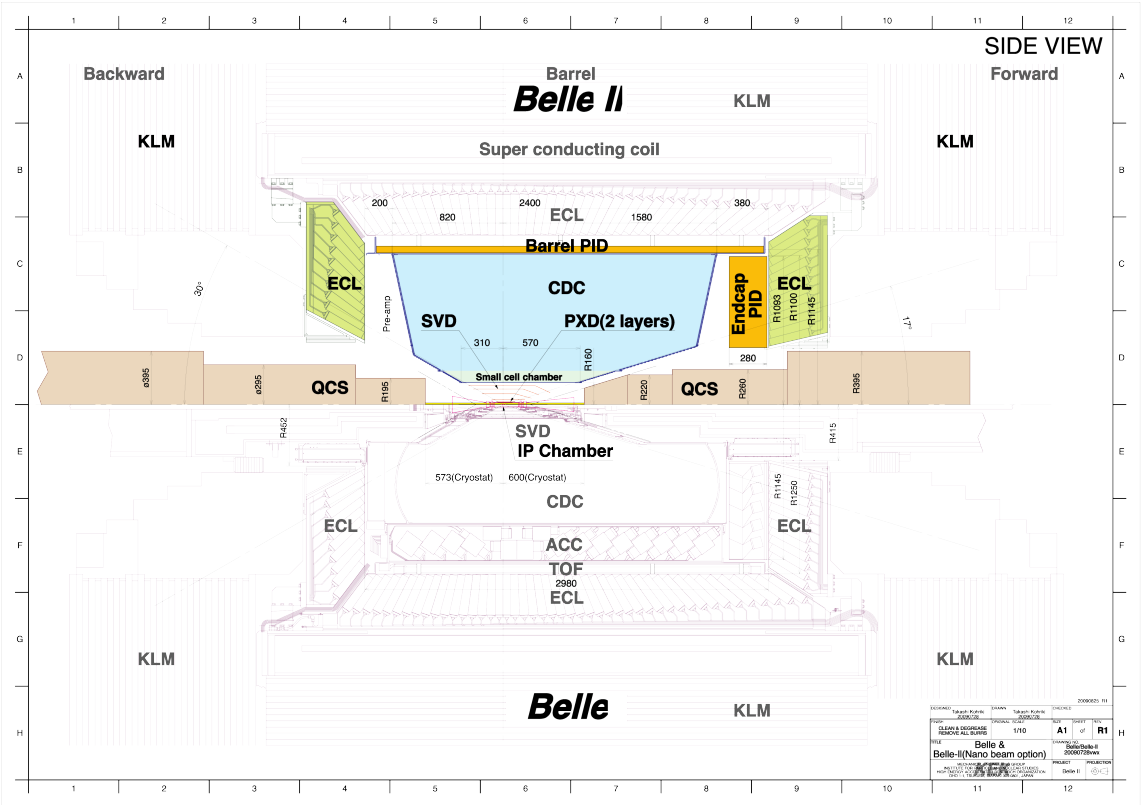

Figure 10.3.: The acceptance region is defined as the polar angle region $17° \leq \theta \leq 150°$.

acceptance region has to be minimised. The space outside the acceptance region can be equipped with readout electronics, power supplies, electronic periphery, cooling systems, cables, etc.

The barrel region is defined for every subdetector individually. A general rule-of-thumb declares the barrel region of a subdetector as the part which has roughly the shape of cylinder layers. The subdetector parts applying a different geometry are called forward or backward part. "Forward" defines as the region in positive z direction, i.e. the direction of the electron beam. Examples for "forward" parts of subdetectors is the conical (or slanted) part of the SVD (see section 2), or the endcaps of the ECL.

10.1.3. Parametrization of the trajectory of charged particles

The SVD (together with PXD and CDC) measures the tracks of charged particles to determine their points of origin and their momentum. The trajectory of a charged particle in a uniform magnetic field, disregarding the energy loss, can be represented by a helix. The helix can be described by five independent parameters, defined at the point of closest approach of the helix to a reference point (origin), called the perigée point. Belle II intends to use the following parametrisation for the trajectory $\vec{\tau}$ [57]:

$$\vec{\tau} = (d_0, \phi_0, \omega, z_0, \cot\vartheta) \tag{10.5}$$

The parameters are defined as follows:

- d_0 [cm]: signed distance from perigee to the origin in the x-y-plane. Negative if the projection of the momentum on this distance points to the origin.
- ϕ_0: track direction angle at the perigee in the x-y-plane $[-\pi;\pi]$. Not to be confused with the azimuthal angle Φ in the global coordinate system.
- ω [1/cm]: signed curvature q/R, with q: charge of the particle and R: the radius of the track circle in the x-y-plane.
- z_0 [cm]: z value at the point of closest approach to the beam line.
- $\cot\vartheta$: inverse slope of the track in the R-z-plane (dz/ds). Again not to be confused with the polar angle θ in the global coordinate system.

The parameters are visualised in figure 10.4.

d_0 is also known as the (projected) impact parameter in $R\Phi$, and z_0 is the impact parameter in z, whose resolution has to be made as small as possible for secondary vertex separation by the PXD, SVD and CDC. The particle momentum (in GeV/c) at any point of the trajectory described by its azimuthal angle ϕ can be calculated as follows:

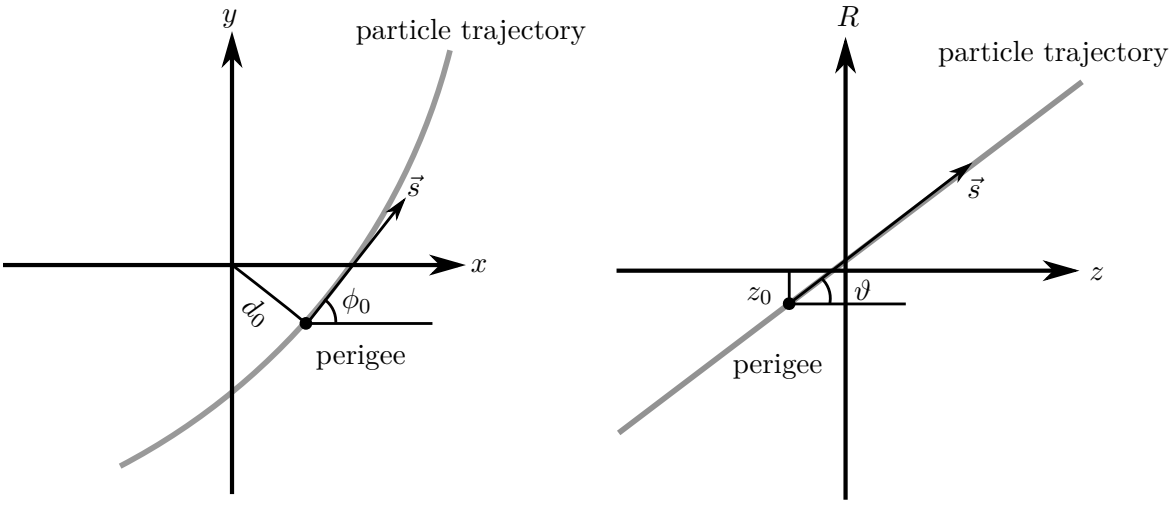

Figure 10.4.: Illustration of the helix parameters in the x-y-plane (left side) and R-z-plane (right side) [57].

$$\begin{pmatrix} p_x \\ p_y \\ p_z \end{pmatrix} = \frac{1}{|\omega \cdot \alpha|} \begin{pmatrix} -\sin(\phi_0 + \phi) \\ \cos(\phi_0 + \phi) \\ \cot\ \vartheta \end{pmatrix} \tag{10.6}$$

with $\alpha = 1/(1.5 \cdot 0.00299792458)$, obtained from the speed of light c and the magnetic field strength of 1.5 T.

The coordinates of the perigee can be expressed using the helix parameters:

$$\begin{pmatrix} x_p \\ y_p \\ z_p \end{pmatrix} = \begin{pmatrix} d_0 \cos\phi_0 \\ d_0 \sin\phi_0 \\ z_0 \end{pmatrix} \tag{10.7}$$

10.2. AMPLE code example - the fundamental shape: a polygon with rounded corners


```
function CreateRoundedPolygon(Corner, CornerRadius, CornerPoints, CallingFunc)
{
// Creates a vector containing the coordinates for a rounded polygon
// with corners at the coordintes 'Corner' with corner radius 'CornerRadius'
// and each corner is drawn with 'CornerPoints' number of points in each corner.
// Corner, CornerRadius and CornerPoints are vectors of the same length, specifying
// position, rounding radius and number of points to be drawn for each corner
// separately. The number of corners is given by the length of the input vectors.
// The sequence of corners can be both clockwise or counter-clockwise. But
// not to provoke peculiar behaviour, try sticking with counter-clockwise!
// To create a sharp corner i without rounding, set CornerRadius[i]=0 or
// CornerPoints[i]=1.
// Corners can point inwards or outwards w.r.t. the area to be drawn. The
// rounding is done inwards for a corner pointing outwards, and vice versa.
// CallingFunc is a string containing the name of the function that called
// CreateRoundedPolygon. This is neccessary to relate error messages due to
// wrong input values for functions basing upon CreateRoundedPolygon, such
// as CreatePolyRing.
//
// Set DebugInfo=1 for detailed text output.

local DebugInfo = 0;

local VecCoordinates;
local Point = 0;
local i, iCorner, h;
local prev, next, dist_first, dist_prev;
local EPrev, ENext, MPrev, MNext, dist;
local NormEPrev, NormENext, NormMPrev, NormMNext;
```

```
local Mid, MidPrev, MidNext, NCorners, NCornersY, NCornerRadius,NCornerPoints;
local AngleStart, AngleStop, AngleStep, PointStart, PointStop;
local PointX, PointY;
local numVecCoordinates=0;
local eps=0.1;

// Number of corners
NCorners=length(Corner);
$message($strcat("Length of Corner: ",NCorners));

// Checking the length of the input vectors
//NCornersY=length(Y);
NCornerRadius=length(CornerRadius);
NCornerPoints=length(CornerPoints);
if (NCornersY!=NCorners || NCornerRadius!=NCorners || NCornerPoints!=NCorners)
    $message($strcat(CallingFunc," calling CreateRoundedPolygon: Input vectors do not have the same length!"));


// Find sharp corners and calculate total number of points to be drawn
for (i=0;i<NCorners;i=i+1)
    // cycle through vectors to find sharp edges
    {
    if (CornerRadius[i]<=0 && CornerPoints[i]<2)
        {

        CornerRadius[i]=0;
        CornerPoints[i]=1;
        }
    // record needed for length of output coordinates
    numVecCoordinates=NumVecCoordinates+CornerPoints[i];
    }
```

```
// *** Init Vectors
   VecCoordinates = $create_vector(numVecCoordinates);
   EPrev  = $create_vector(2);
   ENext  = $create_vector(2);
   MPrev  = $create_vector(2);
   MNext  = $create_vector(2);
   Mid    = $create_vector(2);
   MidPrev= $create_vector(2);
   MidNext= $create_vector(2);
   //Corner = $create_vector(2);


//-------------------------------------------------------------------------
//         Begin of loop over corners
//-------------------------------------------------------------------------

for (iCorner=0;iCorner<NCorners;iCorner=iCorner+1)
  {

  if (DebugInfo!=0) $message($strcat("------ iCorner=",iCorner," -------"));

  //Corner=[X[iCorner],Y[iCorner]];   // Coordinates of the current corner

  // calculate index of the next and the previous corner
  next=iCorner+1;
  prev=iCorner-1;
  if (prev<0) prev=NCorners-1;
  if (next>NCorners-1) next=0;
```

```
// Vectors pointing to the previous and to the next corner
//EPrev = [X[prev]-X[iCorner],Y[prev]-Y[iCorner]];  // Relative vector from current corner to previous corner
//ENext = [X[next]-X[iCorner],Y[next]-Y[iCorner]]; // Relative vector from current corner to next corner

EPrev = Corner[prev]-Corner[iCorner];             // Relative vector from current corner to previous corner
ENext = Corner[next]-Corner[iCorner];             // Relative vector from current corner to next corner
NormEPrev = sqrt(pow(EPrev[0],2)+pow(EPrev[1],2));// Length of EPrev;
NormENext = sqrt(pow(ENext[0],2)+pow(ENext[1],2));// Length of ENext;


if (CornerRadius[iCorner]>0)
  // calculate coordinates of a rounded corner
  {
  // Vectors perpendicular to EPrev and ENext
  MPrev = CornerRadius[iCorner]/NormEPrev*[ EPrev[1],-EPrev[0]]; // Vector normal to EPrev with length
  equal CornerRadius
  MNext = CornerRadius[iCorner]/NormENext*[-ENext[1], ENext[0]]; // Vector normal to ENext with length
  equal CornerRadius
  // Note: with this choice of signs the vectors both point inwards
  // if the corners are sorted counter-clockwise
  NormMPrev = sqrt(pow(MPrev[0],2)+pow(MPrev[1],2)); // Length of MPrev;
  NormMNext = sqrt(pow(MNext[0],2)+pow(MNext[1],2)); // Length of MNext;

  if (DebugInfo!=0)
      {
      $message($strcat("EPrev: ",EPrev));
      $message($strcat("ENext: ",ENext));
      $message($strcat("MPrev: ",MPrev));
      $message($strcat("MNext: ",MNext));
      $message($strcat("NormEPrev: ",NormEPrev));
      $message($strcat("NormENext: ",NormENext));
```

```
    $message($strcat("NormMPrev: ",NormMPrev));
    $message($strcat("NormMNext: ",NormMNext));
    }


// Calculate the distance between the (virtual) sharp corner and the start of the rounding circle
if (EPrev[0]/NormEPrev-ENext[0]/NormENext!=0)   dist = (MNext[0]-MPrev[0])/(EPrev[0]/NormEPrev
- ENext[0]/NormENext); // Distance between (virtual) sharp corner and begin of arc
else                                            dist = (MNext[1]-MPrev[1])/(EPrev[1]/NormEPrev
- ENext[1]/NormENext); // Distance between (virtual) sharp corner and begin of arc
// Note: this distinction is neccessary for the unlikely case that the denominator
// is zero, then the calculation can be done using the y-components of the vectors
if (dist<0) dist=dist*(-1); // Make sure that dist is positive

// Check if distance between corners is long enough for rounding
if (iCorner==0) dist_first=dist;
else if (iCorner==NCorners-1)
    {
    if (dist+dist_prev>NormEPrev)   $message($strcat(CallingFunc," calling CreateRoundedPolygon:
    Not enough distance between corners ",iCorner-1," and ",iCorner,"! Maybe corner radius too large...
    Note: Corner numbering starts at 0"));
    if (dist+dist_first>NormENext)  $message($strcat(CallingFunc," calling CreateRoundedPolygon:
    Not enough distance between corners ",NCorners-1," and 0! Maybe corner radius too large...
    Note: Corner numbering starts at 0"));
    }
else
    {
    if (dist+dist_prev>NormEPrev)   $message($strcat(CallingFunc," calling CreateRoundedPolygon:
    Not enough distance between corners ",iCorner-1," and ",iCorner,"! Maybe corner radius too large...
    Note: Corner numbering starts at 0"));
    }
```

```
    dist_prev=dist;


    // Calculate center point of the rounding circle
    // For a corner pointin outwards, the center points calculated using the
    // vectors of the previous and the next corner are the same (save rounding errors)
    // By that means one can distinguish between corners pointing inwards and outwards.
    MidPrev = MPrev + dist*EPrev/NormEPrev + Corner[iCorner];
    MidNext = MNext + dist*ENext/NormENext + Corner[iCorner];

    // Check if the center points are the same
    // Since rounding errors can occur, center points not farther away than eps are
    // considered equal.
   if (MidPrev[0]>MidNext[0]+eps || MidPrev[0]<MidNext[0]-eps || MidPrev[1]>MidNext[1]+eps ||
MidPrev[1]<MidNext[1]-eps)
        {
        // This branch is carried out for a corner pointing inwards,
        // both perpendicular vectors MPrev and MNext are inverted.
        if (DebugInfo!=0) $message("Corner pointing inwards (outwards for clockwise polygon),
        inverting MPrev and MNext");
        // Inversion of perpendicular vectors
        MPrev=MPrev*(-1);
        MNext=MNext*(-1);
        // New center points
        MidPrev = MPrev + dist*EPrev/NormEPrev + Corner[iCorner];
        MidNext = MNext + dist*ENext/NormENext + Corner[iCorner];
        // Angles of the first and of the last point of the rounded corner
        AngleStart = atan2(-MPrev[1],-MPrev[0]);
        AngleStop  = atan2(-MNext[1],-MNext[0]);
        // Opening angle of the rounding circle arc
```

```
    AngleStep  = AngleStart-AngleStop;
    while (AngleStep>pi)    AngleStep=AngleStep-pi;
    while (AngleStep<0)     AngleStep=AngleStep+pi;
    // For a corner pointing inwards, this angle is defined to be negative
    AngleStep=AngleStep*(-1);
    }
else
    {
    // This branch is carried out carried out for a corner pointing outwards
    if (DebugInfo!=0) $message("Corner pointing outwards (inwards for clockwise polygon), go on normally");
    // Angles of the first and of the last point of the rounded corner
    AngleStart = atan2(-MPrev[1],-MPrev[0]);
    AngleStop  = atan2(-MNext[1],-MNext[0]);
    // Opening angle of the rounding circle arc
    AngleStep  = AngleStop-AngleStart;
    while (AngleStep>pi)    AngleStep=AngleStep-pi;
    while (AngleStep<0)     AngleStep=AngleStep+pi;
    }

// Now it is certain that both center points are the same, go on using only one.
Mid=MidPrev;

if (DebugInfo!=0)
    {
    $message($strcat("Middle point of corner:",MidPrev));
    $message($strcat("Middle point of corner:",MidNext));
    $message($strcat("AngleStart: ",AngleStart*180/pi));
    $message($strcat("AngleStop: ",AngleStop*180/pi));
    $message($strcat("AngleStep: ",AngleStep*180/pi));
    $message($strcat("Distance from corner:",dist));
    }
```

```
    // Calculate starting point of the rounded corner
    PointStart=Corner[iCorner]+dist*EPrev/NormEPrev;
    VecCoordinates[Point] = PointStart;
    Point = Point + 1;

    // loop through the points of the rounding arc
    for(i = 1; i < CornerPoints[iCorner]-1; i = i + 1)
        {
        PointX = Mid[0] + CornerRadius[iCorner]*(cos(AngleStart + (i*AngleStep)/(CornerPoints[iCorner]-1)));
        PointY = Mid[1] + CornerRadius[iCorner]*(sin(AngleStart + (i*AngleStep)/(CornerPoints[iCorner]-1)));
        VecCoordinates[Point] = [PointX,PointY];
        Point = Point + 1;
        }
    // Calculate end point of the rounding arc
    PointStop=Corner[iCorner]+dist*ENext/NormENext;
    VecCoordinates[Point] = PointStop;
    Point=Point+1;
    }
else
    {
    // sharp corner!
    if (iCorner==0) dist_first=0;

    // check distance between the corners
    else if (iCorner==NCorners-1)
        {
        if (dist_prev>NormEPrev)   $message($strcat(CallingFunc," calling CreateRoundedPolygon:
        Not enough distance between corners ",iCorner-1," and ",iCorner,"! Maybe corner radius too large...
        Note: Corner numbering starts at 0"));
```

```
        if (dist_first>NormENext)  $message($strcat(CallingFunc," calling CreateRoundedPolygon:
        Not enough distance between corners ",NCorners-1," and 0! Maybe corner radius too large...
        Note: Corner numbering starts at 0"));
        }
    else
        {
        if (dist_prev>NormEPrev)   $message($strcat(CallingFunc," calling CreateRoundedPolygon:
        Not enough distance between corners ",iCorner-1," and ",iCorner,"! Maybe corner radius too large...
        Note: Corner numbering starts at 0"));
        }

    dist_prev=0;
    // Only point to draw is the corner itself
    VecCoordinates[Point] = Corner[iCorner];
    Point = Point+1;
  }

}
//if (BDebugLevel & 0b10000000) $message($strcat(CallingFunc," calling CreateRoundedPolygon:
Number of Points calculated: ", Point));

// *** return finished Vector
return(VecCoordinates);
}
```

11

Geometry of the Belle II DSSDs - data sheets

11.1. Large rectangular sensor

Chip overall

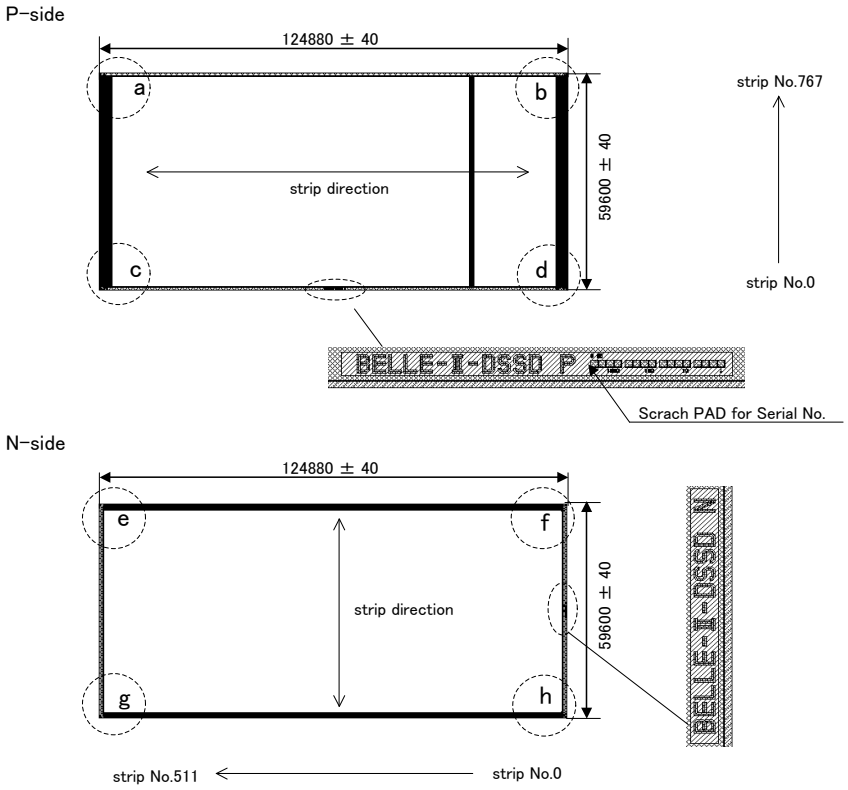

P-side,N-side relation (N-side mirrored)

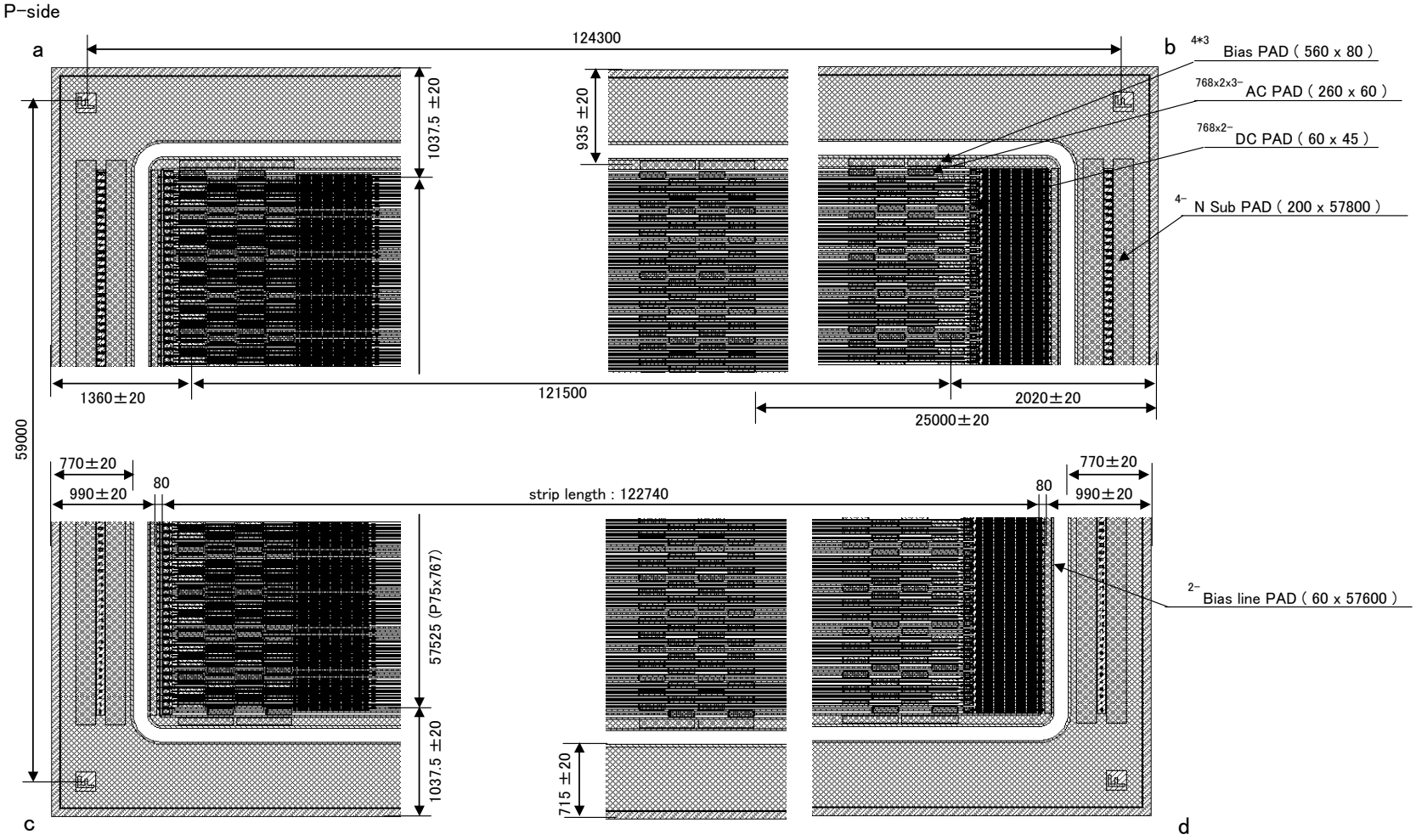
P-side
a
b
c
d
124300
59000
1037.5 ±20
935 ±20
1360±20
121500
2020±20
25000±20
4*3
Bias PAD (560 x 80)
768x2x3-
AC PAD (260 x 60)
768x2-
DC PAD (60 x 45)
4-
N Sub PAD (200 x 57800)
770±20
990±20
80
strip length : 122740
57525 (P75x767)
715 ±20
2-
Bias line PAD (60 x 57600)

N-side

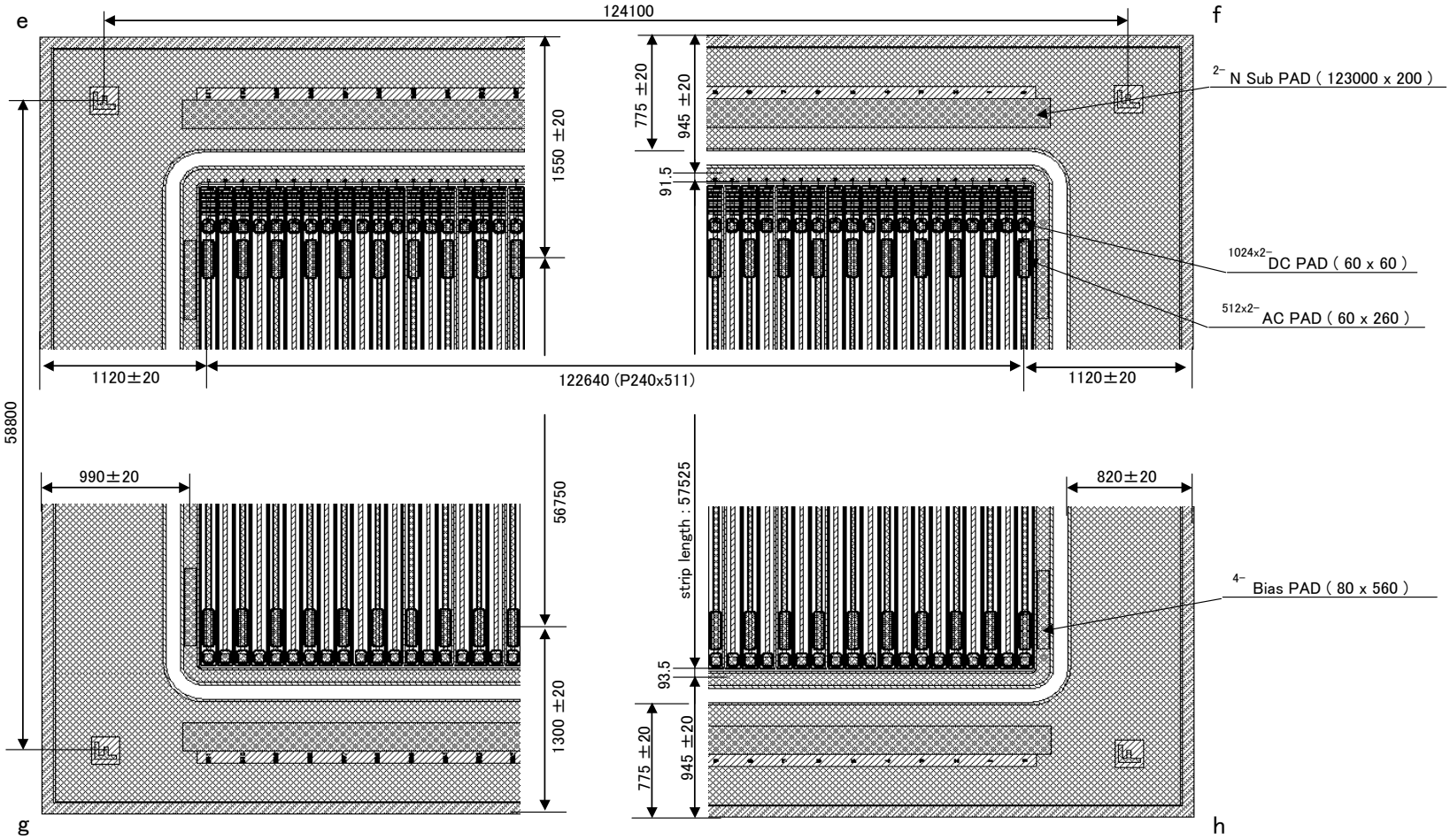
e
f
g
h
124100
58800
56750
1550 ±20
1300 ±20
775 ±20
945 ±20
91.5
93.5
1120±20
122640 (P240x511)
990±20
820±20
strip length : 57525
2- N Sub PAD (123000 x 200)
1024x2- DC PAD (60 x 60)
512x2- AC PAD (60 x 260)
4- Bias PAD (80 x 560)

strips & PADs detail

P-side

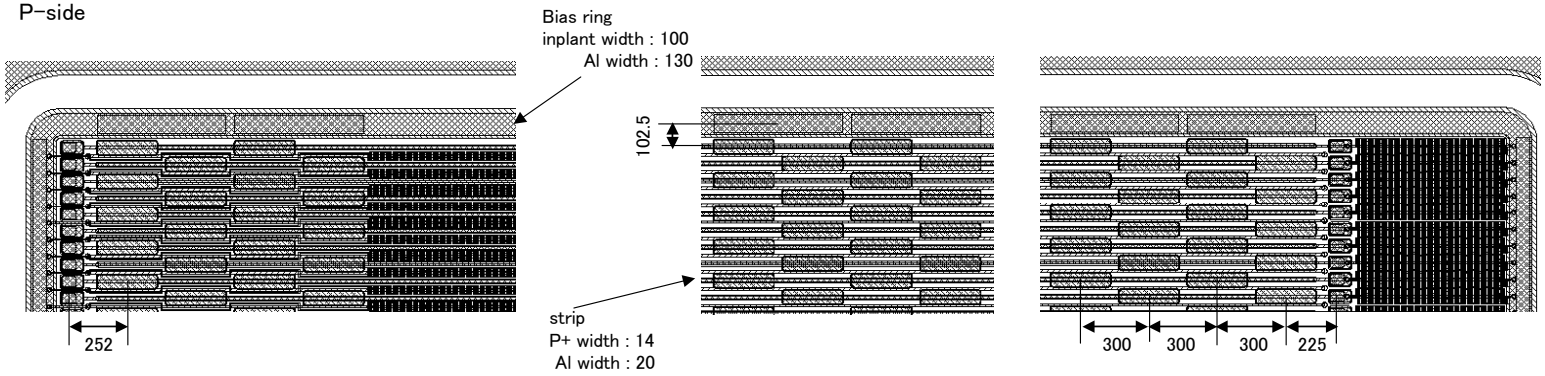

N-side

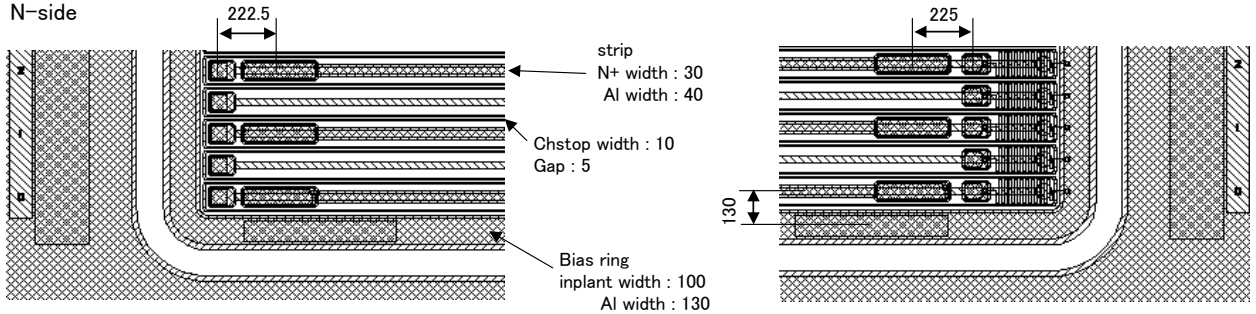

Index PAD detail P-side chNo. 0 / 128 / 256 / 384 / 512 / 640

N-side chNo. 0 / 128 / 256 / 384

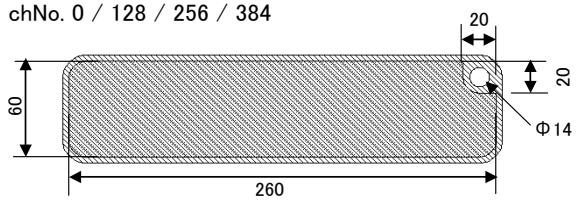

11.2. Small rectangular sensor

Chip overall

P−side

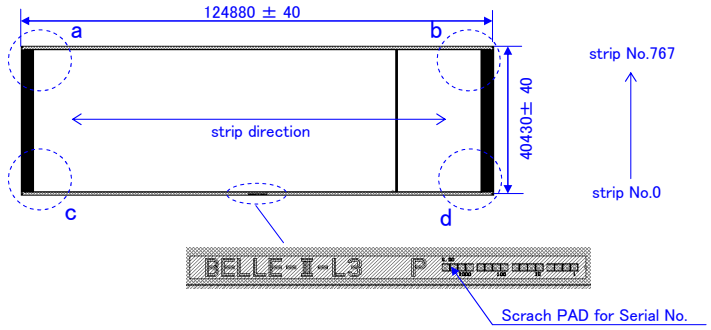

N−side

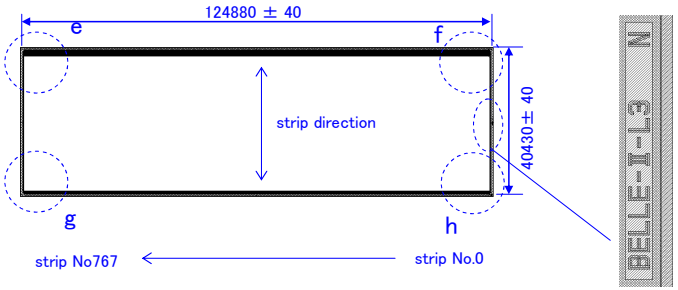

P−side,N−side relation (N−side mirrored)

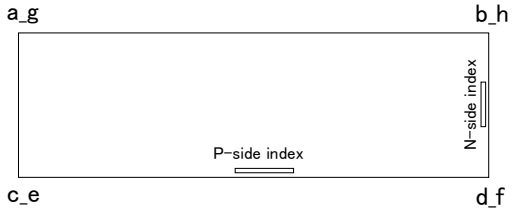

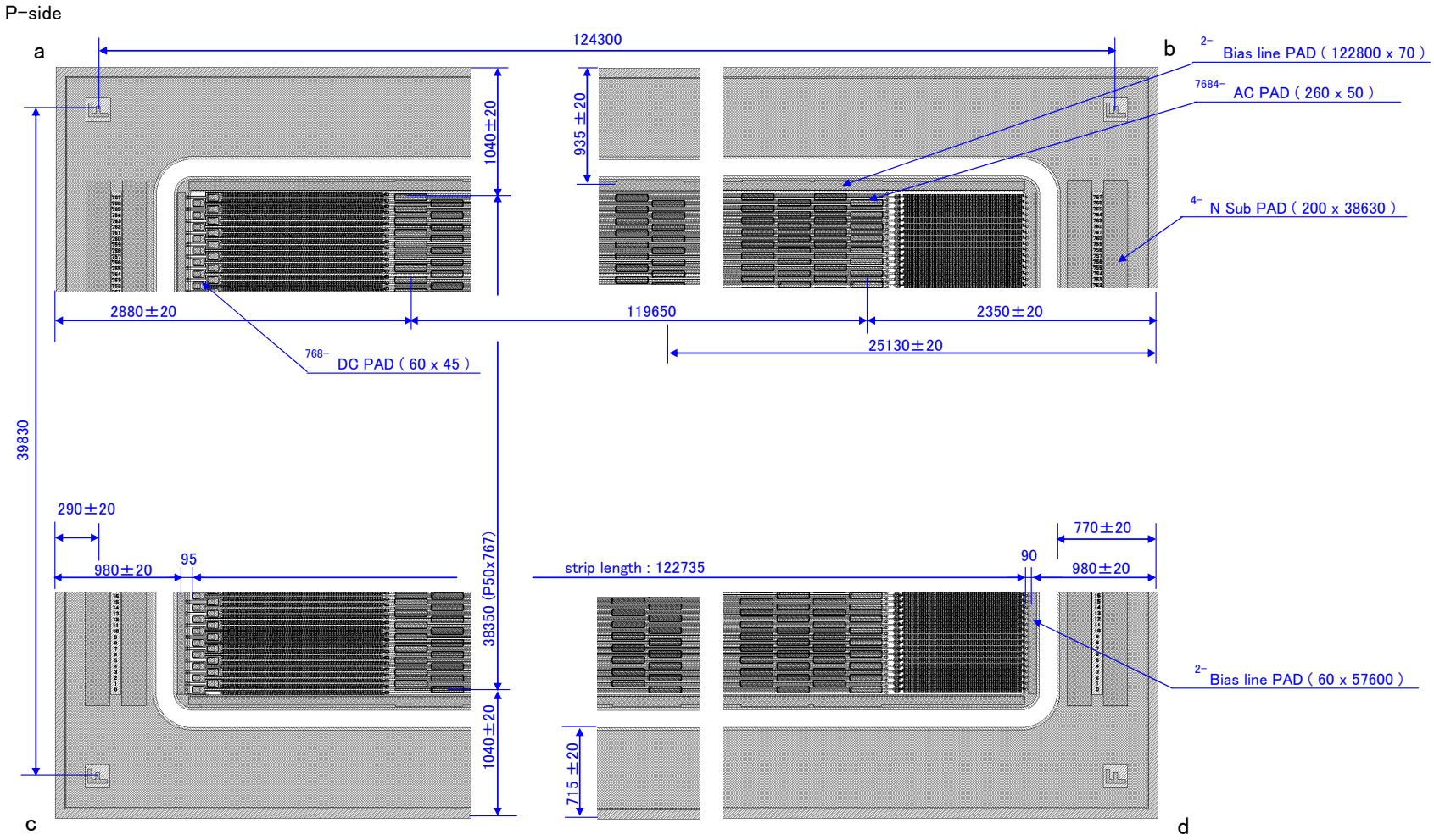
P-side
a
b
c
d
124300
1040±20
935 ±20
2-
Bias line PAD (122800 x 70)
7684-
AC PAD (260 x 50)
4-
N Sub PAD (200 x 38630)
2880±20
119650
2350±20
25130±20
768-
DC PAD (60 x 45)
39830
290±20
980±20
95
38350 (P50x767)
strip length : 122735
90
770±20
980±20
2-
Bias line PAD (60 x 57600)
1040±20
715 ±20

N-side

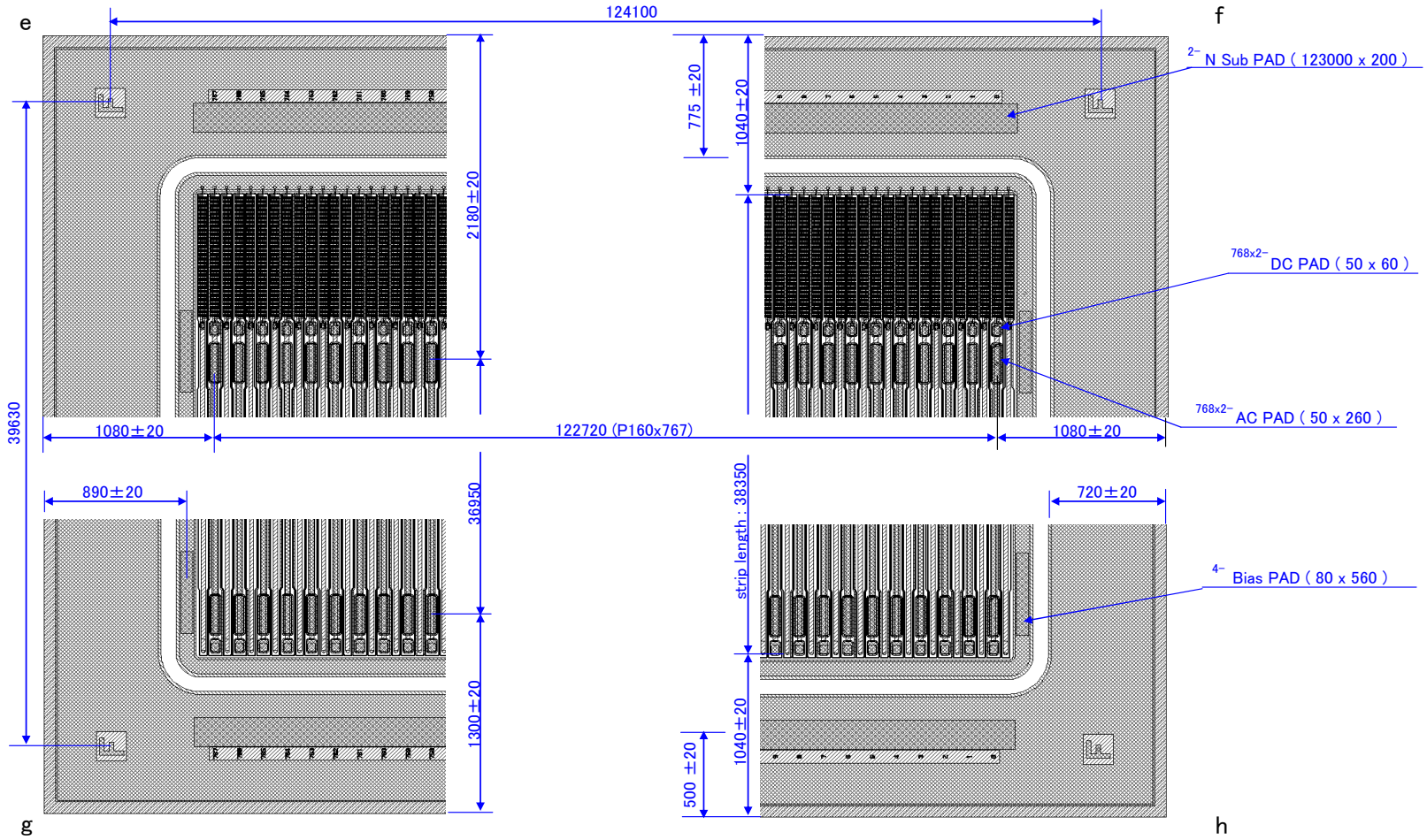
e
f
g
h
124100
39630
2180±20
775 ±20
1040±20
2- N Sub PAD (123000 x 200)
768x2- DC PAD (50 x 60)
768x2- AC PAD (50 x 260)
1080±20
122720 (P160x767)
1080±20
890±20
36950
1300±20
strip length : 38350
720±20
4- Bias PAD (80 x 560)
500 ±20
1040±20

strips & PADs detail

P-side

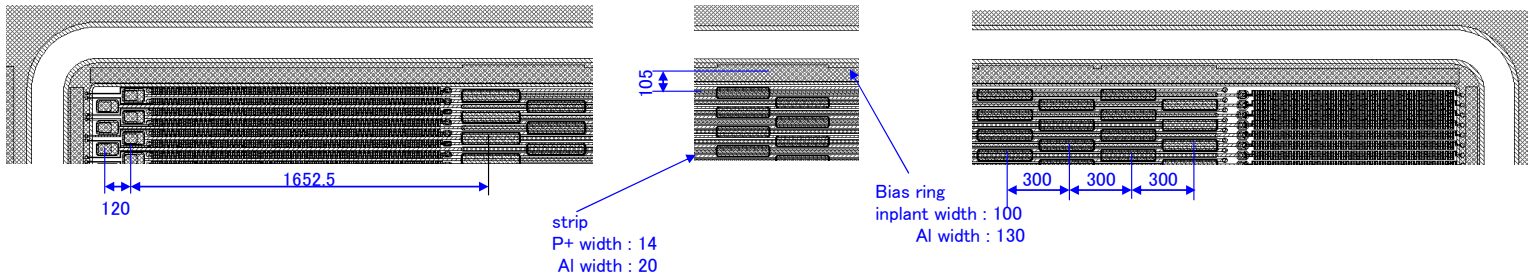

N-side

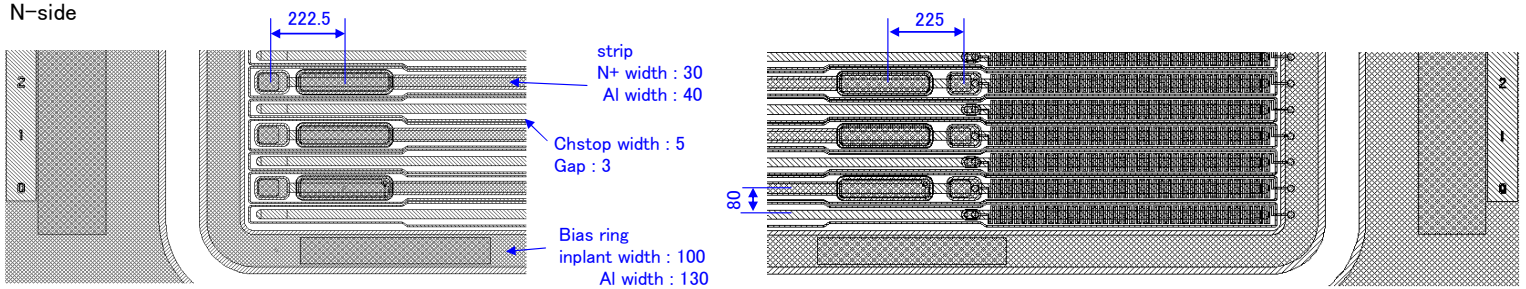

Index PAD detail P-side chNo. 0 / 16 / 32 ・・・ 736 / 752 /

N-side chNo. 0 / 16 / 32 ・・・ 736 / 752 /

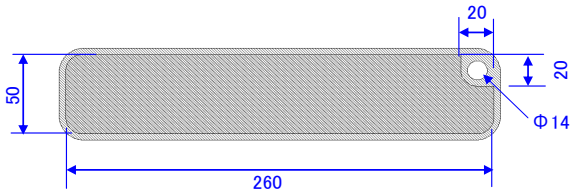

11.3. Trapezoidal sensor

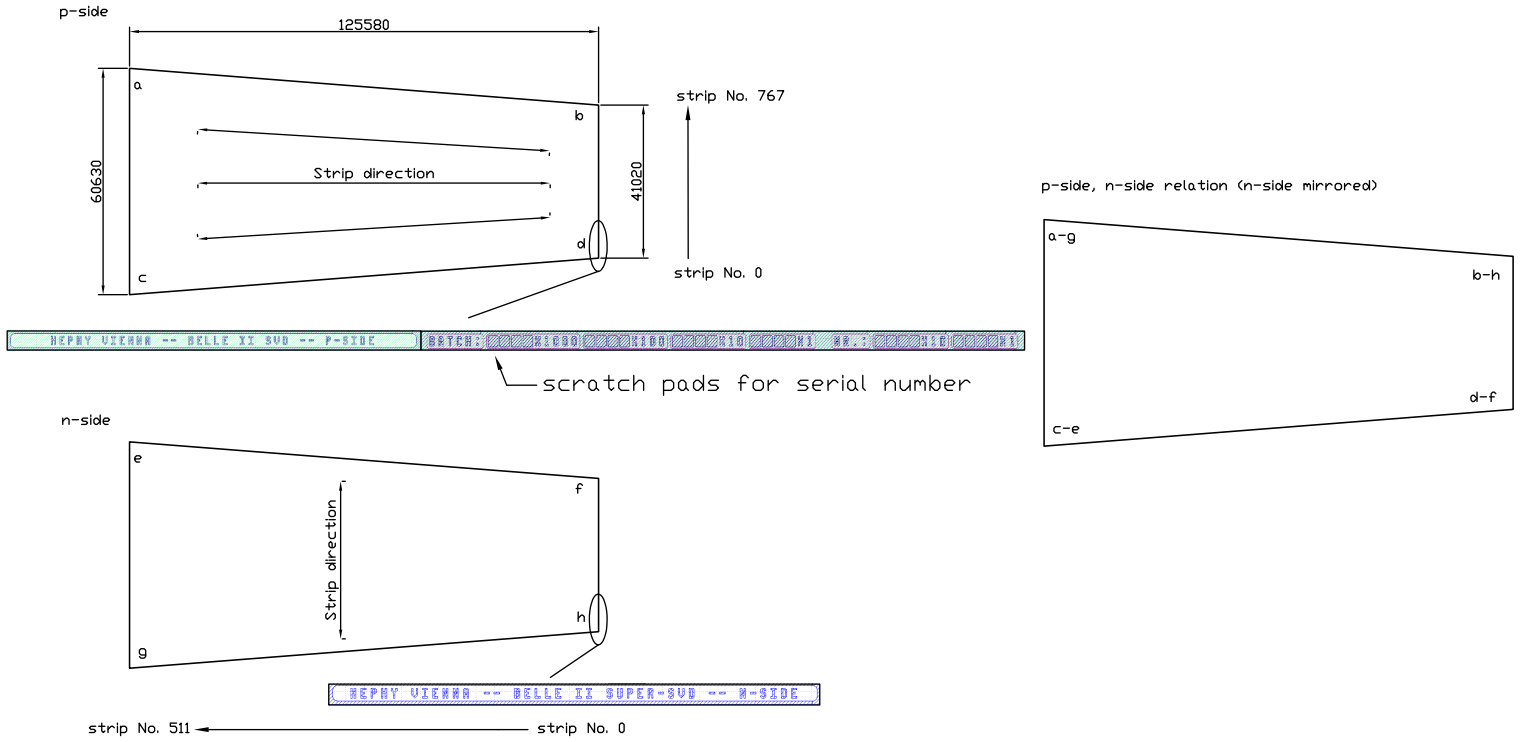

p-side

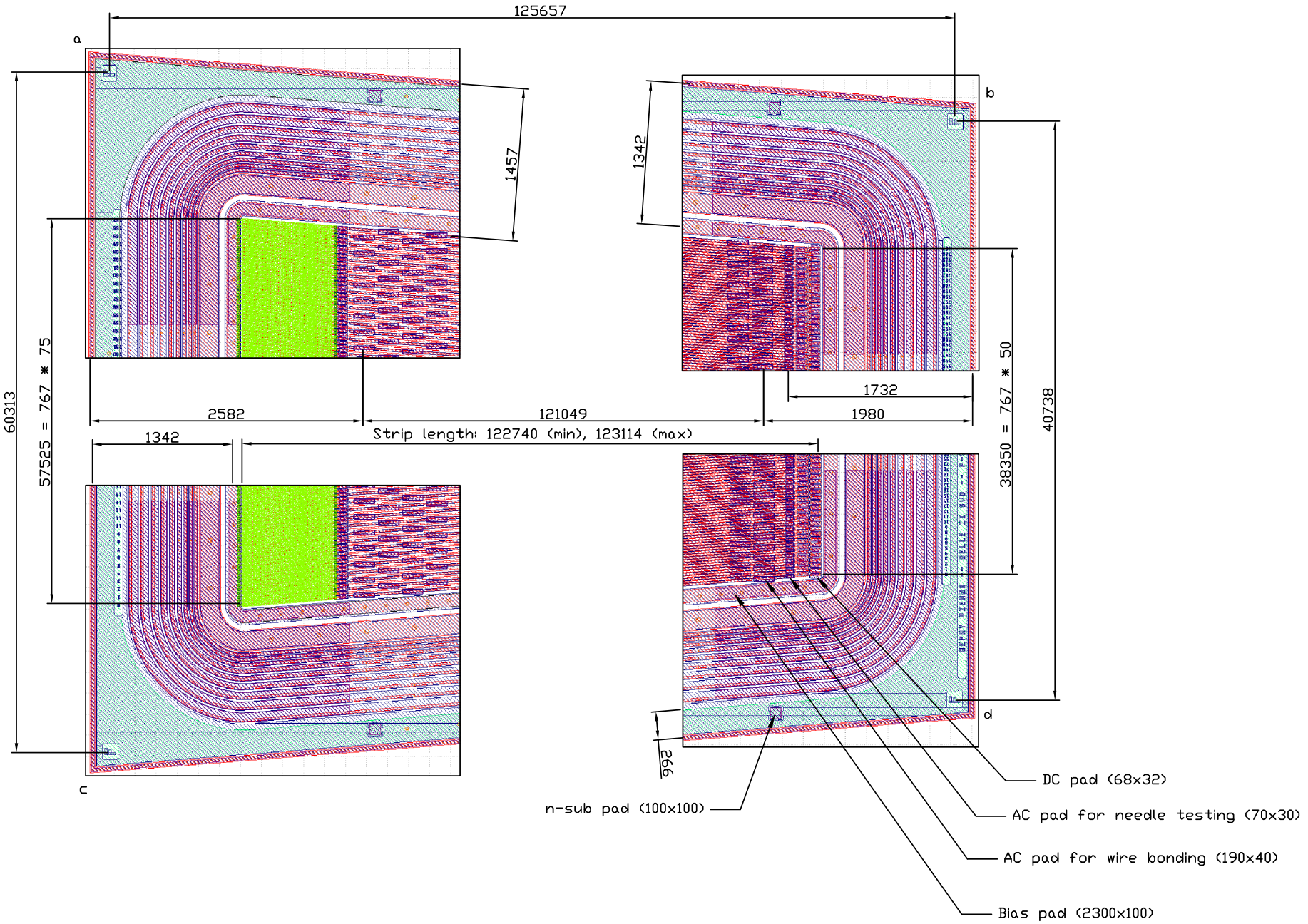
125657
a
b
c
d
1457
1342
60313
57525 = 767 * 75
38350 = 767 * 50
40738
2582
121049
1732
1980
1342
Strip length: 122740 (min), 123114 (max)
266
n-sub pad (100x100)
DC pad (68x32)
AC pad for needle testing (70x30)
AC pad for wire bonding (190x40)
Bias pad (2300x100)

n-side

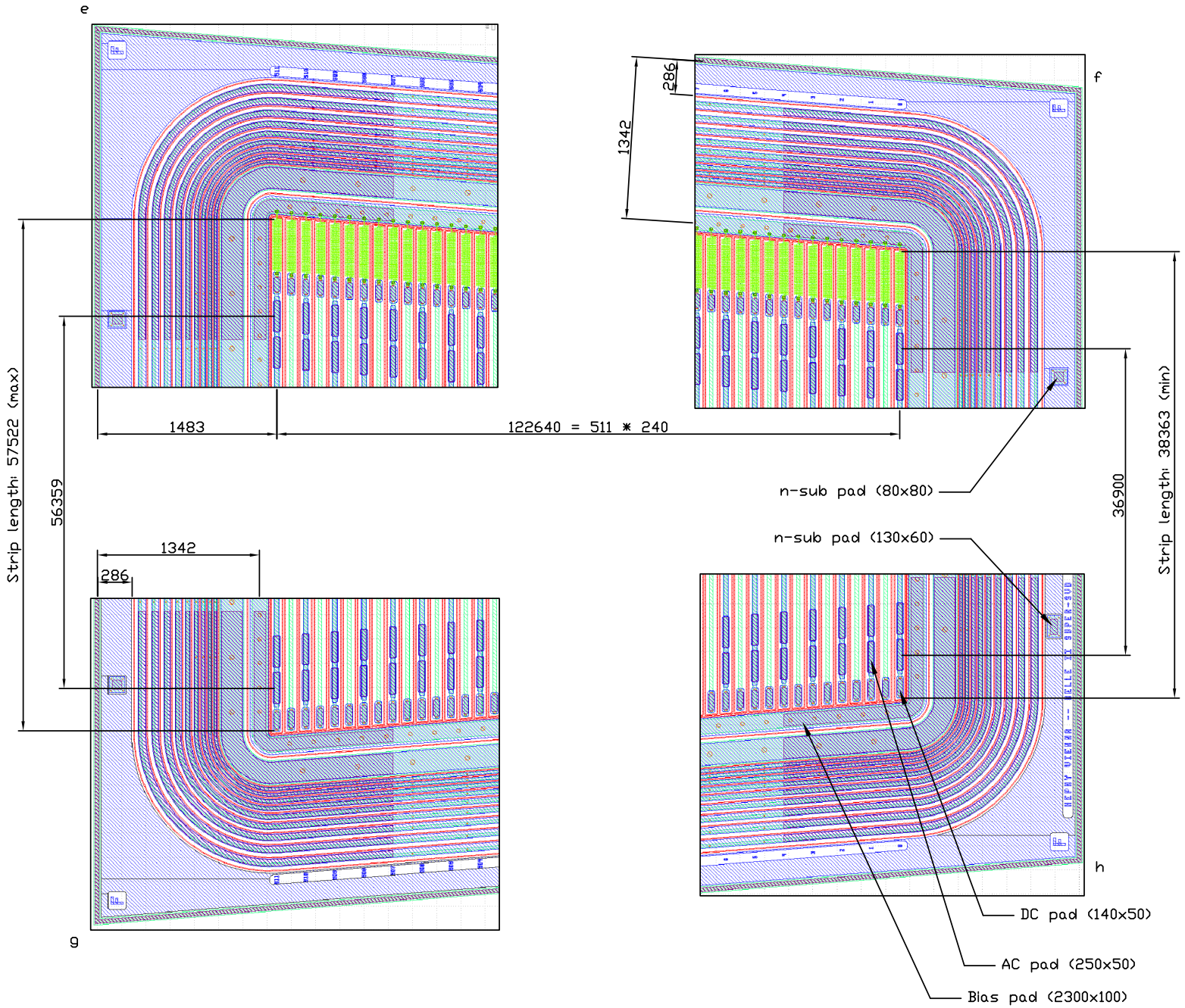
e
f
g
h
1342
286
1483
122640 = 511 * 240
Strip length: 57522 (max)
56359
Strip length: 38363 (min)
36900
n-sub pad (80x80)
n-sub pad (130x60)
DC pad (140x50)
AC pad (250x50)
Bias pad (2300x100)

Strips and pads - details

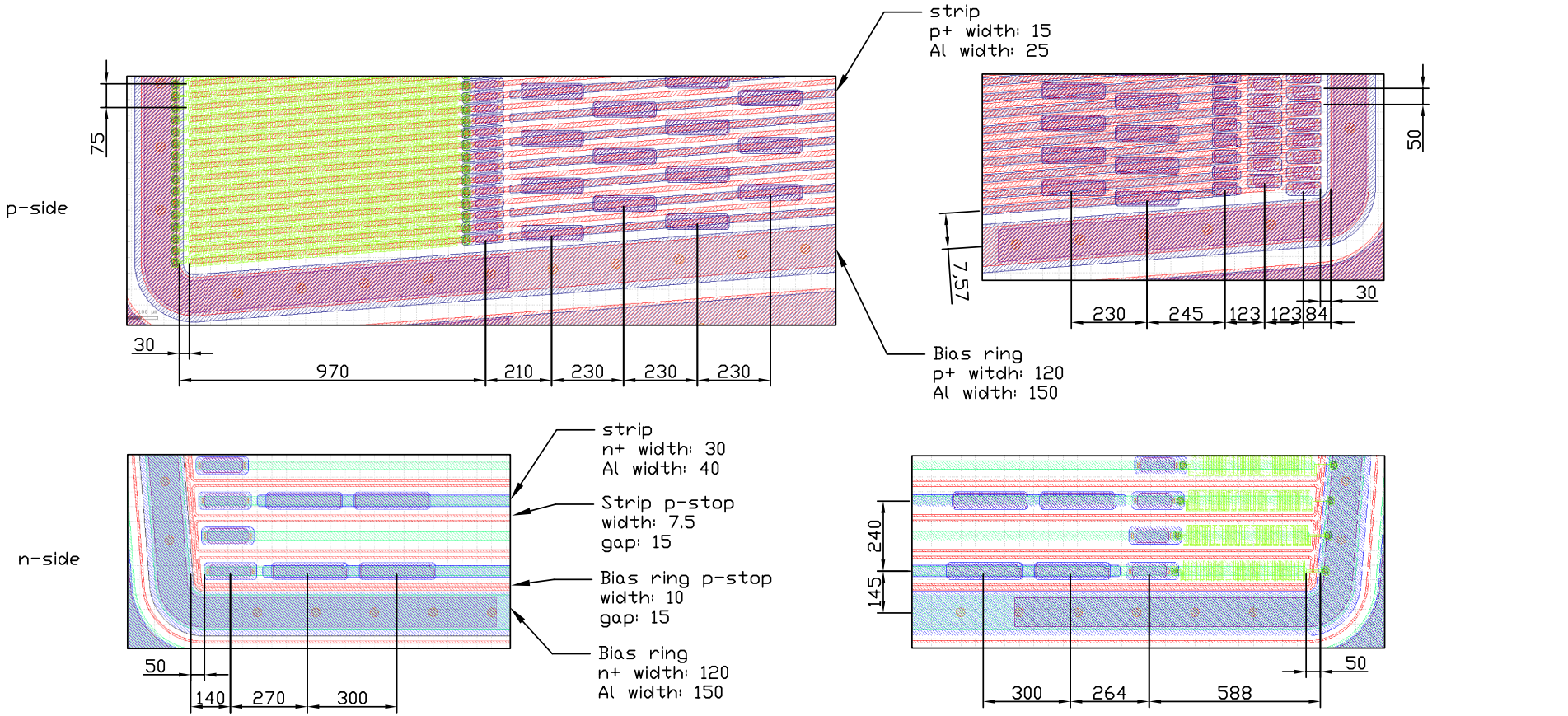

Index pad detail: strips nr. 0, 128, 256,...

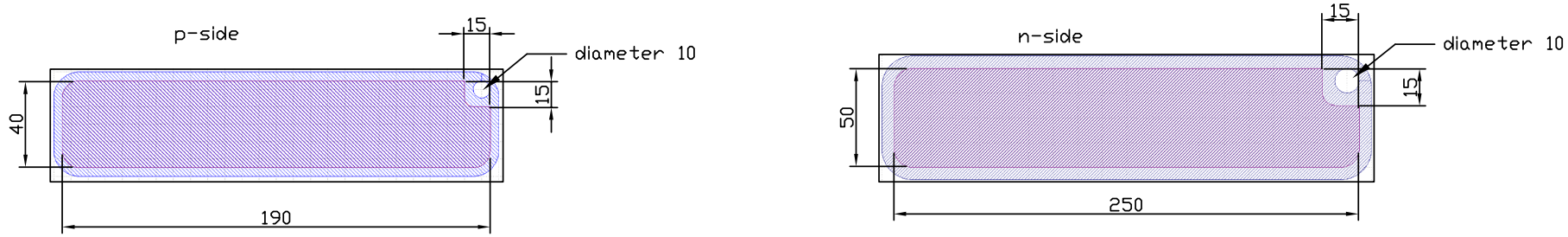

Glossary

Some of the definitions shown here are excerpts from [58].

Υ The Υ meson is a so-called "bottonium", consisting of a b quark and of a $\overline{\text{b}}$ anti-quark. i, iii, 7–9, 11

AC-coupled An AC-coupled sensor strip is connected to the readout electronics via a coupling capacitor. Being only conductive for AC currents, it filters the strip's dark current (a DC current) away. The capacitance of this coupling is called "coupling capacitance". 31, 33, 70

acceptance The acceptance region of Belle II is the polar angle region $17° \leq \theta \leq 150°$. This region is equipped with particle-sensitive devices. See section 10.1.2 for details. 18, 24–26, 33, 37, 39, 42, 234, 235, 273

acceptor In semiconductor physics, an acceptor is a dopant atom that can form a p-type region. For example, when silicon (Si), having four valence electrons, needs to be doped as a p-type semiconductor, elements from group III like boron (B) or aluminium (Al), having three valence electrons, can be used. When substituting a Si atom in the crystal lattice, the three valence electrons of boron form covalent bonds with three of the Si neighbours but the bond with the fourth neighbour remains unsatisfied. At room temperature, an electron from the neighbouring bond will jump to repair the unsatisfied bond thus leaving a hole (a place where an electron is deficient) in a chain-like process, which results in the hole moving around the crystal and able to carry a current thus acting as a charge carrier. The initially neutral acceptor becomes negatively charged (ionised). 31, 49–51, 55, 61, 62, 103, 267, 279, 284

accumulation Accumulation situation occurs in a p-n-junction, when a considerable amount of majority charge carriers are accumulated at an interface between a semiconductor and another material. This situation can occur for weakly bent energy bands, e.g. due to the presence of fixed positive oxide charges. In case of n-type material, the formed accumulation layer consists of electrons and shorts n-type doped regions at the surface. It therefore has to be interrupted by a p-stop or p-spray implantation. 71, 73, 74, 77, 78, 80, 103, 104, 129, 137, 138, 178, 266, 278

active area The active area of a silicon microstrip sensor is the area where it is sensitive to particles, i.e. the area where the electrode is segmented to form strips. To simplify

things, in this thesis the active area is defined as the area outlined by the bias ring. 32–34, 263

AC pad The AC pad is an area in the metal layer of a strip intended to allow contact to the metal strip. It is called "AC" because the metal strip only sees the AC component of the dark current and signal. 99, 106, 118, 134, 136, 151, 154, 199, 225

APV25 The future Belle II experiment will use the APV25 chip for reading out the DSSDs of the SVD. It was developed and is used for the CMS experiment at the LHC at CERN. The acronym stands for Analog Pipeline Voltage (0.25um). 35–41, 86, 87, 89, 101, 157, 159, 161, 167, 213–217, 278, 280

area moment of inertia The area moment of inertia, also known as second moment of area, is a geometrical property of an area which reflects how its points are distributed with regard to an arbitrary axis. It is closely linked to the calculation of stiffness and straws of bent beams. 27

atoll A variant of the p-stop blocking method. Each n-type strip is surrounded by its individual "ring-like" p-type implantation. ii, iv, 34, 135–139, 166, 167, 169–171, 173, 174, 176, 178–180, 182, 184, 185, 187–189, 191, 192, 194, 202, 213, 215, 218, 222, 224, 227, 266

b-tagging b-tagging is the process of identifying a B meson from its decay products, and determining if it contained a b quark or a $\overline{\text{b}}$ anti-quark. 9

BaBar BaBar is the name of a particle physics experiment at the PEP-II collider at SLAC National Accelerator Laboratory, which was operated by Stanford University for the Department of Energy in California. It was a "friendly competitor" of the Belle experiment, also measuring CP violation with B mesons. 6

backplane The backplane of a single-sided silicon microstrip sensor is the sensor side *not* instrumented with strips. A DSSD has no backplane in that sense. 99–101, 105

backplane capacitance The backplane capacitance is the capacitance between an implanted strip and the other side of the sensor. It is usually calculated as the total capacitance (parallel plate capacitor configuration) divided by the number of strips. 88, 192

backward The backward part of Belle II is the side of negative z direction. See section 10.1.2 for details. 19, 29, 30, 236

band gap In solid state physics, a band gap, also called an energy gap, is an energy range in a solid where no electron states can exist. In graphs of the electronic band structure of solids, the band gap generally refers to the energy difference (in eV) between the top of the valence band and the bottom of the conduction band in insulators and semiconductors. For metals the conduction band and the valence band overlap, removing the band gap. 46–51, 56, 61, 68, 70, 268, 270

barrel Usual particle detectors at colliders are shaped like a cylinder around the beam axis. In contrast to the endcap part, the barrel part is the cylindrical part of this detector. 17, 19–21, 31, 32, 236, 270, 275

baryon A baryon is a composite subatomic particle made up of three quarks. 3, 14, 273

beam test In a beam test, sensors are exposed to a particle beam to determine their response to real particles. The beam is usually extracted from a particle accelerator or storage ring, and can be tuned to the user's requirements in composition and energy. iv, 43, 89, 93, 94, 135, 156, 157, 159–161, 164, 166, 171, 180, 182, 183, 193–197, 213, 214, 224, 227–229, 271

Belle Belle is the name of a former particle physics experiment at KEK (Tsukuba, Japan). Belle is not an acronym, so it's written with a capital letter at the beginning only. Belle is the french word for "beautiful", and hints to the b quark, also called "beauty quark". 6, 9, 12, 14–21, 23–25, 39, 262, 263, 285

Belle II Belle II is the name of a future particle physics experiment at KEK (Tsukuba, Japan) which is presently under construction. It is the successor of the Belle experiment. i–iv, 4, 9, 12, 14, 16–21, 23–25, 31, 35, 36, 40, 79, 80, 88, 89, 96, 111, 119, 126, 148, 159, 182, 197, 205, 212, 213, 227–229, 233, 234, 236, 261, 262, 266, 270, 272, 273, 282, 285

Bethe-Bloch equation In nuclear physics and theoretical physics, charged particles moving through matter interact with the electrons of atoms in the material. The interaction excites or ionises the atoms. This leads to an energy loss of the traversing particle. The Bethe-Bloch formula describes the energy loss per distance travelled of swift charged particles (protons, alpha particles, atomic ions, but not electrons) traversing matter (or alternatively the stopping power of the material). 58, 59

Bhabha scattering In quantum electrodynamics, Bhabha scattering is the electron-positron interaction process, where the particle either scatter or annihilate and create a new electron-positron pair. 57

bias resistor The bias resistor connects the strips of a silicon microstrip sensor to the bias ring, which is further connected to the power supply. It is made of polysilicon. 31, 33, 35, 88, 100, 102, 106, 118, 121, 122, 130–135, 151, 154, 155, 170, 189, 200, 203, 204, 263, 267, 274, 281

bias ring The bias ring encloses the active area and is connected to the power supply for biasing the sensor. It hands the potential over to the strips via the bias resistors, FOXFET or punch through biasing. 100, 102, 105, 119, 122, 130, 134, 149, 151, 152, 154, 198, 205, 262, 263, 273

bias voltage Biasing in electronics is the method of establishing predetermined voltages or currents at various points of an electronic circuit for the purpose of establishing proper operating conditions in electronic components. Many electronic devices whose

function is to process time-depending (AC) signals also require a constant (DC) current or voltage to operate correctly. In terms of silicon microstrip sensors, the bias voltage is the voltage applied between the two side of the sensor, which depletes the sensor and establishes the drift field for the signal charge carriers. 56, 64, 66, 105, 267, 272, 275, 281

Boltzmann constant The Boltzmann constant k_B, named after Ludwig Boltzmann, is a physical constant relating energy at the individual particle level with temperature. It is the gas constant R divided by the Avogadro constant N_A: $k_\mathrm{B} = {}^{R}/_{N_\mathrm{A}} = 1.3806 \times 10^{-23}\,\mathrm{J/K} = 8.6173 \times 10^{-5}\,\mathrm{eV/K}$. 48

boson A boson is a (not necessarily fundamental) particle with an integer spin quantum number. It obeys the Bose-Einstein statistics but not the Pauli exclusion principle. So, two bosons with an identical set of quantum numbers can occupy the same state in a system. All mediators of the fundamental interactions are bosons. 4, 273, 286

branching fraction The branching fraction of a decay denotes how often this decay occurs relative to the total number of possible decays (*absolute* branching fraction) or relative to the occurrences of another specific decay mode (*relative* branching fraction). 8

bremsstrahlung Bremsstrahlung (from German bremsen "to brake" and Strahlung "radiation", i.e. "braking radiation" or "deceleration radiation") is electromagnetic radiation produced by the deceleration of a charged particle when deflected by another charged particle, typically an electron by an atomic nucleus. The moving particle loses kinetic energy, which is converted into a photon because energy is conserved. The term is also used to refer to the process of producing the radiation. 57, 282

built-in voltage The built-in voltage is the potential difference introduced by the space charge region in a semiconductor's p-n-junction. 63, 66, 70

bulk The bulk is the volume of a silicon substrate, as opposed to the surface of the substrate. 31, 63, 65–67, 71, 73, 77–83, 86, 102–104, 109, 111, 113, 126–134, 140, 151, 153, 175, 205, 225, 227, 267, 270, 272, 277–279, 282, 283, 285

bunch A bunch is a substructure of the particle beam. The particles are grouped to form "clouds" of several million particles travelling together. 11, 14, 36, 282

B factory A B factory is a particle collider specifically designed to deliver a huge amount of B mesons. iii, 11, 289, 291

B meson B mesons contain a $\overline{\mathrm{b}}$ anti-quark, whereas B anti-mesons contain a b quark. Those quarks are accompanied by u or d quarks or their anti-particles, respectively. i, iii, 4, 7–9, 11, 14–16, 18, 20, 23, 262, 264

B physics B physics deals with the interactions and phenomena found in B meson systems, especially CP violation. 25

calorimeter A calorimeter is an experimental apparatus that measures the energy of particles. Most particles enter the calorimeter and initiate a particle shower and the particles' energy is deposited in the calorimeter, collected, and measured. The energy may be measured in its entirety, requiring total containment of the particle shower, or it may be sampled. Typically, calorimeters are segmented transversely to provide information about the direction of the particle or particles, as well as the energy deposited, and longitudinal segmentation can provide information about the identity of the particle based on the shape of the shower as it develops. 15, 20, 288

charge carrier generation In the solid-state physics of semiconductors, carrier generation is a processes by which mobile charge carriers (electrons and holes) are created. This can happen by thermal excitation, optical excitation by an absorbed photon, and by charged particles. The e-h-pair is the fundamental unit of generation and recombination, corresponding to an electron transitioning between the valence band and the conduction band. 59, 265

charge carrier recombination In the solid-state physics of semiconductors, carrier recombination is a processes by which mobile charge carriers (electrons and holes) are eliminated. It is the reverse process of charge carrier generation. 59, 265

charge collection efficiency The charge collection efficiency is a quality indicator for silicon microstrip sensors. Ideally, every single charge carrier released by a traversing particle should drift all the way to the electrodes, inducing the maximum signal possible. In reality, lattice imperfections trap and scatter the charge carriers, leading to a reduced charge collection efficiency. Note that the exact amount of ionised charge carriers is not known, so that the charge collection efficiency can only be an estimate. 87, 287

charge conjugation The charge conjugation transforms a particle into its anti-particle by reversing all of its quantum numbers, especially the electrical charge. 3, 5, 265

charge sharing In silicon microstrip sensors, charge sharing is the beneficial effect where the charge generated by a traversing particle is collected by two or more adjacent strips. This makes the position measurement more accurate, as long as the amount of the collected charge is measured. Charge sharing is not to be confused with crosstalk, where the signal picked up by a strip is capacitively coupled to an adjacent strip. Crosstalk does *not* improve the position measurement. 93, 94, 162, 193, 274

charge-parity conjugation The charge-parity conjugation is the combination of the charge conjugation and the parity conjugation. iii, 3, 288

chemical vapour deposition Chemical vapor deposition (CVD) is a chemical process used to produce high-purity, high-performance solid materials. The process is often used in the semiconductor industry to produce thin films. In a typical CVD process, the wafer (substrate) is exposed to one or more volatile precursors, which react and/or decompose on the substrate surface to produce the desired deposit. Frequently, volatile by-products are also produced, which are removed by gas flow through the reaction chamber. 110, 287, 288, 290

Cherenkov counter A Cherenkov counter uses the Cherenkov effect to distinguish particle types by determining their velocity. The speed of light in a material is lower than the speed of light in vacuum. A particle traversing a material at a velocity higher than the velocity of light *in that material* causes the material to radiate photons. The angle of this radiation relative to the direction of the particle depends on the velocity of the particle. Together with an energy measurement this allows to determine the mass and thus the identity of the particle. 15, 19, 287, 291

cluster A cluster is composed of two or more adjacent strips with signals above a predefined threshold. In case of the Belle II SVD, a signal five times as high as the strip noise defines the seed strip; for the neighbour strips, signals three times as high as the respective strip noise are required. The total cluster signal has to be at least five times as high as the total cluster noise. 89–92, 160, 162, 163, 170, 174–176, 185, 188, 189, 192, 193, 217, 220, 221, 266, 283

cluster width The cluster width (or cluster size) is the number of strips above threshold for a given hit cluster. 91, 160, 161, 163, 175, 193, 194, 196, 274

combined For the combined p-stop pattern, the n-type doped strips are surrounded by atoll p-stop implants. In addition to that, both strip and atoll implants are embedded in a p-type doped area covering the whole sensor, like in case of the common pattern. Only small regions around the strip and the atoll are left unimplanted. This pattern tries to combine the benefits of the common pattern and the atoll pattern. ii, iv, 136, 138, 166, 167, 169–171, 173, 174, 177, 178, 180, 182, 184, 185, 187–189, 191–194, 202, 213, 218, 222, 224, 227

common For the common p-stop pattern, the n-type doped strips are surrounded by a p-type doped area covering the whole sensor. Only small regions around the strips are left unimplanted. This interrupts the accumulation layer which hence cannot short the n-type strips. The p-stop implant itself is on the same (floating) potential all over the sensor and could therefore distribute any charge introduced in the implant. ii, iv, 137–139, 166, 167, 169–171, 173, 174, 177, 178, 180, 182, 184, 185, 187–189, 191, 192, 194, 215, 227, 266

common mode correction The common mode correction is a correction algorithm in the data acquisition which removes correlated noise of applying to all strips of a silicon microstrip sensor. 40, 162

conduction band The conduction band is the range of electron energies sufficient to free an electron from binding with its atom to move freely within the atomic lattice of the material as a delocalized electron. 47–56, 61, 68, 70, 262, 265, 268, 269

conductivity Electrical conductivity or specific conductance is the reciprocal of electrical resistivity, and measures a material's ability to conduct an electric current. 49, 110, 130, 178, 193

coupling capacitance The coupling capacitance is the capacitance created by the implanted strip and the aluminium line atop of it. It is crucial for removing the DC component of the dark current. 101, 110, 132, 135, 140, 154–156, 201, 203, 204, 261, 280

coupling oxide The coupling oxide (also called "readout oxide") is the thin oxide layer between the implanted strip and its metallisation, which isolates the readout electronics from the silicon bulk. Its purpose is to remove the DC component of the dark current to avoid saturation of the input channels of the readout chip. 99, 100, 106, 121, 128, 129, 134, 135, 155, 201, 203, 278

cross section The cross section is a hypothetical area which describes the likelihood of a reaction in a particle collision. It is different from the geometrical cross sections of the involved particles, and depends strongly on the collision energy. The typical unit is "barn", where $1\,\mathrm{b} = 10^{-28}\,\mathrm{m}^2$ ($100\,\mathrm{fm}^2$). 11, 276

crystal momentum In solid-state physics, crystal momentum or quasimomentum is a momentum-like vector associated with electrons in a crystal lattice. It is defined by the associated wave vectors k of this lattice, according to $p_{\mathrm{crystal}} = \hbar k$, where $\hbar = 6.626 \times 10^{-34}\,\mathrm{Js} = 4.1357 \times 10^{-15}\,\mathrm{eVs}$ is the reduced Planck's constant. Often the wave number k is wrongly called crystal momentum. 56, 61

CV-curve The CV-curve shows the total capacitance of a diode or a silicon microstrip sensor as function of the bias voltage. It can be used to determine the full depletion voltage. 66, 67, 152, 153, 198, 199

dark current A sensor's dark current is the current through the sensor when there is *no* signal present. Since a sensor can be thought of as a large bulk diode, the dark current is basically the leakage current of this diode. 33, 64, 79, 80, 88, 99, 101, 105, 108, 140, 152–154, 198–200, 202, 205–212, 261, 262, 267, 275

DC pad The DC pad is a contact area which allows to contact the implanted strip. It is connected to the implanted strip through an oxide window, and often also connects the end of the bias resistor to the implanted strip. 100, 106, 118, 122, 130, 133, 134, 136, 151, 153, 154, 180, 199, 225

degenerate A degenerate semiconductor is a semiconductor with such a high level of doping that the material starts to act more like a metal than a semiconductor. 70

depletion In semiconductor physics, the depletion region, also called space charge region, is an insulating region within a conductive, doped semiconductor material where the mobile charge carriers have diffused away, or have been forced away by an electric field. The only elements left in the depletion region are ionised donor or acceptor impurities. 61–64, 66, 67, 71, 73, 75, 77, 78, 82, 102, 105, 198, 272, 283

deposition The act and technique of applying a thin film to a surface is thin-film deposition. "Thin" is a relative term, but most deposition techniques control layer thicknesses within a few tens of nanometers. Molecular beam epitaxy allows a single layer of atoms to be deposited at a time. 109, 110, 112, 130, 132, 133, 283, 284

dicing Dicing is the process by which dies are separated from a semiconductor wafer after complete processing of the wafer. The dicing process can be accomplished by scribing and breaking, by mechanical sawing (normally with a machine called a dicing saw) or by laser cutting. During dicing, wafers are typically mounted on dicing tape which has a sticky backing that holds the wafer on a thin sheet metal frame. 100, 105, 113, 121, 123, 134, 268

dicing line The dicing line is a structure prepared to avoid splintering during dicing. In an IC design, one has to make sure that there is no oxide along the path of the dicing. Some manufacturers also include a metallisation of the dicing line. 113, 121, 124, 127, 134

diffusion Diffusion – as opposed to drift – is the random motion of charge carriers which tends to level out geometrical charge carrier distribution inhomogeneities. 54, 55, 63, 64, 70, 111, 147, 161, 269, 278, 285

diode In electronics, a diode is a two-terminal component with asymmetric conductance, it has low (ideally zero) resistance to current flow in one direction, and high (ideally infinite) resistance in the other. A semiconductor diode, the most common type today, is a crystalline piece of semiconductor material with a p-n-junction connected to two electrical terminals. 61, 64, 66, 67, 70, 267, 272, 275, 282, 285

direct In semiconductor physics, the band gap of a semiconductor is always one of two types, a direct band gap or an indirect band gap. The band gap is called "direct" if the momentum of electrons and holes is the same in both the conduction band and the valence band; an electron can directly emit a photon. In an "indirect" gap, a photon cannot be emitted because the electron must pass through an intermediate state and transfer momentum to the crystal lattice. 56, 60, 61

dispersion relation In physics and electrical engineering, dispersion relations describe the effect of dispersion from a medium on the properties of a wave traveling within that medium. A dispersion relation connects different properties of the wave such as its energy, frequency, wavelength and wavenumber. From these relations, the phase velocity and group velocity of the wave have convenient expressions which can thereby determine a refractive index of the medium. 48, 56

distribution function In probability theory and statistics, the cumulative distribution function (CDF), or just distribution function, describes the probability that a real-valued random variable X with a given probability distribution will be found at a value less than or equal to x. In the case of a continuous distribution, it gives the area under the probability density function from minus infinity to x. 93, 94

donor In semiconductor physics, a donor is a dopant atom that can form an n-type region. For example, when silicon (Si), having four valence electrons, needs to be doped as an n-type semiconductor, elements from group V like phosphorus (P) or arsenic (As) can be used because they have five valence electrons. When substituting a Si atom in the crystal lattice, four of the valence electrons of phosphorus form covalent bonds with the neighbouring Si atoms but the fifth one remains weakly bonded. At room temperature, all the fifth electrons are liberated, can move around the Si crystal and can carry a current and thus act as charge carriers. The initially neutral donor becomes positively charged (ionised). 31, 49–51, 53, 55, 61, 62, 267, 277, 284

dopant A dopant, also called a doping agent, is a trace impurity element that is inserted into a substance (in very low concentrations) in order to alter the electrical properties or the optical properties of the substance. In the case of crystalline substances, the atoms of the dopant take the place of elements that were in the crystal lattice of the material. These materials are very commonly either crystals of a semiconductor (silicon, germanium, etc.), for use in solid-state electronics; or else transparent crystals that are used to make lasers of various types. 107, 111, 128, 129, 261, 269, 278

doping In semiconductor production, doping intentionally introduces impurities into an extremely pure ("intrinsic") semiconductor for the purpose of modulating its electrical properties. The impurities are dependent upon the type of semiconductor. Lightly and moderately doped semiconductors are referred to as extrinsic. 49–51, 54, 55, 63, 65, 66, 68, 70, 78, 82, 103–105, 110, 111, 121, 127–129, 131–134, 140, 142, 271, 274, 276, 278, 283

drift Drift – as opposed to diffusion – is the motion of charge carriers caused by an electric field $\vec{E}$. The charge carriers will move along the electric field lines, where the direction of this movement is determined by the charge of the carrier. 46, 53–55, 64, 82, 85, 86, 96, 99, 264, 268, 271, 285

drift chamber In a drift chamber many parallel wires (sense wires) are arranged as a grid and put on high voltage, with the metal casing or field forming wires being on ground potential. The chamber is filled with gas and a traversing particle leaves a trace of ions and electrons, which drift toward the nearest sense or field wires, respectively. By labelling the wires with a current signal it is possible to measure the track of the traversing particle. In a drift chamber, the timing of the pulse and thus the drift time of the charges is measured as well, which improves the spatial resolution within the cell. 15

e-h-pair The electron-hole pair is the fundamental unit of charge carrier generation and recombination, corresponding to an electron transitioning between the valence band and the conduction band. 46, 55–57, 60, 80, 82, 83, 85, 87, 92, 265

edge ring The edge ring is the outermost structure of a silicon microstrip sensor. It contains inscriptions like the strip numbering, and often features an additional implantation

for high-voltage stability and for contacting the bulk material using an n-sub pad. 100, 105, 131–134, 142, 225, 277

eigenstate The word "eigenstate" is derived from the German/Dutch word "eigen", meaning "inherent" or "characteristic". An eigenstate is the measured state of some object possessing quantifiable characteristics such as position, momentum, etc. The state being measured and described must be observable (i.e. something such as position or momentum that can be experimentally measured either directly or indirectly), and must have a definite value, called an eigenvalue. 5, 275

electro-weak The electro-weak interaction is the unified fundamental force that parents the electromagnetic interaction and the weak interaction. 4

electromagnetic The electromagnetic interaction is the force that acts on electrically charged particles, allowing them to be accelerated and trapped in bound states. Thus, it is responsible for the interaction between the atomic nucleus and the electron cloud. It is mediated by the photon. 4, 15, 23, 81, 270, 273, 276, 288

electron The electron (symbol: e^-) is a subatomic particle with a negative elementary electric charge. It is a lepton of the first generation of fundamental particles. i, iii, 4, 11, 14, 16, 20, 23, 45–51, 53–58, 60, 61, 64, 65, 68–71, 73, 74, 78–80, 83, 85–87, 96–99, 103, 104, 147, 161–163, 168, 169, 172, 173, 181, 186, 187, 190, 191, 218, 219, 222, 223, 227, 233, 234, 236, 261–272, 274–278, 281, 282, 284, 286

electron affinity In chemistry and atomic physics, the electron affinity of an atom or molecule is defined as the amount of energy released when an electron is added to a neutral atom or molecule to form a negative ion. 68

end-ring The end-rings form a mechanical support structure of the Belle II SVD, onto which the ladders are mounted. They arrange the ladders in a roughly cylindrical shape. 29, 42

endcap Usual particle detectors at colliders are shaped like a cylinder around the beam axis. In contrast to the barrel part, the endcap is the circular part of this detector, which closes this cylinder on both sides, like lids. 16, 17, 20, 21, 236, 263

energy band In solid-state physics, the electronic band structure (or simply band structure) of a solid describes those ranges of energy that an electron within the solid may have (called energy bands, allowed bands, or simply bands), and ranges of energy that it may not have (called band gaps or forbidden bands). 46, 47, 62, 68–78, 103, 261, 272, 274

epitaxy Epitaxy refers to the deposition of an overlayer on a crystalline substrate, where the overlayer is in registry with the substrate. The overlayer is called an epitaxial film or epitaxial layer. The term epitaxy comes from the Greek roots epi, meaning "above", and taxis, meaning "in ordered manner". 110

equivalent noise charge The equivalent noise charge is the number of electrons one would have to collect from a silicon sensor in order to create a signal equivalent to the noise of this sensor. 87, 288

eta correction The eta correction is an algorithm for linearising the relationship between the particle hit position and the measured charge center-of-gravity in a silicon microstrip sensor. When a particle hits the sensor between two strips, the charge carriers drift towards both strips, but the amount of drifting charge carriers is *not* proportional to the distance from the strips. This effect is especially pronounced for particles traversing the sensor perpendicularly, as is the case for beam tests, and for high energetic tracks in the real experiment. 93, 94

etching Etching is used in microfabrication to chemically remove layers from the surface of a wafer during manufacturing. Etching is a critically important process module, and every wafer undergoes many etching steps before it is complete. For many etch steps, part of the wafer is protected from the etchant by a "masking" material which resists etching. In some cases, the masking material is a photo resist which has been patterned using photolithography. Other situations require a more durable mask, such as silicon nitride. 111–113, 120, 127, 129, 131–134, 283, 284

eV The "electronvolt" is the commonly used energy unit in particle physics. $1\,\mathrm{eV} \approx 1.6 \times 10^{-19}\,\mathrm{J}$ is the energy an electron gains when it is accelerated by a potential difference of 1 Volt. It is often used as $1\,\mathrm{GeV} = 10^9\,\mathrm{eV}$. Derived units are $\mathrm{eV/c}$ for the momentum, and $\mathrm{eV/c^2}$ for the mass. i, iii, 4, 11, 20, 23, 25, 46, 48–50, 56–58, 79, 82–84, 156, 193, 262, 264, 267, 284

extrinsic An extrinsic semiconductor is a semiconductor material whose electrical properties have been altered by doping. 51–54, 73, 269, 276

Fermi energy At the Fermi energy the Fermi-Dirac probability density function has a value of 1/2. 48–52, 61, 68, 70, 71, 73, 77, 78, 286

Fermi-Dirac probability density function In quantum statistics, Fermi-Dirac (F-D) statistics describes distribution of particles in a system comprising many identical particles that obey the Pauli exclusion principle. It applies to identical particles with half-odd-integer spin in a system in thermal equilibrium. It is most commonly applied to electrons, which are fermions with spin 1/2. The Fermi-Dirac probability density function reads: $n_i = \frac{1}{e^{(\epsilon_i - \mu)/k_\mathrm{B}T}+1}$, where k_B is Boltzmann's constant, T is the absolute temperature, ϵ_i is the energy of the single-particle state , and μ is the total chemical potential. For the case of electrons in a semiconductor, μ is typically called the Fermi level or electrochemical potential. 48, 51, 52, 271

fermion A fermion is a (not necessarily fundamental) particle with a half-integer spin quantum number. It obeys the Fermi-Dirac statistics and the Pauli exclusion principle, stating that no two fermions with an identical set of quantum numbers can occupy the same state in a system. All leptons and quarks are fermions. 4, 271, 286

fiducial circle The fiducial circle is an imaginary circular line on a wafer, which divides the reliable inner part from the outermost edge, where the homogeneity of the material cannot be guaranteed. 120

field oxide The field oxide is the thick oxide used for masking in the photolithographic process sequence. 121, 127, 128, 131, 140

flat-band A MOS structure is in flat-band situation, when the intrinsic energy band deformation (e.g. by different work functions) is compensated by an external voltage so that the bands are flat. The external voltage is then called "flat-band voltage". The lower this voltage, the lower is the concentration of fixed oxide charges, which is a quality indicator for silicon microstrip sensors. 71–73, 77

flavour Flavour refers to the type of elementary particles (either quarks or leptons) occurring in the Standard Model. There are flavour quantum numbers which depend on the number of particles of particular flavours which occur in a hadron. In strong interactions, flavour is conserved. In the weak interaction, however, this symmetry is broken, and flavour changing processes exist, such as quark decay or neutrino oscillations. 5, 7, 272

forward The forward part of Belle II is the side of positive z direction. See section 10.1.2 for details. ii, iv, 18, 19, 24–26, 30, 31, 33, 182, 197, 227, 229, 236

forward bias In forward bias mode, a diode becomes conductive. Electrons are injected into the p-type material and holes into the n-type material. 63–65

full depletion voltage When ramping up a reverse bias voltage to a sensor, the depletion region at the p-n-junction is increased, until it reaches the other side of the sensor and the whole bulk to be free of charge carriers. The voltage needed to fully deplete the sensor is called "full depletion voltage". It is mainly determined by the resistivity of the wafer. It is furthermore an important benchmark for the operation of a silicon microstrip sensor, as the operating voltage should always be larger than the full depletion voltage to ensure a maximum of detection efficiency. 33, 35, 66, 67, 107, 108, 134, 140, 152, 198, 267, 275

generation In particle physics, a generation (or family) is a division of the elementary particles. Between generations, particles differ by their (flavour) quantum number and mass, but their interactions are identical. There are three generations according to the Standard Model of particle physics. Each generation is divided into two leptons and two quarks. The two leptons may be classified into one with electric charge -1 (electron-like) and one neutral (neutrino); the two quarks may be classified into one with charge -1/3 (down-type) and one with charge +2/3 (up-type). Every particle has a corresponding anti-particle. 4, 5, 7, 270, 277, 281, 285

ghost hit A ghost hit is a fake position measurement occurring for DSSDs or two combined single-sided silicon microstrip sensors measuring particle positions in two dimensions.

When the sensor(s) is (are) hit by two or more particles simultaneously, there are more than two combinatorial possibilities for the measured particle position. The non-real ones are called "ghost hits", and the true hit position can only be determined by combinatorics using several layers. 95, 96

granularity Granularity is the extent to which a system is broken down into small parts. In terms of particle detectors it means geometrical segmentation for position measurements. 16, 19, 20

gravitation Gravitation is the fourth fundamental interaction known today. It is the agent that gives weight to objects that have mass. Up to now it cannot be described with the same mathematical formalism as is used to describe the other three interactions. Therefore it could not yet be integrated into a consistent theory of all four interactions. Gravitation is described by the theory of general relativity, while the other interactions are described with quantum field theories. 3, 276, 277

guard ring The guard ring is a structure for high voltage protection of a silicon microstrip sensor. It is on floating potential between the bias ring and the edge of the sensor, where it creates a controlled, homogeneous voltage drop. 33, 100, 105, 121, 127, 134, 142, 198

hadron A hadron is a non-fundamental particle composed of quarks. Hadrons with three quarks are called baryons, hadrons with a quark and an anti-quark are called mesons. i, iii, 4, 14, 21, 156, 277, 281, 285, 290

hermetic In common language "hermetic" means "airtight". Applied to particle detectors, it means the absence of blind spots in the detector, which are not equipped with particle sensing devices. Thus, a hermetic detector can measure a particle regardless of its direction (as long as it is inside the acceptance region). 20

Higgs The Higgs boson explains why some fundamental particles have mass when the symmetries controlling their interactions should require them to be massless, and – related to this – why the weak force has a much shorter range than the electromagnetic force. 4, 7

hit time finding The hit time finding is an algorithm in the data acquisition of the Belle II SVD which reconstructs the exact timing of the signal's maximum. 36, 37, 40

hole In semiconductor physics, a hole (or defect electron) is a positive charge carrier, which is understood to be a missing electron in an otherwise fully occupied valence band. 46–51, 54, 55, 60, 61, 64, 65, 70, 73, 76, 78–80, 83, 85, 86, 96–99, 104, 265, 268, 272, 275, 276, 279

hybrid The hybrid board is an electronic board which houses readout chips, supplying power, control signals and routing their output to the subsequent data cables. 26, 32, 37, 39, 40, 42, 157, 159, 160, 213–215, 278

impact parameter The impact parameter is the three-dimensional point of closest approach (PCA) of the reconstructed track with respect to the *real* starting point. It is a quality parameter of a single reconstructed track and has to be determined by simulations. 10, 11, 18

implantation Ion implantation is an engineering process by which ions of a material are accelerated in an electrical field and impacted into a solid. This process is used to change the physical, chemical, or electrical properties of the solid. Ion implantation is used in semiconductor device fabrication and in metal finishing, as well as various applications in materials science research. 103, 104, 111, 112, 118, 119, 121–123, 126, 128–132, 134, 135, 140, 142, 147, 153, 178, 193, 225, 261, 262, 274, 278

ingot An ingot (also called "boule") is a material, usually metal, that is cast into a shape suitable for further processing. Non-metallic and semiconductor materials prepared in bulk form may also be referred to as ingots, particularly when cast by mold based methods. Silicon ingots are usually cylindrical rods, which are cut into circular wafers. 107, 108

intermediate strip An intermediate strip is a strip which is implanted, but has no metallisation to be read out. Its purpose is to pick up the part of the signal generated between the actual readout strips and couple it to them capacitively, thus improving the charge sharing between the readout strips without doubling the number of readout channels. 31, 101, 135–137, 148, 157, 164, 167–169, 171–173, 175, 176, 180, 183, 184, 186, 187, 190, 191, 193, 194, 227, 280

interstitial An interstitial is an unbound atom in a crystal lattice, which has been knocked out of its lattice site. It is usually generated together with a vacancy. The interstitial is mobile and can recombine with a vacancy, disappear at the edge of the material, or be caught by other (stable) defects. 79, 286

interstrip capacitance The interstrip capacitance is the capacitance between two adjacent implanted strips. It is responsible for capacitive coupling of strip signals, which can mimic a cluster of higher width than really present. 88, 93, 101, 180–182, 192

interstrip resistance The interstrip resistance is the ohmic resistance between an implanted strip and its immediate neighbour, disregarding the bias resistors. 35, 134, 140

intrinsic An intrinsic semiconductor is a pure semiconductor material, not altered by doping. 48, 49, 51–53, 73, 269

inversion Inversion situation occurs in a p-n-junction, when a considerable amount of minority charge carriers are aggregated at an interface between a semiconductor and another material. This situation can occur for strongly bent energy bands. In case of p-type material, the formed inversion layer consists of electrons and shorts n-type doped regions at the surface. It therefore has to be interrupted by a p-stop or p-spray implantation. 71, 73, 76–78, 80, 103, 147, 274, 278

ionisation Ionisation is the process of converting an atom or molecule into an ion by adding or removing charged particles such as electrons or ions. 57, 161

IV-curve The IV-curve shows the leakage current of a diode or a silicon microstrip sensor as function of the bias voltage. The current at the full depletion voltage is a quality indicator for a silicon microstrip sensor. 64, 65, 152, 198

junction side The junction side of a double-sided silicon sensor is the one where the p-n-junction is located. This is the p-side for n-type material, and the n-side for p-type material. 31, 225

kaon A kaon (symbol: K) is any of a group of four mesons distinguished by a quantum number called strangeness. In the quark model they are understood to be bound states of a strange quark (s) (or anti-quark $\overline{\mathrm{s}}$) and an up or down anti-quark ($\overline{\mathrm{u}}$ or $\overline{\mathrm{u}}$) (or quark u or d). Although the neutral kaon K^0 and its anti-particle $\overline{\mathrm{K}}^0$ are usually produced via the strong force, they decay weakly. Thus, once created the two are better thought of as superpositions of two weak eigenstates which have vastly different lifetimes: The long-lived neutral kaon is called the $\mathrm{K_L}$ ("K-long") and the short-lived neutral kaon is called the $\mathrm{K_S}$ ("K-short"). 7, 14, 15, 17, 19–21, 25, 289

ladder The ladder is the basic building block of the SVD. It combines the sensors, the front-end readout electronics and the mechanical support structure to an indivisible unit, which is used to build a detector layer. 24, 26–29, 38–40, 270, 275, 282

Landau probability density function In probability theory, the Landau probability density function is a probability distribution named after Lev Landau. Because of the function's long tail, the moments of the distribution, like mean or variance, are undefined. $p(x) = \frac{1}{2\pi i}\int_{c-i\infty}^{c+i\infty} e^{s\log s + xs}\,\mathrm{d}s$. 59, 82, 95, 161–163, 277

latent heat Latent heat is the heat released or absorbed by a body or a thermodynamic system during a process that occurs without a change in temperature. A typical example is a change of state of matter, meaning a phase transition such as the evaporation of CO_2. 41

layer A detector layer is an approximately cylindrical surface of sensing devices, usually in the barrel part of the detector. A layer of the SVD is composed of ladders. 15–19, 21, 25–32, 34, 37, 42, 94, 96, 275, 285

leakage current In semiconductor devices, leakage is a quantum phenomenon where mobile charge carriers (electrons or holes) tunnel through an insulating region. Leakage increases exponentially as the thickness of the insulating region decreases. Tunneling leakage can also occur across semiconductor junctions between heavily doped p-type and n-type semiconductors. Other than tunneling via the gate insulator or junctions, carriers can also leak between source and drain terminals of a MOS transistor. See also dark current. 64, 267, 275, 280

lepton A lepton is an fundamental particle which is assumed to be pointlike. The leptons of the standard model are the electron e^-, the muon μ^-, the tau τ^-, the corresponding neutrinos ν_e, ν_μ and ν_τ, as well as their anti-particles. A lepton does not undergo strong interactions, it interacts electromagnetically, weakly and gravitationally. $\lambda\epsilon\pi\tau\acute{o}\sigma$ (greek): small, thin, tiny. i, iii, 7, 14, 270–272, 277, 285

Lorentz angle When charge carriers drift in a combined electrical and magnetically field, they are deflected from the electric field lines. The deflection angle is called "Lorentz angle". 96, 97

luminosity The luminosity $\mathcal{L}$ is one of the main parameters of a particle colliders, as it translates directly to the reaction rate R via $R = \sigma\mathcal{L}$, where σ is the cross section of the reaction in question. The luminosity can be tuned by proper adjustment of the collider. i, 11–15, 17, 20, 35

Møller scattering Møller scattering is the name given to electron-electron scattering in Quantum Field Theory, named after the danish physicist Christian Møller. The electron interaction that is idealised in Møller scattering forms the theoretical basis of many familiar phenomena such as the repulsion of electrons in the Helium nucleus. 57

majority Majority charge carriers are the charge carriers introduced by doping in an extrinsic semiconductor. A p-type semiconductor has holes as majority charge carriers, whereas for an n-type semiconductor they are electrons. 51, 54, 59, 60, 64, 68, 70, 71, 78, 147, 178, 261, 276

material budget In contrast to the physical thickness of a scatterer, the material budget of a scatterer is the thickness in units of the radiation length, usually expressed in %. This material budget has to be minimised in order to minimise the effects of multiple scattering. The material budget can be minimised by reducing the physical thickness of a scatterer, and/or by using a material with a large radiation length. 24, 26, 27, 31, 33, 37–39, 41, 45, 94, 95, 227, 277, 278

meson A meson is a composite subatomic particle composed of one quark and one antiquark. i, iii, 7, 8, 11, 14, 21, 25, 261, 264, 273, 275, 280

minimum ionising particle In physics, a minimum ionising particle (or MIP) is a particle whose mean energy loss rate through matter is at (or close to) the possible minimum. 58, 59, 290

minority Minority charge carriers are the charge carriers with opposite charge compared to the majority charge carriers, which exist due to thermal excitation at a much lower concentration. 59, 60, 64, 65, 68, 73, 78, 274

most probable value In probability calculation, the most probable value is the peak of a probability density function. In general, it is different from the mean value (expec-

tation value), and it can be used for distributions lacking defined moments, like the Landau probability density function. 82, 83, 290

multiple scattering Multiple scattering is the deflection of a particle when it traverses a material, where information about the origin of the particle is obscured. For tracking purposes it is therefore advisable to minimise the material budget causing the scattering. i, iii, 24, 25, 41, 87, 193, 195, 276

muon The muon (symbol: μ^-) is a subatomic particle with a negative elementary charge. It is a lepton of the second generation of fundamental particles. 4, 14, 15, 21, 58, 59, 276, 288, 289

n-side The n-side of a double-sided silicon sensor is the one with n-type implanted strips. iv, 31, 33–35, 37, 83, 86, 95–97, 99, 103, 119, 121, 122, 124, 126–137, 140, 142, 143, 152, 154, 157, 164–166, 182, 184, 198, 202–206, 210, 211, 213–216, 218, 221–225, 227, 275, 277, 278, 284

n-sub pad The n-sub pad allows contact to the (in our case n-type) substrate of the sensor. It is located in the edge ring of the p-side. This pad allows to bias the sensor when only the p-side is accessible, because the n-sub pad connects to the n-side through the bulk. 205, 225, 270

n-type Semiconductors doped with donor impurities are called n-type and have an excess of electrons as majority charge carriers. 31, 33, 35, 49–54, 60–63, 65, 68–72, 74–76, 78, 79, 82, 83, 85, 86, 95, 98, 99, 103, 104, 119, 121, 123, 126–135, 137–140, 142, 147, 175, 194, 205, 225, 261, 262, 266, 269, 272, 274–278, 282, 285

neighbour strip The neighbour strip of a cluster is a strip near a seed strip with a signal of at least three times its single strip noise. 89, 160, 266, 283

neutrino The neutrino (symbol: ν_e, ν_μ or ν_τ, depending on the particle generation) is an electrically neutral lepton, which only interacts by the weak interaction and by gravitation. Is is therefore extremely difficult to detect. 15, 272, 276, 284

neutron The neutron (symbol: n or n^0) is a subatomic particle with no net electric charge and a mass slightly larger than that of a proton. With the exception of hydrogen-1, nuclei of atoms consist of protons and neutrons, which are therefore collectively referred to as nucleons. In the modern Standard Model of particle physics, the neutron is a hadron, composed of one up quark and two down quarks. 14, 79, 281, 285

occupancy The occupancy is defined as the fraction of responding (hit) readout channels per triggered event. A high occupancy ($\gg 10\%$) renders the discrimination of individual particle tracks impossible due to an exploding number of combinatorial candidates. 15–18, 24, 25, 36, 37, 40, 95, 96

ohmic side The ohmic side of a double-sided silicon sensor is the one where *no* p-n-junction is located. On the ohmic side, a highly doped region is connected to the lowly doped bulk, forming an ohmic contact.This is the n-side for n-type material, and the p-side for p-type material. 31, 225

Origami In the Origami chip-on-sensor concept, the APV25 readout chips are mounted on a flexible hybrid board directly on the sensor, while the strips of the other side are connected using flexible pitch adapters wrapped around the edge of the sensor (hence the name Origami). This puts the readout chip close to the strips – minimising the capacitive load and thus the noise – while maintaining an acceptable material budget. 24, 37–39, 42, 43, 88, 213, 217, 220, 221, 224

oxidation In microfabrication, thermal oxidation is a way to produce a thin layer of oxide (usually silicon dioxide) on the surface of a wafer. The technique forces an oxidizing agent to diffuse into the wafer at high temperature and react with it. The rate of oxide growth is often predicted by the Deal-Grove model. 109, 112, 127

oxide window The oxide window is a hole in the thin coupling oxide, which allows the metallisation to connect to the silicon surface. It is often wrongly called "via", which in contrast to an oxide window is a connection between different metal layers. 100, 106, 109, 118, 121–123, 132, 267, 286

p-n-junction A p-n junction is a boundary or interface between two types of semiconductor material, p-type and n-type, inside a single crystal of semiconductor. It is created by doping, for example by ion implantation, diffusion of dopants, or by epitaxy (growing a layer of crystal doped with one type of dopant on top of a layer of crystal doped with another type of dopant). 56, 61–68, 82, 101, 103, 105, 153, 199, 261, 264, 268, 274, 278

p-side The p-side of a double-sided silicon sensor is the one with p-type implanted strips. 31–35, 37, 83, 86, 95–97, 99, 103, 104, 119–121, 124, 126–135, 137, 141–143, 152, 164–166, 198–201, 203, 205, 206, 210, 211, 213–215, 217–220, 224, 225, 275, 277, 278, 284

p-spray The p-spray blocking is a method to interrupt the accumulation layer or inversion layer forming on the n-side of silicon microstrip sensors. The whole wafer side is p-type implanted with low fluence and high energy, which embeds the n-type strips in local p-type material. The occurring p-n-junction interrupts the electron layer, which otherwise would short any n-type regions present at this surface. ii, iv, 104, 126, 129, 135, 147, 148, 152, 153, 155, 157, 164, 166–171, 173, 174, 180, 182–192, 194, 227, 261, 274

p-stop The p-stop blocking method is a method to ensure electrical strip separation on the n-side of silicon microstrip sensors. It features p-type implantations between the n-type strips. These implantations are called p-stops. The p-stop implants are usually on floating potential, only for special measurements one might want to put them on

a defined potential. ii, iv, 33, 83, 103, 104, 119, 122–124, 126, 129, 134–139, 142, 147, 148, 154, 156, 157, 164–180, 182–194, 202, 213, 215, 218, 222, 224, 225, 227, 228, 261, 262, 266, 274

p-type Semiconductors doped with acceptor impurities are called p-type, and have an excess of holes as majority charge carriers. 31, 50–52, 54, 60–63, 65, 68, 70, 71, 78, 79, 82, 86, 97, 98, 103, 104, 118, 119, 121–123, 127, 128, 134, 135, 137, 138, 140, 142, 167, 261, 262, 266, 272, 274–276, 278, 282, 285

pad A pad is a small metalised area designated for contacting the sensor with probe needles or wire bonds through a window in the passivation. 32

parity conjugation The parity conjugation is a symmetry operation which mirrors a vector at its foot point. 5, 265

passivation The passivation is the final protection layer of CVD deposited silicon dioxide (or similar materials depending on the vendor), which renders the sensor insensitive to a range of environmental influences. 100, 110, 118, 121–123, 133–135, 178, 279

pedestal subtraction The pedestal subtraction is a correction algorithm in the data acquisition, which ensures a mean readout channel reading of zero when no signal is present. 40, 162

perturbation calculation In quantum mechanics, perturbation theory is a set of approximation schemes directly related to mathematical perturbation for describing a complicated quantum system in terms of a simpler one. 285

phonon A phonon is a quasi-particle and understood to be the quantum of vibration modes of the crystal lattice. 53, 56

photo mask A photo mask is an opaque plate with holes or transparencies that allow light to shine through in a defined pattern. They are commonly used in photolithography. 83, 111–113, 117–121, 127, 129–135, 182, 194, 225

photo resist A photo resist is a light-sensitive material used in several industrial processes, such as photolithography and photoengraving to form a patterned coating on a surface. A positive resist is a type of photo resist in which the portion of the photo resist that is exposed to light becomes soluble to the photo resist developer. The portion of the photo resist that is unexposed remains insoluble to the photo resist developer. A negative resist behaves in the opposite way. 111–113, 127, 129, 131, 133, 271, 279, 280

photolithography Photolithography, also termed optical lithography or UV lithography, is a process used in microfabrication to pattern parts of a thin film or the bulk of a substrate. It uses light to transfer a geometric pattern from a photomask to a light-sensitive chemical "photo resist", or simply "resist", on the substrate. A series of chemical treatments then either engraves the exposure pattern into, or enables

deposition of a new material in the desired pattern upon, the material underneath the photo resist. For example, in complex integrated circuits, a modern CMOS wafer will go through the photolithographic cycle up to 50 times. 103, 104, 111, 117, 127, 131–134, 271, 272, 279

photomultiplier Photomultipliers are extremely sensitive detectors of light in the ultraviolet, visible, and near-infrared ranges of the electromagnetic spectrum. These detectors multiply the current produced by incident light by as much as 100 million times in multiple stages, enabling individual photons to be detected when the incident flux of light is very low. 16, 21, 159, 160, 165

photon The photon γ is an elementary particle, the quantum of light and all other forms of electromagnetic radiation, and the mediator of the electromagnetic force, even when static via virtual photons. ii, iv, 14, 15, 19, 20, 23, 57, 79–81, 156–158, 195, 197, 227, 264–266, 268, 270

pinhole A pinhole is a conductive connection between the strip implant and the aluminium strip above it, which renders the coupling capacitance ineffective. A pinhole causes the DC portion of the strip's leakage current to flow into the input amplifier of the readout chip. The APV25 chip can withstand up to seven connected pinholes, beyond that either the whole chip is dysfunctional, or the strips in question have to be disconnected. 154, 156, 201, 204

pion A pion (symbol: π) is any of a group of three mesons. In the quark model they are understood to be bound states of any combination of up quarks and down quarks and their anti-particles. 14, 15, 17, 19, 20, 58, 79, 84, 156

pitch Strip distance from center to center. Distinguish between the pitch of all implanted strips and the pitch of the readout strips (in case of a sensor with intermediate strips). Usually – unless otherwise noted – pitch refers to the distance between the readout strips. 32–34, 67, 84, 90, 92, 98, 101, 117, 119, 122, 135–137, 148, 157, 164, 167–169, 171–173, 175, 183, 184, 186, 187, 190–194, 196, 199, 220, 224, 227, 280

pitch adapter A pitch adapter is a flexible or rigid structure implementing conductive traces for connecting the sensor strips to the readout chip. On one side, the pitch of these connections matches the pitch of the sensor strips, on the other side it matches the pitch of the readout chip's input channels, which is usually narrower than the sensor side. Pitch adapters are also called "fanouts". 37, 38, 157, 213, 214, 217, 220, 221, 224, 278, 286

pixel sensor In particle physics, a pixel sensor is a position sensitive device which delivers unambiguous 2D position measurements of traversing charged particles. In contrast to a silicon microstrip sensor, a silicon pixel sensor segments one electrode in a two-dimensional array of (rectangular) pixels, each a little silicon sensor in it's own right, with a typical size of around $100 \times 100\,\mu m^2$. An electronic silicon chip, one for each tile is attached, using an almost microscopic spot of solder using the so-called "bump bonding" technique, which amplifies the signal. Different architectures include

monolithic active pixel sensors (MAPS) and depleted p-channel field effect transistor sensors (DEPFET). 16, 18, 23, 25, 83, 84, 94–96, 164

polysilicon Polycrystalline silicon, also called polysilicon, is a material consisting of small silicon crystals. It differs from single-crystal silicon – used for electronics and sensors – and from amorphous silicon – used for thin film devices. 78, 100, 102, 106, 110, 111, 121, 122, 130, 131, 135, 140, 142, 263, 281

polysilicon head The polysilicon head is a special implantation at the ends of the bias resistor to avoid a Schottky contact. 122, 130, 131

positron The positron (symbol: e^+) is a subatomic particle with a positive elementary electric charge. It is the anti-particle of the electron. i, iii, 4, 11, 14, 16, 23, 57, 58, 234, 263

probability density function In probability theory, a probability density function (pdf), or density of a continuous random variable, is a function that describes the relative likelihood for this random variable to take on a given value. The probability for the random variable to fall within a particular region is given by the integral of this variable's density over the region. The probability density function is nonnegative everywhere, and its integral over the entire space is equal to one. A (normalised) histogram is a direct measurement of a probability density function. 93, 268, 271, 275, 276

proton The proton (symbol: p or p^+) is a subatomic particle with one positive electric elementary charge. One or more protons are present in the nucleus of each atom. In the modern Standard Model of particle physics, the proton is a hadron, composed of two up quarks and one down quark. 14, 58, 79, 263, 277, 281, 285

punch through A space charge region expands as the reverse bias voltage is increased. For a p-n-p junction (or equivalently a n-p-n junction) punch-through situation is reached when the space charge region of the reverse biased junction touches the forward biased junction. Then, charge carriers from the forward biased junction will be injected into the reversed biased junction through drift and diffusion. This will lead to an exponential rise in the current with respect to the applied voltage. This effect can be used to apply the bias voltage to the strips of a silicon microstrip sensor. 102, 263

quark A quark is an elementary particle and a fundamental constituent of matter. Quarks combine to form composite particles called hadrons, the most stable of which are protons and neutrons, the components of atomic nuclei. The quarks of the first generation are called "up" and "down", those of the second generation are called "charm" and "strange", and those of the third generation are called "top" and "bottom" (or "beauty"). 4, 5, 7, 8, 261–264, 271–273, 275–277, 280, 281, 285

quark mixing Quark mixing describes the mismatch of quantum states of quarks when they propagate freely and when they take part in the weak interactions. The quark mass

eigenstates are not the same as the eigenstates of the weak interaction, but linear combinations of them. This is considered by the CKM matrix. 5

radiation length The radiation length is the mean distance over which a high-energy electron loses all but 1/e of its energy by bremsstrahlung, where e is Euler's number. 19, 27, 39, 46, 58, 276

radio frequency The radio frequency is the frequency at which the accelerator stage of a collider operates. It divides the particles into bunches at a distance of the radio frequency's wave length, and is therefore closely related to the bunch collision rate. However, only every other bunch is filled with particles, so that the collision rate is only half the nominal value; collisions occur approximately every 4 ns.. 14, 35

region of interest The region of interest is the region inside the PXD which is flagged for readout when an event is triggered. Due to the long integration time and high channel count of the sensors it is not feasible to read out every pixel. The regions of interest are found by fast online tracking using the SVD data. 18, 40

resistivity Electrical resistivity (also known as resistivity, specific electrical resistance, or volume resistivity) quantifies how strongly a given material opposes the flow of electric current. 54, 66, 78, 266, 272, 283

resonance A resonance is the peak in reaction probability located around a certain energy. These peaks are associated with subatomic particles and their excitations. The width Γ of a resonance is related to the life time of the corresponding particle (or its excited state). 11

reverse bias In reverse bias mode, a diode becomes an insulator. The p-type bulk band edges are raised relative to the n-type bulk by the reverse bias voltage, so that the two bulk occupancy levels are separated again by an energy determined by the applied voltage. 63–67, 79, 82–86, 88, 100–102, 152, 153, 157, 158, 164, 183, 198, 199, 205, 213, 281

rib The rib is the main support structure of a ladder of the Belle II SVD. It is a sandwich of two carbon fiber plies separated by an Airex® core. Each ladder is supported by two ribs. 24, 26, 27

Schottky contact A Schottky contact (or Schottky barrier), named after Walter H. Schottky, is a potential energy barrier for electrons formed at a metal-semiconductor junction. Schottky barriers have rectifying characteristics, suitable for use as a diode. 68–70, 78, 99, 130, 281

scintillator A scintillator is a material that exhibits scintillation – the property of luminescence – when excited by ionising radiation. Luminescent materials, when struck by an incoming particle, absorb its energy and scintillate, i.e. re-emit the absorbed energy in form of light. 15, 16, 21, 159, 160, 165

seed strip The seed strip of a cluster is the first strip found to have a signal of five times its single strip noise. The cluster finding algorithm first looks for a strip complying with this threshold, and once found, it continues to search for neighbour strips adjacent to the seed strip. 89, 160, 266, 277

selectivity If the etching is intended to make a cavity in a material, the depth of the cavity may be controlled approximately using the etching time and the known etch rate. More often, though, etching must entirely remove the top layer of a multilayer structure, without damaging the underlying or masking layers. The etching system's ability to do this depends on the ratio of etch rates in the two materials, and is called "selectivity". 112, 113

sheet resistance Sheet resistance is a measure of resistance of thin films that are nominally uniform in thickness. It is commonly used to characterise materials made by semiconductor doping, metal deposition, resistive paste printing, and glass coating. The total resistance R of a film is calculated as $R = \frac{\rho}{t}\frac{L}{W} = R_\mathrm{s}\frac{L}{W}$, where ρ is the resistivity, t, L and W are thickness, length and width if the film, and R_s is the sheet resistance. A commonly used unit for the sheet resistance is $\Omega/\square$ (read Ohms per square). For a quadratic film we can write $L = W$ and therefore $R = R_\mathrm{s}$. The resistance value R of a line-shaped film can be expressed using the number of squares, regardless of the actual size of the squares. 103, 104, 121, 122

signal-to-noise ratio Signal-to-noise ratio (often abbreviated SNR or S/N) is a measure used in science and engineering that compares the level of a desired signal to the level of background noise. It is defined as the ratio of signal power to the noise power, often expressed in decibels. A ratio higher than 1:1 (greater than 0 dB) indicates more signal than noise. While SNR is commonly quoted for electrical signals, it can be applied to any form of signal. In terms of silicon microstrip sensors, the signal-to-noise ratio is the division of the signal released by a traversing particle and the quadratically added noise of all hit strips. A value in the order of 10 or higher is needed to safely detect ionising particles and perform tracking. 39, 41, 87, 89, 93, 94, 291

silicon microstrip sensor A silicon microstrip sensor is in principle a large-area bulk diode manufactured on a silicon wafer, with one ore both electrodes segmented to form strips. When an ionising particle traverses the sensor, the segments near the particle will register a signal, thus measuring the position of the particle. i–iv, 15, 17, 18, 23–25, 31, 45, 53, 57, 61, 64, 67, 70, 79–82, 84, 89, 94, 95, 98–102, 105–108, 117–119, 125, 128, 136, 140, 142, 152, 153, 198, 227, 261–267, 269, 271–273, 275, 278, 280, 281, 283, 284, 286, 288

solenoid A solenoid is a coil wound into a tightly packed helix. Such a coil produces a very homogenous magnetic field in its center. 4, 15, 18, 20, 21, 96, 233, 234, 288

space charge region In semiconductor physics, the depletion region, also called depletion layer, depletion zone, junction region or the space charge region, is an insulating region within a conductive, doped semiconductor material where the mobile charge

carriers have diffused away, or have been forced away by an electric field. The only elements left in the depletion region are ionised donor or acceptor impurities. 61, 63–68, 79, 80, 82, 85, 86, 103, 105, 264, 267, 281

sputtering Sputtering is a process whereby atoms are ejected from a solid target material due to bombardment of the target by energetic particles. It only happens when the kinetic energy of the incoming particles is much higher than conventional thermal energies ($\gg 1$ eV). This process can lead, during prolonged ion or plasma bombardment of a material, to significant erosion of materials, and can thus be harmful. On the other hand, it is commonly utilised for thin-film deposition, etching and analytical techniques. 110, 132

standard deviation In statistics and probability theory, standard deviation (represented by the symbol sigma, σ) shows how much variation or dispersion can be expected from the average (mean) value. 90

Standard Model The Standard Model of particle physics is a theory concerning the electromagnetic, weak, and strong nuclear interactions, which mediate the dynamics of the known subatomic particles. Because of its success in explaining a wide variety of experimental results, the Standard Model is sometimes regarded as a "theory of almost everything". However, the Standard Model falls short of being a complete theory of fundamental interactions because it makes certain simplifying assumptions. It does not incorporate the full theory of gravitation as described by general relativity, or predict the accelerating expansion of the universe (as possibly described by dark energy). It also does not correctly account for neutrino oscillations (and their non-zero masses). 3, 291

state density In solid-state and condensed matter physics, the density of states (DOS) of a system describes the number of states per interval of energy at each energy level that are available to be occupied by electrons. Unlike isolated systems, like atoms or molecules in gas phase, the density distributions are not discrete like a spectral density but continuous. 48, 51, 52

stereo angle The stereo angle is the angle between the strip directions of n-side and p-side strips of a DSSD. It is often 90°, but in some cases it is beneficial to choose a very small stereo angle, which would imply vastly different position resolutions in the two measured dimensions, but would allow to put the readout electronics on one side of the sensor only. 94, 96

strip scan A strip scan is an electrical characterisation method for silicon microstrip sensors. A number of measurements is carried out on every strip, yielding thorough insight into the performance and quality of the sensor. Strip scans are performed using fully automated "probe stations". One can either have stationary probe needles, moving the sensor to make contact to the strips, or one can have automatically moving probe needles. The latter is more versatile, but only available through commercial vendors, and expensive. 136, 199, 202, 225

strong The strong interaction (or strong force) is the force that binds protons and neutrons (nucleons) together to form the nucleus of an atom. It furthermore is the force (carried by gluons) that holds quarks together to form protons, neutrons and other hadrons. 4, 79, 80, 272, 275, 276

SVD2 The SVD2 is the upgraded Silicon Vertex Detector of the former Belle experiment. Not to be mixed up with the Belle II SVD, which is being built at the moment. 39, 159, 285

tau The tau particle (symbol: τ^-) is a subatomic particle with a negative elementary charge. It is a lepton of the third generation of fundamental particles. 7, 276

tracking Tracking (also called track reconstruction) is the process of combining individual three-dimensional space points measured by several layers of track sensitive devices, to reconstruct the trajectory of the physical particle. Efficient tracking algorithms allow to extract a maximum of information from the track, such as the curvature in the magnetic field for measuring the momentum of the particle. 23, 26, 277, 282, 283

trapping Trapping is the process of interrupting a charge carrier's drift or diffusion by binding it to a lattice impurity. The impurity is often charged in that process, representing a scattering center further on. 61, 87

tree level In theoretical particle physics, tree level denotes the 0^{th} iteration of a perturbation calculation. 7, 8

tunneling Quantum tunnelling refers to the quantum mechanical phenomenon where a particle tunnels through a barrier that it classically could not surmount. This plays an essential role in several physical phenomena, such as the nuclear fusion that occurs in main sequence stars like the Sun. It has important applications to modern devices such as the tunnel diode and the scanning tunneling microscope. 70

type inversion Type inversion is an effect occurring in heavily irradiated n-type materials. The radiation damage to the bulk makes the n-type material more and more p-type-like, eventually reversing its polarity. This naturally can't happen in a p-type material. 79, 80

unitary A complex square matrix U is unitary if $U^*U = UU^* = I$, where I is the identity matrix and U^* is the conjugate transpose of U. The real analogon of a unitary matrix is an orthogonal matrix. 5, 6

VA1TA The VA1TA is the chip of the former Belle experiment used for reading out the DSSDs of the SVD2. 35, 36

vacancy A vacancy is an empty crystal lattice site. It is usually generated together with an interstitial. The vacancy is mobile and can recombine with an interstitial, disappear at the edge of the material, or be caught by other (stable) defects. 79, 274

valence band In solids, the valence band is the highest range of electron energies in which electrons are normally present at absolute zero temperature. 47–52, 55, 56, 61, 70, 262, 265, 268, 269

vertex A vertex is the common origin of two or more particle trajectories. i, iii, 7, 9–11, 15–18, 23, 81

via See oxide window. 100, 101

wafer A wafer is a thin, approximately round slice of pure silicon, which is used to produce microchips or – as in our case – sensors. ii, iv, 31, 32, 35, 66, 107–113, 120, 121, 123–128, 130, 131, 133, 134, 136, 140, 142, 147, 155, 182, 210, 265, 268, 271, 272, 274, 278, 280, 283

weak The weak interaction is responsible for the radioactive decay of subatomic particles and initiates the process known as hydrogen fusion in stars. Weak interactions affect all known fermions. It is mediated by the exchange of the Z, W^+ and W^- bosons. 4, 5, 7, 15, 270, 272, 273, 275–277, 281, 282

weighting field According to [33] the weighting field is the electric field which would exist at the charge carrier's instantaneous position under the following circumstances: the charge carrier is removed, the chosen strip is raised to unit potential, and all other strips are grounded. The weighting field allows the calculation of the signal induced in a particular strip by a moving charge carrier as a function of the relative position of strip and charge carrier. 97, 98

wire bonding Wire bonding is the primary method of making interconnections between an integrated circuit (IC) and a device package, or (occasionally), directly onto a printed circuit board (PCB) during semiconductor device fabrication. Although less common, wire bonding can be used to connect an IC to other electronics or to connect from one PCB to another. Wire bonding is generally considered the most cost-effective and flexible interconnect technology, and is used to assemble the vast majority of semiconductor packages. In the assembly of silicon microstrip sensor modules, wire bonding is used to connect the strips to the pitch adapter, and further to the readout chip. 28, 37, 106, 136, 148, 157, 164, 166, 167, 171, 182, 183, 225

work function In solid-state physics, the work function is the minimum energy needed to remove an electron from a solid to a point immediately outside the solid surface. This minimum energy defines the Fermi energy of metals. 68, 71, 272

zero suppression The zero suppression removes data of strips with no signal – which is usually the vast majority – and thus reduces the data rate drastically. 40

Acronyms

AC AC: Alternating Current. 77, 100–102, 106, 261, 264

ACC ACC: silica-Aerogel Cherenkov Counter. 15, 19

ADC ADC: Analog-to-Digital-Converter. 40, 161, 163

AMPLE AMPLE: Advanced Multi-Purpose LanguagE. 117, 291

APCVD APCVD: Atmospheric Pressure Chemical Vapour Deposition. 110

APSP APSP: Analog Pulse Shape Processor. 36

ARICH ARICH: Aerogel Ring Imaging Cherenkov Counter. 19

ATLAS ATLAS: A Toroidal LHC AparatuS. 4

BPSG BPSG: BoroPhosphoSilicate Glass. 110

BRIGITTE BRIGITTE: Big Radius Installation under Gamma Irradiation for Tailoring and Testing Experiments. 158

CAD CAD: Computer Aided Design. ii, iv, 111, 117

CCE CCE: Charge Collection Efficiency. 87, 163

CDC CDC: Central Drift Chamber. i, iii, 15, 16, 18, 19, 23–25, 236

CERN CERN: Organisation (Conseil) Européenne pour la Recherche Nucléaire, Europäische Organisation für Kernforschung. ii

CERN CERN: Organisation (Conseil) Européenne pour la Recherche Nucléaire, European Organization for Nuclear Research. iv, 4, 81, 156, 262

CKM matrix CKM matrix: Cabbibo-Kobayashi-Maskawa matrix. 4–6, 282

CLW CLW: CLuster Width. 160, 161, 181

CMOS CMOS: Complementary Metal-Oxide-Semiconductor, a technology for constructing integrated circuits. 35, 280

CMS CMS: Compact Muon Solenoid. 4, 18, 35, 140, 141, 225, 262

CO_2 CO_2 : Carbon Dioxide. 24, 41–43, 213, 216, 275

COG COG: Center-Of-Gravity. 92, 94

COPPER COPPER: COmmon Pipeline Platform for Electronics Readout. 40

CP CP: Charge-Parity (Ladung-Parität), kurz für Ladungs-Paritäts-Konjugation. i

CP CP: Charge-Parity, short for charge-parity conjugation. iii, 3–7, 23, 262, 264

CPU CPU: Central Processing Unit. 40

CVD CVD: Chemical Vapour Deposition. 110, 279

CZ CZ: CZochralski. 106, 107

DAQ DAQ: Data AcQuisition. 16, 40, 159

DATCON DATCON: DATa CONcentrator. 40, 159

DC DC: Direct Current. 40, 77, 99, 101, 149, 261, 264, 267, 280

DEPFET DEPFET: DEpleted P-channel Field Effect Transistor. 16, 18, 40, 96, 281

DSSD DSSD: Double-Sided Silicon Detector. 18, 31, 38, 81, 83, 84, 95, 96, 99, 103, 104, 119, 120, 124–126, 137, 140, 150, 151, 197, 199, 205, 213, 217, 221, 225, 227, 228, 262, 272, 275, 277, 278, 284, 285

DUT DUT: Device Under Test. 156–158, 164–166, 183, 195, 213, 227, 229

ECL ECL: Electromagnetic CaLorimeter. 15–17, 20, 23, 57, 236

EGS EGS: Electronic Grade Silicon. 106, 107

ENC ENC: Equivalent Noise Charge. 87–89

EUDET EUDET: Detector R&D towards the International Linear Collider, a project supported by the European Union in the 6^{th} Framework Programme (FP6) structuring the European Research Area. 159, 164, 165, 228

FADC FADC: Flash Analog-to-Digital-Converter. 40, 159

FEA FEA: Finite Elements Analysis. 28

FIFO FIFO: First In First Out, a kind of low-level memory array. 36

FOXFET FOXFET: Field OXide Field Effect Transistor. 102, 263

FPGA FPGA: Field Programmable Gate Array. 40

FTB FTB: Finesse Transmitter Board. 40, 159

FZ FZ: Float Zone. 107

GCD GCD: Gate Controlled Diode. 124, 140, 142, 143

GPIB GPIB: General Purpose Interface Bus. 149, 205

HEPHY HEPHY: Institute of High Energy PHYsics. 198

HER HER: High Energy Ring. 11, 14

HTO HTO: High Temperature Oxidation. 109, 110

IC IC: Integrated Circuit. 35, 45, 61, 105, 106, 108, 117, 125, 268, 286, 288

IISS IISS: Institute for Integrated Sensor Systems. 205

ILC ILC: International Linear Collider. 159, 288

IP IP: Interaction Point. 12, 13, 17, 81, 94, 96, 97, 99

KEK KEK (Kō Enerugī Kasokuki Kenkyū Kikō) ist eine japanische Organization, die das größte Teilchenforschungslabor Japans in Tsukuba (Präfektur Ibaraki) betreibt. i

KEK KEK (Kō Enerugī Kasokuki Kenkyū Kikō) is a japanese organization whose purpose is to operate the largest particle physics laboratory in Japan, which is located in Tsukuba of Ibaraki prefecture. iii, 11, 263, 291

KEKB KEKB: KEK B-Mesonen-“Fabrik”. i, 291

KEKB KEKB: KEK B factory. iii, 4, 11–13, 227, 291

KLM KLM: K_L and Muon detection system. 15, 16, 20, 21

LCR LCR: Inductance (L), capacitance (C), resistance (R). 149, 151–154, 180, 198, 199

LDT LDT: LiC Detector Toy, where LiC stands for "Linear Collider". 10

LED LED: Light Emitting Diode. 150

LER LER: Low Energy Ring. 11, 14

LHC LHC: Large Hadron Collider. 4, 18, 35, 262

LINAC LINAC: LINear ACcelerator. 12

LPCVD LPCVD: Low Pressure Chemical Vapour Deposition. 110

MAD MAD: Median Absolute Deviation. 10

MAMBO MAMBO: Mother (MAMa) BOard. 159

MIP MIP: Minimum Ionising Particle. 58, 82, 163, 276

MOS MOS: Metal-Oxide-Semiconductor. 70–72, 74–78, 101, 102, 104, 140, 142, 272, 275, 290

MOSFET MOSFET: Metal-Oxide-Semiconductor Field Effect Transistor. 102, 128

MPV MPV: Most Probable Value. 82, 161, 163, 164, 171, 174, 188, 192, 220, 224

NDA NDA: Non Disclosure Agreement. 121

NIM NIM: Nuclear Instrumentation Module. 160

PCA PCA: Point of Closest Approach. 10, 274

PCB PCB: Printed Circuit Board. 39, 205, 286

PDF PDF: Probability Density Function. 161–163

PECVD PECVD: Plasma Enhanced Chemical Vapour Deposition. 110, 130, 133

ppb ppb: parts per billion. 106

PXD PXD: PiXel Detector. i, iii, 16, 18, 23–26, 36, 40, 236, 282

QTC QTC: Quality Test Center. 149, 150, 180, 198

R&D R&D: Research and Development. 197, 225

RAVE RAVE: Reconstruction Algorithms in Versatile Environments. 10

REBO REBO: REpeater BOard. 159

RF RF: Radio Frequency. 107

RICH RICH: Ring Imaging Cherenkov Counter. 19

RITA RITA: Radio Isotope Test Arrangement. 158

RMS RMS: Root Mean Square. 162

RPM RPM: Revolutions Per Minute. 112

SCK•CEN SCK•CEN: StudieCentrum voor Kernenergie • Centre d'Etude de l'énergie Nucléaire. 158

SiDDaTA SiDDaTA: Silicon Detector Design and Teststructures using AMPLE. 117–119, 227, 229

SiO_2 SiO_2: Silicon Dioxide. 70, 80, 101, 103, 104, 106, 108, 109, 127, 133, 151, 227

SM SM: Standard Model of particle physics. 3–5, 7, 272, 276

SMU SMU: Source Measurement Unit. 149, 151, 152, 154, 198, 205, 206, 208, 212

SNR SNR: Signal-to-Noise Ratio. 89, 94, 161–164, 167–174, 180–183, 186–188, 190–192, 194, 196, 217–224, 283

SPS SPS: Super Proton Synchrotron. 156, 160

SRP SRP: Spreading Resistance Profiling. 103, 104, 178, 179

SuperKEKB SuperKEKB: Super KEK B-Mesonen-"Fabrik", die Verbesserung von KEKB[1]. i

SuperKEKB SuperKEKB: Super KEK B factory, the upgrade of KEKB. iii, 12–15, 21, 23, 24, 35, 36, 227

SUSY SUSY: SUperSYmmetry. 4

SVD SVD: Silicon Vertex Detector. i–iv, 15–18, 23–33, 35, 39–42, 79, 88, 89, 96, 97, 111, 119, 126, 159, 182, 197, 212, 213, 227, 229, 236, 262, 266, 270, 273, 275, 282, 285

[1]KEKB: KEK B-Mesonen-"Fabrik"

TLU TLU: Trigger Logic Unit. 159

TOF TOF: Time Of Flight. 15, 19

TOP TOP: Time Of Propagation. 19

TRHX TRHX: Temperature and Relative Humidity eXtended [48]. 149, 205, 206

VME VME bus: Versa Module Eurocard-bus. 40, 159, 160

Bibliography

[1] Sakharov, A., *Violation of CP invariance, C asymmetry, and baryon asymmetry of the universe*, JETP Letters, 5 (1967) 24–27, URL http://www-itp.particle.uni-karlsruhe.de/~hofmann/lehre/GR/semSS2007LIT/Sakharov.pdf. 3

[2] CMS Collaboration, *Observation of a new boson at a mass of 125 GeV with the CMS experiment at the LHC*, Physics Letters B, 716(1) (2012) 30–61, ISSN 0370-2693, URL http://www.sciencedirect.com/science/article/pii/S0370269312008581. 4

[3] Noether, E., *Invariant variational problems*, Königliche Gesellschaft der Wissenschaften zu Göttingen, Nachrichten, Math-phys. Klasse, pp. 235–257, URL http://neo-classical-physics.info/uploads/3/0/6/5/3065888/noether_-_invariant_variational_problems.pdf. 5

[4] Christenson, J. et al., *Evidence for the* 2π *Decay of the* K_2^0 *Meson*, Physical Review Letters, 13 (1964) 138–140, URL http://link.aps.org/doi/10.1103/PhysRevLett.13.138. 5

[5] Kobayashi, M. and Maskawa, T., *CP-Violation in the Renormalizable Theory of Weak Interaction*, Progress of Theoretical Physics, 49 (1973) 652–657, URL http://ptp.ipap.jp/link?PTP/49/652/. 5

[6] Glashow, S., Iliopoulos, J. and Maiani, L., *Weak Interactions with Lepton-Hadron Symmetry*, Physical Review Letters D, 2 (1970) 1285–1292, URL http://prd.aps.org/pdf/PRD/v2/i7/p1285_1. 5

[7] Wolfenstein, L., *Parametrization of the Kobayashi-Maskawa Matrix*, Physical Review Letters, 51 (1983) 1945–1947, URL http://link.aps.org/abstract/PRL/v51/p1945. 5

[8] Royal Swedish Academy of Sciences, *Press release of the nobel prize in physics 2008*, URL http://www.nobelprize.org/nobel_prizes/physics/laureates/2008/press.html. 6

[9] Beringer, J. et al., *Particle Data Group*, Physical Review Letters, 86 (2012) 1, URL http://pdg.lbl.gov/. 7, 11

[10] Valentan, M. et al., *PoS(Vertex 2011)026: The LiC Detector Toy fast simulation program*, Proceedings of Science, Vertex 2011 (2011) 1–10, URL http://pos.sissa.it/archive/conferences/137/026/Vertex%202011_026.pdf. 10

[11] Waltenberger, W., *RAVE – A Detector-Independent Toolkit to Reconstruct Vertices*, Nuclear Science, IEEE Transactions on, 58(2) (2011) 434–444, ISSN 0018-9499, URL http://ieeexplore.ieee.org/xpls/abs_all.jsp?arnumber=5734880&tag=1. 10

[12] KEK, *High Energy Accelerator Research Organization (Tsukuba, Ibaraki, Japan)*, URL http://www.kek.jp. 11

[13] Flanagan, J. W. and Ohnishi, Y. (editors) *Letter of Intent for KEK Super B Factory, Part III: Accelerator Design*, KEK Report 04-4 (2004), URL http://www-superkekb.kek.jp/documents/LoI_accelerator.pdf. 12

[14] Tanaka, M. and Funakoshi, Y., *Operation Scheme and Statistics of KEKB*, Proceedings of IPAC2011, pp. 1–3, URL http://accelconf.web.cern.ch/accelconf/ipac2011/papers/thpz022.pdf. 12

[15] Doležal, Z. and Uno, S. (editors) *Belle II Technical design report, KEK Report 2010-1 (arXiv:1011.0352 [physics.ins-det])*, arXiv (2010), URL http://arxiv.org/abs/1011.0352. 13, 14, 17, 25, 27, 33, 34, 35, 36, 38, 39, 234

[16] Gfall, I., *Mechanical Design of the Belle II Silicon Vertex Detector*, Master's thesis, University of Vienna (2012), URL http://www.hephy.at/fileadmin/user_upload/Publikationen/Thesis-Gfall.pdf. 26, 28, 30, 38, 40, 41, 42

[17] ALCAN Composites, *Airex® R82 High Performance Foam* (2006), URL http://www.corematerials.3acomposites.com/index.php?id=58&L=1. 27

[18] Hamamatsu Photonics K.K. (Hamamatsu Hotonikusu Kabushiki-gaisha – short HPK), *Photon is our business*, URL http://www.hamamatsu.com. 31, 32

[19] Micron Semiconductor Ltd., *Custom silicon detector design and manufactures*, URL http://www.micronsemiconductor.co.uk. 31, 34, 120, 126

[20] French, M. J. et al., *Design and results from the APV25, a deep sub-micron CMOS front-end chip for the CMS tracker*, Nuclear Instruments and Methods in Physics Research A, 466 (2001) 359–365, URL http://www.sciencedirect.com/science/article/B6TJM-43CK059-M/1/95c4f953856a6ea6c85bcb87e36fd005. 35

[21] Friedl, M. et al., *The Belle II Silicon Vertex Detector readout chain*, Journal of Instrumentation, 8(02) (2013) C02037, URL http://stacks.iop.org/1748-0221/8/i=02/a=C02037. 35

[22] Bergauer, T. et al., *Recent Progress in Sensor- and Mechanics-R&D for the Belle II Silicon Vertex Detector*, Nuclear Instruments and Methods in Physics Research A,

Proceedings Elba Conference, URL http://www.hephy.at/fileadmin/user_upload/Publikationen/bergauer_elba2012.pdf. 37

[23] Friedl, M. et al., *The silicon vertex detector of the Belle II experiment*, Nucl. Instrum. Methods Phys. Res., Sect. A, 628 (2011) 103–106, URL http://www.sciencedirect.com/science/article/pii/S0168900210014853. 41

[24] Frankenberger, A., *Cooling of the Belle II SVD*, Master's thesis, University of Vienna (to be published 2013). 42, 43

[25] Lutz, G., *Semiconductor Radiation Detectors: Device Physics*, Springer, Berlin (2007), ISBN 3540716785. 46, 63, 65, 66, 73, 79, 80

[26] Dragicevic, M., *The New Silicon Strip Detectors for the CMS Tracker Upgrade*, Ph.D. thesis, University of Technology Vienna (2010). 47, 51, 52, 62, 67, 72, 74, 75, 76, 102, 109, 111, 113, 118, 140, 227

[27] Sze, S. M., *Physics of Semiconductor Devices*, Wiley & Sons (1981), ISBN 0471056618. 48, 53, 54, 64, 70

[28] Yao, W.-M. et al., *Review of Particle Physics – Passage of particles through matter*, Journal of Physics G, 33, URL http://pdg.lbl.gov. 57, 58, 59, 82, 84

[29] Barberis, E. et al., *Capacitances in silicon microstrip detectors*, Nucl. Instrum. Methods Phys. Res., Sect. A, 342 (1994) 90–95, URL http://scipp.ucsc.edu/outreach/hartmut/Pubs/NIMA342_Cap.pdf. 67, 88, 192

[30] Haba, J. (editor) *Letter of Intent for KEK Super B Factory, Part II: Detector*, KEK Report 04-4 (2004). 79

[31] Fretwurst, E. et al., *Radiation Damage in Silicon Detectors Caused by Hadronic and Electromagnetic Irradiation arXiv:physics/0211118 [physics.ins-det]*, DESY 02-199 physics/0211118, pp. 1–35, URL http://arxiv.org/abs/physics/0211118. 79

[32] Kemmer, J., *Fabrication of low noise silicon radiation detectors by the planar process*, Nuclear Inst. and Methods, 169(3) (1980) 499–502. 81

[33] Ramo, S., *Currents Induced by Electron Motion*, Proceedings of the IRE, 27(9) (1939) 584–585, ISSN 0096-8390, URL http://ieeexplore.ieee.org/xpl/articleDetails.jsp?arnumber=1686997. 82, 85, 97, 286

[34] Landau, D., *On the Energy Loss of Fast Particles by Ionization*, *Collected Papers of L. D. Landau*, Pergamon Press, Oxford (1965). 82

[35] Bichsel, H., *Straggling in thin silicon detectors*, Reviews of Modern Physics, 60(3) (1988) 664–669. 82

[36] Friedl, M., Bauer, T. and Krammer, M., *A simple model of charge collection in silicon detectors*, Nuclear Instruments and Methods in Physics Research A, 461 (2001) 192–196, URL http://www.sciencedirect.com/science/article/B6TJM-430WX8M-20/1/ddc195950f8878efb8683f2d6a5efa6d. 85, 86

[37] Bergauer, T., *Design, construction and commissioning of the CMS tracker at CERN and proposed improvements for detectors at the future International Linear Collider*, Ph.D. thesis, University of Technology Vienna (2008), URL http://www.hephy.at/fileadmin/user_upload/Publikationen/diss.pdf. 88, 149, 154, 198, 227

[38] Turchetta, R., *Spatial resolution of silicon microstrip detectors*, Nuclear Instruments and Methods in Physics Research Section A: Accelerators, Spectrometers, Detectors and Associated Equipment, 335(1-2) (1993) 44–58, ISSN 0168-9002, URL http://www.sciencedirect.com/science/article/pii/016890029390255G. 93, 94

[39] Friedl, M., *Lorentz angle and revisited windmill direction* (2011), talk at the Open Meeting of the Belle II Collaboration. 97, 98, 99

[40] Hartmann, F., *Evolution of Silicon Sensor Technology in Particle Physics*, vol. 231 of *0081-3869*, Springer Tracts in Modern Physics (2009), URL http://link.springer.com/book/10.1007/b106762/page/1. 100

[41] Treberspurg, W. et al., *Measuring doping profiles of silicon detectors with a custom-designed probe station*, Journal of Instrumentation, 7(11) (2012) P11009, URL http://iopscience.iop.org/1748-0221/7/11/P11009. 103, 104

[42] Hilleringmann, U., *Silizium-Halbleitertechnologie*, Teubner, Wiesbaden (2004). 107, 108, 109

[43] Mentor Graphics, *The EDA Technology Leader*, URL http://www.mentor.com. 117

[44] *KLayout - High Performance Layout Viewer And Editor*, URL http://www.klayout.de. 118, 227

[45] Unno, Y. et al., *Evaluation of p-stop structures in the n-side of n-on-n silicon strip detector*, Nuclear Science, IEEE Transactions on, 45(3) (1998) 401–405, ISSN 0018-9499, URL http://ieeexplore.ieee.org/xpls/abs_all.jsp?arnumber=682416. 136, 138, 182, 227

[46] Iwata, Y. et al., *Optimal p-stop pattern for the N-side strip isolation of silicon microstrip detectors*, Nuclear Science, IEEE Transactions on, 45(3) (1998) 303–309, ISSN 0018-9499, URL http://ieeexplore.ieee.org/xpls/abs_all.jsp?arnumber=682398. 136, 138, 167, 182, 227

[47] Bergauer, T., *Process Quality Control of Silicon Strip Detectors for the CMS Tracker*, Master's thesis, Vienna University of Technology (2004), URL http://bergi.hephy.at/papers/diploma_thesis_bergauer.pdf. 140

[48] Friedl, M., *TRHX Temperature and Humidity Measurement System Project* (2001), URL `http://www.hephy.at/project/electronic2/ELEC2/index.html`. 149, 292

[49] SCK•CEN, *Studiecentrum voor Kernenergie • Centre d'Etude de l'énergie Nucléaire*, URL `http://www.sckcen.be`. 158

[50] Jones, L., *APV25-S1 User Guide Version 2.2*, RAL Microelectronics Design Group (2001), URL `http://www.te.rl.ac.uk/med/projects/High_Energy_Physics/CMS/APV25-S1/pdf/User_Guide_2.2.pdf`. 163

[51] Treberspurg, W., *The developement of a Spreading Resistance Profiling measurement station*, *Proceedings of the 13th ICATPP Conference on Astroparticle, Particle, Space Physics and Detectors for Physics Applications, Como* (2011). 178

[52] Leitl, B., *Interstrip capacitance measurements on double sided silicon strip sensors*, Master's thesis, University of Technology Vienna (2013). 180

[53] Frühwirth, R. et al., *Analysis of beam test data by global optimization methods*, Nucl. Instrum. Methods Phys. Res., Sect. A, in press (2013) 1, URL `http://www.sciencedirect.com/science/article/pii/S0168900213006165`. 193, 194

[54] Dolejschi, P., *Characterisation of interstrip parameters on silicon sensors for the Belle II vertex detector*, Master's thesis, Vienna University of Technology (2012), URL `http://www.hephy.at/fileadmin/user_upload/Publikationen/Diplomarbeit%20Paul.pdf`. 204

[55] Treberspurg, W., *Manufacturing Process of Silicon Strip Sensors and Analysis of Detector Structures*, Master's thesis, Vienna University of Technology (2011), URL `http://www.hephy.at/forschung/alle/publikationen/diplomarbeiten/?no_cache=1&user_publikationen_pi1%5Bitem%5D=211`. 205

[56] Hara, T., Kuhr, T. and Ushiroda, Y., *Belle II Coordinate System and Guidline of Belle II Numbering Scheme*, Belle II Note, 1 (2011) 1–3, URL `https://belle2.cc.kek.jp/~twiki/pub/Archive/Belle2note0009/Belle2NumberingScheme.pdf`. 233

[57] Lutz, O., *Search for* $B \to h^{(*)}\nu\bar{\nu}$ *decays at Belle and Development of Track Finding for Belle II*, Ph.D. thesis, Fakultät für Physik des Karlsruher Institut für Technologie (KIT) (2012), URL `http://d-nb.info/1029320659/34`. 236, 237

[58] *Wikipedia – The free encyclopedia*, URL `www.wikipedia.org`. 261

Manfred Valentan

HEPHY Vienna

Nikolsdorfer Gasse 18
1050 Wien, Austria
+43-680-1127359
+43-1-544 73 28-36
FAX +43-1-544 73 28-54
manfred.valentan@oeaw.ac.at
www.hephy.at

Personal data

Date of birth	18.02.1983
Place of birth	Graz, Austria
Nationality	Austria
Marital status	unmarried

Education

2009-present	**Postgraduate studies**, *University of Technology*, Vienna. Persued academic grade: PhD in technical sciences
2007	**Erasmus semester**, *Universidad Autónoma de Madrid*, Spain.
2003-2009	**Studies of Technical Physics**, *University of Technology*, Vienna. Academic grade: Master of Science in technical physics
2002-2003	**Studies of Technical Physics**, *University of Technology*, Graz.
2002	**Higher Technological College for Mechanical Engineering and Automation**, *Kaindorf/Sulm*, A-Levels.

PhD thesis

Title *The Silicon Vertex Detector for b-tagging at Belle II*

Master thesis

Title *Tracking detector optimization for collider experiments with fast simulation and by analytical methods*

Employment

2009-2013 **Scientific associate**, *Institute for High Energy Physics (abbrev. HEPHY) of the Austrian Academy of Sciences*, Vienna, Austria.
group: Semiconductor Detector Development

2007-2009 **Scientific assistant**, *HEPHY*, Vienna, Austria.
group: Algorithms and Software Development

Professional Activities

2009–present Development of the Silicon Vertex Detector (SVD) of the Belle II experiment at KEK (Japan)

2007–2009 Work for the International Large Detector (ILD) at the International Linear Collider (ILC)

Teaching

2009–present Tutor of laboratory courses on experimental particle physics

Publications

2013 **Performance Studies on the Ohmic Side of Silicon Microstrip Sensors**, *Proceedings of the 13$^{\text{th}}$ Vienna Conference on Instrumentation*, to be published in Nucl. Instrum. Meth. A, main author.

Analysis of beam test data by global optimization methods, *Proceedings of the 13$^{\text{th}}$ Vienna Conference on Instrumentation*, to be published in Nucl. Instrum. Meth. A, contributing author.

The Belle II Silicon Vertex Detector readout chain , *JINST 8 C02037*, contributing author.

Comparing Spreading Resistance Profiling and C-V Characterisation to Identify Defects in Silicon Sensors, *JINST 8 C02018*, contributing author.

Interstrip Parameters on Silicon Sensors for the Belle II Vertex Detector, *Nucl. Instrum. Meth. A*, contributing author.

Origami chip-on-sensor design: progress and new developments, *JINST 8 C01014*, contributing author.

2012 **Comparison of n-side strip isolation methods for silicon sensors**, *Journal of Instrumentation, Volume 7, Issue 11, November 2012*, main author.

Recent Progress in Sensor- and Mechanics-R&D for the Belle II Silicon Vertex Detector, *Nucl. Instrum. Meth. A*, contributing author.

The Belle II Silicon Vertex Detector, *Physics Procedia 37 (2012) 867 - 873*, contributing author.

Measuring Doping Profiles of Silicon Detectors with a Custom-designed Probe Station, *JINST*, contributing author.

The Silicon Vertex Detector of Belle II, *Science PoS(Vertex 2011) 022*, contributing author.

2011 **The LiC Detector Toy fast simulation program**, *Proceedings Of Science, Vertex 2011*, main author.

Optimization of Strip Isolation for Silicon Sensors, *Physics Procedia TIPP 2011*, main author.

2010 **Electronics and Mechanics for the Silicon Vertex Detector of the Belle II Experiment**, *JINST, Volume 5, 2010*, contributing author.

Belle II Technical Design Report, *KEK Report 2010-1*, contributing author.

The Silicon Vertex Detector of the Belle II experiment, *Nucl. Instrum. Meth. A Vol. 628, Iss. 1, 2011, 103-106*, contributing author.

Silicon Strip Sensors with integrated pitch adapters, *EUDET Memo*, contributing author.

2009 **Generalization of the Gluckstern formulas II: Multiple scattering and non-zero dip angles**, *Nucl. Instrum. Meth. A606 (2009) 728 - 742*, main author.

The International Large Detector - Letter of Intent, *DESY 2009-87 / Fermilab-Pub-09-682-E / KEK Report 2009-6*, contributing author.

2008 **LiC Detector Toy - Tracking detector optimization with fast simulation and its application to the ILD design**, *Proceedings of LCWS 2008, Chicago*, main author.

Invited Talks at Conferences

June 2011 **The LiC Detector Toy fast simulation program**, *International Workshop on Vertex Detectors*, Rust, Austria.

Schools & Internships

2011 **TCAD Introduction Course**, *Rutherford Appleton Laboratory*, Oxfordshire, England.

2010 **GEANT4 und ROOT Workshop**, *DESY*, Hamburg, Germany.

2008 **CERN School of Computing**, *Gjøvik*, Norway.

2006 **DESY Summer Student**, *within the MSK (Maschinen-Strahlkontrolle) Group*, Hamburg, Germany.

Languages

German	**mother tongue**
English	**fluent**
Spanish	**advanced knowledge**

Computer skills

OS	Windows, OSX
Scientific	Labview, LaTeX
Graphics	AutoCAD, Inkscape
Programming	Matlab (advanced knowledge), C/C++ (basic knowledge)

Private Interests

Music	13 years of musical education on string instruments made their way into my daily life in form of songwriting, playing in a band, collecting vinyl records, and dancing (Salsa, Lindy Hop, Rock 'n' Roll Acrobatics)
Cycling	For the daily way to work and for excursions
Volleyball	Indoors and outdoors
T-shirt designs	`www.redegewand.at`

Last update: June 12, 2013